

**UNIVERSIDADE DE LISBOA  
INSTITUTO SUPERIOR TÉCNICO**

**Monte Carlo Algorithms for  
Low-Temperature Plasmas**

**Tiago Cunha Dias**

**Supervisor:** Doctor Vasco António Dinis Leitão Guerra

**Co-Supervisors:** Doctor Milan Šimek  
Doctor Olivier Guaitella

Thesis approved in public session to obtain the PhD Degree in  
**Technological Physics Engineering**

Jury final classification: **Pass with Distinction and Honour**

**2023**



**UNIVERSIDADE DE LISBOA  
INSTITUTO SUPERIOR TÉCNICO**

**Monte Carlo Algorithms for  
Low-Temperature Plasmas**

**Tiago Cunha Dias**

**Supervisor:** Doctor Vasco António Dinis Leitão Guerra

**Co-Supervisors:** Doctor Milan Šimek  
Doctor Olivier Guaitella

Thesis approved in public session to obtain the PhD Degree in  
**Technological Physics Engineering**

Jury final classification: **Pass with Distinction and Honour**

**Jury**

**Chairperson:** Doctor Luís Paulo da Mota Capitão Lemos Alves, Instituto Superior Técnico, Universidade de Lisboa

**Members of the Committee:**

Doctor Saša Dujko, Laboratory for non-equilibrium processes and plasma applications, Institute of Physics Belgrade, National Institute of the Republic of Serbia, Sérvia  
Doctor Vasco António Dinis Leitão Guerra, Instituto Superior Técnico, Universidade de Lisboa

Doctor Zdeněk Bonaventura, Faculty of Science, Masaryk University, República Checa  
Doctor Pedro Arsénio Nunes Aleixo Viegas, Instituto Superior Técnico, Universidade de Lisboa

**Funding Institution**

Fundaçao para a Ciênciа e a Tecnologia



# Acknowledgments

This work was supported by the Portuguese FCT - Fundação para a Ciência e a Tecnologia, under projects PTDC/FISPLA/1616/2021, MIT-EXPL/ACC/0031/2021, UIDB/50010/2020 and UIDP/50010/2020, and grant PD/BD/150414/2019.



# Abstract

The main aim of this thesis is to develop and employ Monte Carlo (MC) modelling techniques for the investigation and taming of low-temperature plasmas (LTPs). MC methods simulate physical systems by tracking the temporal evolution of test particles. The stochastic evolution is performed by generating random numbers sampled from distributions that emulate the underlying physics. In Chapter 2, we present a MC method for solving the complex chemical kinetics of heavy species in LTPs. Additionally, novel variance reduction methods are developed to improve the description of minority species without impacting computation time. In Chapter 3, we present the first version of the LoKI-MC open-source code, which addresses electron kinetics in a gas discharge subjected to a uniform DC electric field. In Chapter 4, we expand the LoKI-MC capabilities to include anisotropic scattering in any collision type. Moreover, we demonstrate that the inclusion of anisotropic scattering in rotational collisions with H<sub>2</sub>O molecules is fundamental to obtain accurate agreement between modelling and experiment. In Chapter 5, we extend the formulation to configurations involving AC/DC electric and DC magnetic fields. The code is thoroughly verified, and novel benchmark calculations are produced. Additionally, we analyze the impact of magnetic fields in detail, distinguishing between configurations with DC and AC electric fields. Finally, in Chapter 6, we consider the rigorous time-dependent MC solution as the gold standard to evaluate the accuracy of two common assumptions for solving space- and time- dependent electron kinetics: the local-field approximation (LFA) and the local-energy approximation (LEA). The study focuses on homogeneous electron kinetics in nanosecond-pulsed discharges. It is observed that the LEA generally provides more accurate results than the LFA. In general, the methods presented in this thesis allowed for a better understanding of LTPs and an assessment of the accuracy of common approximations used in LTP modelling.

# Keywords

Low-temperature plasmas; Monte Carlo modelling; electron kinetics; two-term approximation; time-locality assumptions.



# Resumo

O principal objetivo desta tese é desenvolver e aplicar técnicas de modelização de Monte Carlo (MC) para investigação e controlo de plasmas de baixa temperatura (LTPs). Os métodos de MC simulam sistemas físicos rastreando a evolução temporal de partículas de teste. A evolução estocástica é realizada gerando números aleatórios amostrados de distribuições que descrevem a física subjacente. No Capítulo 2, apresentamos um método de MC para resolver a cinética química de espécies pesadas em LTPs. Além disso, novos métodos de redução de variância são desenvolvidos para melhorar a descrição de espécies minoritárias sem afetar o tempo de cálculo. No Capítulo 3, apresentamos a primeira versão do código aberto LoKI-MC, que aborda a cinética eletrónica numa descarga de gás sujeita a um campo elétrico DC. No Capítulo 4, expandimos as capacidades do LoKI-MC para incluir espalhamento anisotrópico em qualquer tipo de colisão. Adicionalmente, demonstramos que a inclusão de espalhamento anisotrópico em colisões rotacionais com moléculas de H<sub>2</sub>O é fundamental para obter acordo entre modelização e experiência. No Capítulo 5, estendemos a formulação para campos elétricos AC/DC e magnéticos DC. O código é minuciosamente verificado, e novos cálculos de referência são produzidos. Além disso, analisamos o impacto do campo magnético em detalhe, distinguindo entre configurações com campos elétricos DC e AC. Finalmente, no Capítulo 6, consideramos a solução de MC estritamente dependente do tempo como padrão para avaliar a precisão de duas suposições comuns para resolver a cinética eletrónica espaço-temporal: a aproximação do campo local (LFA) e a aproximação de energia local (LEA). O estudo concentra-se na cinética eletrónica homogénea em descargas pulsadas de nanosegundos. Observa-se que a LEA fornece resultados mais precisos do que a LFA. Em geral, os métodos apresentados nesta tese permitiram uma melhor compreensão dos LTPs e uma avaliação da precisão de aproximações usadas na modelização de LTPs.

# Palavras Chave

Plasmas de baixa temperatura; modelização de Monte Carlo; cinética eletrónica; aproximação de dois termos; aproximações de localidade temporal.



# Contents

Acknowledgments . . . . .	i
Abstract . . . . .	iii
Resumo . . . . .	v
Contents . . . . .	vii
List of Figures . . . . .	xi
List of Tables . . . . .	xvii
<b>1 Introduction</b>	<b>1</b>
1.1 Importance of modelling low-temperature plasmas . . . . .	2
1.2 Thesis outline . . . . .	3
1.3 Scientific contributions . . . . .	4
References . . . . .	5
<b>2 Kinetic Monte Carlo simulations of plasma chemistry</b>	<b>9</b>
2.1 Introduction . . . . .	10
2.2 Stochastic description . . . . .	11
2.3 Kinetic Monte Carlo algorithm . . . . .	12
2.4 Validation . . . . .	13
2.5 Variance Reduction . . . . .	17
2.5.1 Equal Reaction Weights . . . . .	17
2.5.2 Variable Species Weights . . . . .	19
2.5.3 Comparison . . . . .	19
2.6 Conclusions . . . . .	23
References . . . . .	23
<b>3 The LisbOn KInetics Monte Carlo solver</b>	<b>27</b>
3.1 Introduction . . . . .	28
3.2 Methods . . . . .	29
3.2.1 Cross sections . . . . .	30
3.2.2 Free flight . . . . .	31

3.2.3	Collision choice . . . . .	32
3.2.4	Conservative collisions . . . . .	33
3.2.5	Non-conservative collisions . . . . .	35
3.2.6	Asynchronous advancement of electrons . . . . .	37
3.2.7	Data sampling . . . . .	38
3.2.8	Stopping criteria . . . . .	43
3.3	The LoKI-MC code . . . . .	44
3.3.1	Input . . . . .	44
3.3.2	Output . . . . .	45
3.4	Results . . . . .	45
3.4.1	Verifications in model gases . . . . .	45
3.4.2	Benchmark in real gases . . . . .	48
3.4.2.A	Molecular gas: oxygen . . . . .	48
3.4.2.B	Atomic gas: argon . . . . .	52
3.4.3	Anisotropies . . . . .	54
3.4.4	Anisotropic ionization scattering induced by momentum conservation . . . . .	56
3.4.5	Effects of superelastic collisions . . . . .	57
3.4.6	Computation time . . . . .	59
3.5	Final remarks and future work . . . . .	62
	References . . . . .	62
<b>4</b>	<b>The role of anisotropic scattering in electron-neutral collisions: H<sub>2</sub>O rotational collisions as an example</b>	<b>69</b>
4.1	Introduction . . . . .	70
4.2	Angular distribution of dipole rotational collisions . . . . .	70
4.3	Anisotropic scattering in a two-term Boltzmann solver . . . . .	72
4.4	Anisotropic scattering in a Monte Carlo solver . . . . .	74
4.5	Anisotropic Cross Section Set . . . . .	75
4.6	Validation . . . . .	76
4.7	The importance of rotational collisions in H <sub>2</sub> O . . . . .	81
4.8	Conclusion . . . . .	82
	References . . . . .	84
<b>5</b>	<b>Exploring the electron kinetics under magnetic field and AC/DC electric fields</b>	<b>91</b>
5.1	Introduction . . . . .	92
5.2	Electron free flight under electric and magnetic fields . . . . .	93
5.3	Results and discussion . . . . .	93

5.3.1	DC electric field . . . . .	94
5.3.2	AC electric field: phenomenon of electron cyclotron resonance . . . . .	99
5.4	Final remarks . . . . .	104
5.A	Integration of the collision-free motion . . . . .	106
5.B	Benchmark with $B = 0$ and AC electric field . . . . .	107
	References . . . . .	108
<b>6</b>	<b>A close look at time-locality assumptions in nanosecond discharges</b>	<b>111</b>
6.1	Introduction . . . . .	112
6.2	Theoretical background . . . . .	113
6.2.1	Problem statement . . . . .	113
6.2.2	Monte Carlo time-dependent solver . . . . .	114
6.2.3	The local-field and local-energy approximations . . . . .	115
6.2.4	Two-term time-dependent solver . . . . .	116
6.3	Results . . . . .	117
6.3.1	Electron swarm coefficients . . . . .	117
6.3.2	Characteristic relaxation frequencies . . . . .	121
6.3.3	Distribution functions . . . . .	124
6.4	Final remarks . . . . .	127
	References . . . . .	128
<b>7</b>	<b>Conclusion</b>	<b>131</b>
	References . . . . .	136



# List of Figures

2.1	Temporal evolution of O <sub>2</sub> (X), O <sub>2</sub> (a), O( <sup>3</sup> P), comparing KMC (10 <sup>6</sup> particles) with deterministic LoKI simulations. . . . .	14
2.2	Temporal evolution of O <sub>2</sub> (b), comparing KMC with deterministic LoKI simulations. . . . .	15
2.3	Temporal evolution of O <sub>3</sub> (X), comparing KMC with deterministic LoKI simulations. . . . .	15
2.4	Temporal evolution of O( <sup>1</sup> D), comparing KMC with deterministic LoKI simulations. . . . .	16
2.5	Relative error of the species densities ( $\Delta_{rel}$ ) as a function of the initial number of particles in the simulation. . . . .	16
2.6	Relative error of the species densities ( $\Delta_{rel}$ ) as a function of the number of particles weighted by the deterministic fraction. . . . .	17
2.7	Reaction selection: standard (a) and ERW (b) methods. . . . .	18
2.8	Temporal evolution of the various species, comparing KMC with/without variance reduction and using 10 <sup>8</sup> particles. . . . .	20
2.8	Temporal evolution of the various species, comparing KMC with/without variance reduction and using 10 <sup>8</sup> particles. Continuation. . . . .	21
2.9	Temporal evolution of O <sup>+</sup> (10 <sup>8</sup> particles) for different O <sup>+</sup> weights. . . . .	22
3.1	Example of stochastic trajectory of one electron with one collision. Taken from [32]. . . . .	30
3.2	Selection of the collision type. . . . .	33
3.3	Normalized values of the ejected electron energy, $\frac{\epsilon_{ei}}{\epsilon - \Delta\epsilon_{ion}}$ , and the scattered electron energy, $\frac{\epsilon'}{\epsilon - \Delta\epsilon_{ion}}$ , as a function of the unit uniform random number $p_{ion}$ , and for different incident electron energies $\epsilon$ , when using the SDCS proposed by Opal <i>et al</i> [43]. . . . .	36
3.4	Example of the temporal evolution of the swarm energy (O <sub>2</sub> , E/N = 10 Td, p = 133.32 Pa, $T_g$ = 300 K), comparing the newly implemented asynchronous advancement of electrons with the old synchronous advancement implemented in LoKI-MC 1.0.0. The steady-state time is $\simeq 0.6 \mu s$ . . . . .	38

3.5	Example of the temporal evolution of the swarm mean position (a) and mean squared width (b), in the same conditions as figure 3.4. The bulk transport coefficients are determined from the slopes of the lines (see text). . . . .	41
3.6	Electron energy distribution functions obtained in LoKI-MC using the Druyvesteyn model for $E/N$ values from 1 to 20 Td. . . . .	46
3.7	Temporal evolution of the swarm energy in zero-field conditions for three initial electron temperatures ( $0.5T_g$ , $T_g$ , $1.5T_g$ , with $T_g = 300$ K), with and without the gas-temperature effect. . . . .	48
3.8	Comparison of the steady-state EEDF, in zero-field conditions, with the theoretical Maxwellian at 300 K. . . . .	48
3.9	Electron energy distribution functions in oxygen obtained with LoKI-MC and LoKI-B (two-term solver), for various reduced electric fields: (a) 0.01 - 10 Td; (b) 50 - 1000 Td. .	48
3.10	Electron swarm coefficients in molecular oxygen ( $T_g = 300$ K) as a function of $E/N$ , obtained with LoKI-MC and LoKI-B (2-term solver): (a) reduced mobility, $\mu N$ ; (b) reduced transverse diffusion coefficient, $D_{\perp}N$ ; (c) characteristic energy, $\epsilon_{\text{char}}$ ; (d) temperature, $T_e$ ; (e) ionization rate-coefficient, $k_{\text{ion}}$ ; (f) attachment rate-coefficient, $k_{\text{att}}$ . . . . .	50
3.11	Two-term errors in molecular oxygen, defined as $\frac{\text{2-term-MC}}{\text{MC}}$ , for $\mu^f N$ , $D_{\perp}^f N$ , $T_e$ , $k_{\text{ion}}$ and $k_{\text{att}}$ . . . . .	51
3.12	Normalized electron power transferred to various channels in oxygen, as a function of the reduced electric field. The positive and negative values correspond, respectively, to electron energy gain and loss. . . . .	51
3.13	Electron energy distribution functions in argon, obtained with LoKI-MC, LoKI-B (2-term solver) and MultiBolt (10-term solver) for various reduced electric fields: (a) 1-20 Td; (b) 50-1000 Td. . . . .	52
3.14	Electron swarm coefficients in argon ( $T_g = 300$ K) as a function of $E/N$ , obtained with LoKI-MC, LoKI-B (2-term solver) and MultiBolt (10-term solver): (a) reduced mobility; (b) reduced transverse diffusion coefficient; (c) characteristic energy; (d) temperature; (e) ionization rate coefficient; (f) reduced longitudinal diffusion coefficient. . . . .	53
3.15	Two-term errors in argon, defined as $\frac{\text{2-term-MC}}{\text{MC}}$ , for $\mu^f N$ , $D_{\perp}^f N$ , $T_e$ and $k_{\text{ion}}$ . . . . .	54
3.16	Electron velocity distribution function ( $\text{m}^{-3}\text{s}^3$ ) in molecular oxygen for the following $E/N$ values: (a) 10 Td; (b) 500 Td. . . . .	55
3.17	Average anisotropy ratios in oxygen and argon, as a function of $E/N$ : $\frac{\langle f_1 \rangle}{\langle f_0 \rangle}$ (full lines); $\frac{\langle f_2 \rangle}{\langle f_0 \rangle}$ (dashed). . . . .	55
3.18	Electron energy distribution functions in argon using isotropic (black) and anisotropic (blue) scattering in ionization events, at various $E/N = 500, 800$ and $1000$ Td. . . . .	56

3.19 Transport coefficients in argon, as a function of $E/N$ , using isotropic and anisotropic scattering in ionization events: (a) reduced mobility; (b) reduced transverse (full lines) and longitudinal (dashed) flux diffusion coefficients; (c) reduced transverse (full lines) and longitudinal (dashed) bulk diffusion coefficients. . . . .	57
3.20 Electron energy distribution functions in oxygen at $E/N = 50$ Td, for different fractions $[O_2(a)]/N$ . . . . .	58
3.21 Electron energy distribution functions in nitrogen at $E/N = 50$ Td, for different vibrational temperatures $T_v$ . . . . .	58
3.22 Monte Carlo computation times using LoKI-MC and METHES [20], with (a) $10^4$ and (b) $10^6$ electrons, in argon at $E/N = 500$ Td, as a function of the total number of simulated collisions. . . . .	61
3.23 Ratio of the computation times, METHES/LoKI-MC, with (a) $10^4$ and (b) $10^6$ electrons, in argon at $E/N = 500$ Td, as a function of the total number of simulated collisions. . . . .	61
3.24 Comparison between the speedup factor of LoKI-MC, $S_{\text{LoKI-MC}}$ , and the theoretical Am-dahl formula, $S_{\text{th}}(\tau)$ , presented in the text. . . . .	61
4.1 Angular distribution function $I_i(\varepsilon, \theta)$ from dipole-Born theory, for the rotational transition in water from $(J, \tau) = (1, -1)$ to $(J', \tau') = (1, 1)$ , whose threshold is $V_{J\tau, J'\tau'} = 0.0023$ eV. . . . .	72
4.2 Proposed cross sections $\sigma$ , plotted against the electron energy $\varepsilon$ , divided into conservative and non-conservative collisional processes. ICS and MTCS (dashed lines) are the sums of all individual rotational cross sections weighted by the populations of the lower rotational levels assuming a Boltzmann distribution at 293 K. In the left-side panel, the elastic and rotational cross section extend down to sub-meV range which is not shown for better visibility of the remaining conservative collision cross sections. CSs are obtained from [18, 32–41]. See the main text and [7] for more details. . . . .	77
4.3 Illustration of differences in rotational cross sections $\sigma$ by means of the rotational transition $(JK'K'') = (000) \rightarrow (111)$ . Dashed lines correspond to CSs that we recommend either here (light blue lines) or in our isotropic set (grey line) [7]. The dash-dotted dark blue line is taken from Faure, Gorfinkel, and Tennyson [42] and the solid green line from Song et al. [31]. . . . .	77

4.4	Comparison of experimental transport coefficients (markers), when known with error bars, with those obtained from LoKI-B or LoKI-MC simulations with the proposed isotropic [7] and anisotropic cross section sets (lines). References to the experimental transport coefficients can be found in the text. As indicated by the arrows in the centre two panels, $v_D$ , $\mu N$ and $\varepsilon_{\text{char}}$ are calculated assuming temporal growth of the electron number while for $\alpha/N$ and $\eta/N$ spatial growth is assumed. LoKI-B provides exclusively flux transport coefficients and all shown LoKI-MC results include anisotropic rotational scattering. . . . .	80
4.5	Longitudinal diffusion coefficient times gas number density $D_L N$ against the reduced electric field $E/N$ in water vapour from literature and calculations with Monte Carlo simulation tool LoKI-MC [52, 61]. . . . .	81
4.6	EEDFs of water vapour as calculated with the present cross sections using either LoKI-B (dashed) or LoKI-MC (solid) for four different reduced electric fields. The inset on the top right shows the very low energy part of the same EEDFs. . . . .	82
4.7	Normalized electron power transferred to various channels in $H_2O$ , as a function of the reduced electric field. The positive and negative values correspond, respectively, to electron energy gain and loss. . . . .	83
4.8	Average anisotropy ratios in $H_2O$ , as a function of $E/N$ : $\frac{\langle  f_1  \rangle}{\langle f_0 \rangle}$ (black full lines); $\frac{\langle  f_2  \rangle}{\langle f_0 \rangle}$ (red dashed). . . . .	83
5.1	Electron mean energy $\langle \epsilon \rangle$ , drift velocity $v_{d,i}$ and diffusion coefficients $ND_{ij}$ , in the Reid-ramp model, as a function of $B/N$ , for $E/N = 12$ Td and $\Psi = 90^\circ$ . The calculations are compared with the MC results of Raspopovic et al. [1]. . . . .	97
5.2	Electron mean energy $\langle \epsilon \rangle$ , bulk drift speed $\ v_d^b\ $ and ionization coefficient $k_{\text{ion}}$ , in the Lucas-Saelee model, as a function of $\Psi$ , for $E/N = 10$ Td, $B/N = 200, 1000$ Hx and $F = 0, 0.5, 1$ . The calculations are compared with the MC results of Dujko et al. [2]. . . . .	97
5.3	Electron mean energy $\langle \epsilon \rangle$ and reduced Townsend coefficient $\alpha/N$ , in $N_2$ (a) and Ar (b), as a function of $E/N$ , for various $B/N$ . For $N_2$ , $\alpha/N$ is compared against experiments [31]. . . . .	97
5.4	Electron mean energy $\langle \epsilon \rangle$ , in $N_2$ (a) and Ar (b), as a function of $E/N$ , for $B/N = 0 - 50000$ Hx. In $N_2$ , the results for $B/N = 0$ and 10 Hx are almost superposed. The black-dashed lines represent the results with null $B$ and an effective AC E-field. . . . .	98
5.5	Electron-impact cross sections in Ar, available at the IST-Lisbon database of LXCat [30]. . . . .	98
5.6	Temporal evolution of the electron swarm energy ( $\epsilon$ ) in $N_2$ , for $E/N = 100$ Td and different $B/N$ . The black curves represent the results with null $B$ and an effective AC E-field. . . . .	98
5.7	EEDFs in $N_2$ (a) and Ar (b), at $E/N = 100$ Td and $B/N = 0 - 50000$ Hx. The results for $B/N = 0, 10, 100$ Hx are almost superposed. The black-dashed lines represent the results with an effective AC E-field. . . . .	99

5.8	Electron mean energy $\langle \epsilon \rangle$ (a) and reduced electric-field power $\langle P_E/N \rangle$ (b), as a function of $B/N$ , for different excitation frequencies $f$ , in the Reid-ramp model. The results are compared against [9], except for $f = 50$ MHz (value considered here to provide additional insight to the present study). Vertical dotted lines indicate the values of $B/N$ for which ECR occurs. Horizontal dotted lines represent the calculations using a DC electric field with $E_{DC}/N = E_0/N/2 = 10/\sqrt{2}$ Td and null magnetic field, and should match the value at ECR for high frequencies. . . . .	101
5.9	Angle between the electron drift velocity $\mathbf{v}_d$ and the right-hand (a) and left-hand (b) circular electric fields, along the AC period, in the Reid-ramp model. . . . .	102
5.10	Reduced electric-field power absorbed due to the right-hand (a) and left-hand (b) circular fields, along the AC period, in the Reid-ramp model. The horizontal dotted line represents the power due to a DC electric field with $E_{DC}/N = E_0/N/2 = 10/\sqrt{2}$ Td and null $B$ . . . . .	102
5.11	Electron mean energy $\langle \epsilon \rangle$ , as a function of $B/N$ , for different excitation frequencies $f$ , in $N_2$ (a) and Ar (b). Vertical dotted lines indicate the values of $B/N$ for which ECR occurs. Horizontal dotted lines represent the calculations using a DC electric field with $E_{DC}/N = E_0/N/2 = 100/\sqrt{2}$ Td and null $B$ . . . . .	103
5.12	Electron mean energy $\langle \epsilon \rangle$ (left) and reduced electric-field power $\langle P_E/N \rangle$ (right), as a function of $B/N$ , for three sets of $f$ and $N$ values, keeping $\omega/N$ constant, in the Reid-ramp model. . . . .	103
5.13	Time-averaged electron mean energy (a), as a function of $\Psi$ . Electron drift velocity along an AC cycle, in 3D (b), $xy$ plane (c) and $xz$ plane (d), for $\Psi = 0, 30, 60$ and $90^\circ$ . The calculations are made in the Reid-ramp gas, with $f = 400$ MHz, $N = 3.54 \times 10^{22} \text{ m}^3$ and $B/N$ such that $\Omega = \omega$ (resonance conditions). . . . .	104
5.14	Comparison between the LoKI-MC calculations of the mean electron energy and drift velocity and the results from [23], for $B = 0$ , different $\omega/N$ and using the Reid-ramp model. The results are shown as a function of the period phase $\omega t$ and the reduced electric field $-E_z/N$ is shown in yellow. . . . .	108
6.1	Reduced electric field pulse analyzed in this study, as defined by expression (6.1), with $E_0/N = 500$ Td and $t_{\text{pulse}} = 5$ ns. In addition, the figure presents a linear reconstruction of the $E/N$ pulse, achieved by considering intervals between different slopes of 0.05 ns. . . . .	114
6.2	Temporal evolution of the mean electron energy ( $\langle \epsilon \rangle$ ), drift velocity ( $v_d$ ) and ionization coefficient ( $k_{\text{ion}}$ ), in air, at (a) 10 Torr and (b) 100 Torr conditions. . . . .	118
6.3	Temporal evolution of electron-impact $O_2$ dissociation (top), $e + O_2(X) \rightarrow e + 2O(^3P)$ , and $N_2^+$ dissociative recombination (bottom), $e + N_2^+ \rightarrow 2N$ , in air, at (a) 10 Torr and (b) 100 Torr conditions. . . . .	119

6.4	Temporal evolution of the mean electron energy ( $\langle \epsilon \rangle$ ), drift velocity ( $v_d$ ) and ionization coefficient ( $k_{\text{ion}}$ ), in argon, at (a) 10 Torr and (b) 100 Torr conditions. . . . .	120
6.5	Energy-dependent frequencies of momentum transfer ( $\nu_m$ ) and energy relaxation ( $\nu_\epsilon$ ), at 10 Torr, in (a) air and (b) argon. . . . .	122
6.6	Temporal evolution of energy-averaged frequencies of momentum transfer ( $\langle \nu_m \rangle$ , dashed) and energy relaxation ( $\langle \nu_\epsilon \rangle$ , full), at 10 and 100 Torr, in (a) air and (b) argon. The characteristic frequency of $E/N$ variation ( $\nu_{E/N}$ ) is represented with full black lines. . . .	123
6.7	Temporal evolution of $\nu_{E/N}/\langle \nu_m \rangle$ (dashed) and $\nu_{E/N}/\langle \nu_\epsilon \rangle$ (full), at 10 and 100 Torr, in (a) air and (b) argon. . . . .	123
6.8	EEDFs in air, at 10 Torr, for different time instants $t_1 - t_6$ . . . . .	125
6.9	EEDFs in argon, at 10 Torr, for different time instants $t_1 - t_6$ . . . . .	126

# List of Tables

3.1	Comparison of LoKI-MC solutions with MultiBolt calculations [19] and previous MC results [47, 53], for the Reid-ramp model [41]. The standard deviations $\sigma[\%]$ of the LoKI-MC simulations are shown in squared parenthesis. The deviations $\delta$ between LoKI-MC results (LMC) and previous results (PR), defined as $\delta[\%] = (1 - PR/LMC) \times 100$ , are shown in curved parenthesis. . . . .	47
3.2	Comparison of the LoKI-MC solutions with the MultiBolt calculations [19] and previous MC results [47, 49], for the Lucas-Saelee model. The LoKI-MC standard deviations $\sigma[\%]$ and the errors $\delta[\%]$ are calculated and presented as in table 3.1. . . . .	47
5.1	List of the AC frequencies $f$ (in MHz), reduced angular frequencies $\omega/N$ (in $10^{-14}\text{rad s}^{-1} \text{m}^3$ ) and $(\omega/N)/k_m^{\text{typ}}$ (in $10^{-14}\text{rad}$ ), in the Reid-ramp model, N <sub>2</sub> and Ar. The gas density is $N = 3.54 \times 10^{22}\text{m}^3$ . In the Reid-ramp model, $E_{\text{rms}}/N = 10 \text{ Td}$ , while in N <sub>2</sub> and Ar, $E_{\text{rms}}/N = 100 \text{ Td}$ . . . . .	103



# 1

## Introduction

## 1.1 Importance of modelling low-temperature plasmas

Low-temperature plasmas (LTPs), often referred to as non-equilibrium or cold plasmas, exhibit unique features and advantages that make them invaluable in a wide range of applications. These plasmas are marked by their strong reactivity, featuring a low density of charged particles (ionization degrees  $\sim 10^{-6}$ – $10^{-3}$ ), high electron temperature ( $\sim 1$  eV) and heavy-species translational and internal temperatures ranging from 300 K to  $\sim 10^4$  K. Electrons, being extremely lighter than ions, are more easily accelerated by the electric field. Moreover, due to the low mass ratio between electrons and heavy particles, electrons lose minimal energy during elastic collisions with heavy particles, keeping the high energy acquired from the electric field. High-energy electrons can then lead to excitation of atomic/molecular species (involving electronic, vibrational and rotational levels), dissociation, attachment and ionization. The generated excited states and radicals can activate chemical pathways that are fundamental for many applications.

One key feature of LTPs is the ability to operate at low gas temperatures of  $\sim 300$  K. This characteristic allows for the treatment and modification of temperature-sensitive materials, such as polymers and biological tissues, without causing thermal damage. LTPs also exhibit exceptional control over electron energy distributions, enabling precise control of chemical reactions and surface processes. Another notable advantage of LTPs is that, unlike high-temperature plasmas that require substantial energy input to sustain, LTPs can be generated with relatively low power consumption.

The strong non-equilibrium nature of LTPs can efficiently stimulate several chemical processes relevant for industrial [1, 2], medical [3–5], agricultural [6–8] and environmental [9, 10] applications. However, without knowledge about the fundamental physical processes governing LTPs, we cannot fully unlock their potential. The diversity of temperatures and species within these systems makes understanding them extremely complex. Experimental measurements play an important role in assessing and understanding the behavior of LTPs. Nevertheless, numerical models are essential to complement the experimental knowledge since we cannot experimentally access every information in the plasma operation. Therefore, modelling allows us to simulate plasma behavior consistently with the measured parameters and infer the best framework for a plasma reactor. Moreover, it provides physical insight and can serve as an optimization tool for technological processes.

The general goal of this thesis is to develop and employ Monte Carlo (MC) modelling techniques for the investigation of LTPs. MC methods simulate physical systems by tracking the temporal evolution of multiple test particles. These test particles undergo various primary processes, such as accelerations, collisions or reactions, which are described by generating random numbers sampled from appropriate distributions that emulate the underlying physics. The required random numbers can be calculated using the following theorem from probability theory [11, 12]: given a random number  $r_i$  obtained from a uniform distribution between 0 and 1, a random number  $y_i$  distributed according to the function  $f(y)$  in

$[a, b]$  can be expressed as:

$$\int_a^{y_i} f(x)dx = r_i \int_a^b f(x)dx . \quad (1.1)$$

Once the integrals are computed, this expression transforms into an equation for  $y_i$  which must be solved. Depending on the specific case, the integration and solution of the resulting equation will be carried out either analytically or numerically. Since common computer random-number generator routines can supply the random numbers  $r_i$ , it becomes possible to simulate any physical random process characterized by known probability distributions. The MC technique is simple, direct and exact. However, it can be computationally demanding because the relative error in macroscopic averaged quantities, attributed to statistical fluctuations, decreases slowly with the number  $N_{\text{samp}}$  of samples, typically following  $N_{\text{samp}}^{-1/2}$ , assuming a Poisson distribution. Therefore, efficiency in MC algorithms is essential to gather a substantial amount of statistical data.

## 1.2 Thesis outline

In the general context of LTP modelling, this thesis focuses on the development of MC techniques for studying chemical and electron kinetics. The code developed for electron kinetics (LoKI-MC) is open-source and remains the most versatile MC tool available in the community. The thesis comprises seven chapters, which are as follows:

- The current chapter provides a brief overview of the thesis content.
- Chapter 2 introduces a Kinetic Monte Carlo (KMC) method for solving complex chemical kinetics of heavy species in low-temperature plasmas [13]. This marks the first time that gas-phase chemistry in gas discharges has been approached using a MC method. To mitigate the statistical errors associated with the description of minority species without impacting computation time, two novel variance reduction methods are proposed. These methods result in a substantial improvement in calculation times, approximately on the order of  $10^4$  times faster than the standard KMC approach.
- Chapter 3 presents the first version of the LoKI-MC open-source code [14], which was developed from scratch during this thesis. The code employs MC techniques to address electron transport in a gas subjected to a uniform DC electric field. The chapter delves into the physics underlying the code, verifies the code performance against multiple benchmarks, and showcases the versatility and significance of its features. LoKI-MC is demonstrated to be both accurate and computationally efficient.
- Chapter 4 expands the capabilities of the electron kinetics solver LoKI-MC to include anisotropic scattering in any electron-neutral collision type [15]. The importance of considering anisotropic scattering is illustrated in rotational collisions with H<sub>2</sub>O molecules, where its inclusion significantly

improves the agreement between modelling calculations and experimental measurements of electron transport coefficients.

- Chapter 5 extends LoKI-MC to handle configurations involving AC/DC electric fields and DC magnetic fields oriented at arbitrary angles [16]. The chapter assesses the code accuracy through various benchmarks and produces novel benchmark calculations for evaluating electron kinetics solvers in scenarios with coexisting AC electric and DC magnetic fields. Additionally, the impact of magnetic fields is thoroughly analyzed, both in model gases (Reid-ramp [17] and Lucas-Saelee [18]) and real gases ( $N_2$  and Ar), differentiating between configurations with DC and AC electric fields.
- Chapter 6 further expands the scope of LoKI-MC to encompass time-dependent  $E/N$  pulses. By considering the rigorous time-dependent MC solution as the golden standard, this chapter evaluates the accuracy of two common assumptions for solving space- and time-dependent electron kinetics: the local-field approximation (LFA) and the local-energy approximation (LEA). The study primarily focuses on time-locality, assessing the accuracy of the LFA and the LEA for solving homogeneous electron kinetics in nanosecond-pulsed discharges. It is observed that the LEA generally provides more accurate results than the LFA, with differences becoming more pronounced at lower pressures where energy relaxation is slower.
- Chapter 7 concludes the thesis by summarizing the work and key findings from each chapter while also outlining future research directions.

Chapters 2-6 are structured similarly to research papers, featuring a chapter summary, comprehensive introduction, methods description, results, conclusions and references. The latter are numbered from [1] onwards in each chapter.

### 1.3 Scientific contributions

The development of MC algorithms and the associated studies on LTPs have been published in high-impact journals, such as *Plasma Sources Science and Technology* [13, 16], *Journal of Physics D: Applied Physics* [15] and *Computer Physics Communications* [14]. These works are detailed in various chapters of this thesis. Furthermore, the scientific research has been presented at several conferences, including:

- Two oral communications [19, 20] at the *Gaseous Electronics Conference (GEC) 2021*, in virtual format;
- Oral [21] and poster [22] communications at the *Europhysics Conference on Atomic and Molecular Physics of Ionized Gases (ESCAPEIG) 2022* in Paris, France, with the former selected as a *Hot Topic*;

- Oral communication [23] at *GEC 2022* in Sendai, Japan;
- Oral [24] and poster [25] communications at the *International Conference on Phenomena in Ionized Gases (ICPIG) 2023* in Egmond aan Zee, The Netherlands;
- Oral [26] and poster [27] communications at *The plasma road to sustainable chemical conversion workshop 2023* in Madeira, Portugal;
- Oral [28] and poster [29] communications at *GEC 2023* in Michigan, U.S.A., where I won the *GEC Student Excellence Award*.

Although this document primarily focuses on LTP modelling using MC techniques, the work conducted over the past four years extends beyond that, including:

- I participated on the experimental study of streamer-induced kinetics of excited states in pure N<sub>2</sub>, involving the determinations of the streamer propagation velocity, reduced electric field ( $E/N$ ) and vibrational distributions of N<sub>2</sub>(B), N<sub>2</sub>(C) and N<sub>2</sub><sup>+</sup>(B) states [30, 31]. This work stems from a collaboration between the Institute of Plasma Physics (IPP) in Prague and Instituto de Plasmas e Fusão Nuclear (IPFN) in Lisbon, with me spending five months in Prague conducting experimental work.
- I led the development and validation of a reaction mechanism for oxygen plasmas [32], which was also presented at *ICPIG 2023* [33] and received the *Best Poster Prize*.
- I participated on the investigation of the influence of dimensionality on the modelling of low-pressure oxygen DC glow discharges [34].
- Finally, I played secondary roles in developing kinetic schemes for CO<sub>2</sub>-N<sub>2</sub> and CO<sub>2</sub>-O<sub>2</sub> discharges [35, 36] and electron-impact cross-sections for H<sub>2</sub>O molecules [37].

## References

- [1] Oehrlein, G. S. and Hamaguchi, S. 2018 “Foundations of low-temperature plasma enhanced materials synthesis and etching” *Plasma Sources Sci Technol.* **27**, 023001.
- [2] Gudmundsson, J. T., Brenning, N., Lundin, D., and Helmersson, U. 2012 “High power impulse magnetron sputtering discharge” *J. Vac. Sci. Technol. A* **30**, 030801.
- [3] Labay, C., Hamouda, I., Tampieri, F., Ginebra, M.-P., and Canal, C. 2019 “Production of reactive species in alginate hydrogels for cold atmospheric plasma-based therapies” *Sci. Rep.* **9**, 16160.
- [4] Bauer, G. and Graves, D. B. 2016 “Mechanisms of Selective Antitumor Action of Cold Atmospheric Plasma-Derived Reactive Oxygen and Nitrogen Species” *Plasma Process Polym* **13**, 1157–1178.

- [5] Fridman, G., Friedman, G., Gutsol, A., Shekhter, A. B., Vasilets, V. N., and Fridman, A. 2008 “Applied Plasma Medicine” *Plasma Process Polym* **5**, 503–533.
- [6] Gherardi, M., Puač, N., and Shiratani, M. 2018 “Special issue: Plasma and agriculture” *Plasma Process Polym* **15**, 1877002.
- [7] Min, S. C., Roh, S. H., Niemira, B. A., Sites, J. E., Boyd, G., and Lacombe, A. 2016 “Dielectric barrier discharge atmospheric cold plasma inhibits Escherichia coli O157:H7, Salmonella, Listeria monocytogenes, and Tulane virus in Romaine lettuce” *Int. J. Food Microbiol.* **237**, 114–120.
- [8] Kitazaki, S., Koga, K., Shiratani, M., and Hayashi, N. 2012 “Growth Enhancement of Radish Sprouts Induced by Low Pressure O<sub>2</sub> Radio Frequency Discharge Plasma Irradiation” *Jpn J Appl Phys* **51**, 01AE01.
- [9] Rooij, G. J. van, Bekerom, D. C. M. van den, Harder, N. den, Minea, T., Berden, G., Bongers, W. A., Engeln, R., Graswinckel, M. F., Zoethout, E., and Sanden, M. C. M. van de 2015 “Taming microwave plasma to beat thermodynamics in CO<sub>2</sub> dissociation” *Faraday Discuss.* **183** (0), 233–248.
- [10] Snoeckx, R., Aerts, R., Tu, X., and Bogaerts, A. 2013 “Plasma-Based Dry Reforming: a Computational Study Ranging from the Nanoseconds to Seconds Time Scale” *J. Phys. Chem. C* **117**, 4957–4970.
- [11] Longo, S. 2000 “Monte Carlo models of electron and ion transport in non-equilibrium plasmas” *Plasma Sources Sci. Technol.* **9**, 468–476.
- [12] Hockney, R. W. and Eastwood, J. 1988 *Computer simulation using particles (1st ed.)* CRC Press.
- [13] Dias, T. C. and Guerra, V. 2020 “Kinetic Monte Carlo simulations of plasma-chemistry” *Plasma Sources Sci. Technol.* **29**, 115003.
- [14] Dias, T. C., Tejero-del-Caz, A., Alves, L. L., and Guerra, V. 2023a “The LisbOn KInetics Monte Carlo solver” *Comput. Phys. Commun.* **282**, 108554  
<https://github.com/IST-Lisbon/LoKI-MC>.
- [15] Budde, M., Dias, T. C., Vialletto, L., Pinhão, N., Guerra, V., and Silva, T. 2023 “Electron-neutral collision cross sections for H<sub>2</sub>O: II. Anisotropic scattering and assessment of the validity of the two-term approximation” *J. Phys. D: Appl. Phys.* **56**, 255201.
- [16] Dias, T. C., Pintassilgo, C. D., and Guerra, V. 2023 “Effect of the magnetic field on the electron kinetics under AC/DC electric fields: benchmark calculations and electron cyclotron resonance” *Plasma Sources Sci. Technol.* **32**, 095003.
- [17] Reid, I. 1979 “An Investigation of the Accuracy of Numerical Solutions of Boltzmann’s Equation for Electron Swarms in Gases with Large Inelastic Cross Sections” *Aust. J. Phys.* **32**, 231.
- [18] Lucas, J. and Saelee, H. T. 1975 “A comparison of a Monte Carlo simulation and the Boltzmann solution for electron swarm motion in gases” *J. Phys. D Appl. Phys.* **8**, 640–650.

- [19] Dias, T. C. and Guerra, V. (a) “Kinetic Monte Carlo simulations of plasma-chemistry” *74th Annual Gaseous Electronics Conference (GEC)* Virtual format, October 2021.
- [20] Dias, T. C., Tejero-del-Caz, A., Alves, L. L., and Guerra, V. (a) “A new electron transport Monte Carlo code” *74th Annual Gaseous Electronics Conference (GEC)* Virtual format, October 2021.
- [21] Dias, T. C. and Guerra, V. (b) “Unified Monte Carlo formulation of plasma-chemistry in nanosecond-pulsed discharges” *ESCAMPIG XXV* Paris, France, July 2022.
- [22] Dias, T. C., Pintassilgo, C. D., Mrózek, K., Tejero-del-Caz, A., Alves, L. L., and Guerra, V. (b) “Electron swarm kinetics in electric and magnetic fields crossed at arbitrary angles” *ESCAMPIG XXV* Paris, France, July 2022.
- [23] Dias, T. C., Tejero-del-Caz, A., Alves, L. L., Pintassilgo, C. D., and Guerra, V. (c) “The LisbOn KInetics Monte Carlo solver” *75th Annual Gaseous Electronics Conference (GEC)* Senday, Japan, October 2022.
- [24] Dias, T. C. and Guerra, V. (c) “Assessment of time-locality assumptions on the modelling of nanosecond-pulsed discharges” *XXXV ICPIG* Egmond aan Zee, The Netherlands, July 2023.
- [25] Pintassilgo, C. D., Dias, T. C., and Guerra, V. “Effect of the magnetic field on the electron kinetics under AC/DC electric fields” *XXXV ICPIG* Egmond aan Zee, The Netherlands, July 2023.
- [26] Dias, T. C. and Guerra, V. (d) “A close look at time-locality assumptions on the modelling of nanosecond-pulsed discharges” *The plasma road to sustainable chemical conversion workshop* Madeira, Portugal, September 2023.
- [27] Dias, T. C., Pintassilgo, C. D., and Guerra, V. (a) “Effect of the magnetic field on the electron kinetics under AC/DC electric fields” *The plasma road to sustainable chemical conversion workshop* Madeira, Portugal, September 2023.
- [28] Dias, T. C. and Guerra, V. (e) “Unified Monte Carlo formulation of nanosecond discharges” *76th Annual Gaseous Electronics Conference (GEC)* Michigan, U.S.A., October 2023.
- [29] Dias, T. C., Pintassilgo, C. D., and Guerra, V. (b) “Electron kinetics under AC/DC electric and magnetic fields: benchmark calculations and electron cyclotron resonance” *76th Annual Gaseous Electronics Conference (GEC)* Michigan, U.S.A., October 2023.
- [30] Bílek, P., Dias, T. C., Prukner, V., Hoffer, P., Guerra, V., and Šimek, M. 2023a “Streamer-induced kinetics of excited states in pure N<sub>2</sub>: I. Propagation velocity, E/N and vibrational distributions of N<sub>2</sub>(C<sup>3</sup>Π<sub>u</sub>) and N<sub>2</sub><sup>+</sup>(B<sup>2</sup>Σ<sub>u</sub><sup>+</sup>) states” *Plasma Sources Sci. Technol.*
- [31] Bílek, P., Dias, T. C., Prukner, V., Guerra, V., and Šimek, M. 2023b “Streamer-induced kinetics of excited states in pure N<sub>2</sub>: II. Formation and quenching of N<sub>2</sub>(B<sup>3</sup>Π<sub>g</sub>, v = 0 – 12) through advanced analysis of emission produced by the first positive system” *In preparation.*
- [32] Dias, T. C., Fromentin, C., Alves, L. L., Tejero-del-Caz, A., Silva, T., and Guerra, V. 2023b “A reaction mechanism for oxygen plasmas” *Plasma Sources Sci. Technol.* **32**, 084003.

- [33] Dias, T. C., Fromentin, C., Alves, L. L., Tejero-del-Caz, A., Silva, T., and Guerra, V. (d) “A reaction mechanism for oxygen plasmas” *XXXV ICPIG* Egmond aan Zee, The Netherlands, July 2023.
- [34] Viegas, P., Dias, T. C., Fromentin, C., Chukalovsky, A., Mankelevich, Y., Proshina, O., Rakhimova, T., Guerra, V., and Voloshin, D. 2023 “Comparison between 1D radial and 0D global models for low-pressure oxygen DC glow discharges” *Plasma Sources Sci. Technol.* **32**, 024002.
- [35] Fromentin, C., Silva, T., Dias, T. C., Morillo-Candas, A. S., Biondo, O., Guaitella, O., and Guerra, V. 2023a “Study of vibrational kinetics of CO<sub>2</sub> and CO in CO<sub>2</sub>–O<sub>2</sub> plasmas under non-equilibrium conditions” *Plasma Sources Sci. Technol.* **32**, 024001.
- [36] Fromentin, C., Silva, T., Dias, T. C., Baratte, E., Guaitella, O., and Guerra, V. 2023b “Study of vibrational kinetics of CO<sub>2</sub> and CO in CO<sub>2</sub>–O<sub>2</sub> plasmas under non-equilibrium conditions” *Plasma Sources Sci. Technol.*
- [37] Budde, M., Dias, T. C., Vialeto, L., Pinhão, N., Guerra, V., and Silva, T. 2022 “Electron-neutral collision cross sections for H<sub>2</sub>O: I. Complete and consistent set” *J. Phys. D: Appl. Phys.* **55**, 445205.

# 2

## Kinetic Monte Carlo simulations of plasma chemistry Chapter summary

This chapter presents a Kinetic Monte Carlo algorithm to solve the gas-phase chemistry in low-temperature plasmas, as a first effort to achieve a unified formulation of the electron, heavy-particle and surface kinetics based on Monte Carlo techniques. The implemented algorithm is successfully validated in the thermodynamic limit from the comparison with the traditional deterministic description using rate-balance equations.

The accuracy of the Monte Carlo description of the rare species strongly depends on the number of particles used in the simulation. To surpass this limitation, two novel variance reduction techniques that significantly reduce the statistical fluctuations on the concentrations of the minor species are proposed and evaluated. These techniques lead to significant gains in computational time, up to factors of the order of  $10^4$  times in the cases studied, while ensuring the same quality of the solution.

All results presented in this chapter have been published in [1].

## 2.1 Introduction

The strong non-equilibrium nature of low-temperature plasmas (LTPs) can efficiently enhance several chemical processes relevant for industrial [2, 3], medical [4–6], agricultural [7–9] and environmental [10, 11] applications. However, these systems are highly complex, and require modelling studies to (i) complement and interpret measured data, (ii) access information not available from experiments, and (iii) understand their overall behaviour at a fundamental level. In particular, the detailed modelling of chemical kinetics (often studied using 0D approaches) is of utmost interest.

The problem of *homogeneous* chemical kinetics in a LTP (or in any other system) may be formulated as follows [12–14]: consider a spatially uniform mixture of  $N_s$  chemical species inside a fixed volume  $V$ , which can interact through  $M$  reaction channels; then, given the initial numbers of molecules per species, what is the time evolution of the molecular population?

If we follow the traditional deterministic approach, we need to translate this into ordinary differential equations. Assuming that the number of molecules of the  $i$ th species at time  $t$  can be represented by a continuous, single-valued function  $X_i(t)$  ( $i = 1, \dots, N_s$ ), and considering that the  $M$  chemical reactions are described by continuous rate processes, we may write  $N_s$  coupled ordinary differential equations of the form

$$\frac{dX_i}{dt} = f_i(X_1, \dots, X_{N_s}), \quad (2.1)$$

where the function  $f_i$  may be different for each species and is determined by the types and rate coefficients of the  $M$  chemical reactions. These equations are commonly referred as rate-balance equations or reaction-rate equations. By knowing the initial number of molecules per species, we can determine the time evolution of the system through a typical finite-differences method.

Despite the power and simplicity of the deterministic method, some remarks should be made about its validity. The time evolution of a real system is not continuous, as the number of molecules of a given species can only change in discrete amounts. Additionally, the time evolution is not purely deterministic; there are statistical fluctuations that this description fails to account for. For instance, in nonlinear chemical systems near an instability, the deterministic method may fail due to the inherent importance of fluctuations and correlations [13–16].

In this work, we employ the Kinetic Monte Carlo (KMC) algorithm developed by Gillespie [12] to simulate the temporal evolution of coupled chemical reactions in LTPs. KMC simulations are exact, in the sense that they follow the time evolution of one element of the statistical ensemble, simulated without any subjacent approximations. They provide answers to the questions “when and what”, determining the dynamics of the chemical species, and allow to study the fluctuations on the physical parameters of the system, as opposed to the deterministic formulation. To the best of our knowledge, gas-phase chemistry in gas discharges was never described with a MC approach, despite the success of the stochastic methods

in describing relatively complex surface kinetics [17–19], and biochemical [20] and interstellar medium [21–23] systems.

The structure of this chapter is as follows. Section 2.2 briefly formulates the stochastic approach. Section 2.3 details the basis of the KMC algorithm. Section 2.4 presents the validation of the implemented formulation, including a detailed analysis of the error associated to KMC simulations. Section 2.5 presents two innovative variance reduction techniques that decrease the statistical error associated with the description of minority species. Finally, section 2.6 summarizes the main results of this chapter and establishes the prospects for the future work.

## 2.2 Stochastic description

The temporal evolution of a physical system can be analytically described by the master equation [13, 15, 16, 18]

$$\frac{\partial \mathcal{P}(\sigma, t)}{\partial t} = \sum_{\sigma'} [W(\sigma' \rightarrow \sigma) \mathcal{P}(\sigma', t) - W(\sigma \rightarrow \sigma') \mathcal{P}(\sigma, t)], \quad (2.2)$$

where  $\mathcal{P}(\sigma, t)$  represents the probability of the system being in state  $\sigma$  at time  $t$ . Here,  $\sigma$  and  $\sigma'$  denote successive states of the system and  $W(\sigma \rightarrow \sigma')$  stands for the probability per unit time that the system transitions from state  $\sigma$  to state  $\sigma'$ . In the context of chemical kinetics, a state  $\sigma$  corresponds to a specific configuration of the number of particles of each species,  $\{X_1, \dots, X_{N_s}\}$ , and the transitions  $\sigma \rightarrow \sigma'$  depend on the  $M$  possible reactions  $\{R_1, \dots, R_M\}$ , which are characterized by transition rates  $\{a_1, \dots, a_M\}$ .

The master equation characterizes a memoryless process in which transitions to the next state depend solely on the current state, constituting a Markovian process. While formulating this equation for a given system is straightforward, solving it for real systems remains unfeasible. Kinetic Monte Carlo algorithms do not solve this equation; rather, they numerically simulate the underlying Markov process.

To describe the temporal evolution of a system in the state  $\{X_1, \dots, X_{N_s}\}$ , we need answers to two fundamental questions: “When will the next reaction occur?” and “What reaction type will it be?”. Given the stochastic nature of the chemical reactions, these questions can only be addressed probabilistically. In mathematical terms, we aim to find

$P(\tau, \mu) d\tau \equiv$  probability that, given the state  $\{X_1, \dots, X_{N_s}\}$  at time  $t$ , the next reaction in the volume  $V$  will occur in the infinitesimal time interval  $(t + \tau, t + \tau + d\tau)$ ,  
and it will be a  $R_\mu$  reaction.

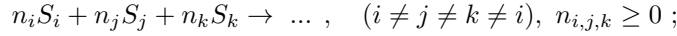
$P(\tau, \mu)$  is a joint probability density function on the space of the continuous variable  $\tau \in [0, \infty[$  - the time-interval at which the next reaction will occur - and the discrete variable  $\mu = 1, \dots, M$  - an index representing a specific reaction. Gillespie [12] demonstrated that the reaction probability density function

of such system may be expressed as

$$P(\tau, \mu) = \begin{cases} a_\mu \exp(-a_0\tau), & \text{if } 0 \leq \tau < \infty \text{ and } \mu = 1, \dots, M \\ 0, & \text{otherwise} \end{cases}, \quad (2.4)$$

where  $a_0$  is the sum of all reaction rates. This function describes a simple Poisson distribution with decay constant  $a_0$ , partitioned over the different reaction channels based on their respective rates.

The transition rates  $a_\mu$  are calculated from the numbers of particles of the reactant species  $X_i$  and the usual reaction rate coefficients  $k_\mu$ . For example, if the reaction  $\mu$  is  $S_1 + S_2 \rightarrow \dots$ , then  $a_\mu = X_1 X_2 \frac{k_\mu}{V}$ , or if the reaction is  $2S_1 \rightarrow \dots$ , then  $a_\mu = X_1 (X_1 - 1) \frac{k_\mu}{V}$ , where  $V$  is the volume of the system considered in the simulation and  $k_\mu$  is expressed in  $\text{m}^3/\text{s}$  for a binary reaction. In a general reaction:



$$a_\mu = \prod_{\alpha=1}^{n_i} (X_i + 1 - \alpha) \prod_{\beta=1}^{n_j} (X_j + 1 - \beta) \prod_{\gamma=1}^{n_k} (X_k + 1 - \gamma) \frac{k_\mu}{V^{n_i+n_j+n_k-1}}, \quad (2.5)$$

where expressions like  $\prod_{\alpha=1}^0 (\dots)$  should be considered as 1. More details regarding the connection between the reaction rates and the corresponding rate coefficients can be found in [12, 14].

## 2.3 Kinetic Monte Carlo algorithm

The kinetic Monte Carlo algorithm was first introduced by Gillespie [12–14]. It simulates the stochastic evolution of a chemical system based on the reaction probability density function (2.4) using the following elementary steps [12]:

1. Set the simulation time  $t = 0$  and define the initial numbers of particles per species  $X_i$  ( $i = 1, \dots, N_s$ );
2. Calculate the transition rates  $a_\nu$  ( $\nu = 1, \dots, M$ ) and the total transition rate  $a_0 = \sum_\nu a_\nu$ ;
3. Generate two random numbers from a uniform distribution between 0 and 1: one for “when” ( $r_1$ ) and another for “what” ( $r_2$ );
4. Calculate the time at which the next reaction will occur:  $\tau = \frac{1}{a_0} \ln \frac{1}{r_1}$ ;
5. Find the reaction  $\mu$  for which  $\sum_{\nu=1}^{\mu-1} \frac{a_\nu}{a_0} < r_2 \leq \sum_{\nu=1}^\mu \frac{a_\nu}{a_0}$ ;
6. Update the numbers of particles  $X_i$  according to the selected reaction  $R_\mu$  and set  $t = t + \tau$ ;
7. If  $t > t_{stop}$ , stop the simulation; else, return to step (ii).

Note that the time is derived from the probability density function  $P_1(\tau) = a_0 \exp(-a_0\tau)$  and the reaction  $R_\mu$  is selected according to  $P_2(\mu) = a_\mu/a_0$ . Hence, in practical terms,  $P(\tau, \mu) = P_1(\tau)P_2(\mu)$ .

In this work, the random numbers  $r_1$  and  $r_2$  are generated with a 64-bit version of the Mersenne Twister pseudorandom number generator using the function `mt19937_64` implemented at the C++ library `random` [24–26], which is characterized by a high period and good uniformity. The effect of correlations between generated random numbers was not studied, since this generator is already well established and implemented in the standard libraries of most programming languages.

## 2.4 Validation

The KMC algorithm used here was validated by Gillespie in [13] through a comparison of the MC results with deterministic calculations. However, this comparison was performed only for very simple model systems, with no more than 6 species and 5 reactions. Later on, the method was applied and validated in the astrophysics field to study the gas-grain chemistry in interstellar media, where a complex gas-phase chemistry and surface kinetics were solved using an unified KMC approach [21, 22].

Here, we investigate its applicability to real plasma-chemistry in gas discharges, where reactivity stems from electron impact processes, with the inherent wide range of involved time-scales and species concentrations varying over several orders of magnitude. We use a realistic and complex system for the validation of the KMC algorithm: the heavy-species kinetics in an O<sub>2</sub> DC glow discharge, including heavy-particle reactions and electron impact excitation, dissociation and ionization mechanisms. The simulation conditions used in the model are:  $p = 1$  Torr,  $T_g = 396$  K,  $E/N = 48$  Td and  $n_e = 6.5 \times 10^{15}$  m<sup>-3</sup>. These parameters correspond to experimental values of a DC discharge operating at 1 Torr with a current of 40 mA, which is ignited in a pyrex tube with radius of 1 cm and length of 56 cm [27].

The kinetic scheme is taken from Annušová *et al.* [28], considering 10 different species which interact through 63 reactions, and it describes relatively well the available experimental results. The species taken into account are O<sub>2</sub>(X) and O<sub>3</sub>(X) ground-state molecules, O<sub>2</sub>(a) and O<sub>2</sub>(b) electronically excited metastable states, O<sub>3</sub>(exc) vibrationally excited molecules, ground-state O(<sup>3</sup>P) and metastable O(<sup>1</sup>D) atoms, and O<sub>2</sub><sup>+</sup>, O<sup>+</sup> and O<sup>-</sup> ions. The kinetic scheme was previously used to study inductive coupled plasmas [28], and very similar schemes were used to successfully describe microwave [29, 30] and DC [31, 32] discharges. The deterministic simulations are performed using the 0-D chemistry solver of the LisbOn KInetics (LoKI) tool suite [33–35], for the same conditions and using the same kinetic scheme as in the KMC calculations.

Figure 2.1 shows the temporal evolution of the most abundant species in the discharge, O<sub>2</sub>(X), O<sub>2</sub>(a) and O(<sup>3</sup>P), comparing KMC simulations, using  $10^6$  simulation particles, with LoKI simulations. The agreement is remarkable, which indicates that the methods are equivalent in this case. In a standard desktop computer, such KMC simulation with  $10^6$  particles takes around 1 min to run.

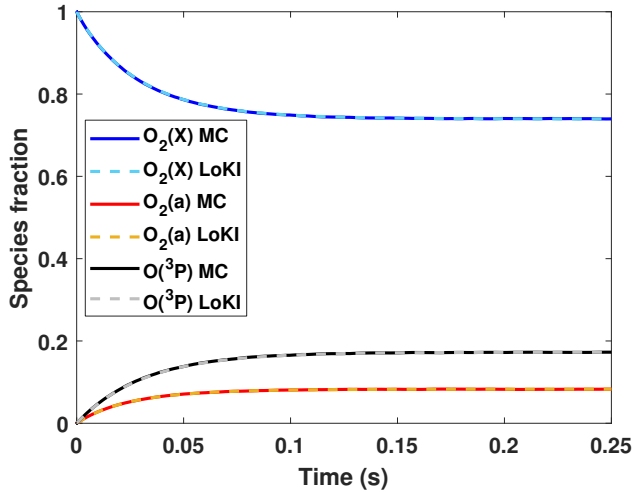


**Figure 2.1:** Temporal evolution of  $O_2(X)$ ,  $O_2(a)$ ,  $O(^3P)$ , comparing KMC ( $10^6$  particles) with deterministic LoKI simulations.

A substantial factor for the smoothness of a MC simulation is the initial number of particles in the system. To analyze this effect, we performed simulations with the same input conditions but with a different number of simulation particles, ranging from  $10^4$  to  $10^8$  particles. Figure 2.2a presents the time-evolution of the  $O_2(b)$  fraction, where it can be observed that the more particles we put in the simulation, the smaller are the fluctuations of the results, as expected.

Another way to improve the accuracy of MC results is to average the results over several realizations of the system, while keeping the same number of initial simulation particles. In figure 2.2b, we find that, after averaging 100 runs with  $10^4$  particles, the statistical fluctuations around the average value of  $O_2(b)$  are strongly reduced and comparable with those obtained with  $10^4 \times 100 = 10^6$  particles. This approach is interesting from a computational point of view because the simulations may be launched at the same time in different computer cores. Since the simulation time is proportional to the initial number of particles (see figure 2.5), the total CPU time is very nearly the same, but the real time to obtain a result with a given accuracy decreases significantly. A similar conclusion was drawn in [18] regarding the application of KMC to describe surface kinetics.

The descriptions of  $O_3(X)$  and  $O(^1D)$  are presented in figures 2.3 and 2.4. Due to the low abundance of these species, with fractional concentrations of  $\sim 10^{-4}$  and  $10^{-5}$ , respectively, the order of magnitude starts to be well described with  $10^6$  particles, where the steady-state concentrations are described on average by  $\sim 100$  particles, while for an accurate description we need at least  $10^8$  particles. As in the case shown in figure 2.2, the statistical fluctuations are strongly reduced with the averaging over the different MC runs, and the results obtained by either increasing the number of particles in the simulation or averaging over several realizations of the system are equivalent, both in terms of accuracy and of total CPU time. These figures strikingly confirm the interest and power of the averaging procedure.

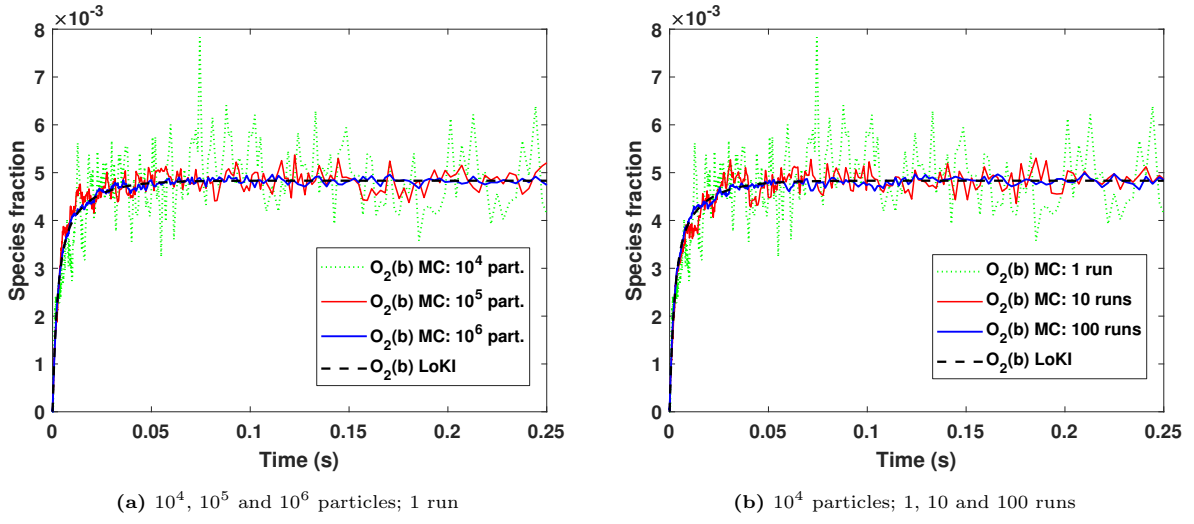


**Figure 2.2:** Temporal evolution of  $O_2(b)$ , comparing KMC with deterministic LoKI simulations.

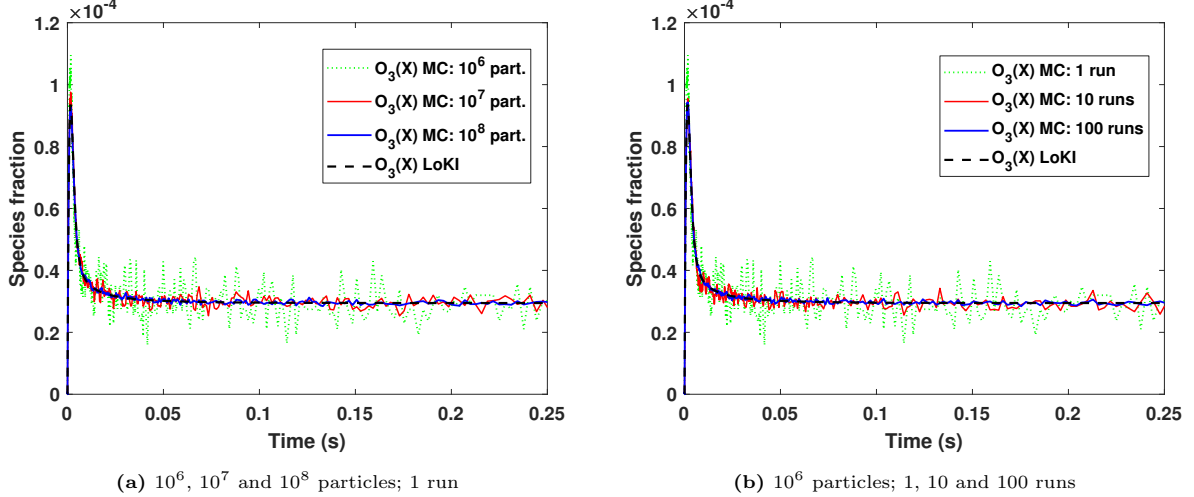


**Figure 2.3:** Temporal evolution of  $O_3(X)$ , comparing KMC with deterministic LoKI simulations.

The importance of the number of particles used in the simulation can be evaluated through the dispersion of single MC results [18]. Taking into account that the standard deviation of a random discrete variable  $X$  may be calculated as  $\sigma = \sqrt{\frac{\sum_{i=1}^N (x_i - \mu)^2}{N}}$ , we define the relative error of the density of a species  $S$  as:

$$\Delta_{rel} = \sqrt{\frac{\sum_{i=1}^N ([S]_{MC}(i) - [S]_D)^2}{N [S]_D^2}}, \quad (2.6)$$

where the deterministic density  $[S]_D$  is the average value and  $[S]_{MC}(i)$  denotes the density of the MC run  $i$ . To obtain a statistically meaningful error, we applied this formula to the results of 100 MC independent runs. The evaluation of this formula could be done at any instant of time (or even along time), but here we opt by comparing the Monte Carlo and deterministic results at the final simulation time. In figure 2.5,

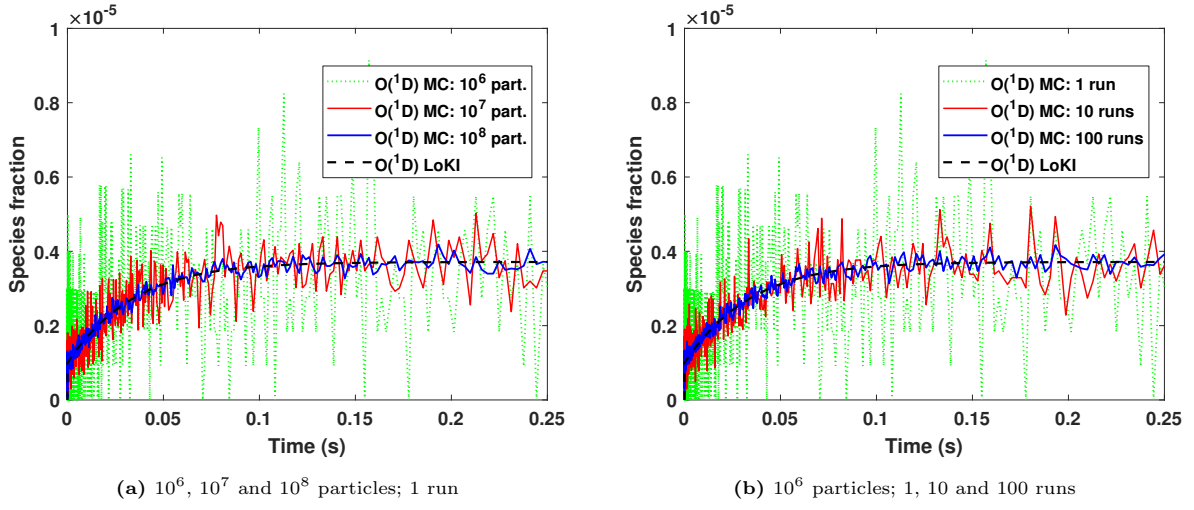


**Figure 2.4:** Temporal evolution of  $O(^1D)$ , comparing KMC with deterministic LoKI simulations.

we present the relative error of the various species as a function of the initial number of particles used in the simulation. As expected, the relative error of the prevalent species is smaller. Moreover,  $\Delta_{rel}$  varies oppositely with the number of particles. However, the CPU time increases linearly with the number of particles. The parameter defining the error associated with a species is the number of particles of that species that are simulated, as we can see in figure 2.6, where the error is plotted as a function of the total number of particles weighted by the deterministic fraction of the species. With the exception of the parent gas, ground-state  $O_2(X)$  molecules, the curves corresponding to all the other species fall into a single line. It is unclear why  $O_2(X)$  lies below the trend formed by the other species. The reason might be related to the fact that  $O_2(X)$  is the main species of the discharge chemistry, appearing in most of the reactions used in the kinetic scheme, but further investigation is required to clarify this question.

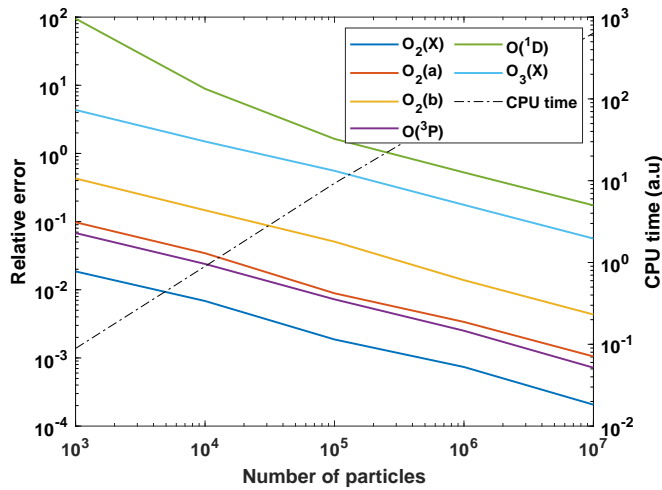


**Figure 2.5:** Relative error of the species densities ( $\Delta_{rel}$ ) as a function of the initial number of particles in the simulation.

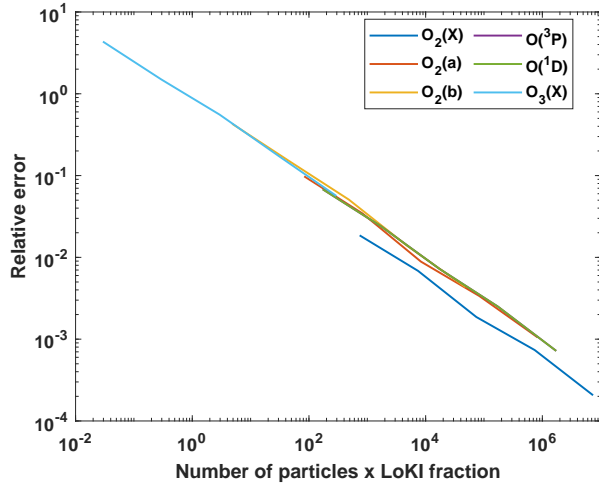


**Figure 2.6:** Relative error of the species densities ( $\Delta_{rel}$ ) as a function of the number of particles weighted by the deterministic fraction.

## 2.5 Variance Reduction

Figures 2.2-2.4 reveal a major drawback of the standard KMC method: to describe accurately the rare species, we need a large number of particles in the simulation (or, equivalently, average over a large number of realizations of the system), which may become very expensive in terms of CPU time. The unphysical statistical fluctuations on the calculation of the densities of the rare species are larger because the associated transition rates are usually much smaller and the correspondent reactions are rarely chosen. In this section, we propose two novel variance reduction techniques that strongly improve the description of the minority species: Equal Reaction Weights (ERW) and Variable Species Weights (VSW).

It is worth to mention some efforts to considerably reduce the statistical error in the MC calculation of the EEDF, such as the splitting/gathering technique by Pacelli *et al* [36] and the Monte Carlo flux method by Vialletto *et al* [37]. These interesting techniques are designed for the treatment of the electron kinetics and their analysis goes beyond the scope of the present work.

### 2.5.1 Equal Reaction Weights

We start by presenting a variance reduction method where the reaction selection is uniform, so as to treat each reaction equally: instead of having different intervals for each reaction  $\nu$  with length  $L_\nu = a_\nu/a_0$ , we consider a single interval for each reaction given by  $L' = 1/M$ , where  $M$  is the number of reactions. The idea is represented schematically in figure 2.7. In this case, when a reaction  $\mu$  is chosen, we have to correct its influence with the factor  $L_\mu/L'$ . Hence, the importance of the reaction is corrected accordingly with the overestimation/underestimation made by homogenizing the reaction rates. For example, consider

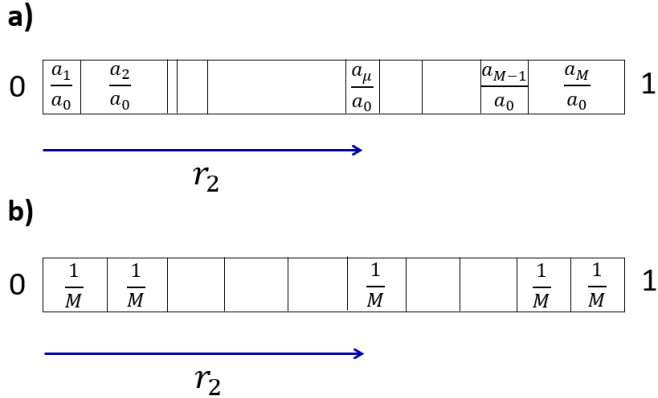
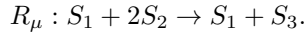


**Figure 2.7:** Reaction selection: standard (a) and ERW (b) methods.

that the following reaction is chosen:



Then, the number of particles should be updated as follows:

$$X_2 \rightarrow X_2 - 2 \times \frac{L_\mu}{L'},$$

$$X_3 \rightarrow X_3 + 1 \times \frac{L_\mu}{L'}.$$

We should note that the reaction correction may be fractional, leading to a fractional number of simulation particles. This implies a change in the calculation of the reaction rates. Instead of calculating them using expression (2.5), now the reaction rates should be obtained exactly as in the deterministic description:

$$a_\mu = X_i^{n_i} X_j^{n_j} X_k^{n_k} \frac{k_\mu}{V^{n_i+n_j+n_k-1}} , \quad (2.7)$$

which amounts to approximate terms  $X_i(X_i - 1)$  by  $X_i^2$ ,  $X_i(X_i - 1)(X_i - 2)$  by  $X_i^3$ , etc.

Bear in mind that with this method we are no longer solving exactly the stochastic evolution of the system, as it is done in the standard KMC algorithm. Instead, we are acknowledging that there are some unphysical statistical fluctuations due to the fact that we use a small number of sample particles (e.g.  $10^8$ ), compared with the real number of particles in the discharge (e.g.  $\sim 10^{21}$ ). In this way, we give a small step closer to the deterministic approach, keeping the rest of the standard algorithm intact. If we are simulating a system which satisfies the thermodynamic limit and without chemical instabilities, this method should be valid. If the number of particles of the real system is low or if there are chemical instabilities leading to a rapid growth of concentrations, such that the statistical fluctuations are significant and physical, then we should use the standard KMC algorithm, and avoid

any variance reduction method, in order to capture the properties of the real fluctuations and identify possible extraordinary behaviours of the system [38–40]. However, in principle, most plasma-chemistry systems should be within the conditions of validity for the use of variance-reduction techniques, since these are essentially the same as the ones for allowing the use of rate-balance equations.

### 2.5.2 Variable Species Weights

The second variance reduction method consists on changing the reaction weights through the species weights that intervene in the reactions. As we found in figure 2.6, the relative error of a species density depends mainly on the number of particles of that species that are simulated. Therefore, if we want to have similar relative fluctuations in the concentrations of all species, we have to correct their weight with the inverse of their prevalence. To do so, after each reaction, we adjust the species weights  $W_i^s$  in the following way:

$$W_i^s = \frac{\max_j X_j}{X_i}. \quad (2.8)$$

Moreover, we define the reaction weights  $W_\mu^r$  as follows:

$$W_\mu^r = \max_{react_j, prod_j} W_{j,\mu}^s. \quad (2.9)$$

Once more, when we correct the reaction influence with the inverse of the weight, we may obtain a fractional number of particles. Therefore, the reaction rates are also calculated using equation 2.7. Furthermore, the comments regarding the validity of this method are analogous to the ones made for the first variance reduction method.

A somewhat similar technique was proposed by Longo in [41] to reduce the statistical error associated with minority species when using a PIC/MC formulation to stochastically solve the Boltzmann equation of charged species. Although the method is used for a different scope, the species also have varying weights depending on their prevalence.

If we want to improve the description of only some minority species, in place of using expression 2.8, we can tune the species weights case-by-case, keeping the rest unchanged. This may be useful to describe accurately the ions, since they are important for the calculation of  $E/N$ , while leaving the remaining species untouched.

### 2.5.3 Comparison

To evaluate the potentialities of the presented methods, we performed simulations employing ERW and VSW techniques and compared them with the standard approach, considering always  $10^8$  particles in the simulations. The results are shown in figure 2.8. The first four graphs reveal that the most prevalent species are remarkably well described with both standard and ERW KMC. However, the VSW results

present significant fluctuations around the mean value. The ERW and VSW variance reduction techniques give similar results as the standard KMC, respectively for  $O_3(X)$  and  $O(^1D)$ . Sharp differences are found in the last four plots, corresponding to the rarest species, where the fluctuations in the results of the developed methods are similar, and much smaller than the ones found with the standard algorithm. In the standard KMC, the concentrations of  $O_2^+$  and, specially,  $O^+$  obtained with  $10^8$  simulation particles have no relevant meaning (the latter is described by 0 particles in the majority of the simulation time). However, a precise description of these species may be essential to self-consistently calculate the reduced electric field, which can now be done with the help of the variance reduction methods. Note that to have a description of  $O^+$  with resembling fluctuations using the standard approach, we would need at least  $10^{12}$  particles, and hence a  $10^4$  times higher CPU time, which stresses the power of the proposed techniques.

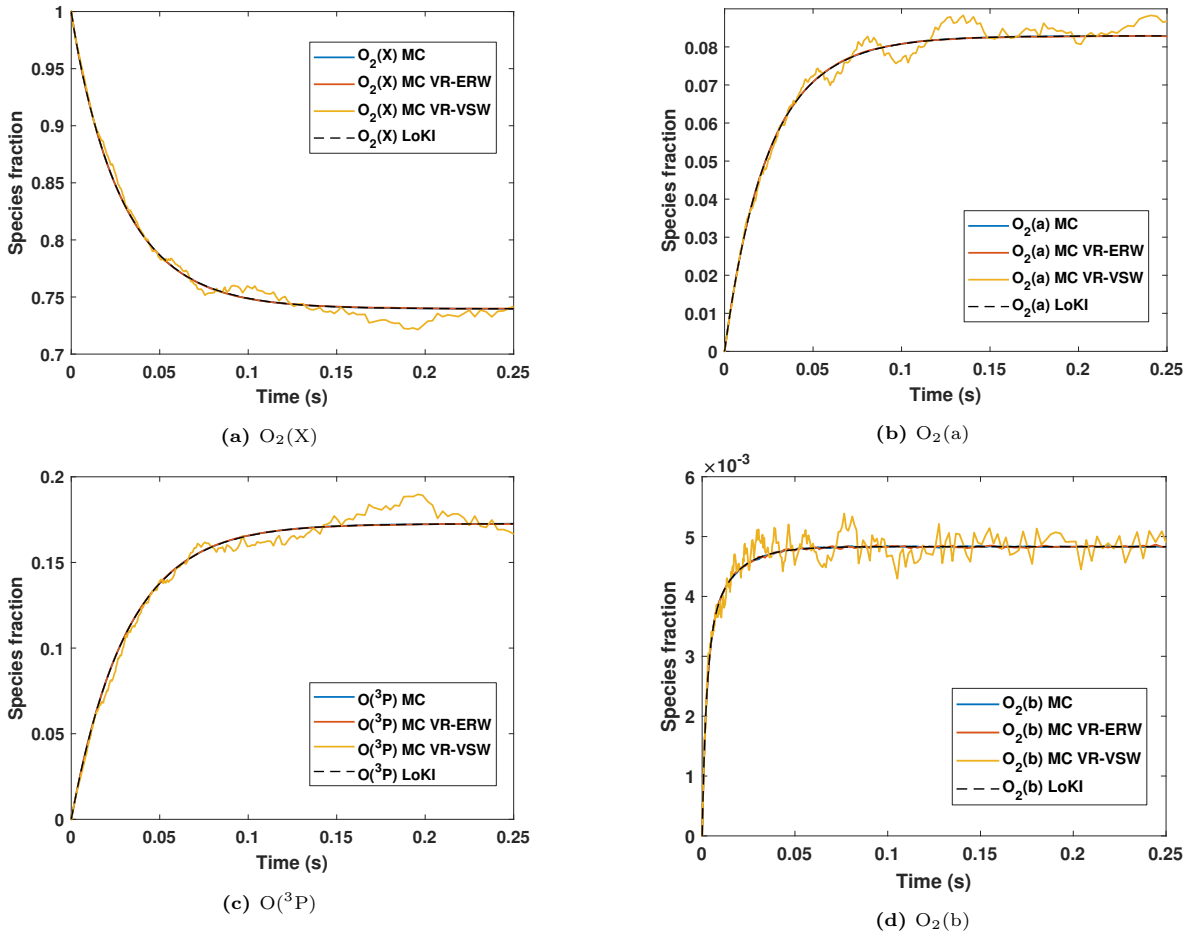


**Figure 2.8:** Temporal evolution of the various species, comparing KMC with/without variance reduction and using  $10^8$  particles.

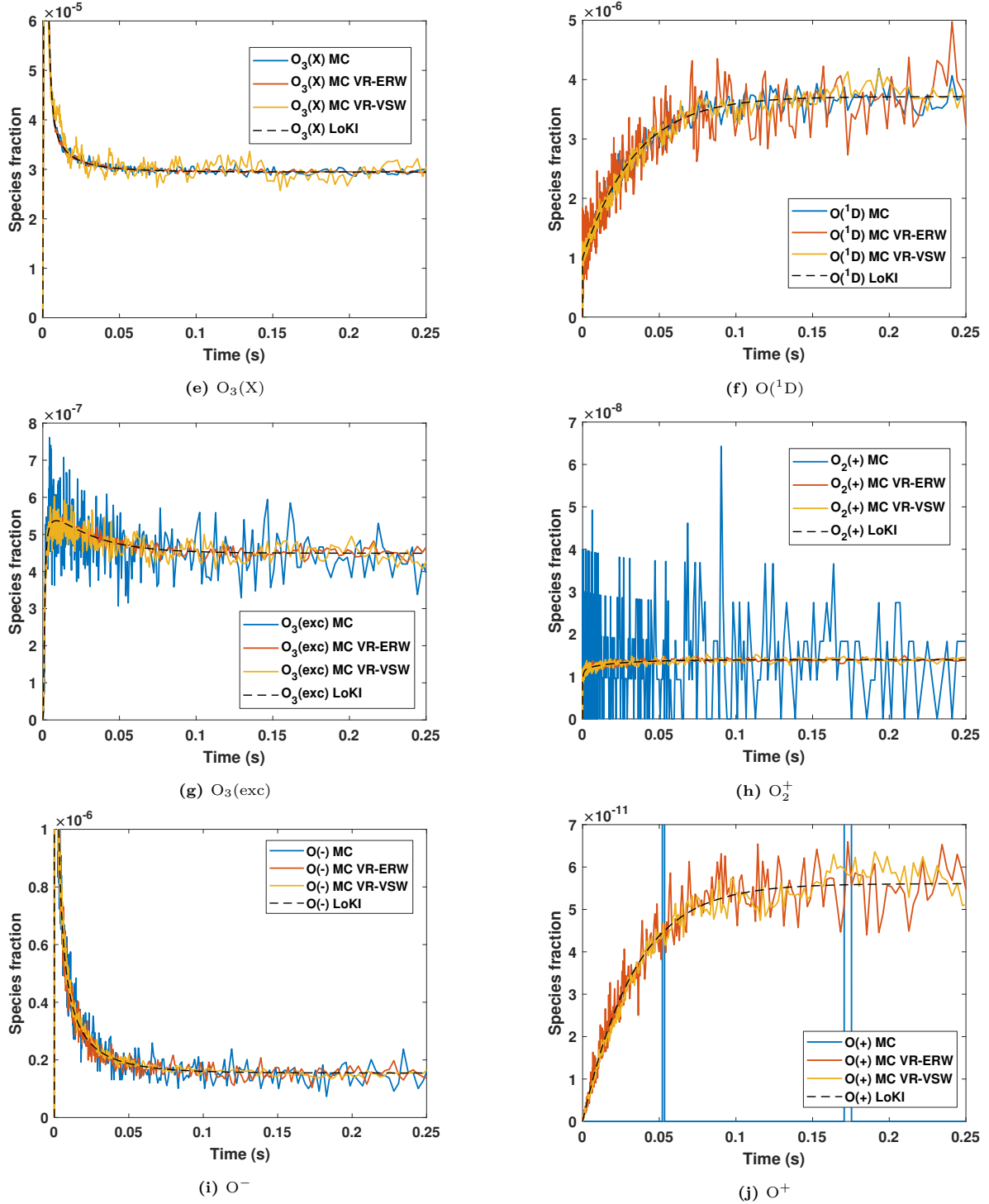


**Figure 2.8:** Temporal evolution of the various species, comparing KMC with/without variance reduction and using  $10^8$  particles. Continuation.

This comparison clarifies the way the variance reduction methods help on reducing the stochastic error of the minority species. In both cases, we lose precision in the more frequent species in order to describe better the rare ones. However, the reaction weights that help on the description of the less prevalent species are quite different in the two methods. While the reaction weights in ERW are no larger than 50, in VSW they can reach  $10^5$ . This large disparity is reflected on the description of the main species. The large reaction weights associated to VSW generate noticeable fluctuations in these species, since this technique induces similar relative fluctuations in all species. In turn, the smaller reaction weights associated to ERW allow a good description of the main species, while improving a lot the description of the minority species.

The CPU times of ERW and VSW are 1.45 and 1.69 times higher than the standard one, respectively. However, this difference is small compared with the improvements found on the description, taking into account that these methods provide descriptions of the rare species which would only be obtained in the standard approach with a significantly higher number of particles. Moreover, since the CPU time of ERW is smaller than VSW and the overall description is better, we consider that the former method is more promising and effective.

Finally, we tried to improve the description of a single species while keeping the other ones equal. In figure 2.9, we present the temporal evolution of  $O^+$  for different  $O^+$  weights and fixing the rest to 1. We find that the description with weight =  $10^7$  is significantly better than the one found with the automatic weight, i.e. the first version of the VSW method where all the species weights are changed. The CPU time of VSW with fixed weights is 1.3 times smaller than the one with the same method using automatic weights. Besides, to obtain a description of  $O^+$  with similar fluctuations using the standard approach, we would need  $\sim 10^{13}$  particles and, hence, a  $10^5$  times higher CPU time. Therefore, if we only want to characterize well the ions (for example), without paying attention to species like  $O_3(\text{exc})$ , this method might be interesting.

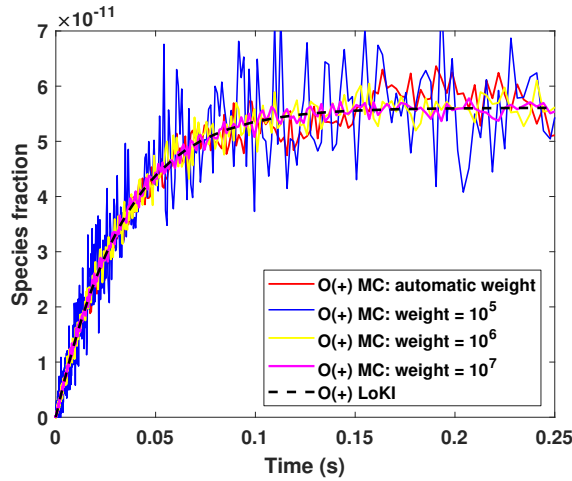


**Figure 2.9:** Temporal evolution of  $O^+$  ( $10^8$  particles) for different  $O^+$  weights.

## 2.6 Conclusions

In this chapter, a Kinetic Monte Carlo algorithm to simulate plasma chemistry was implemented, tested and compared with the traditional deterministic method. If the initial number of particles and Monte Carlo runs are properly chosen, and when the system is according to the thermodynamic limit, the results of the present formulation are entirely analogous to the ones of the 0-D rate balance equations. Moreover, the method is applicable in situations where the deterministic simulations may fail, for instance if fluctuations and correlations can play an important role in the dynamics.

The precision of the KMC description scales with the number of particles in a single run simulation, but also with the number of realizations of the system. In fact, adding more particles or more realizations of the same system configuration is completely equivalent in terms of accuracy and total CPU time. In addition, if we just want to obtain the steady-state results, we can increase their accuracy by performing a time-average of a single KMC run.

To reduce the statistical error associated with the description of the minority species densities, two variance reduction methods were developed: Equal Reaction Weights (ERW) and Variable Species Weights (VSW). Although both techniques improve remarkably the representation of the rare species densities, the former was found to be more promising, since it conserves the accurate description of the prevalent species, while the second adds considerable noise. The application of the variance reduction methods, specially ERW, is fundamental to guarantee an acceptable description of all species, including ions, which have relative densities varying between  $10^{-7}$  and  $10^{-10}$ , but whose description is essential to obtain a correct charge-balance and a good characterization of the plasma properties. The variance reduction methods are applicable to real systems and solve the multi-time-scale problem intrinsic to plasma-chemistry in low-temperature plasmas, improving the calculation times in the order of  $10^4$  times relatively to the standard approach.

Future work could involve coupling the present KMC formulation for heavy species with surface and/or electron kinetics.

## References

- [1] Dias, T. C. and Guerra, V. 2020 “Kinetic Monte Carlo simulations of plasma-chemistry” *Plasma Sources Sci. Technol.* **29**, 115003.
- [2] Oehrlein, G. S. and Hamaguchi, S. 2018 “Foundations of low-temperature plasma enhanced materials synthesis and etching” *Plasma Sources Sci Technol.* **27**, 023001.
- [3] Gudmundsson, J. T., Brenning, N., Lundin, D., and Helmersson, U. 2012 “High power impulse magnetron sputtering discharge” *J. Vac. Sci. Technol. A* **30**, 030801.

- [4] Labay, C., Hamouda, I., Tampieri, F., Ginebra, M.-P., and Canal, C. 2019 “Production of reactive species in alginate hydrogels for cold atmospheric plasma-based therapies” *Sci. Rep.* **9**, 16160.
- [5] Bauer, G. and Graves, D. B. 2016 “Mechanisms of Selective Antitumor Action of Cold Atmospheric Plasma-Derived Reactive Oxygen and Nitrogen Species” *Plasma Process Polym* **13**, 1157–1178.
- [6] Fridman, G., Friedman, G., Gutsol, A., Shekhter, A. B., Vasilets, V. N., and Fridman, A. 2008 “Applied Plasma Medicine” *Plasma Process Polym* **5**, 503–533.
- [7] Gherardi, M., Puač, N., and Shiratani, M. 2018 “Special issue: Plasma and agriculture” *Plasma Process Polym* **15**, 1877002.
- [8] Min, S. C., Roh, S. H., Niemira, B. A., Sites, J. E., Boyd, G., and Lacombe, A. 2016 “Dielectric barrier discharge atmospheric cold plasma inhibits Escherichia coli O157:H7, Salmonella, Listeria monocytogenes, and Tulane virus in Romaine lettuce” *Int. J. Food Microbiol.* **237**, 114–120.
- [9] Kitazaki, S., Koga, K., Shiratani, M., and Hayashi, N. 2012 “Growth Enhancement of Radish Sprouts Induced by Low Pressure O<sub>2</sub> Radio Frequency Discharge Plasma Irradiation” *Jpn J Appl Phys* **51**, 01AE01.
- [10] Rooij, G. J. van, Bekerom, D. C. M. van den, Harder, N. den, Minea, T., Berden, G., Bongers, W. A., Engeln, R., Graswinckel, M. F., Zoethout, E., and Sanden, M. C. M. van de 2015 “Taming microwave plasma to beat thermodynamics in CO<sub>2</sub> dissociation” *Faraday Discuss.* **183** (0), 233–248.
- [11] Snoeckx, R., Aerts, R., Tu, X., and Bogaerts, A. 2013 “Plasma-Based Dry Reforming: a Computational Study Ranging from the Nanoseconds to Seconds Time Scale” *J. Phys. Chem. C* **117**, 4957–4970.
- [12] Gillespie, D. 1976 “A General Method for Numerically Simulating the Stochastic Time Evolution of Coupled Chemical Reactions” *J. Comput. Phys.* **22**, 403–34.
- [13] Gillespie, D. 1977 “Exact Stochastic Simulation of Coupled Chemical Reactions” *J. Phys. Chem.* **81**, 2340–61.
- [14] Gillespie, D. T. 2007 “Stochastic Simulation of Chemical Kinetics” *Annu. Rev. Phys. Chem.* **58**, 35–55.
- [15] Gardiner, C. W., McNeil, K. J., Walls, D. F., and Matheson, I. S. 1976 “Correlations in stochastic theories of chemical reactions” *J. Stat. Phys.* **14**, 307–331.
- [16] McQuarrie, D. A. 1967 “Stochastic Approach to Chemical Kinetics” *J. Appl. Probab.* **4**, 413–478.
- [17] Cuppen, H. M., Karssemeijer, L. J., and Lamberts, T. 2013 “The Kinetic Monte Carlo Method as a Way To Solve the Master Equation for Interstellar Grain Chemistry” *Chem. Rev.* **113**, 8840–8871.
- [18] Guerra, V. and Marinov, D. 2016 “Dynamical Monte Carlo methods for plasma-surface reactions” *Plasma Sources Sci. Technol.* **25**, 045001.

- [19] Marinov, D., Teixeira, C., and Guerra, V. 2017 “Deterministic and Monte Carlo methods for simulation of plasma-surface interactions” *Plasma Process Polym* **14**, 1600175.
- [20] Slepoy, A., Thompson, A. P., and Plimpton, S. J. 2008 “A constant-time kinetic Monte Carlo algorithm for simulation of large biochemical reaction networks” *J. Chem. Phys* **128**, 205101.
- [21] Chang, Q., Cuppen, H., and Herbst, E. 2007 “Gas-grain chemistry in cold interstellar cloud cores with a microscopic Monte Carlo approach to surface chemistry” *Astron. Astrophys.* **469**, 973–983.
- [22] Vasyunin, A. I., Semenov, D. A., Wiebe, D. S., and Henning, T. 2009 “A Unified Monte Carlo Treatment of Gas-Grain Chemistry for Large Reaction Networks. I. Testing Validity of Rate Equations in Molecular Clouds” *Astrophys. J.* **691**, 1459–1469.
- [23] Tsvetkov, A. and Shematovich, V. 2009 “Kinetic Monte Carlo method for simulating astrochemical kinetics: Test calculations of molecular hydrogen formation on interstellar dust particles” *Solar Sys. Res.* **43**, 301–312.
- [24] Matsumoto, M. and Nishimura, T. 1998 “Mersenne Twister: A 623-Dimensionally Equidistributed Uniform Pseudo-Random Number Generator” *ACM Trans. Model. Comput. Simul.* **8**, 3–30.
- [25] Nishimura, T. 2000 “Tables of 64-bit Mersenne Twisters” *ACM Trans. Model. Comput. Simul.* **10**, 348–357.
- [26] [http://www.cplusplus.com/reference/random/mt19937\\_64/](http://www.cplusplus.com/reference/random/mt19937_64/).
- [27] Morillo-Candas, A. 2019 “Investigation of fundamental mechanisms of CO<sub>2</sub> plasmas” PhD thesis Université Paris-Saclay (ComUE).
- [28] Annušová, A., Marinov, D., Booth, J.-P., Sirse, N., Silva, M. L., Lopez, B., and Guerra, V. 2018 “Kinetics of highly vibrationally excited O<sub>2</sub>(X) molecules in inductively-coupled oxygen plasmas” *Plasma Sources Sci Technol.* **27**, 045006–36.
- [29] Stancu, G. D., Leroy, O., Coche, P., Gadonna, K., Guerra, V., Minea, T., and Alves, L. L. 2016 “Microwave air plasmas in capillaries at low pressure II. Experimental investigation” *J. Phys. D: Appl. Phys.* **49**, 435202.
- [30] Guerra, V. and Loureiro, J. 1999 “Kinetic model of a low-pressure microwave discharge in O<sub>2</sub>-H<sub>2</sub> including the effects of O-ions on the characteristics for plasma maintenance” *Plasma Sources Sci Technol.* **8**, 110–124.
- [31] Marinov, D., Guerra, V., Guaitella, O., Booth, J.-P., and Rousseau, A. 2013 “Ozone kinetics in low-pressure discharges: vibrationally excited ozone and molecule formation on surfaces” *Plasma Sources Sci Technol.* **22**, 055018.
- [32] Guerra, V. and Loureiro, J. 1997 “Self-consistent electron and heavy-particle kinetics in a low-pressure N<sub>2</sub>-O<sub>2</sub> glow discharge” *Plasma Sources Sci Technol.* **6**, 373–385.
- [33] Tejero-del-Caz, A., Guerra, V., Gonçalves, D., Lino da Silva, M., Marques, L., Pinhão, N., Pintasilgo, C. D., and Alves, L. L. 2019 “The LisbOn KInetics Boltzmann solver” *Plasma Sources Sci.*

*Technol.* **28**, 043001

<https://github.com/IST-Lisbon/LoKI>.

- [34] Tejero-del-Caz, A., Alves, L. L., Guerra, V., Gonçalves, D., Lino da Silva, M., Pinhão, N., Marques, L., and Pintassilgo, C. D. “The LisbOn Kinetics tool suit” *ESCAPE XXIV* p. 99, Glasgow, U.K., July 2018.
- [35] <https://github.com/IST-Lisbon/LoKI>.
- [36] Pacelli, A. and Ravaioli, U. 1997 “Analysis of variance-reduction schemes for ensemble Monte Carlo simulation of semiconductor devices” *Solid State Electron. Lett.* **41**, 599–605.
- [37] Vialeto, L., Longo, S., and Diomede, P. 2019 “Benchmark calculations for electron velocity distribution function obtained with Monte Carlo Flux simulations” *Plasma Sources Sci. Technol.* **28**, 115015.
- [38] McNeil, K. J. and Walls, D. F. 1974 “Nonequilibrium phase transitions in chemical reactions” *J. Stat. Phys.* **10**, 439–448.
- [39] Nitzan, A., Ortoleva, P., Deutch, J., and Ross, J. 1974 “Fluctuations and transitions at chemical instabilities: The analogy to phase transitions” *J. Chem. Phys.* **61**, 1056–1074.
- [40] Longo, S. 1997 “Chemical instabilities in the XeCl laser discharge: a stochastic approach” *Chem. Phys. Lett.* **268**, 306–312.
- [41] Longo, S. 2006 “Monte Carlo simulation of charged species kinetics in weakly ionized gases” *Plasma Sources Sci. Technol.* **15**, S181–S188.

# 3

## The LisbOn KInetics Monte Carlo solver

### Chapter summary

The LisbOn KInetics Monte Carlo (LoKI-MC) is an open-source simulation tool that solves the electron kinetics for low-temperature plasmas in different gas mixtures, using Monte Carlo techniques. Following the data organization of the LisbOn KInetics Boltzmann (LoKI-B) solver, the program easily addresses any complex mixture of atomic/molecular species, describing electron collisions with any target state (electronic, vibrational and rotational), characterized by any user-prescribed population.

LoKI-MC is written in C++, benefiting from a highly-efficient object-oriented structure. On input, the code requires the working conditions, the gas-mixture composition, the distributions of populations for the levels of the atomic/molecular gases considered, and the relevant sets of electron-scattering cross sections obtained from the open-access website LXCat. On output, it yields the electron energy and velocity distribution functions, the electron transport coefficients, the collision rate-coefficients, and the electron power absorbed from the electric field and transferred to the different collisional channels.

This chapter presents LoKI-MC and gives examples of results obtained for different model and real gases, verifying and benchmarking the simulation tool against analytical solutions and other available codes, and assesses its computational performance. Moreover, the effects of the gas temperature, anisotropic ionization scattering (induced by momentum conservation) and superelastic collisions are analyzed in real gases.

The majority of the present chapter is based on [1]. However, two important improvements relatively to [1] are introduced, namely, on the asynchronous advancement of electrons and on the renormalization of the electron number. The former leads to higher statistical precision in the results and the latter avoids systematic errors when ionization is strong. These improvements are described in detail and all simulations presented in [1] were re-run.

### 3.1 Introduction

Low-temperature plasmas (LTPs) are strongly reactive systems, characterized by a low density of charged particles (ionization degrees  $\sim 10^{-6} - 10^{-3}$ ), high electron temperature ( $\sim 1$  eV) and heavy-species translational and internal temperatures ranging from 300 K to  $\sim 10^4$  K. The strong non-equilibrium nature of LTPs can efficiently stimulate several chemical processes relevant for industrial [2, 3], medical [4–6], agricultural [7–9] and environmental [10, 11] applications. Electrons play a major role in these plasmas, since they transmit the energy acquired from the electric field to the heavy particles through various collisional channels, thereby enhancing the reactivity of the environment. Therefore, the taming and tuning of the energy distribution of the electrons is essential to maximize the capability of LTPs.

The electron kinetics in gas discharges can be described in detail by solving numerically the differential electron Boltzmann equation (EBE), or by tracking the stochastic motion of the individual electrons using Monte Carlo methods [12]. Publicly available simulation tools based on either approach were developed in the last decades, for the benefit of the LTP community. Some examples are ELENDIF [13], BOLSIG+ [14], EEDF [15], BOLOS [16], LoKI-B [17, 18], MultiBolt [19], METHES [20] and Magboltz [21], the latter five being open-source codes. The first five codes rely on a low-anisotropy approximation, keeping only two terms in an expansion of the electron distribution in Legendre polynomials over the velocity space [22]. Multibolt is a multi-term Boltzmann equation solver and METHES is a Monte Carlo collision code [23], both written in MATLAB. Magboltz is a Fortran code that uses a Monte Carlo integration technique for solving the EBE. BOLSIG+, BOLOS, LoKI-B, MultiBolt and METHES accept input files with electron scattering cross sections obtained from the LXCat open-access website [24]. The LisbOn KInetics Boltzmann solver (LoKI-B) was developed as a response to the need of having an electron Boltzmann solver easily addressing the simulation of the electron kinetics in any complex gas mixture of atomic/molecular species, describing electron collisions with any target state (electronic, vibrational and rotational), characterized by any user-prescribed population, and accounting for superelastic and stepwise excitation processes.

The range of reduced electric fields  $E/N$  (the ratio of the electric field to the gas density) where the two-term approximation is valid strongly depends on the background gas mixture and, without benchmark with more accurate formulations, one can never be sure about the accuracy of this approach [25–28]. Nevertheless, in all gases the two-term approximation fails for sufficiently high values of  $E/N$ , as strong electric fields induce a preferential direction in the electron motion, thus leading to important anisotropies. Multibolt, as multi-term solver, and METHES and Magboltz, as Monte Carlo solvers, do not have this drawback. However, Magboltz uses hardcoded cross sections. Furthermore, MultiBolt and METHES do not consider the thermal motion of the background gas molecules, and do not address the internal levels

of the atoms/molecules nor superelastic collisions<sup>1</sup>.

It is clear that the community is still lacking a general and flexible Boltzmann equation solver that does not depend on the two-term approximation. This work presents the LisbOn KInetics Monte Carlo (LoKI-MC) open-source code, which solves the electron transport in a gas subject to an uniform DC electric field using Monte Carlo techniques. LoKI-MC is written in C++, benefiting from an efficient object-oriented structure, and follows the data organization of LoKI-B. Compared with the previously mentioned open-source codes that do not use the two-term expansion, the solver presented in this work has the following advantages: (i) inclusion of the thermal motion of the gas molecules, allowing to describe the electron swarms at low  $E/N$  and to obtain the correct thermodynamic properties in the limit of vanishingly small fields; (ii) straightforward insertion of gas internal levels (electronic, vibrational and rotational) and, accordingly, of superelastic and stepwise processes; (iii) possibility of describing anisotropic scattering in ionization, induced by momentum conservation, and availability of different models for the energy sharing between primary and secondary electrons; (iv) calculation of the electron power balance, available on output; (v) provision of the higher-order anisotropies of the distribution function.

The present version of the code has several additional capabilities, whose discussion is left for subsequent chapters, such as: general anisotropic scattering in *any* collision type (chapter 4); inclusion of DC magnetic fields together with AC/DC electric fields (chapter 5); and time-dependent electric-field pulses (chapter 6).

This chapter is organized as follows. Section 3.2 discusses in detail the Monte Carlo formalism adopted to study the electron kinetics. Section 3.3 summarizes the scope of the LoKI-MC code, focusing on the required input data and the possible output information. Section 3.4 presents an extensive benchmarking and verification in model gases and real gases, and discusses the influence of anisotropic ionization scattering and superelastic collisions on the results. Section 3.5 closes the work with final remarks and future guidelines.

## 3.2 Methods

The Monte Carlo method presented here involves the study of an electron swarm moving under the influence of a uniform DC electric field  $\mathbf{E}$  through a spatially homogeneous background of gas molecules. The number density of the swarm is assumed to be so low that the charged particles can be neglected. Electrons move in an unbounded environment, performing series of free flights interrupted by elastic, inelastic or superelastic collisions with gas molecules. Figure 3.1 schematizes the electron motion with one collision. The collision-free times and the collision dynamics are calculated by generating random numbers

---

<sup>1</sup>After the writing of [1], MultiBolt now allows to consider the thermal motion of the background gas molecules and superelastic collisions, the latter done in a similar way as in Bolsig. Furthermore, the current version is written in C++.

sampled from probability distributions based on the underlying physics. In the first code release [1], with the exception of ionization, electron collisions are assumed isotropic. The random numbers are produced with a 64-bit version of the Mersenne Twister pseudorandom number generator using the function `mt19937_64` implemented at the C++ library `random` [29–31], which is characterized by a high period and good uniformity. During the simulation, the information of the electrons is stored in order to calculate distribution functions, transport coefficients and other relevant quantities.

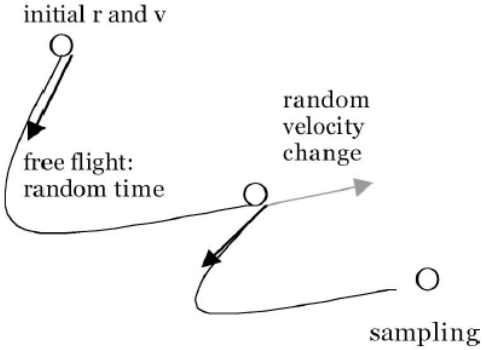


**Figure 3.1:** Example of stochastic trajectory of one electron with one collision. Taken from [32].

### 3.2.1 Cross sections

The momentum-transfer cross section for an electron-neutral collision, described by a differential (angle-resolved) cross section  $\frac{d\sigma(\epsilon, \theta)}{d\Omega}$ , is generally defined as [33]

$$\sigma_{\text{MT}}(\epsilon) \equiv 2\pi \int_0^\pi \frac{d\sigma(\epsilon, \theta)}{d\Omega} (1 - \cos \theta) \sin \theta d\theta, \quad (3.1)$$

where  $\epsilon$  is the incident electron energy,  $\theta$  is the polar scattering angle and  $d\Omega = \sin \theta d\theta d\phi$  is the differential solid angle, assuming symmetry regarding the azimuthal angle  $\phi$ . For a gas  $k$ , the electron-neutral momentum-transfer cross section  $\sigma_{k,\text{MT}}(\epsilon)$  is constructed by weighting the contributions of the different types of collisional mechanisms to give [17]

$$\sigma_{k,\text{MT}}(\epsilon) = \sum_i \xi_{k_i} \sigma_{k_i,\text{MT}}^{\text{el}}(\epsilon) + \sum_{i,j > i} [\xi_{k_i} \sigma_{k_{(i,j)},\text{MT}}(\epsilon) + \xi_{k_j} \sigma_{k_{(j,i)},\text{MT}}(\epsilon)], \quad (3.2)$$

where the sums span the internal states of the gas,  $\xi_{k_i}$  is the fractional population of the level  $k_i$ ;  $\sigma_{k_i,\text{MT}}^{\text{el}}$ ,  $\sigma_{k_{(i,j)},\text{MT}}$  and  $\sigma_{k_{(j,i)},\text{MT}}$  are the electron-neutral momentum-transfer cross sections for the elastic scattering of level  $k_i$ , the inelastic excitation  $k_i \rightarrow k_j$ , and the superelastic de-excitation  $k_j \rightarrow k_i$ , respectively. The latter cross sections are frequently taken assuming an *isotropic scattering*, in which case one can identify the momentum-transfer cross section with the integral cross section  $\sigma_{k_{(i,j)}}$  (integrated over all scattering angles), i.e.,  $\sigma_{k_{(i,j)},\text{MT}} \simeq \sigma_{k_{(i,j)}}$ . Moreover, the elastic momentum-transfer is usually

identified with that of the highly-populated ground-state of the gas, which amounts to assume the same momentum-transfer cross section for all states of the gas. Therefore,

$$\sigma_{k,\text{MT}}(\epsilon) \simeq \sigma_{k,\text{MT}}^{\text{el}}(\epsilon) + \sum_{i,j>i} [\xi_{k_i} \sigma_{k_{(i,j)}}(\epsilon) + \xi_{k_j} \sigma_{k_{(j,i)}}(\epsilon)] . \quad (3.3)$$

In some cases, the elastic momentum-transfer cross section is not available and only the total momentum-transfer cross section is known, which in databases is usually termed as *effective*  $\sigma_{k,\text{MT}}^{\text{eff}}$ . In such cases, the elastic component can be deduced by subtracting the inelastic and superelastic contributions

$$\sigma_{k,\text{MT}}^{\text{el}}(\epsilon) = \sigma_{k,\text{MT}}^{\text{eff}}(\epsilon) - \sum_{i,j>i} [\xi_{k_i}^{\text{prescribed}} \sigma_{k_{(i,j)}}(\epsilon) + \xi_{k_j}^{\text{prescribed}} \sigma_{k_{(j,i)}}(\epsilon)] ,$$

where the populations  $\xi_{k_i}^{\text{prescribed}}$  and  $\xi_{k_j}^{\text{prescribed}}$  correspond to some prescribed distribution, coherent with the measured/estimated data of  $\sigma_{k,\text{MT}}^{\text{eff}}$ , and allowing to obtain a *unique* result (density independent) for the elastic cross section [17]. By default, LoKI-MC adopts a Boltzmann distribution at the room temperature for  $\xi_{k_i}^{\text{prescribed}}$ . We recommend to replace, whenever possible, the data for effective momentum-transfer cross sections with that for elastic momentum-transfer cross sections.

The cross-section values are matched to an energy grid by linear interpolation [17]. Following the ontology of separating the data from the code, no extrapolation is made for energies larger than the maximum energy of the provided cross section. The maximum energy of the grid is updated dynamically along the simulation depending on the energy of the electron ensemble.

Finally, the cross sections of the superelastic processes  $k_j \rightarrow k_i$  are determined from the Klein-Rosseland relation, expressing the principle of detailed balance [34]:

$$\sigma_{k_{(j,i)}}(\epsilon) = \frac{g_{k_i}}{g_{k_j}} \frac{\epsilon + \Delta\epsilon_{k_{(i,j)}}}{\epsilon} \sigma_{k_{(i,j)}}(\epsilon + \Delta\epsilon_{k_{(i,j)}}) , \quad (3.4)$$

where  $g_{k_i}$  and  $g_{k_j}$  denote the statistical weights of the levels  $k_i$  and  $k_j$ , respectively, and  $\Delta\epsilon_{k_{(i,j)}}$  is the energy threshold of the inelastic collision  $k_i \rightarrow k_j$ .

### 3.2.2 Free flight

To describe the free flight of an electron, we need to determine when the next collision will occur. This can be done using either the integration method [35] or the null collision technique introduced by Skullerud [36]. We employ the latter, where the times between collisions are calculated without any numerical integration through the use of a constant trial collision frequency  $\nu'$  which must satisfy

$$\nu' \geq \max_{\text{all } v_r} \{\nu_T(v_r)\} , \quad (3.5)$$

where  $\nu_T(v_r)$  is the total collision frequency for a given relative speed  $v_r = |\mathbf{v} - \mathbf{V}|$ , and  $\mathbf{v}$  and  $\mathbf{V}$  are the velocities of the incident electron and the target molecule, respectively. In this case, the distribution of collision times  $t_c$  is exponential:  $P(t_c) = \nu' \exp(-\nu' t_c)$ . Using simple theorems of probability theory, the time between two successive collisions can be obtained by generating an uniform random number  $p_t$  in the  $]0,1[$  range [37]:

$$t_c = -\frac{\ln(p_t)}{\nu'} . \quad (3.6)$$

Pay attention that  $p_t = 0$  or  $1$  are excluded to avoid an infinite or null collision time, respectively. Effectively, with the null collision technique, we introduce another collisional process (where no real interaction occurs) with a collision frequency which, when added to the total collision frequency  $\nu_T(v_r)$ , gives a constant value  $\nu'$  for all relative speeds  $v_r$ .

Having determined the collision time  $t_c$ , the position  $\mathbf{r}$  and velocity  $\mathbf{v}$  of the  $N_e$  electrons at the end of the free flight are calculated by integrating analytically the classical equations of motion:

$$\mathbf{r}(t + t_c) = \mathbf{r}(t) + \mathbf{v}(t)t_c - \frac{e\mathbf{E}}{2m}t_c^2 , \quad (3.7)$$

$$\mathbf{v}(t + t_c) = \mathbf{v}(t) - \frac{e\mathbf{E}}{m}t_c , \quad (3.8)$$

where  $e$  and  $m$  are the electron charge and mass, respectively. Note that, in this chapter, the electric field  $\mathbf{E}$  is DC and antiparallel to the  $z$  axis ( $\mathbf{E} = -E\hat{\mathbf{z}}$ ). In chapter 5, we generalize the formulation to AC/DC electric fields together with DC magnetic fields crossed at an arbitrary angle. Finally, we should mention that the Leapfrog/Velocity-Verlet method is used very often to integrate the equations of motion in space- and time- varying fields (see e.g. [38]). However, in this case such approach is not needed since we are dealing with an uniform electric field, and equations (3.7) and (3.8) are the exact solution of the motion.

### 3.2.3 Collision choice

After propagating the electrons during the free flight, we should determine the type of electron-neutral collision that each of them undergoes. The likelihood of the occurrence of a collision of kind  $\mathcal{K}$ , out of the  $N_c$  kinds available, is proportional to the corresponding collision frequency  $\nu_{\mathcal{K}}$ :

$$P_{\mathcal{K}} = \frac{\nu_{\mathcal{K}}(v_r)}{\nu'} = \frac{n_{\mathcal{K}}^s \sigma_{\mathcal{K}}(v_r) v_r}{\nu'} . \quad (3.9)$$

Here,  $n_{\mathcal{K}}^s$  is the density of the target species  $s$  and  $\sigma_{\mathcal{K}}(v_r)$  is the collision cross section.

The relative speed  $v_r$  requires the knowledge of the target velocity  $\mathbf{V}$ , which is assumed to follow a Maxwell-Boltzmann distribution at the gas temperature  $T_g$ . The three components  $V_{x,y,z}$  can be sampled

from the distribution using the Box and Mueller method [39]:

$$\begin{cases} V_x = \sigma_{V_{th}} \sqrt{-2 \ln p_{V,1}} \cos(2\pi p_{V,2}) \\ V_y = \sigma_{V_{th}} \sqrt{-2 \ln p_{V,1}} \sin(2\pi p_{V,2}) \\ V_z = \sigma_{V_{th}} \sqrt{-2 \ln p_{V,3}} \cos(2\pi p_{V,4}) \end{cases}, \quad (3.10)$$

where  $p_{V,1-4} \in ]0, 1]$  are uniform random numbers,  $\sigma_{V_{th}} = \sqrt{k_B T_g / M}$  is the standard deviation associated to the normal distribution of each component,  $k_B$  is the boltzmann constant and  $M$  is the target mass. It should be noted that the random velocities  $V_{x,y}$  are statistically independent, although the pair of uniform random numbers used for the generation is the same [39].

Considering the overestimation of the collision frequency in the calculation of the free-flight time, expressed by equation (3.5), we add a null collision process with probability  $P_{\text{null}} = \frac{\nu_{\text{null}}(v_r)}{\nu'} = \frac{\nu' - \nu_T(v_r)}{\nu'}$ . Based on the generation of a random number  $p_c \in ]0, 1]$ , the collision kind is chosen as illustrated in figure 3.2:

- if  $p_c \leq \sum_{\kappa=1}^{N_c} P_{\kappa}$ , choose the collision kind  $\lambda$  for which  $\sum_{\kappa=1}^{\lambda-1} P_{\kappa} < p_c \leq \sum_{\kappa=1}^{\lambda} P_{\kappa}$ ;
- else, the collision is null.

Note that  $\lambda$  is found using the bisection method. This procedure is repeated for each electron.

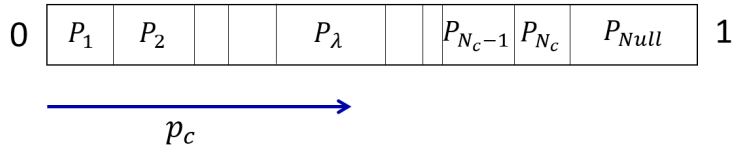


**Figure 3.2:** Selection of the collision type.

The collisions chosen for each electron are then performed. To do so, we admit that the collisions are local ( $\mathbf{r} = \mathbf{r}'$ ) and instantaneous ( $t = t'$ ), where ' means “immediately after the collision”. The electrons undergoing null collisions have no velocity changes ( $\mathbf{v} = \mathbf{v}'$ ). The velocity changes during real electron-neutral collisions depend on their type, as discussed in the following couple of sections.

### 3.2.4 Conservative collisions

For the treatment of conservative collisions, we mainly follow the work of Yousfi *et al.* [40], where the influence of the non-null target velocity is considered and isotropic scattering is assumed<sup>2</sup>. The electron velocity after the collision,  $\mathbf{v}'$ , is determined from the conservation equation of momentum transfer in the laboratory frame,

$$\mathbf{v}' = \frac{M}{m_e + M} \mathbf{v}'_r + \frac{m_e \mathbf{v} + M \mathbf{V}}{m_e + M}. \quad (3.11)$$

---

<sup>2</sup>The formulation is generalized to anisotropic scattering in chapter 4.

The second term of the right-hand side represents the velocity of the center-of-mass frame, which is known. Thus, we only need to determine the relative velocity after the collision  $\mathbf{v}'_r$ .

The relative speed  $v'_r$  is calculated from energy conservation:

$$v'_r = \left[ v_r^2 - \frac{2}{\mu} E_{\text{loss}} \right]^{1/2}, \quad (3.12)$$

where  $E_{\text{loss}}$  represents the energy lost in the collision, which is zero, positive or negative, if the collision is elastic, inelastic or superelastic, respectively;  $\mu = m_e M / (m_e + M)$  is the reduced mass of the system electron + molecule.

The direction of the relative velocity  $\mathbf{v}'_r$  is determined in the center-of-mass frame from the calculation of the scattering angle  $\chi'$  and the azimuthal angle  $\eta'$ . The scattering angle  $\chi' \in [0, \pi]$  consists on the angle between  $\mathbf{v}'_r$  and  $\mathbf{v}_r$ . Assuming *isotropic scattering*<sup>2</sup>, this angle is calculated from an uniform distribution of random numbers  $p_\chi \in [0, 1]$ :

$$\chi' = \arccos(1 - 2p_\chi). \quad (3.13)$$

Similarly, the azimuthal angle  $\eta'$  is calculated with another random number  $p_\eta \in ]0, 1]$ :

$$\eta' = 2\pi p_\eta, \quad (3.14)$$

where we assume that  $\eta'$  is uniformly distributed in  $]0, 2\pi]$ .

The knowledge of the relative speed  $v'_r$  together with the angles  $\chi'$  and  $\eta'$  defines the relative velocity  $\mathbf{v}'_r$  in the center-of-mass frame. Using the well-known Euler relations, this vector is projected into the laboratory frame according to

$$\begin{cases} v'_{rx} = v'_r (-\sin \chi' \sin \eta' \sin \phi_r + \sin \chi' \cos \eta' \cos \theta_r \cos \phi_r \\ \quad + \cos \chi' \sin \theta_r \cos \phi_r) \\ v'_{ry} = v'_r (\sin \chi' \sin \eta' \cos \phi_r + \sin \chi' \cos \eta' \cos \theta_r \sin \phi_r \\ \quad + \cos \chi' \sin \theta_r \sin \phi_r) \\ v'_{rz} = v'_r (-\sin \chi' \cos \eta' \sin \theta_r + \cos \chi' \cos \theta_r) \end{cases}, \quad (3.15)$$

where  $\theta_r$  is the polar angle and  $\phi_r$  is the azimuthal angle in the laboratory frame of vector  $\mathbf{v}_r$ . Finally, using equation (3.11), the electron velocity after the collision  $\mathbf{v}'$  is calculated in the laboratory frame.

A very common approximation involves neglecting the molecular motion, since the mass of the electron is much smaller than that of the molecule ( $m_e + M \simeq M$ ). In this case, the electron speed after the collision is [41]

$$v' = \left\{ \left( v^2 - \frac{2E_{\text{loss}}}{m_e} \right) \left[ 1 - \frac{2m_e M}{(m_e + M)^2} (1 - \cos \chi') \right] \right\}^{1/2}, \quad (3.16)$$

and the velocity  $\mathbf{v}'$  is determined in the laboratory frame after generating the scattering angles and applying them in the Euler relations.

In LoKI-MC, it is possible to choose between the approximative treatment of (3.16), or preserving the effect of the gas temperature calculating relative velocities from (3.11)-(3.12). Furthermore, to improve the computational efficiency while ensuring a correct treatment for low electron energies, it is also possible to choose a hybrid solution where the molecular motion is taken into account only when the electron energy  $\epsilon$  is comparable to the gas mean energy:  $\epsilon \leq 20 \times \frac{3}{2}k_B T_g$ . This constitutes a very good approach since, even when the electron and molecule energies are similar, the electron speed is much larger than the molecule speed, due to a much lower mass.

### 3.2.5 Non-conservative collisions

We consider two types of non-conservative processes: attachment and ionization. In attachment, the electron is simply removed from the simulation. In ionization, the dynamics is more complex since it involves three bodies. However, as the ionization energy is much higher than the gas thermal energy, considering target molecules at rest is a very good approximation in the treatment of ionization, which strongly simplifies the calculations. Following this approach, the energies of the scattered ( $\epsilon'$ ) and ejected ( $\epsilon_{ej}$ ) electrons are restrained by

$$\epsilon' + \epsilon_{ej} = \epsilon - \Delta\epsilon_{ion}, \quad (3.17)$$

where  $\epsilon$  is the incident electron energy and  $\Delta\epsilon_{ion}$  is the ionization potential.

Upon the knowledge of the single differential ionization cross section (SDCS)  $\sigma_{ion}(\epsilon, u)$ , the energy of one electron (for instance, the ejected electron) can be obtained from a unit uniform distribution of random numbers  $p_{ion}$  using [42]

$$p_{ion} = \frac{\int_0^{\epsilon_{ej}} \sigma_{ion}^{ej}(\epsilon, u) du}{\sigma_{ion}(\epsilon)}, \quad (3.18)$$

where  $\sigma_{ion}(\epsilon)$  is the integral ionization cross section. This equation is solved to find  $\epsilon_{ej}$  and the energy of the scattered electron  $\epsilon'$  is calculated from the conservation equation (3.17). We use a fitting expression for the SDCS proposed by Opal *et al* based on a comprehensive set of measurements [43, 44]:

$$\sigma_{ion}^{ej}(\epsilon, u) = \frac{\sigma_{ion}(\epsilon)}{w \arctan[(\epsilon - \Delta\epsilon_{ion})/(2w)]} \frac{1}{1 + (u/w)^\beta}, \quad (3.19)$$

where  $\beta \simeq 2$  and  $w$  is a parameter close to the ionization threshold  $\Delta\epsilon_{ion}$ , which is set for each gas according to the original estimates. By inserting expression (3.19) in (3.18) and after solving the integral, we obtain:

$$\epsilon_{ej} = w \tan \left\{ p_{ion} \arctan \frac{\epsilon - \Delta\epsilon_{ion}}{2w} \right\}. \quad (3.20)$$

The normalized values of the ejected electron energy,  $\frac{\epsilon_{ej}}{\epsilon - \Delta\epsilon_{ion}}$ , and the scattered electron energy,  $\frac{\epsilon'}{\epsilon - \Delta\epsilon_{ion}}$ , are represented in figure 3.3, as a function of the unit uniform random number  $p_{ion}$ , and for different incident electron energies  $\epsilon$ . For low incident energies  $\epsilon \lesssim \Delta\epsilon_{ion} + w \sim 2\Delta\epsilon_{ion}$ , the energy is shared

uniformly between the ejected and scattered electrons. For high incident energies  $\epsilon \gg \Delta\epsilon_{\text{ion}}$ , one of the electrons takes most of the energy left after the collision.

As the differential ionization cross section is not always known, LoKI-MC provides the freedom of using various simpler models for the energy sharing after an ionization collision. One possibility is to assume a fixed energy sharing factor  $\gamma$  between the two electrons:  $\epsilon_{ej} = \gamma(\epsilon - \Delta\epsilon_{\text{ion}})$ . For  $\gamma = 0.5$ , there is equal energy sharing; for  $\gamma = 0$ , the scattered electron takes all the residual energy. Lastly,  $\gamma$  may be provided by a unit uniform random number, equivalent to the low energy limit of Opal's formula.

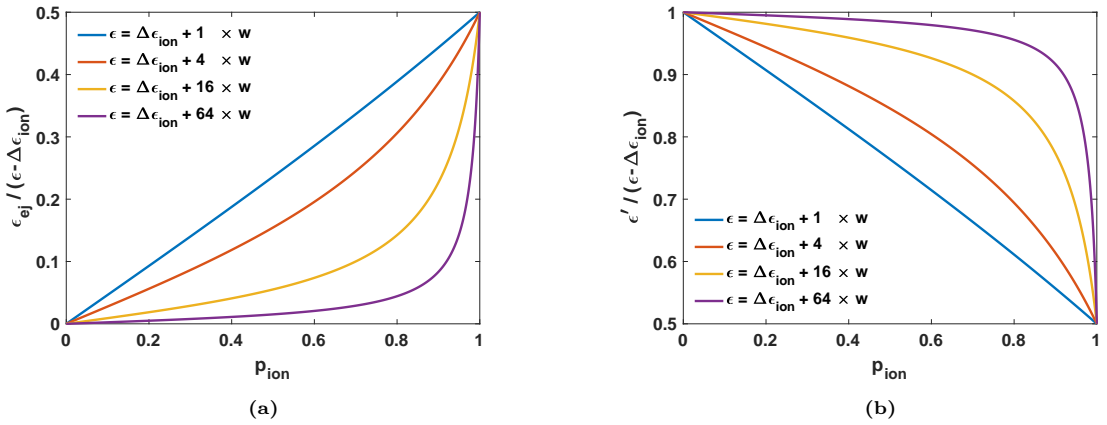


**Figure 3.3:** Normalized values of the ejected electron energy,  $\frac{\epsilon_{ej}}{\epsilon - \Delta\epsilon_{\text{ion}}}$ , and the scattered electron energy,  $\frac{\epsilon'}{\epsilon - \Delta\epsilon_{\text{ion}}}$ , as a function of the unit uniform random number  $p_{\text{ion}}$ , and for different incident electron energies  $\epsilon$ , when using the SDCS proposed by Opal *et al* [43].

With the energies (and speeds) of the two electrons determined, it is still necessary to define the directions of the velocities. One possibility is to assume isotropic scattering for both electrons using equations similar to (3.13) and (3.14). However, in this situation the linear momentum is not conserved. In fact, the general problem is undetermined and two additional assumptions may be taken as an alternative to isotropic scattering [45]: the incident, ejected and scattered electron velocities are coplanar; the scattered and ejected electron velocities are perpendicular. Considering the conservation of energy and momentum, these assumptions lead to [45]:

$$\cos \chi' = \sqrt{\frac{\epsilon'}{\epsilon - \epsilon_{\text{ion}}}}, \quad (3.21a)$$

$$\cos \chi_{ej} = \sqrt{\frac{\epsilon_{ej}}{\epsilon - \epsilon_{\text{ion}}}}. \quad (3.21b)$$

The azimuthal angle of the scattered electron is determined assuming a uniform distribution in  $]0, 2\pi]$ :  $\eta' = 2\pi p_\eta$ . The azimuthal angle of the ejected electron is  $\eta_{ej} = \eta' + \pi$ . Finally, the velocities of the scattered ( $\mathbf{v}'$ ) and ejected ( $\mathbf{v}_{ej}$ ) electrons are obtained in the laboratory frame using Euler transformations similar to the relations (3.15).

In LoKI-MC, the ionization scattering can be defined to be either isotropic or anisotropic (induced by momentum conservation). This flexibility is important since most Boltzmann solvers assume isotropic scattering in ionization and the cross-section sets are usually optimized in this condition (see section 3.4.4).

The number of electrons  $N_e$  in the simulation is fixed to a constant value using the particle-replacement method, which is frequently applied and does not affect the average properties of the ensemble [20, 46–48]. This technique was extensively analyzed by Mirić *et al* [48] and Rabie and Franck [20], in conditions where non-conservative processes have a strong influence. When there is an ionization event, a randomly chosen electron is removed, and when there is an attachment, a random electron from the ensemble is copied. This technique confers stability to the code and does not affect the average properties of the ensemble [32, 48]. However, the renormalization must be performed with care; in particular, it should be done according to the distribution of electrons that were previously in the ensemble, plus the newly-born electrons from ionization events, less the attached electrons. In the first version presented in [1], the newly-born electrons were being replaced by a random electron from the ensemble, which is not correct, since it gives a preferential weight to this kind of electrons. This imprecision was creating slight differences from multi-term results [19], for conditions where ionization is dominant (e.g., in Ar, for  $E/N \gtrsim 500$  Td, see figure 5 of [1]). With the correct renormalization of the electron number, the differences have vanished, as shown in section 3.4. Take note that another valid approach would be to use a dynamical particle list, whose size grows/decreases depending on ionization/attachment events, and remove/copy electrons only when the total number of electrons lies outside of a defined interval [32, 49].

### 3.2.6 Asynchronous advancement of electrons

The time interval between collisions  $t_c$  given by equation 3.6 is random and different for each electron. Therefore, the evolution of the ensemble is not synchronized, which poses challenges in sampling electron properties required for calculating the swarm coefficients. In the previous version of LoKI-MC [1], this issue was circumvented by generating a single random time-step and applying it uniformly to all electrons. Nevertheless, it was observed that while this approach yields the correct average values, it introduces significant statistical fluctuations (see figure 3.4), leading to longer computation times, specially when inelastic processes are dominant. Therefore, in this chapter we relax that approximation and allow the electrons to evolve freely in time until specific time-instants where they are once again synchronized (see chapter 10.3.3 of [50] for more details).

We set the time interval as a multiple,  $\mathcal{N}_{\text{sync}}$ , of the constant trial collision frequency  $\nu'$ :  $\Delta t_{\text{sync}} = \mathcal{N}_{\text{sync}}/\nu'$ . The default value of  $\mathcal{N}_{\text{sync}} = 1$  ensures good computational efficiency, but users have the flexibility to change it in the setup file. The sampling of electron positions and velocities is performed at each synchronization instant. Alternatively, users can specify in the setup file to sample these properties

only at arbitrary multiples of synchronization points.

### 3.2.7 Data sampling

After the electron swarm reaches a steady-state, the positions  $\mathbf{r}$  and velocities  $\mathbf{v}$  of the electrons are sampled along time in order to calculate the electron transport properties: mean energy, distribution functions, transport coefficients, collision rates and power balance. The steady-state time  $t_{ss}$  is considered automatically when the swarm energy (average over the ensemble of electrons) is constant apart from statistical fluctuations, which is verified when two conditions are fulfilled: the temporal average of the swarm energy in the interval  $[0.5t, 0.75t]$  is larger than the one in the interval  $[0.75t, t]$ ; the relative standard deviation of the temporal average in the latter interval is smaller than 1%.

An example of the temporal evolution of the swarm energy and the corresponding steady-state time is illustrated in figure 3.4. Additionally, this figure highlights that the asynchronous electron advancement, which is currently employed, significantly enhances the statistical precision of the results compared to the synchronous advancement implemented in the first version of LoKI-MC.

Since each sampling time may not be statistically independent, the standard deviation of the mean value should be determined with care. We divide the manifold of statistical points in 50 subgroups and calculate the mean value of each one. Then, the statistical error of the total mean value is estimated through the dispersion of the 50 mean values calculated. For example, if the simulation describes  $10^5$  sampling points after the steady-state is reached, the number of points between subgroup centers is  $10^5/50 = 2000$ .

The techniques used to calculate the electron transport properties from the sampled electrons are discussed in the upcoming subsections.

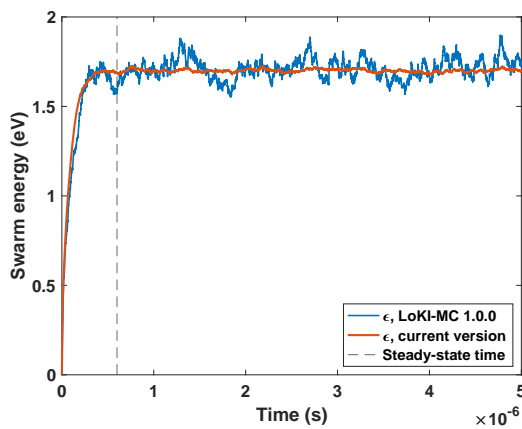


**Figure 3.4:** Example of the temporal evolution of the swarm energy ( $O_2$ ,  $E/N = 10$  Td,  $p = 133.32$  Pa,  $T_g = 300$  K), comparing the newly implemented asynchronous advancement of electrons with the old synchronous advancement implemented in LoKI-MC 1.0.0. The steady-state time is  $\simeq 0.6 \mu s$ .

## Electron mean energy and distribution functions

The mean energy  $\langle \epsilon \rangle$  is calculated by averaging the kinetic energies  $\epsilon_{\alpha\beta}$  of the  $N_e$  electrons during  $N_{\text{int}}$  integration points

$$\langle \epsilon \rangle = \frac{1}{N_{\text{int}} N_e} \sum_{\alpha=1}^{N_{\text{int}}} \sum_{\beta=1}^{N_e} \epsilon_{\alpha\beta}. \quad (3.22)$$

One of the most meaningful quantities extractable from the Monte Carlo simulations is the electron energy distribution function (EEDF). For comparison with other codes that solve the electron Boltzmann equation in a deterministic way, we calculate not only the EEDF, but also the different anisotropies of the electron distribution function, following its usual decomposition in a series of Legendre polynomials  $P_l(\cos \theta)$  with  $l = 0, 1, \dots$ , where  $\theta$  is the angle between  $\mathbf{v}$  and the direction of the anisotropy (in this case defined exclusively by the electric field).

Concerning the EEDF calculation, let the energies be discretized into  $\mathcal{N}_E$  cells of energies  $\{E_1, \dots, E_m, \dots, E_{\mathcal{N}_E}\}$ , with constant energy step  $\Delta_E = E_{m+1} - E_m$ . Similarly to the mean energy, the EEDF is calculated by averaging over all electrons and all integration points [40]:

$$f_0(E_m) = \frac{\sum_{\alpha=1}^{N_{\text{int}}} \sum_{\beta=1}^{N_e} \delta(\epsilon_{\alpha\beta})}{N_{\text{int}} N_e \sqrt{E_m} \Delta_E}, \quad (3.23)$$

where

$$\delta(\epsilon_{\alpha\beta}) = \begin{cases} 1, & \text{if } E_m - \frac{\Delta_E}{2} \leq \epsilon_{\alpha\beta} < E_m + \frac{\Delta_E}{2} \\ 0, & \text{otherwise} \end{cases}.$$

Note that the EEDF is normalized as to satisfy  $\sum_{m=1}^{\mathcal{N}_E} f_0(E_m) \sqrt{E_m} \Delta_E = 1$ . By default, the energies in LoKI-MC are discretized into  $\mathcal{N}_E = 1000$  cells.

To obtain the higher-order anisotropies, we first calculate the electron angular distribution function  $f(E_m, \cos \Theta_n)$ , which requires a discretization on the angles:  $\{\cos \Theta_1, \dots, \cos \Theta_n, \dots, \cos \Theta_{\mathcal{N}_{\Theta}}\}$ , with constant step  $\Delta_{\Theta} = \cos \Theta_{n+1} - \cos \Theta_n$ . The angular distribution function is discretized as follows:

$$f(E_m, \cos \Theta_n) = \frac{2 \sum_{\alpha=1}^{N_{\text{int}}} \sum_{\beta=1}^{N_e} \delta(\epsilon_{\alpha\beta}, \cos \theta_{\alpha\beta})}{N_{\text{int}} N_e \sqrt{E_m} \Delta_E \Delta_{\Theta}}, \quad (3.24)$$

where

$$\delta(\epsilon_{\alpha\beta}, \cos \theta_{\alpha\beta}) = \begin{cases} 1, & \text{if } E_m - \frac{\Delta_E}{2} \leq \epsilon_{\alpha\beta} < E_m + \frac{\Delta_E}{2} \text{ and} \\ & \cos \Theta_n - \frac{\Delta_{\Theta}}{2} \leq \cos \theta_{\alpha\beta} < \cos \Theta_n + \frac{\Delta_{\Theta}}{2}; \\ 0, & \text{otherwise} \end{cases},$$

and is normalized as to satisfy  $\frac{1}{2} \sum_{m=1}^{\mathcal{N}_E} \sum_{n=1}^{\mathcal{N}_{\Theta}} f(E_m, \cos \Theta_n) \sqrt{E_m} \Delta_E \Delta_{\Theta} = 1$ . Then, the anisotropies  $f_l(E_m)$

are determined from [51]

$$f_l(E_m) = \frac{2l+1}{2} \sum_{n=1}^{\mathcal{N}_\Theta} P_l(\cos \Theta_n) f(E_m, \cos \Theta_n) \Delta_\Theta. \quad (3.25)$$

By default, the angles are discretized into  $\mathcal{N}_\Theta = 50$  cells.

Finally, the electron velocity distribution function (EVDF) is determined in a similar way through a discretization of the radial ( $v_{r,m}$ ) and axial ( $v_{z,n}$ ) velocity space, ensuring that  $f(v_r, v_z)$  verifies  $\int_0^\infty 2\pi v_r dv_r \int_{-\infty}^{+\infty} dv_z f(v_r, v_z) = 1$ . By default, the velocity space is discretized using 200 cells for both the radial and the axial components.

### Electron-impact rate coefficients

The electron-impact rate coefficients  $k_{\mathcal{K}}$  are determined using two methods. The direct way is to count the collision events of type  $\mathcal{K}$  per electron during the sampling time  $t - t_{ss}$ ,  $C_{\mathcal{K}}/N_e$  [47, 52]:

$$k_{\mathcal{K}} = \frac{1}{t - t_s} \frac{C_{\mathcal{K}}/N_e}{n_{\mathcal{K}}^s}. \quad (3.26)$$

However, when the density of the target species  $n_{\mathcal{K}}^s$  is too low, the result is statistically imprecise due to the low number of events during the simulation. The second approach relies only on the convolution of the EEDF with the collision cross section:

$$k_{\mathcal{K}} = \sqrt{\frac{2e}{m_e}} \int_0^\infty \sigma_{\mathcal{K}}(\epsilon) \epsilon f_0(\epsilon) d\epsilon. \quad (3.27)$$

Both methods are correct but the latter should be preferred to obtain the steady-state rate-coefficients, since it depends only on the quality of the EEDF, regardless of the target densities used in the simulation.

### Transport coefficients

For the determination of the transport coefficients, we distinguish between “flux” and “bulk” components, which may differ when non-conservative processes are significant [52]. The flux drift velocity  $v_{d,i}^f$  and diffusion tensor  $D_{ij}^f$  ( $i, j = x, y, z$ ) are determined from the averages over the instantaneous positions ( $r_i$ ) and velocities ( $v_i$ ) of the electrons in the swarm [52]:

$$v_{d,i}^f = \langle v_i \rangle, \quad (3.28)$$

$$D_{ij}^f = \langle r_i v_j \rangle - \langle r_i \rangle \langle v_j \rangle. \quad (3.29)$$

The bulk drift velocity  $v_{d,i}^b$  and diffusion tensor  $D_{ij}^b$  are defined relatively to the swarm center-of-mass  $\langle r_i \rangle$  [20, 53],

$$v_{d,i}^b = \frac{d}{dt} \langle r_i \rangle , \quad (3.30)$$

$$D_{ij}^b = \frac{1}{2} \frac{d}{dt} (\langle r_i r_j \rangle - \langle r_i \rangle \langle r_j \rangle) , \quad (3.31)$$

and can be obtained from linear regressions to the temporal evolution of  $\langle r_i \rangle$  and  $\langle r_i r_j \rangle - \langle r_i \rangle \langle r_j \rangle$ , respectively (see figure 3.5).

Additionally, we calculate both bulk and flux components of the following transport coefficients:

- electron mobility -  $\mu_e = v_{d,z}/E$ ;
- reduced Townsend coefficient -  $\alpha_{\text{ion}}/N = k_{\text{ion}}/v_{d,z}$ ;
- reduced attachment coefficient -  $\eta_{\text{att}}/N = k_{\text{att}}/v_{d,z}$ ;
- characteristic energy -  $\epsilon_{\text{char}} = D_{\perp}/\mu_e$ , with  $D_{\perp} = (D_x + D_y)/2$ .

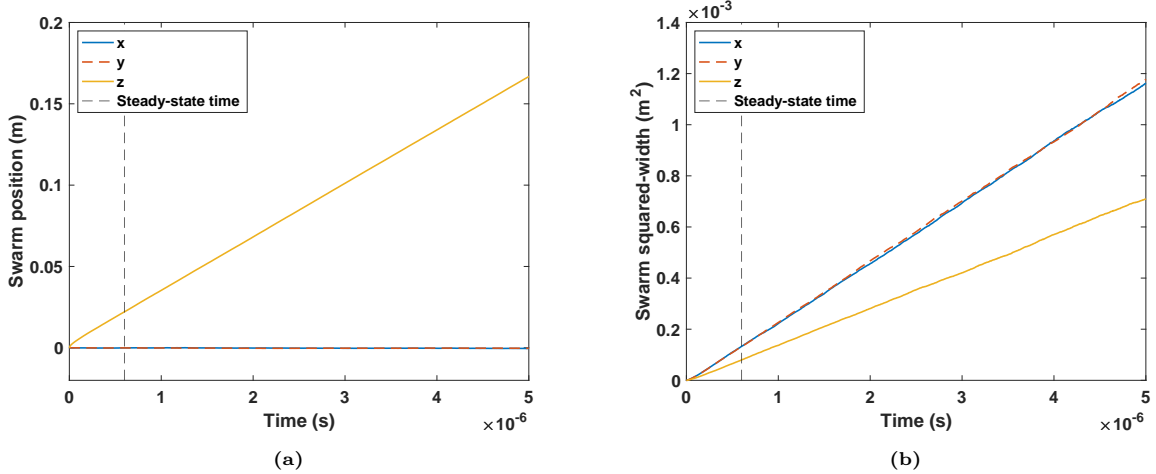


**Figure 3.5:** Example of the temporal evolution of the swarm mean position (a) and mean squared width (b), in the same conditions as figure 3.4. The bulk transport coefficients are determined from the slopes of the lines (see text).

Townsend and attachment coefficients are usually measured in so-called steady-state Townsend (SST) conditions, i.e., with the electron number growing in space and without time dependence. On the contrary, the current version of LoKI-MC simulates only Time-of-Flight (TOF) configurations, i.e., with the electron number growing in time. However, the Townsend and attachment coefficients in SST conditions can be derived from the TOF bulk coefficients using the following approximate relation in equation (3.32) deduced from [54–56]:

$$\frac{\alpha_{\text{SST}^*}}{N} = \frac{k_{\text{ion}}}{v_{\text{SST}^*}} = \frac{k_{\text{ion}}}{v_{d,\text{TOF}}^b/2 + \sqrt{\left(v_{d,\text{TOF}}^b/2\right)^2 - D_{L,\text{TOF}}^b N k_{\text{eff}}} , \quad (3.32)$$

where  $\alpha_{\text{SST}^*}$  is the SST ionization Townsend coefficient;  $v_{\text{SST}^*}$  is the SST averaged velocity;  $k_{\text{eff}} = k_{\text{ion}} - k_{\text{att}}$  is the effective ionization rate-coefficient;  $v_{\text{d,TOF}}^b$  and  $D_{\text{L,TOF}}^b$  are the bulk components of the drift velocity and longitudinal diffusion coefficient, respectively, calculated in a TOF simulation. A similar expression for the attachment coefficient  $\eta_{\text{SST}^*}$  is used, with  $k_{\text{att}}$  instead of  $k_{\text{ion}}$ . These coefficients can be directly compared with experimental measurements<sup>3</sup>.

### Power balance

The electron power-balance is analyzed by evaluating the kinetic energy changes in the ensemble of  $N_e$  electrons due to electric-field acceleration and collisions during the integration interval.

In the case of the electric-field acceleration, the energy change of one electron is simply  $\Delta\epsilon_E^{\mathcal{F}} = \epsilon_a^{\mathcal{F}} - \epsilon_b^{\mathcal{F}}$ , where  $\epsilon_b^{\mathcal{F}}$  and  $\epsilon_a^{\mathcal{F}}$  are the energies of the electron before and after the free-flight  $\mathcal{F}$ . Therefore, the total energy change of the electron ensemble during the integration interval is

$$\Delta E_E = \sum_{\text{all free-flights } \mathcal{F}} \epsilon_a^{\mathcal{F}} - \epsilon_b^{\mathcal{F}}. \quad (3.33)$$

To calculate the power gained/lost due to a collision kind  $\mathcal{K}$ , we must distinguish between conservative and non-conservative processes. For conservative processes, with no change in the number of electrons, the procedure is equivalent to the electric-field case:

$$\Delta E_{\text{coll},\mathcal{K}} = \sum_{\text{all coll. } c \text{ of kind } \mathcal{K}} \epsilon_a^c - \epsilon_b^c. \quad (3.34)$$

If the collision type  $\mathcal{K}$  is an attachment, we subtract the energies of the incident electrons  $\epsilon_b^c$ :

$$\Delta E_{\text{coll,att}} = \sum_{\text{all att. coll. } c} -\epsilon_b^c. \quad (3.35)$$

However, as we copy a random electron to keep  $N_e$  constant, we include an additional *electron energy growth* term [17]:

$$\Delta E_{\text{growth}}^{\text{att}} = \sum_{\text{all att. coll. } c} +\epsilon_r^c, \quad (3.36)$$

where  $\epsilon_r^c$  is the energy of the copied electron. Concerning ionization, there is a loss of the ionization potential  $\Delta\epsilon_{\text{ion}}$  for each collision event:

$$\Delta E_{\text{coll,ion}} = \sum_{\text{all ion. coll. } c} -\Delta\epsilon_{\text{ion}}. \quad (3.37)$$

Moreover, we include a growth contribution regarding the elimination of randomly-chosen electrons in

---

<sup>3</sup>These formulae were not present in the first version of the code.

ionization events:

$$\Delta E_{\text{growth}}^{\text{ion}} = \sum_{\text{all ion. coll. } c} -\epsilon_r^c, \quad (3.38)$$

where  $\epsilon_r^c$  is the energy of the random electron removed after the ionization  $c$ .

The energy changes of the different processes  $\zeta$  are converted into electron power-densities (per electron at unit gas density) as follows:

$$\frac{P_\zeta}{N} = \frac{1}{t - t_{ss}} \frac{\Delta E_\zeta}{NN_e}, \quad (3.39)$$

where  $N$  is the total gas density. As the sampling occurs only after the steady-state, the sum of the power densities should be null apart from statistical fluctuations:

$$\frac{P_E}{N} + \frac{P_{\text{coll}}}{N} + \frac{P_{\text{growth}}}{N} \simeq 0. \quad (3.40)$$

Besides, by separating the terms above in gain and loss components, we can estimate the power-balance error using  $\frac{\sum_\zeta (P/N)_{\text{gain},\zeta} + (P/N)_{\text{loss},\zeta}}{\sum_\zeta (P/N)_{\text{gain},\zeta}}$ . This parameter provides an alternative way to quantify the statistical significance of the simulation.

### 3.2.8 Stopping criteria

The Monte Carlo simulation is stopped when the quality of the results fulfills the stipulated conditions.

In LoKI-MC, there are various types of stopping criteria:

- minimum number of integration points;
- minimum number of real collisions per electron after reaching the steady-state;
- maximum tolerances for the relative standard deviations of the mean energy, flux drift velocity, flux diffusion coefficients and power balance;
- integration time-period, given as absolute number or as multiples of the steady-state time.

At least one of these criteria must be defined. The simulation is stopped when all defined criteria are achieved<sup>4</sup>. For the common user, the first criterion together with an integration time-period given as of the SS time ( $\gtrsim 5$ ) is more suited, since the appropriate values for the others may vary substantially with the gas and with  $E/N$ .

---

<sup>4</sup>In the first version, the simulation was stopped when one of the criteria was achieved.

### 3.3 The LoKI-MC code

In this section, we present the input data necessary to run the code, focusing on its high flexibility, and we summarize the physical information given on the output.

#### 3.3.1 Input

LoKI-MC solves the electron kinetics given: the physical working conditions (reduced field  $E/N$ , gas pressure  $p$ , gas temperature  $T_g$  and the gas-mixture composition); the distributions of populations  $\xi_{k_i}$ ,  $\xi_{k_{i_\nu}}$ ,  $\xi_{k_{i_\nu J}}$  of electronic levels  $k_i$ , vibrational levels  $k_{i_\nu}$  and rotational levels  $k_{i_\nu J}$ , respectively (if applicable); and the sets of cross sections  $\sigma_{k,c}^{\text{el}}$  (or  $\sigma_{k,c}^{\text{eff}}$ , see section 3.2.1),  $\sigma_{k(i,j)}$ ,  $\sigma_{k_i,\text{att}}$  and  $\sigma_{k_i,\text{ion}}$ , where here  $i, j$  stand for any level of any gas  $k$  in the system.

Input parameters are set from a text input-file, in a user-friendly flexible way, e.g. allowing to (i) prepare simulations for either a sole value or a range of values of the applied reduced electric field; (ii) choose among different ionization models (SDCS/equal-sharing/no-sharing/uniform-sharing and isotropic/momentum-conservation scattering, see section 3.2.5); (iii) define the distributions of populations directly in the input file, from user-defined text files, or via functions for typical distributions at user-defined temperatures (e.g. Boltzmann or Treanor); (iv) list the filename(s) with the set(s) of cross sections to adopt in the simulations; (v) provide details about the numerical solution; (vi) select the output information (see next section). The code uses SI units for all physical quantities, except the energies, that are expressed in eV (electron-volt), and the reduced fields, that are expressed in Td (Townsend; 1 Td =  $10^{-21}$  Vm<sup>2</sup>).

LoKI-MC uses electron scattering cross sections from the LXCat open-access website [24]. As input, the code accepts also *extra* sets of cross sections, which are not used in the calculation of the EEDF, but remain available for integration over the calculated EEDF, to obtain rate coefficients with interest for various purposes (e.g. global models, spectroscopy analysis, actinometry diagnostics, etc.). For more details on the format of the LXCat files used in the code, see the section 3.3 of the LoKI-B paper [17].

The numerical conditions are set by defining: (i) the number of electrons in the ensemble; (ii) inclusion (or not) of a thermal motion for the neutral gas; (iii) criteria for finishing the simulation. Additionally, it is possible to set the numbers of cells used in the discretization of the distribution functions (see section 3.2.7) and the number of grid points used to linearly interpolate the cross sections (by default,  $5 \times 10^4$ ). The maximum energy of the cross-section grid is defined dynamically during the simulation. If, at any point of the simulation, this value is higher than the maximum energy of one elastic cross section, the code stops and throws an error.

### 3.3.2 Output

The simulation tool provides as output: (i) the EEDF  $f_0$  and the anisotropies  $f_1$  and  $f_2$ ; (ii) the EVDF  $f(v_r, v_z)$ ; (iii) bulk and flux transport coefficients together with statistical errors; (iv) collision rate-coefficients, including the *extra* ones; (v) power balance; (vi) spatiotemporal evolution of the electron swarm (mean values of the energy, position, velocity and squared-width, as a function of time); (vii) details of the Monte Carlo simulation (e.g. number of electron collisions before and after the steady-state). If the graphical interface is activated, most of this information can be plotted in the end of the simulation, allowing the user to check immediately the quality of the results.

## 3.4 Results

This section provides a comprehensive set of results obtained using LoKI-MC for different gases. Firstly, the formulation is verified in well-established model gases by comparing it against analytical solutions and other published works. Then, the code is benchmarked against the two-term solver LoKI-B and the ten-term solver MultiBolt using the real gases O<sub>2</sub> and Ar. Finally, the effects of anisotropic ionization scattering and superelastic collisions, which are neither considered in MultiBolt nor in METHES, are analyzed in real gases. These examples were chosen so as to highlight the reliability and flexibility of the present code.

In all simulations, we keep the default values for the numbers of cells used to discretize the distribution functions and for the number of grid points to interpolate the cross sections (c.f. section 2). The number of electrons followed in the ensemble ranges from  $3 \times 10^4$  to  $10^6$ . As the renormalization of the electron number presented in [1] has an imprecision, detailed in section 3.2.5 and already addressed within this chapter, the simulations were re-run. Cases of strong ionization, where differences from the previous version arise, are properly identified.

### 3.4.1 Verifications in model gases

We start by analyzing a simple model where scattering events are restricted to elastic collisions with the gas molecules ( $M = 4$  amu), characterized by a constant elastic cross-section  $\sigma_{\text{el}} = 6 \times 10^{-20}$  m<sup>2</sup>. In this case, the system can be described analytically and the Druyvesteyn distribution is obtained at steady-state [57]. Since the model assumes the neutrals at rest, the thermal motion of the molecules is deactivated in these simulations. In figure 3.6, the EEDFs from Monte Carlo simulations are compared with the analytical Druyvesteyn solutions for reduced electric fields from 1 to 20 Td, revealing a remarkable agreement over at least five orders of magnitude.

In the next verification, we add to the previous model a linearly-increasing excitation cross-section  $\sigma_{\text{ex}} = (\epsilon - 0.2) \times 10^{-19}$  m<sup>2</sup>, with energy threshold of 0.2 eV, obtaining the well-known Reid-ramp

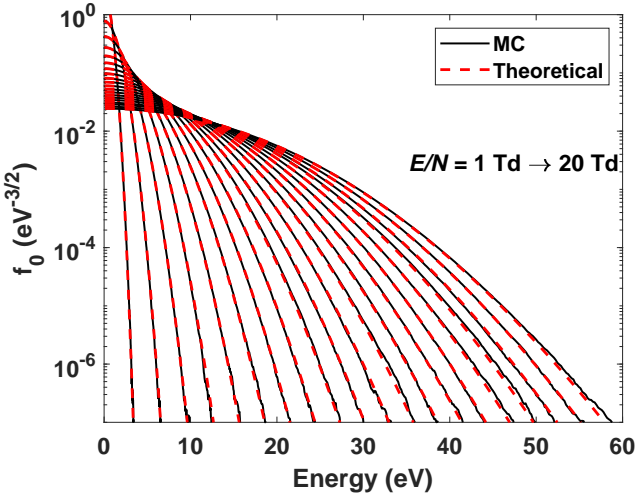


**Figure 3.6:** Electron energy distribution functions obtained in LoKI-MC using the Druyvesteyn model for  $E/N$  values from 1 to 20 Td.

model [41]. Three values of  $E/N$  are used: 1, 12 and 24 Td. LoKI-MC simulations are compared with MultiBolt [19] and the Monte Carlo results of Raspopović *et al* [47] and White *et al* [53], as shown in table 3.1. There is an excellent agreement with the results obtained by other codes, for all parameters.

To verify LoKI-MC in the presence of non-conservative collisions, both *ionization* and *attachment*, the non-conservative model gas of Lucas-Salee [58] is employed, along with the attachment modifications of Ness and Robson [19, 59]:

$$\left\{ \begin{array}{l} \sigma_{\text{el}} = 4\epsilon^{-1/2} \times 10^{-20} \text{ m}^2 \\ \sigma_{\text{exc}} = 0.1(1 - F)(\epsilon - 15.6) \times 10^{-20} \text{ m}^2 \\ \sigma_{\text{ion}} = 0.1F(\epsilon - 15.6) \times 10^{-20} \text{ m}^2 \\ \sigma_{\text{att}} = a\epsilon^p \times 10^{-20} \text{ m}^2 \end{array} \right. . \quad (3.41)$$

The parameter  $F$  controls the fraction of inelastic excitation and ionization. For  $F = 1$ , the excitation cross section,  $\sigma_{\text{exc}}$ , is zero, and for  $F = 0$ , the ionization cross section,  $\sigma_{\text{ion}}$ , is zero. The attachment cross section,  $\sigma_{\text{att}}$ , scales with  $a$ , and  $p$  determines the proportionality of the cross section. Different sets of  $\{F, a, p\}$  are used to test the code, including cases of strong ionization or attachment. For all simulations with this model,  $E/N$  is fixed to 10 Td, the gas density is  $N = 10^{20} \text{ m}^{-3}$  and the heavy-particle mass is  $M = 1000 m_e$ . The LoKI-MC calculations are compared with MultiBolt [19] and the MC results of Raspopović *et al.* [47] and Nolan *et al.* [49], as shown in table 3.2. The general agreement is very good, exhibiting differences typically below 1%.

Another important verification consists on analyzing the swarm behavior in zero-field conditions, in order to assess the validity of the treatment of low energy electron-molecule collisions. In this case, the electron swarm should relax towards a Maxwellian distribution at the background gas temperature ( $T_g$ ), independently of the initial condition. To test this behavior, we use the Druyvesteyn model, but now

including the influence of the thermal motion of the molecules. Figure 3.7 presents the temporal evolution of the swarm energy for three initial electron temperatures ( $0.5T_g$ ,  $T_g$ ,  $1.5T_g$ , with  $T_g = 300$  K) at  $E/N = 0$  Td. As expected, the swarm energy tends to the gas mean energy,  $\frac{3}{2}k_B T_g$ , independently of the initial conditions. Note also that, if we do not consider the gas-temperature effect in the collision dynamics, the electron swarm tends to zero energy, which stresses the importance of the correct treatment of electron-molecule collisions at low  $E/N$ . Finally, figure 3.8 shows that, in zero-field conditions, the EEDF from Monte Carlo simulations is in fact a Maxwellian at the temperature of the background gas.

	$\langle \epsilon \rangle$ (eV)	$v_d$ ( $10^4$ m s $^{-1}$ )	$D_T N$ ( $10^{24}$ m $^{-1}$ s $^{-1}$ )	$D_L N$ ( $10^{24}$ m $^{-1}$ s $^{-1}$ )
$E/N = 1$ Td	LoKI-MC	0.10148 [0.007]	1.2718 [0.016]	0.9760 [0.15]
	MultiBolt[19]	0.1014 (-0.07)	1.272 (0.01)	0.9746 (-0.14)
	MCC[47]	0.1017 (0.22)	1.273 (0.09)	0.966 (-1.02)
	MCC[53]	0.1015 (0.02)	1.271 (-0.06)	0.974 (-0.20)
$E/N = 12$ Td	LoKI-MC	0.26890 [0.004]	6.8368 [0.007]	1.135 [0.14]
	MultiBolt[19]	0.2688 (-0.04)	6.839 (0.03)	1.134 (-0.10)
	MCC[47]	0.2703 (0.52)	6.834 (-0.04)	1.140 (0.43)
	MCC[53]	0.2693 (0.15)	6.833 (-0.06)	1.136 (0.07)
$E/N = 24$ Td	LoKI-MC	0.40791 [0.004]	8.8850 [0.006]	1.1325 [0.13]
	MultiBolt[19]	0.40922 (0.32)	8.8522 (-0.37)	1.137 (0.40)
	MCC[47]	0.4113 (0.83)	8.804 (-0.91)	1.131 (-0.13)
	MCC[53]	0.4085 (0.14)	8.878 (-0.08)	1.140 (0.67)

**Table 3.1:** Comparison of LoKI-MC solutions with MultiBolt calculations [19] and previous MC results [47, 53], for the Reid-ramp model [41]. The standard deviations  $\sigma[\%]$  of the LoKI-MC simulations are shown in squared parenthesis. The deviations  $\delta$  between LoKI-MC results (LMC) and previous results (PR), defined as  $\delta[\%] = (1 - PR/LMC) \times 100$ , are shown in curved parenthesis.

	$\langle \epsilon \rangle$ (eV)	$\nu_{\text{eff}}$ ( $10^3$ s $^{-1}$ )	$v_d^f$ ( $10^4$ m s $^{-1}$ )	$v_d^b$ ( $10^4$ m s $^{-1}$ )	$D_T^f N$ ( $10^{25}$ m $^{-1}$ s $^{-1}$ )	$D_T^b N$ ( $10^{25}$ m $^{-1}$ s $^{-1}$ )	$D_L^f N$ ( $10^{25}$ m $^{-1}$ s $^{-1}$ )	$D_L^b N$ ( $10^{25}$ m $^{-1}$ s $^{-1}$ )
$F = 0$	LoKI - MC	5.5619 [0.007]	0	7.3189 [0.018]	7.319 [0.56]	2.719 [0.24]	2.723 [0.37]	2.645 [0.27]
	MultiBolt[19]	5.56 (-0.03)	0 (0.00)	7.33 (0.15)	7.33 (0.15)	2.72 (0.05)	N/A	2.65 (0.20)
	MCC[49]	5.57 (0.15)	0 (0.00)	7.32 (0.02)	7.32 (0.01)	2.72 (0.05)	2.72 (-0.10)	2.66 (0.58)
	MCC[47]	5.57 (0.15)	0 (0.00)	7.28 (-0.53)	7.32 (0.01)	2.71 (-0.32)	2.73 (0.26)	2.65 (0.20)
$F = 0.5$	LoKI - MC	5.2239 [0.01]	1.333	7.3285 [0.018]	8.588 [0.43]	2.555 [0.21]	2.715 [0.69]	2.503 [0.22]
	MultiBolt[19]	5.22 (-0.08)	1.33 (-0.21)	7.33 (0.02)	8.59 (0.03)	2.55 (-0.19)	N/A	2.50 (-0.13)
	MCC[49]	5.22 (-0.08)	1.33 (-0.21)	7.32 (-0.12)	8.58 (-0.09)	2.55 (-0.19)	2.73 (0.56)	2.49 (-0.53)
	MCC[47]	5.22 (-0.08)	1.33 (-0.21)	7.31 (-0.25)	8.58 (-0.09)	2.56 (0.21)	2.73 (0.56)	2.49 (-0.53)
$F = 1.0$	LoKI - MC	4.9723 [0.008]	2.418	7.3315 [0.017]	9.483 [0.25]	2.432 [0.26]	2.753 [0.53]	2.390 [0.21]
	MultiBolt[19]	4.97 (-0.05)	2.42 (0.10)	7.34 (0.12)	9.49 (0.08)	2.43 (-0.09)	N/A	2.38 (-0.40)
	MCC[49]	4.97 (-0.05)	2.42 (0.10)	7.32 (-0.16)	9.47 (-0.13)	2.43 (-0.09)	2.72 (-1.19)	2.38 (-0.40)
	MCC[47]	4.97 (-0.05)	2.42 (0.10)	7.30 (-0.43)	9.51 (0.29)	2.42 (-0.51)	2.72 (-1.19)	2.37 (-0.82)
$F = 0$	LoKI - MC	5.4404 [0.009]	-1.613	7.3244 [0.019]	7.018 [0.50]	2.659 [0.20]	2.623 [0.74]	2.600 [0.18]
	MultiBolt[19]	5.43 (-0.19)	-1.60 (-0.83)	7.33 (0.08)	7.03 (0.17)	2.67 (0.43)	N/A	2.59 (-0.37)
	MCC[49]	5.44 (-0.01)	-1.62 (0.41)	7.33 (0.08)	7.02 (0.02)	2.67 (0.43)	2.61 (-0.51)	2.61 (0.40)
	MCC[47]	5.45 (0.18)	-1.60 (-0.83)	7.30 (-0.33)	7.01 (-0.12)	2.67 (0.43)	2.63 (0.25)	2.60 (0.01)
$F = 0$	LoKI - MC	5.5623 [0.009]	-1.186	7.3214 [0.019]	7.324 [0.68]	2.729 [0.22]	2.740 [0.70]	2.659 [0.22]
	MultiBolt[19]	5.55 (-0.22)	-1.18 (-0.50)	7.33 (0.12)	7.33 (0.08)	2.72 (-0.32)	N/A	2.65 (-0.34)
	MCC[49]	5.56 (-0.04)	-1.19 (0.34)	7.32 (-0.02)	7.32 (-0.06)	2.73 (0.05)	2.73 (-0.37)	2.66 (0.04)
	MCC[47]	5.57 (0.14)	-1.17 (-1.35)	7.29 (-0.43)	7.34 (0.22)	2.72 (-0.32)	2.74 (-0.01)	2.65 (-0.34)
$F = 0$	LoKI - MC	5.7255 [0.009]	-2.595	7.3176 [0.019]	7.552 [0.69]	2.798 [0.22]	2.849 [0.70]	2.733 [0.25]
	MultiBolt[19]	5.72 (-0.10)	-2.59 (-0.21)	7.32 (0.03)	7.55 (-0.03)	2.80 (0.08)	N/A	2.73 (-0.10)
	MCC[49]	5.73 (0.08)	-2.60 (0.18)	7.32 (0.03)	7.55 (-0.03)	2.79 (-0.28)	2.86 (0.39)	2.73 (-0.10)

**Table 3.2:** Comparison of the LoKI-MC solutions with the MultiBolt calculations [19] and previous MC results [47, 49], for the Lucas-Saelee model. The LoKI-MC standard deviations  $\sigma[\%]$  and the errors  $\delta[\%]$  are calculated and presented as in table 3.1.

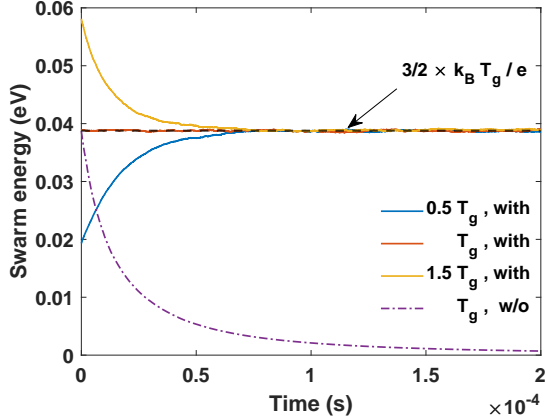


**Figure 3.7:** Temporal evolution of the swarm energy in zero-field conditions for three initial electron temperatures ( $0.5T_g$ ,  $T_g$ ,  $1.5T_g$ , with  $T_g = 300$  K), with and without the gas-temperature effect.

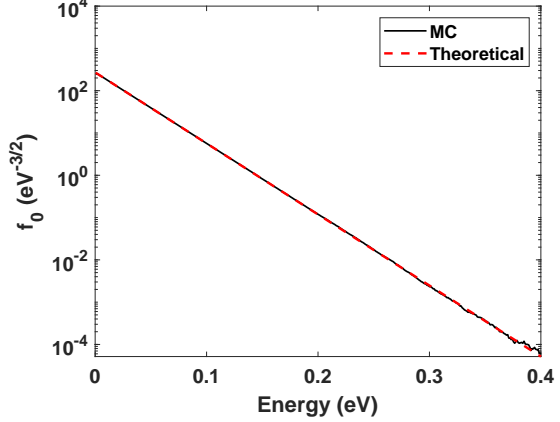
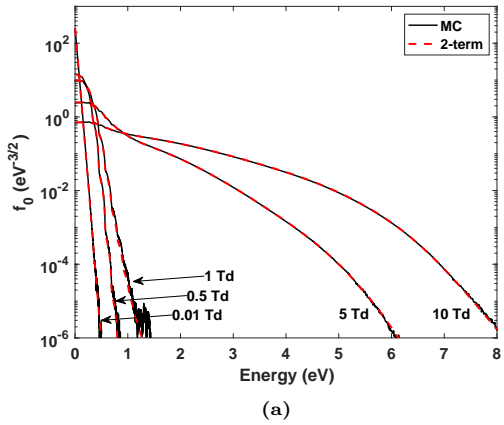
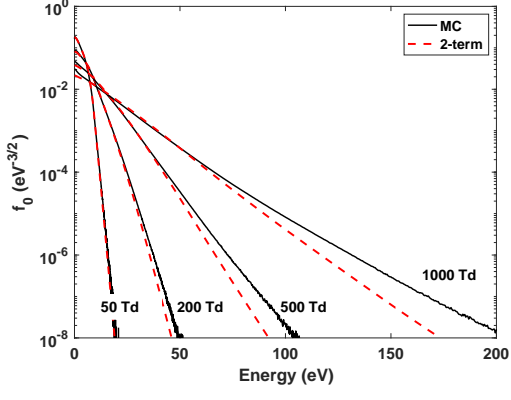


**Figure 3.8:** Comparison of the steady-state EEDF, in zero-field conditions, with the theoretical Maxwellian at 300 K.



(a)



(b)

**Figure 3.9:** Electron energy distribution functions in oxygen obtained with LoKI-MC and LoKI-B (two-term solver), for various reduced electric fields: (a) 0.01 - 10 Td; (b) 50 - 1000 Td.

### 3.4.2 Benchmark in real gases

For the benchmark in real gases, the gas temperature is 300 K and isotropic ionization scattering is considered. We start by presenting the results in molecular oxygen, comparing the present simulations with the two-term solver LoKI-B. Then, we compare the results in atomic argon obtained with both LoKI-B and MultiBolt.

#### 3.4.2.A Molecular gas: oxygen

In molecular oxygen, the simulations are performed for reduced electric fields from 0.005 to 1000 Td and the energy sharing in ionization is described by a SDCS [43]. LoKI-B simulations are done in an energy grid with 1000 cells and dynamical maximum energy value, ensuring a decay of 12 decades in the EEDF and a power-balance error of  $10^{-9}$ . LoKI-B and LoKI-MC simulations use data published in the IST-Lisbon database of LXCat [60], namely the  $O_2$  complete set of electron-scattering cross sections, complemented by the  $O_2$ -rot dataset for the description of rotational transitions. For details on these cross sections, see section 4.4 of the LoKI-B paper [17].

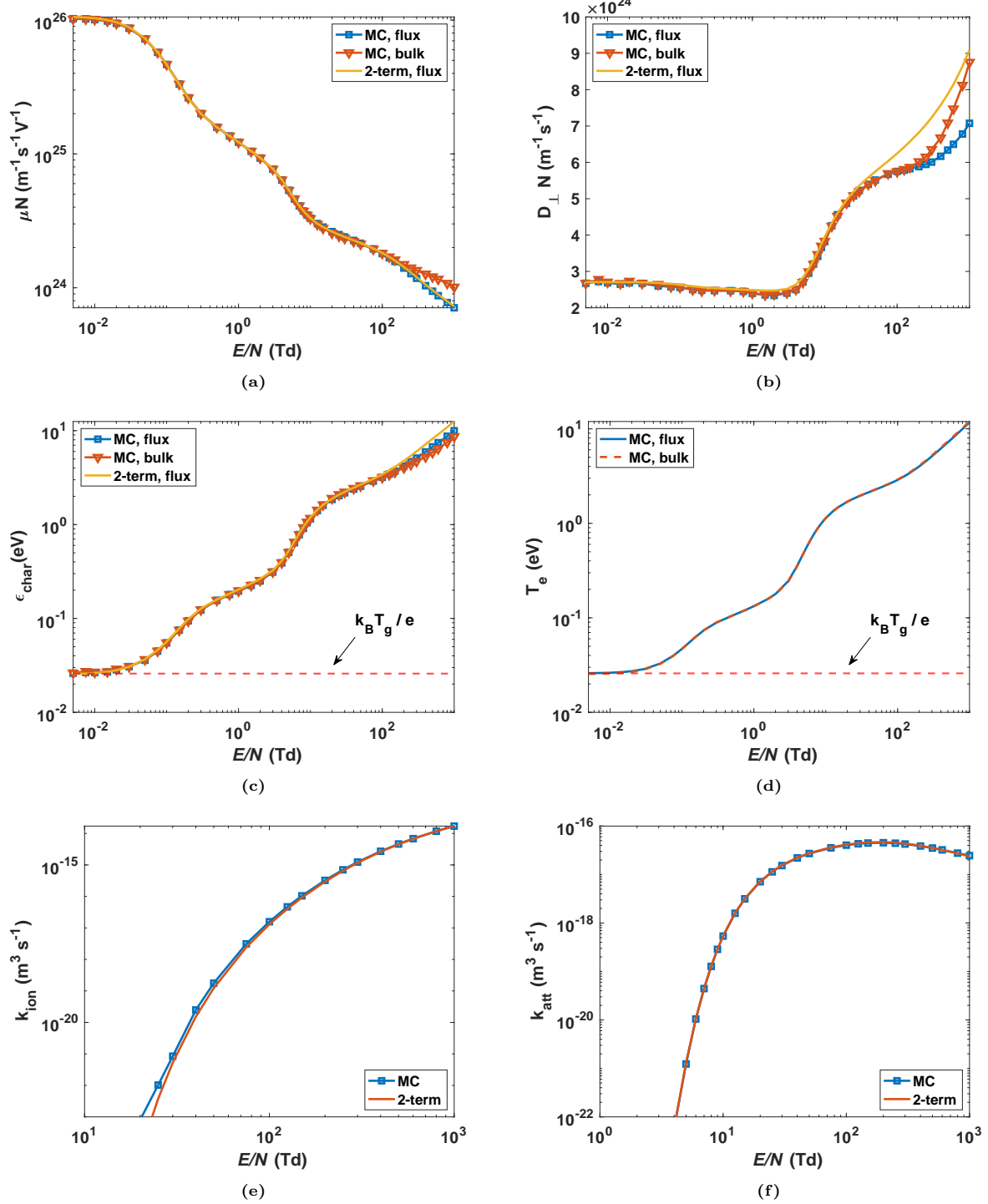
In figure 3.9, the EEDFs are presented for several values of the reduced field. Until 50 Td, the agreement between LoKI-MC and LoKI-B is remarkable. For  $E/N \gtrsim 200$  Td, the anisotropies start to be significant, thereby leading to visible deviations from the two-term calculations.

Figure 3.10 shows various electron swarm coefficients in oxygen as a function of  $E/N$ . As expected, the flux component of the mobility coincides with the LoKI-B results. For  $\sim 200$  Td, the bulk mobility starts to deviate from the flux component due to the significant contribution of secondary electrons in ionization. The agreement in the transverse diffusion coefficient is poor for  $E/N \gtrsim 50$  Td. This inaccuracy of the diffusion coefficients calculated by means of the two-term approximation is well known [20, 27]. The same splitting between flux and bulk components is observed for the diffusion coefficient. The flux characteristic energy and the electron temperature from LoKI-MC are in accordance with LoKI-B, and for low electric fields both quantities tend to the corresponding values at 300 K gas temperature, as expected. The deviations for  $E/N > 100$  Td in the flux characteristic energy are related to the transverse diffusion coefficient. Finally, the ionization and attachment rate-coefficients reveal an overall good agreement between the MC and 2-term calculations, with ionization showing poorer agreement, specially at the onset of this process.

The two-term errors in O<sub>2</sub> are depicted in figure 3.11 for  $\mu^f N$ ,  $D_{\perp}^f N$ ,  $T_e$ ,  $k_{\text{ion}}$  and  $k_{\text{att}}$ . The errors for  $\mu^f N$ ,  $T_e$  and  $k_{\text{att}}$  are generally below 5%. However,  $D_{\perp}^f N$  is systematically overestimated, with the discrepancy increasing for high  $E/N$  values, reaching approximately 30% at 1000 Td. Lastly, the  $k_{\text{ion}}$  values are underestimated by several tens of percent at the onset of ionization, and this discrepancy decreases with higher  $E/N$  values.

This latter result may seem puzzling when considering the two-term approximation's diminishing accuracy at higher  $E/N$  (as seen in Figure 3.9b). However, the reason is as follows: the two-term approximation for O<sub>2</sub> underestimates the high-energy tail of the EEDF. This leads to an underestimation of the number of electrons near the ionization threshold for intermediate  $E/N$  values. Nevertheless, at high  $E/N$  values around 1000 Td, where  $T_e$  is higher, electrons with energies near the ionization threshold already belong to the bulk of the distribution. This bulk is adequately described by the two-term approximation.

The normalized electron power-transfer in oxygen is detailed in figure 3.12. The electron energy gain is controlled by rotational superelastic collisions for reduced fields  $E/N \lesssim 0.5$  Td and by the electric field for higher  $E/N$ . The electron energy loss is driven mainly by rotational excitation for  $E/N \lesssim 0.5$  Td, followed by vibrational excitation until  $E/N \lesssim 10$  Td, and by electronic and ionization collisions for higher  $E/N$ . Note that the contribution of the secondary electrons in ionization, accounted in the electron growth term, is very important above 200 Td. The significant influence of rotations and vibrations in the electron power balance reinforces the idea that a detailed description of the internal states of the molecules is essential to obtain accurate results in a wide range of conditions, specially if the associated temperatures are high, as discussed in section 3.4.5.



**Figure 3.10:** Electron swarm coefficients in molecular oxygen ( $T_g = 300$  K) as a function of  $E/N$ , obtained with LoKI-MC and LoKI-B (2-term solver): (a) reduced mobility,  $\mu N$ ; (b) reduced transverse diffusion coefficient,  $D_{\perp}N$ ; (c) characteristic energy,  $\epsilon_{\text{char}}$ ; (d) temperature,  $T_e$ ; (e) ionization rate-coefficient,  $k_{\text{ion}}$ ; (f) attachment rate-coefficient,  $k_{\text{att}}$ .

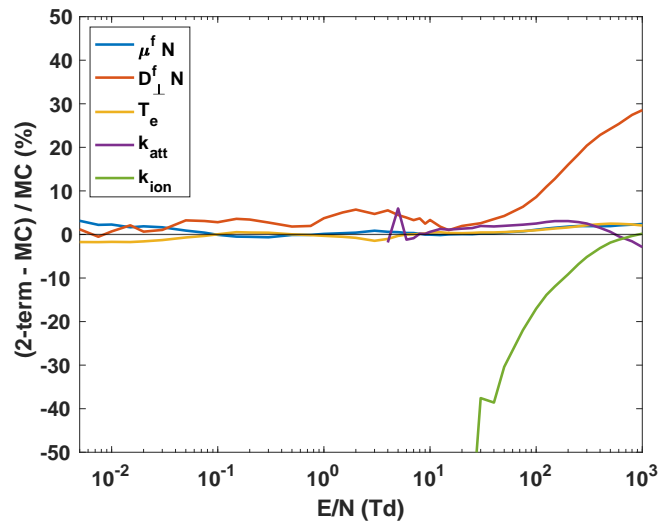


**Figure 3.11:** Two-term errors in molecular oxygen, defined as  $\frac{2\text{-term-MC}}{\text{MC}}$ , for  $\mu^f N$ ,  $D_{\perp}^f N$ ,  $T_e$ ,  $k_{\text{ion}}$  and  $k_{\text{att}}$ .

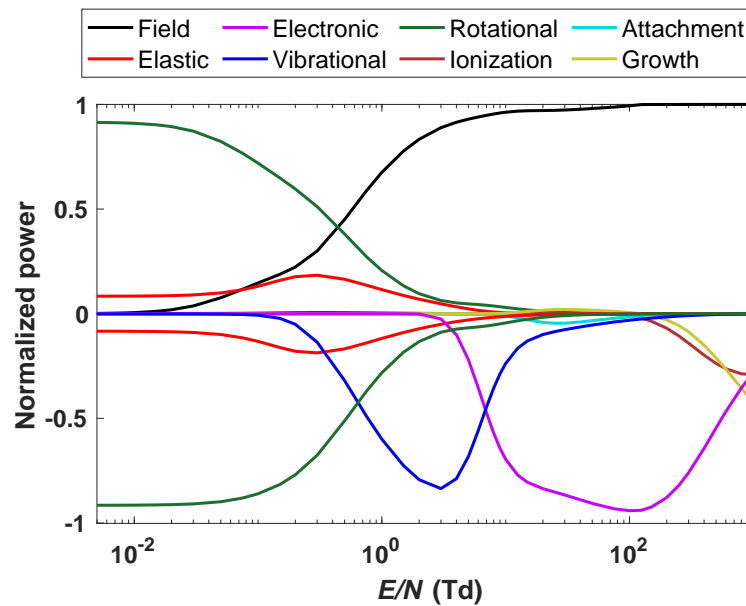


**Figure 3.12:** Normalized electron power transferred to various channels in oxygen, as a function of the reduced electric field. The positive and negative values correspond, respectively, to electron energy gain and loss.

### 3.4.2.B Atomic gas: argon

The simulations in argon are performed for reduced electric fields from 1 to 1000 Td, considering equal-energy sharing in ionization, to allow for a direct comparison with MultiBolt. MultiBolt was run with a ten-term expansion in Legendre polynomials in hydrodynamic regime [19], using 1000 energy points and ensuring a convergence error of  $5 \times 10^{-6}$  for the electron mean energy. The numerical parameters in LoKI-B are the same as in the previous section. All calculations use the Ar complete set of cross sections, published in the IST-Lisbon database of LXCat [61].

The EEDFs in argon are shown in figure 3.13. For  $E/N$  below 50 Td, the agreement between the three solvers is remarkable. For higher fields, the two-term solutions diverge from the Monte Carlo and the multi-term results, due to the breakdown of the low-anisotropy condition, while the latter two preserve the good agreement.

The electron swarm coefficients in argon are presented in figure 3.14. The flux contribution of the mobility reveals excellent agreement between the three approaches. Both LoKI-MC and MultiBolt predict the same splitting in the trends of bulk and flux components of the mobility, above  $\sim 50$  Td. The transverse diffusion coefficient from LoKI-MC agrees well with those predicted by MultiBolt, for the range of  $E/N$  considered, while the two-term values are significantly shifted. As expected, this difference also affects the characteristic energy calculated with the two-term code. Very good agreement is observed among the predictions of the three codes for electron temperature and ionization rate-coefficient. Finally the LoKI-MC and MultiBolt results for the longitudinal diffusion coefficient are in remarkable accord.

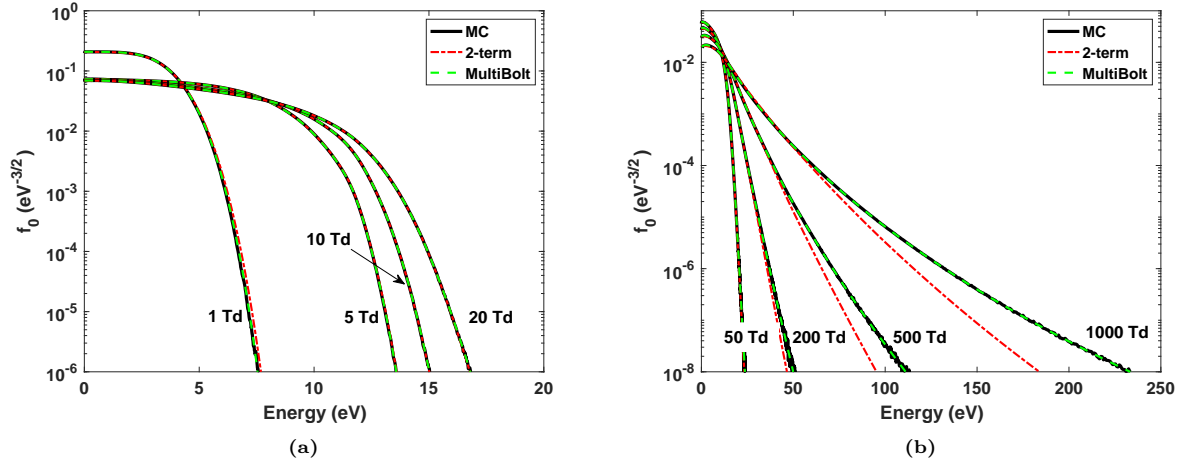


**Figure 3.13:** Electron energy distribution functions in argon, obtained with LoKI-MC, LoKI-B (2-term solver) and MultiBolt (10-term solver) for various reduced electric fields: (a) 1-20 Td; (b) 50-1000 Td.

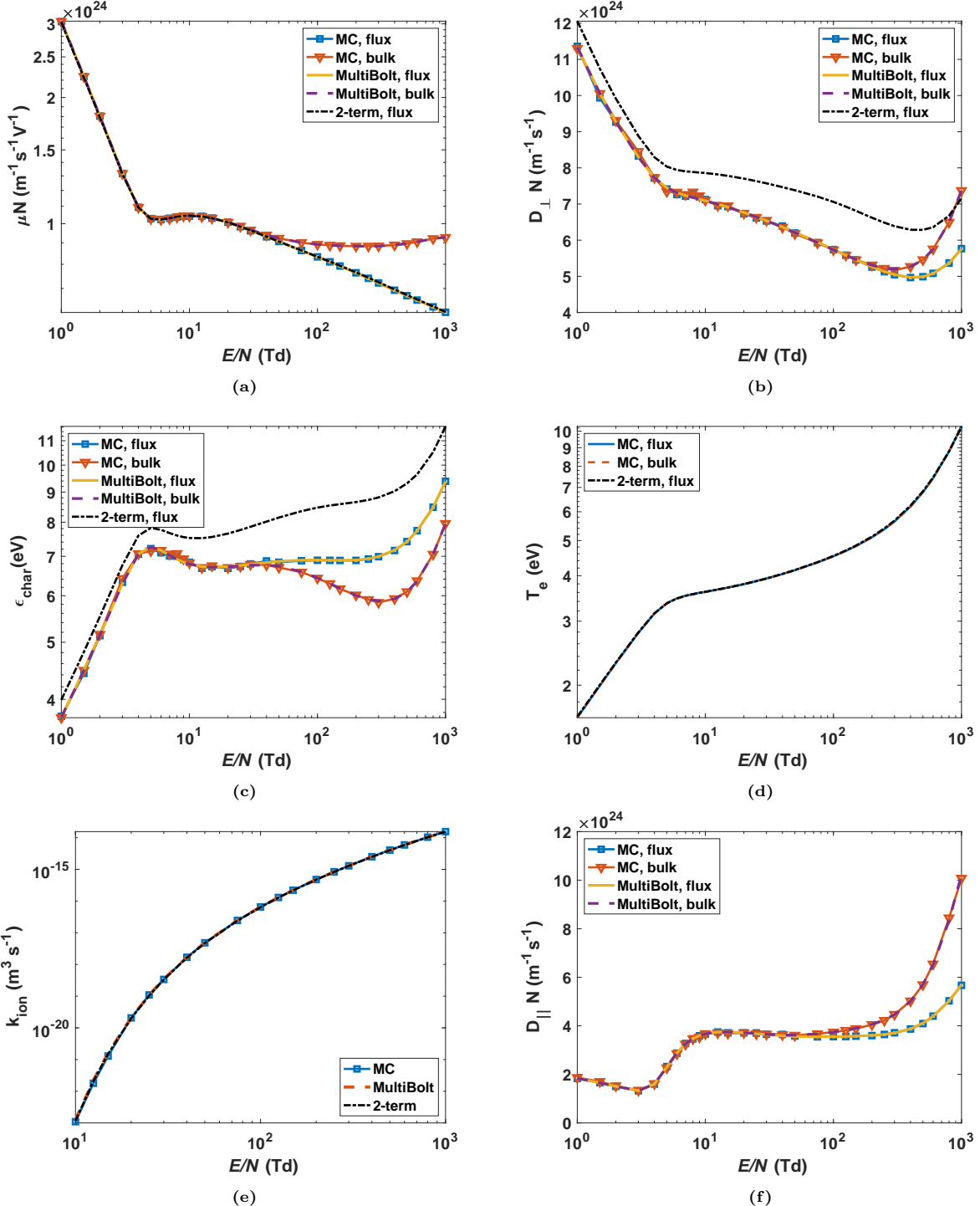


**Figure 3.14:** Electron swarm coefficients in argon ( $T_g = 300$  K) as a function of  $E/N$ , obtained with LoKI-MC, LoKI-B (2-term solver) and MultiBolt (10-term solver): (a) reduced mobility; (b) reduced transverse diffusion coefficient; (c) characteristic energy; (d) temperature; (e) ionization rate coefficient; (f) reduced longitudinal diffusion coefficient.

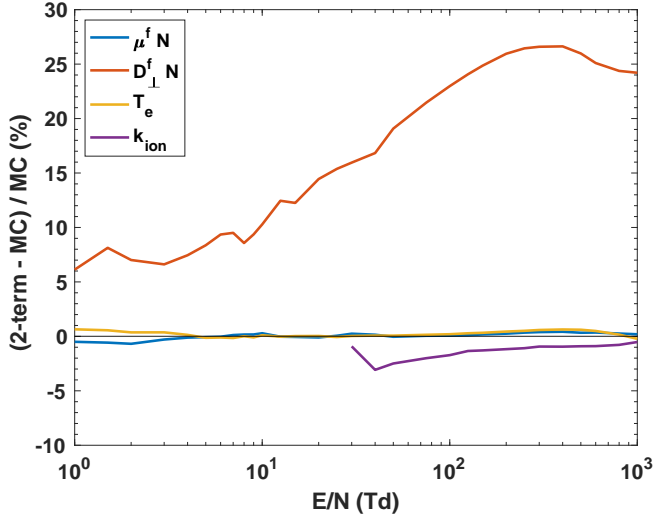


**Figure 3.15:** Two-term errors in argon, defined as  $\frac{\text{2-term} - \text{MC}}{\text{MC}}$ , for  $\mu^f N$ ,  $D_{\perp}^f N$ ,  $T_e$  and  $k_{\text{ion}}$ .

It is important to mention that the LoKI-MC calculated values for diffusion and mobility coefficients presented in [1] exhibited slight disagreement with MultiBolt for higher  $E/N \gtrsim 300$  Td. In [1], such discrepancy was attributed to a possible breakdown of the second-order density-gradient expansion used in Multibolt for calculating diffusion and mobility coefficients [19]. Nevertheless, given that all LoKI-MC results shown in this chapter have an excellent accordance with MultiBolt, we can now confidently state that the deviation was due to the imprecision in the electron number renormalization implemented in the initial version of LoKI-MC. This issue is detailed in section 3.2.5 and has been resolved in the new version presented here. As ionization becomes dominant for higher values of  $E/N$ , systematic errors were more pronounced within this range of conditions.

The two-term errors in Ar are illustrated in Figure 3.15 for  $\mu^f N$ ,  $D_{\perp}^f N$ ,  $T_e$  and  $k_{\text{ion}}$ . As in O<sub>2</sub>, the errors for  $\mu^f N$  and  $T_e$  are generally low, and  $D_{\perp}^f N$  is systematically overestimated, with the disagreement increasing for high  $E/N$  values. However, the error in the ionization coefficient is much lower than in O<sub>2</sub>.

### 3.4.3 Anisotropies

In the last sections, we have confirmed that the two-term approximation fails for sufficiently high reduced electric fields (and possibly in other conditions, depending on the gas), as discussed in the literature [25–28]. We can gain insight into the underlying reasons for this limitation by analyzing the EVDFs. Figure 3.16 shows the EVDFs in molecular oxygen obtained for two  $E/N$  values. At 10 Td, the center of the EVDF is still close to the origin, exhibiting various “striations” caused by vibrational and electronic transitions. However, at 500 Td, the large electric field visibly shifts the entire distribution towards the forward z-direction. Since the two-term approximation lies on a nearly isotropic EVDF with small deviations around the axial direction, this is clearly not valid at 500 Td.

Figure 3.17 presents the ratio of the lower-order anisotropies, averaged over all energies,  $\frac{\langle |f_{1,2}| \rangle}{\langle f_0 \rangle} \equiv \int_0^\infty |f_{1,2}(\epsilon)| d\epsilon / \int_0^\infty f_0(\epsilon) d\epsilon$ , calculated using LoKI-MC in both oxygen and argon. In molecular oxygen, the anisotropies increase in the regions where the rotations and vibrations are relevant. Moreover, in both gases, there is a continuous increase of the ratios with the reduced electric field. Taking  $\frac{\langle f_1 \rangle}{\langle f_0 \rangle} \lesssim 0.2$  as a criterion for the validity of the two-term approximation, one concludes that this condition breaks for  $E/N \gtrsim 50$  Td in the case of oxygen and for  $E/N \gtrsim 200$  Td in the case of argon. For example, in typical nanosecond discharges, where the reduced field may reach several hundreds of Td [62, 63], the two-term approximation can lead to faulty results. However, the question of whether the two-term approximation is valid is more intricate than this simple criterion, as evidenced in section 3.4.2, since, for example, (i) at low  $E/N$  where anisotropies are minimal, the transverse diffusion coefficient is already inaccurate within this approximation, and (ii) at higher  $E/N \sim 1000$  Td the ionization coefficient calculated by this approximation becomes more accurate than for low  $E/N$  values.

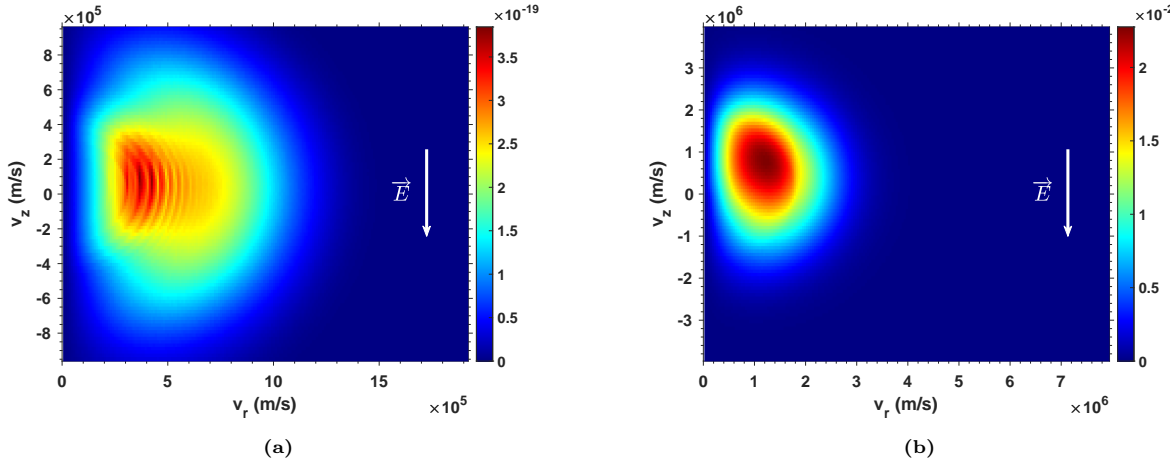


**Figure 3.16:** Electron velocity distribution function ( $\text{m}^{-3}\text{s}^3$ ) in molecular oxygen for the following  $E/N$  values: (a) 10 Td; (b) 500 Td.

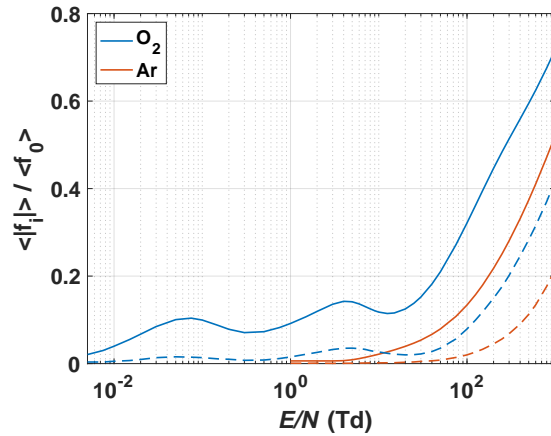


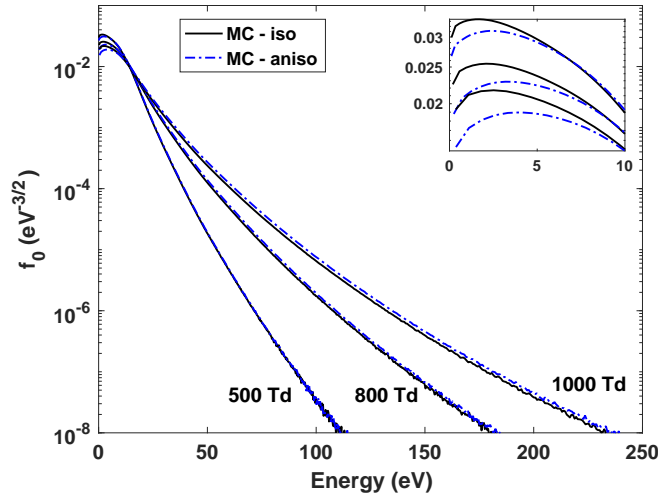
**Figure 3.17:** Average anisotropy ratios in oxygen and argon, as a function of  $E/N$ :  $\frac{\langle |f_1| \rangle}{\langle f_0 \rangle}$  (full lines);  $\frac{\langle |f_2| \rangle}{\langle f_0 \rangle}$  (dashed).

### 3.4.4 Anisotropic ionization scattering induced by momentum conservation

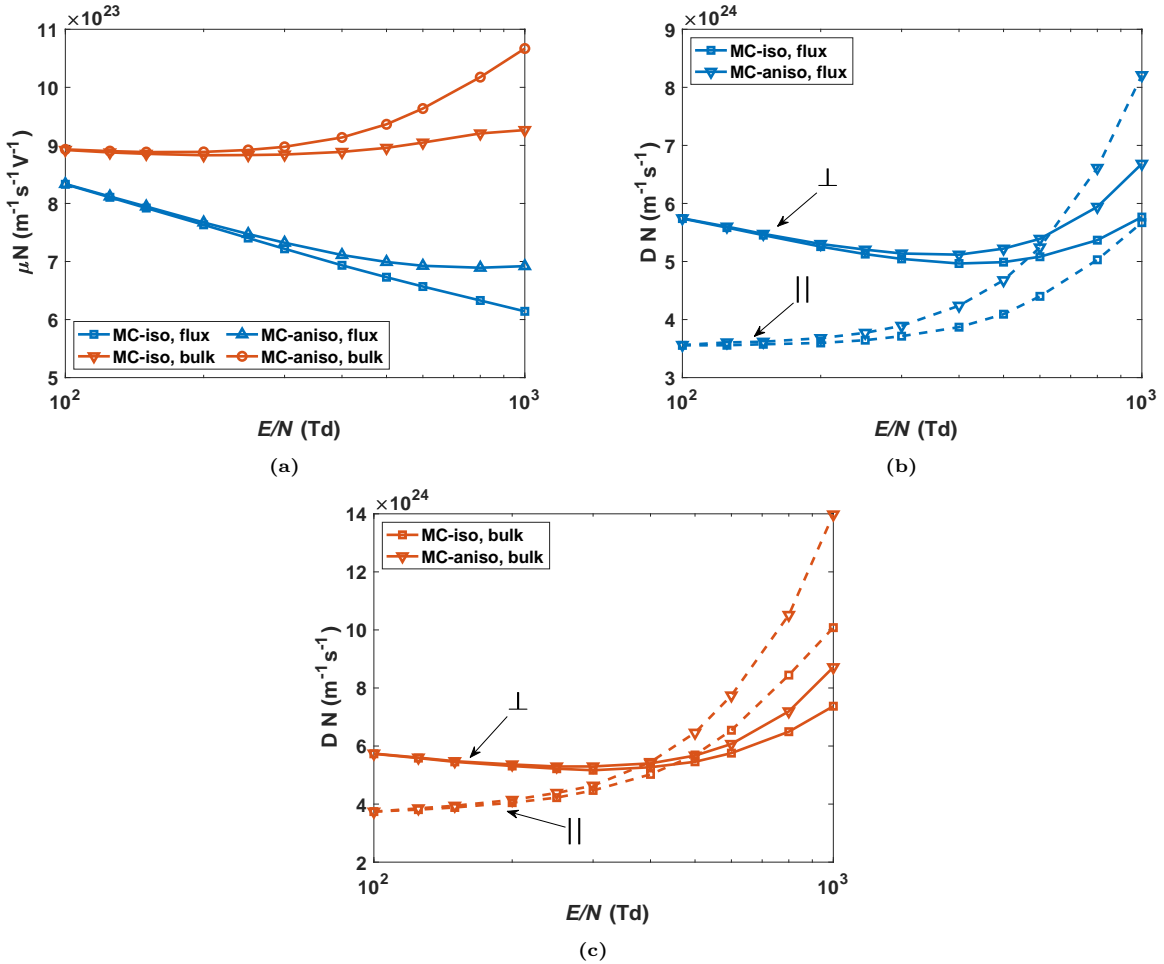
In the previous sections, we considered isotropic scattering in ionization collisions for both scattered and secondary electrons, since this assumption is used in the Boltzmann solvers LoKI-B and MultiBolt. However, as discussed in section 3.2.5, this approach does not conserve the linear momentum in the collision and, if possible, should be avoided. Here, the influence of anisotropic scattering in ionization collisions, induced by momentum conservation, is analyzed in argon.

Figure 3.18 shows that, at 500 Td, the EEDFs with/without anisotropic scattering are still similar, while for 800 and 1000 Td, the tails of the distributions are clearly higher when using an anisotropic description. As shown in figure 3.19, this effect is also noticed in the mobility and the diffusion coefficients, where the quantities are significantly higher when anisotropic scattering is considered for reduced fields  $E/N \gtrsim 200$  Td (deviations up to 13%, 15%, 16% and 45%, for the flux mobility, bulk mobility, flux transverse diffusion and flux longitudinal diffusion coefficients, respectively). The previous observations do not imply that anisotropic scattering should be adopted in all cases, since most cross-section sets were optimized assuming isotropic scattering in ionization events. Therefore, the use of anisotropic scattering, while physically more correct, may lead to a worst comparison with the measurements of swarm coefficients, depending on the cross-section data used.

We should note that, due to the imprecision in the renormalization of the electron number present in the initial version of the code, the figures presented in [1] concerning this section are slightly different. However, the conclusions of the discussion are the same.



**Figure 3.18:** Electron energy distribution functions in argon using isotropic (black) and anisotropic (blue) scattering in ionization events, at various  $E/N = 500, 800$  and  $1000$  Td.



**Figure 3.19:** Transport coefficients in argon, as a function of  $E/N$ , using isotropic and anisotropic scattering in ionization events: (a) reduced mobility; (b) reduced transverse (full lines) and longitudinal (dashed) flux diffusion coefficients; (c) reduced transverse (full lines) and longitudinal (dashed) bulk diffusion coefficients.

### 3.4.5 Effects of superelastic collisions

This section analyzes the effects of superelastic collisions in two systems, using a typical reduced electric field of 50 Td, so as to demonstrate the importance of a detailed description of the internal states of the gas. Molecular oxygen and molecular nitrogen are used to illustrate the influence on the electron kinetics of electronically and vibrationally excited states, respectively.

The first electronically excited state of molecular oxygen,  $O_2(a^1\Delta_g)$ , is significantly present in typical discharge conditions, with fractional populations of the order of 0.15 [64–68]. The EEDFs in molecular oxygen are shown in figure 3.20 for different  $[O_2(a)]/N$  fractions. We find that the larger the excited  $O_2(a)$  population, the higher is the tail of the distribution, as expected, due to the increasing influence of the electron superelastic collisions with this excited state [64]. The differences at high energies may have a significant impact when coupling the results of the electron kinetics to the heavy-species chemistry.

For example, the ionization rate coefficient, in units of  $10^{-19}\text{m}^3/\text{s}$ , is 1.77, 3.03 and 5.18, for  $[\text{O}_2(\text{a})]/N$  fractions of 0, 0.1 and 0.2, respectively. Therefore, the modelling of oxygen discharges with relative  $\text{O}_2(\text{a})$  populations as low as 0.1 should not be based on the ground-state approximation.

It is well known that the vibrationally excited states of nitrogen strongly influence the electron kinetics [69–73]. To illustrate this effect, we use the  $\text{N}_2$  complete set of cross sections, together with the  $\text{N}_2\text{-vib}$  cross sections describing the vibrational electron-molecule collisions, published in the IST-Lisbon database of LXCat [74]. The latter set of cross sections describes all vibrational excitations/de-excitations between the first 11 levels of the ground state. For more details on the  $\text{N}_2$  cross-section set, see section 4.3 of [17]. The energies of the vibrational levels are set according to the energy thresholds of the cross sections for vibrational excitation.<sup>5</sup> The EEDFs in nitrogen are presented in figure 3.21, considering Maxwell-Boltzmann vibrational distribution functions at three temperatures,  $T_v = 300, 2000, 5000$  K. The results show that the EEDFs strongly change with the vibrational temperature, exhibiting an enhanced plateau above 2 eV as  $T_v$  increases, due to the effects of vibrational de-excitation and the associated transfer of energy to the electrons. These changes affect significantly the electron rate coefficients. For example, the ionization rate coefficient, in units of  $10^{-22}\text{m}^3/\text{s}$ , is 2.25, 4.51 and 24.7, for vibrational temperatures of 300, 2000 and 5000 K, respectively. Considering that the vibrational temperatures in  $\text{N}_2$  discharges can reach 10000 K, the electron kinetics should be described taking into account the vibrational distribution function.

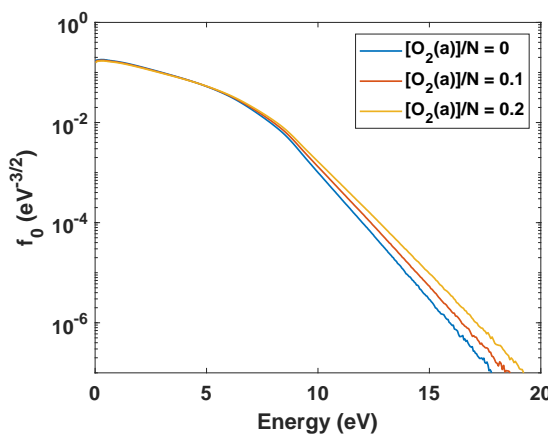


**Figure 3.20:** Electron energy distribution functions in oxygen at  $E/N = 50$  Td, for different fractions  $[\text{O}_2(\text{a})]/N$ .

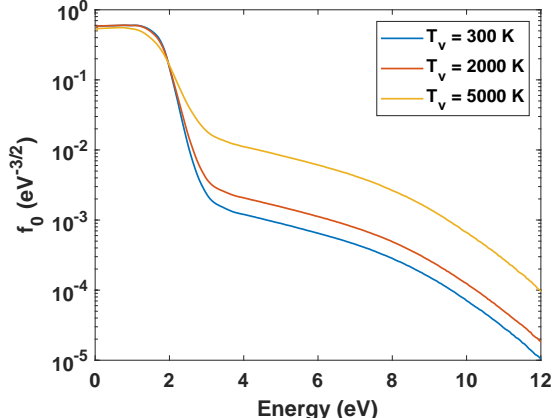


**Figure 3.21:** Electron energy distribution functions in nitrogen at  $E/N = 50$  Td, for different vibrational temperatures  $T_v$ .

<sup>5</sup>We checked that in conditions of null electric field and temperature of 2000 K, where thermalization is significantly influenced by the vibrational distribution, the EEDF tends to a Maxwellian at the corresponding temperature, as expected.

### 3.4.6 Computation time

The major drawback of Monte Carlo simulations is the long computation time. However, as computing efficiency continues to advance, the utilization of Monte Carlo codes is becoming increasingly affordable. Furthermore, LoKI-MC is relatively fast.

Figures 3.22 and 3.23 compare the computation times of LoKI-MC and METHES [20]. The simulations were conducted on an ensemble of (a)  $10^4$  and (b)  $10^6$  electrons, in argon at  $E/N = 500$  Td. Both codes are run using one thread of a eight-core processor Apple M1 Pro @ 3.22 GHz. LoKI-MC considered three different options for the gas-temperature effect: false (not considering this effect), true (activating this effect) and smart activation (considering the thermal motion of the molecules only at low electron energy, see section 3.2.4). Note that the LoKI-MC simulation with  $2 \times 10^8$  collisions, using an ensemble of  $10^6$  electrons and the “smart activation” option, takes around 1.2 min and already provides good results, with relative standard deviations of 0.01%, 0.03% and 0.2% for the mean energy, the flux drift velocity and the flux diffusion coefficients, respectively.

Remarkably, in all scenarios, the computation time of LoKI-MC significantly outperforms METHES. When simulating  $2 \times 10^8$  electron collisions with an ensemble of  $10^4$  electrons and either “false” or “smart activation” for the gas-temperature effect, LoKI-MC demonstrates approximately an 18-fold acceleration compared to METHES; with “true”, the acceleration is around 11-fold. This performance difference is attributed to two factors: for the type of calculations required in a MC code, C++ is much more efficient than MATLAB; METHES alters class objects several times, which is computationally expensive in MATLAB.

For an ensemble of  $10^6$  electrons, LoKI-MC is approximately 7 times faster than METHES with “false” or “smart activation”, and around 4.3 times faster with “true”. Notice that the LoKI-MC computation time per total simulated collisions is essentially constant, independently of the electron number used in the ensemble. Consequently, the divergence in computational efficiency between  $10^4$  and  $10^6$  electrons is due to METHES. This implies that METHES expends significant computational resources on averaging sampling points, which is more pronounced for lower electron numbers under the same total collision count.

If the simulations are run with two threads, the difference between the computation times of LoKI-MC and METHES is  $\sim 1.5$  times larger than before, since LoKI-MC is partially parallelized, contrarily to METHES. The parallelization is performed using OpenMP [75] for handling free-flights, collision dynamics and generation of random numbers. More parallelization might happen outside of the LoKI-MC itself: the Eigen library [76] is used for matrix/vector data types and operations, and that can parallelize various operations itself, depending on the capabilities of the host architecture and on compiler flags that can be specified at build-time. For large problems, the usage of distributed methods (MPI) may be required in addition to the local parallelization implemented at this moment.

The speedup factor associated with the LoKI-MC parallelization<sup>6</sup> is studied in a workstation with two processors Intel(R) Xeon(R) Platinum 8170 @ 2.10 GHz, each composed by 26 cores with hyperthreading. Using the same simulation conditions, the code is run with different number of threads: 1, 2, 4, 8, 16. The speedup factor of LoKI-MC,  $S_{\text{LoKI-MC}}$ , is presented in figure 3.24, as a function of the number of threads. The trend is compatible with the theoretical behavior of the Amdahl's law [77], typical in tasks with fixed size:  $S_{\text{th}}(\tau) = (1 - p + p/\tau)^{-1}$ , where  $p$  is the proportion of the code that is parallelized and  $\tau$  is the number of threads used in the tasks. As shown in figure 3.24,  $S_{\text{LoKI-MC}}$  agrees rather well with  $S_{\text{th}}(\tau)|_{p=0.64}$ , which suggests that approximately 64% of the tasks are parallelized. Therefore, in principle, the speedup factor cannot be higher than  $(1 - 0.64)^{-1} \simeq 2.78$ .

One may ask why the rest of the code is not parallelized. The calculations are parallelized along the ensemble of electrons. Most of the operations concerning free flights, collision choices and collision dynamics can be performed in parallel. However, part of the calculations rely on shared-memory reading, which may harm the parallelization efficiency. Moreover, there are some operations that cannot be fully parallelized: to obtain the swarm coefficients at each sampling-instant, several sums and averages are done; after solving the collision dynamics of the ensemble, the collision and power-balance counters need to be updated. Computation profiling, e.g. using Valgrind's callgrind [78], may help to understand and mitigate parallelization bottlenecks, and even to optimize the single-thread behavior in the future. Nevertheless, users can always run various single-thread simulations at the same time, one per CPU core, where the parallelization efficiency is almost ideal.

Using one thread of the M1 processor mentioned previously, the simulations in real gases presented in section 3.4.2 require an average of approximately 10 minutes per  $E/N$  value. The computation times are higher for small  $E/N$  values and lower for large  $E/N$  values. This duration is significantly longer than the computation times of LoKI-B ( $\sim 1 - 10$  s) and MultiBolt ( $\sim 40$  s). Nonetheless, the Monte Carlo LoKI-MC provides additional insights into the behavior of the plasma electron kinetics, as it: (i) provides the EVDF, instead of only some of its anisotropies, (ii) enables the inclusion of thermal motion of the gas in describing collisional events, (iii) considers the impact of the internal states of neutral atoms/molecules on electron kinetics, and (iv) easily incorporates new physical effects, as demonstrated in subsequent chapters. Furthermore, LoKI-MC demonstrates computational efficiency in regions with high values of  $E/N$  and/or a high ratio of inelastic to elastic processes. Notably, these are precisely the regions where the expansions used in deterministic codes might encounter limitations.

---

<sup>6</sup>This particular study has not been repeated for the current version of the code but it was verified that the parallelization efficiency has not significantly changed.

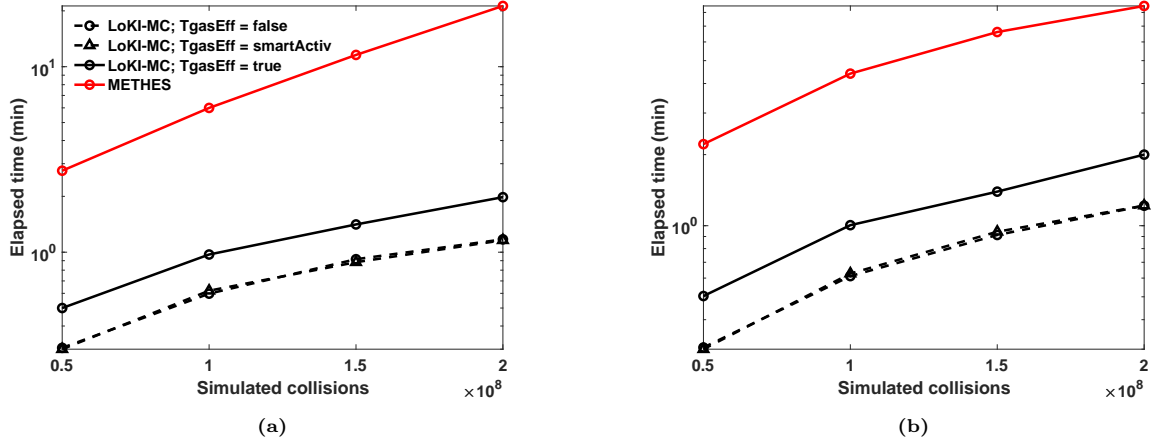


**Figure 3.22:** Monte Carlo computation times using LoKI-MC and METHES [20], with (a)  $10^4$  and (b)  $10^6$  electrons, in argon at  $E/N = 500$  Td, as a function of the total number of simulated collisions.

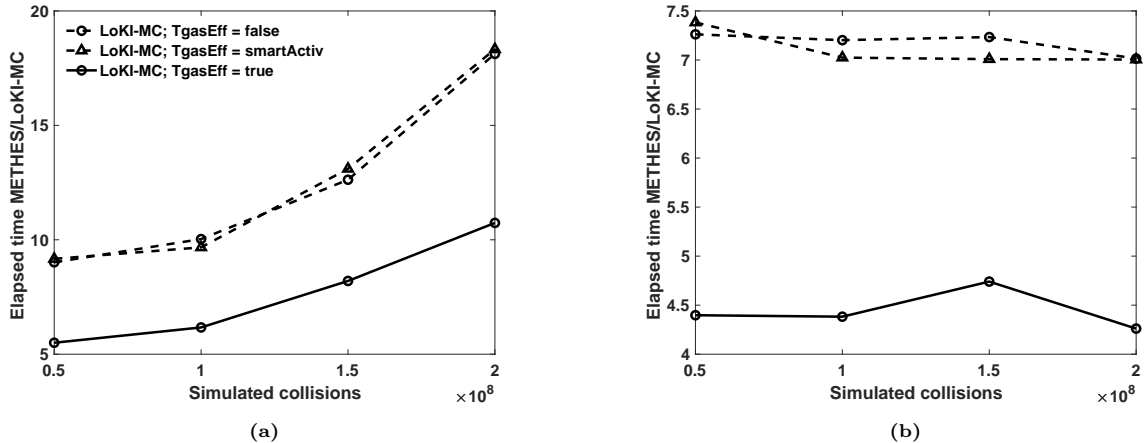


**Figure 3.23:** Ratio of the computation times, METHES/LoKI-MC, with (a)  $10^4$  and (b)  $10^6$  electrons, in argon at  $E/N = 500$  Td, as a function of the total number of simulated collisions.

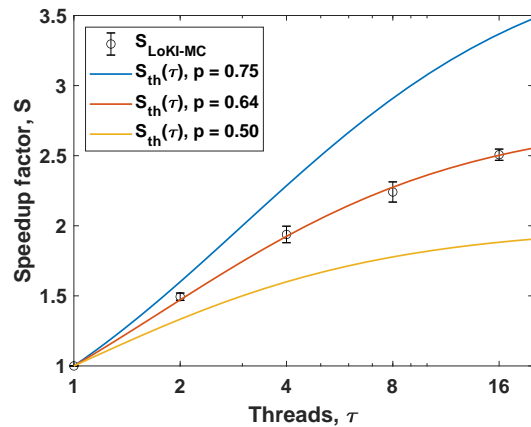


**Figure 3.24:** Comparison between the speedup factor of LoKI-MC,  $S_{\text{LoKI-MC}}$ , and the theoretical Amdahl formula,  $S_{\text{th}}(\tau)$ , presented in the text.

### 3.5 Final remarks and future work

This chapter presented LoKI-MC, a flexible and highly-performant open-source simulation tool, which uses Monte Carlo techniques to solve the non-equilibrium electron kinetics of plasmas excited by uniform DC electric fields. LoKI-MC simulates plasmas produced in any gas mixture, accounting for the distributions of populations for the electronic, vibrational and rotational atomic/molecular levels. The output comprises the EEDF, the EVDF, the electron transport coefficients, the distribution of electron power transferred to the different collisional channels and the spatiotemporal evolution of the electron swarm. The simulation tool has been verified and benchmarked in model gases and real gases, through the comparison with analytical solutions, previous works and other simulation tools. Furthermore, the effects of the gas temperature, anisotropic ionization scattering (induced by momentum conservation) and superelastic collisions were assessed in real gases.

LoKI-MC is freely available for users to perform electron kinetics calculations. Moreover, modellers are invited to continue testing and/or improving the simulation tool. Due to the efficient nature of the C++ code, LoKI-MC can be embedded in plasma-chemistry or fluid models for the calculation of electron rate coefficients and transport coefficients.

The upcoming chapters of this thesis already encompass extensions to the formulation presented in this chapter. These extensions include: general anisotropic scattering in *any* collision type (chapter 4); incorporation of DC magnetic fields alongside AC/DC electric fields (chapter 5), and time-dependent electric-field pulses (chapter 6). Besides that, future versions may provide the capability to investigate charged-particle collisions, bounded environments and ion swarm kinetics.

## References

- [1] Dias, T. C., Tejero-del-Caz, A., Alves, L. L., and Guerra, V. 2023 “The LisbOn KInetics Monte Carlo solver” *Comput. Phys. Commun.* **282**, 108554  
<https://github.com/IST-Lisbon/LoKI-MC>.
- [2] Oehrlein, G. S. and Hamaguchi, S. 2018 “Foundations of low-temperature plasma enhanced materials synthesis and etching” *Plasma Sources Sci Technol.* **27**, 023001.
- [3] Gudmundsson, J. T., Brenning, N., Lundin, D., and Helmersson, U. 2012 “High power impulse magnetron sputtering discharge” *J. Vac. Sci. Technol. A* **30**, 030801.
- [4] Labay, C., Hamouda, I., Tampieri, F., Ginebra, M.-P., and Canal, C. 2019 “Production of reactive species in alginate hydrogels for cold atmospheric plasma-based therapies” *Sci. Rep.* **9**, 16160.
- [5] Bauer, G. and Graves, D. B. 2016 “Mechanisms of Selective Antitumor Action of Cold Atmospheric Plasma-Derived Reactive Oxygen and Nitrogen Species” *Plasma Process Polym* **13**, 1157–1178.

- [6] Fridman, G., Friedman, G., Gutsol, A., Shekhter, A. B., Vasilets, V. N., and Fridman, A. 2008 “Applied Plasma Medicine” *Plasma Process Polym* **5**, 503–533.
- [7] Gherardi, M., Puač, N., and Shiratani, M. 2018 “Special issue: Plasma and agriculture” *Plasma Process Polym* **15**, 1877002.
- [8] Min, S. C., Roh, S. H., Niemira, B. A., Sites, J. E., Boyd, G., and Lacombe, A. 2016 “Dielectric barrier discharge atmospheric cold plasma inhibits Escherichia coli O157:H7, Salmonella, Listeria monocytogenes, and Tulane virus in Romaine lettuce” *Int. J. Food Microbiol.* **237**, 114–120.
- [9] Kitazaki, S., Koga, K., Shiratani, M., and Hayashi, N. 2012 “Growth Enhancement of Radish Sprouts Induced by Low Pressure O<sub>2</sub> Radio Frequency Discharge Plasma Irradiation” *Jpn J Appl Phys* **51**, 01AE01.
- [10] Rooij, G. J. van, Bekerom, D. C. M. van den, Harder, N. den, Minea, T., Berden, G., Bongers, W. A., Engeln, R., Graswinckel, M. F., Zoethout, E., and Sanden, M. C. M. van de 2015 “Taming microwave plasma to beat thermodynamics in CO<sub>2</sub> dissociation” *Faraday Discuss.* **183** (0), 233–248.
- [11] Snoeckx, R., Aerts, R., Tu, X., and Bogaerts, A. 2013 “Plasma-Based Dry Reforming: a Computational Study Ranging from the Nanoseconds to Seconds Time Scale” *J. Phys. Chem. C* **117**, 4957–4970.
- [12] Alves, L. L., Bogaerts, A., Guerra, V., and Turner, M. M. 2018 “Foundations of modelling of nonequilibrium low-temperature plasmas” *Plasma Sources Sci. Technol.* **27**, 023002.
- [13] Morgan, W. L. and Penetrante, B. M. 1990 “ELENDIF: A time-dependent Boltzmann solver for partially ionized plasmas” *Comput. Phys. Commun.* **58**, 127–152.
- [14] Hagelaar, G. J. M. and Pitchford, L. C. 2005 “Solving the Boltzmann equation to obtain electron transport coefficients and rate coefficients for fluid models” *Plasma Sources Sci. Technol.* **14**, 722–733  
<https://bolsig.laplace.univ-tlse.fr/>.
- [15] Dyatko, N., Kochetov, I., Napartovich, A., and Sukharev, A. 2015 “EEDF: The software package for calculations of Electron Energy Distribution Function”  
<http://www.lxcat.net/software/EEDF/>.
- [16] Luque, A. 2014 <https://github.com/aluque/bolos>.
- [17] Tejero-del-Caz, A., Guerra, V., Gonçalves, D., Lino da Silva, M., Marques, L., Pinhão, N., Pintasilgo, C. D., and Alves, L. L. 2019 “The LisbOn KInetics Boltzmann solver” *Plasma Sources Sci. Technol.* **28**, 043001  
<https://github.com/IST-Lisbon/LoKI>.

- [18] Tejero-del-Caz, A., Guerra, V., Pinhão, N., Pintassilgo, C. D., and Alves, L. L. 2021 “On the quasi-stationary approach to solve the electron Boltzmann equation in pulsed plasmas” *Plasma Sources Sci. Technol.* **30**, 065008.
- [19] Stephens, J. 2018 “A multi-term Boltzmann equation benchmark of electron-argon cross-sections for use in low temperature plasma models” *J. Phys. D Appl. Phys.* **51**, 125203  
<https://gitlab.com/LXCatThirdParty/MultiBolt>.
- [20] Rabie, M. and Franck, C. M. 2016 “METHES: A Monte Carlo collision code for the simulation of electron transport in low temperature plasmas” *Comput. Phys. Commun.* **203**, 268–277  
[www.lxcat.net/download/METHES](http://lxcat.net/download/METHES).
- [21] Biagi, S. 1999 “Monte Carlo simulation of electron drift and diffusion in counting gases under the influence of electric and magnetic fields” *Nucl. Instrum. Methods Phys. Res A* **421**, 234–240  
<http://magboltz.web.cern.ch/magboltz/>.
- [22] Phelps, A. V. and Pitchford, L. C. 1985 “Anisotropic scattering of electrons by N<sub>2</sub> and its effect on electron transport” *Phys. Rev. A* **31** (5), 2932–2949.
- [23] Skullerud, H. R. 1969 “Longitudinal diffusion of electrons in electrostatic fields in gases” *J. Phys. B-At. Mol. Opt.* **2**, 696–705.
- [24] [www.lxcat.net](http://www.lxcat.net).
- [25] White, R. D., Robson, R. E., Schmidt, B., and Morrison, M. A. 2003 “Is the classical two-term approximation of electron kinetic theory satisfactory for swarms and plasmas?” *J. Phys. D Appl. Phys.* **36**, 3125.
- [26] White, R. D., Robson, R. E., Dujko, S., Nicoletopoulos, P., and Li, B. 2009 “Recent advances in the application of Boltzmann equation and fluid equation methods to charged particle transport in non-equilibrium plasmas” *J. Phys. D Appl. Phys.* **42**, 194001.
- [27] Petrović, Z. L., Dujko, S., Marić, D., Malović, G., Nikitović, Ž., Šašić, O., Jovanović, J., Stojanović, V., and Radmilović-Radjenović, M. 2009 “Measurement and interpretation of swarm parameters and their application in plasma modelling” *J. Phys. D Appl. Phys.* **42**, 194002.
- [28] Dujko, S., White, R. D., Petrović, Z. L., and Robson, R. E. 2011 “A multi-term solution of the nonconservative Boltzmann equation for the analysis of temporal and spatial non-local effects in charged-particle swarms in electric and magnetic fields” *Plasma Sources Sci Technol* **20**, 024013.
- [29] Matsumoto, M. and Nishimura, T. 1998 “Mersenne Twister: A 623-Dimensionally Equidistributed Uniform Pseudo-Random Number Generator” *ACM Trans. Model. Comput. Simul.* **8**, 3–30.
- [30] Nishimura, T. 2000 “Tables of 64-bit Mersenne Twisters” *ACM Trans. Model. Comput. Simul.* **10**, 348–357.
- [31] [http://www.cplusplus.com/reference/random/mt19937\\_64/](http://www.cplusplus.com/reference/random/mt19937_64/).

- [32] Longo, S. 2006 “Monte Carlo simulation of charged species kinetics in weakly ionized gases” *Plasma Sources Sci. Technol.* **15**, S181–S188.
- [33] Pitchford, L. C. et al. 2013 “Comparisons of sets of electron–neutral scattering cross sections and swarm parameters in noble gases: I. Argon” *J. Phys. D Appl. Phys.* **46**, 334001.
- [34] Klein, O. and Rosseland, S. 1921 “Über Zusammenstöße zwischen Atomen und freien Elektronen” *Z. Physik* **4**, 46–51.
- [35] Itoh, T. and Musha, T. 1960 “Monte Carlo Calculations of Motion of Electrons in Helium” *J. Phys. Soc. Jpn* **15**, 1675–1680.
- [36] Skullerud, H. R. 1968 “The stochastic computer simulation of ion motion in a gas subjected to a constant electric field” *J. Phys. D Appl. Phys.* **1**, 1567–1568.
- [37] Longo, S. 2000 “Monte Carlo models of electron and ion transport in non-equilibrium plasmas” *Plasma Sources Sci. Technol.* **9**, 468–476.
- [38] Dujko, S., Raspopović, Z. M., and Petrović, Z. L. 2005 “Monte Carlo studies of electron transport in crossed electric and magnetic fields in CF<sub>4</sub>” *J. Phys. D Appl. Phys.* **38**, 2952.
- [39] Box, G. E. and Muller, M. E. 1958 “A note on the generation of random normal deviates” *Ann. Math. Stat.* **29**, 610–611.
- [40] Yousfi, M., Hennad, A., and Alkaa, A. 1994 “Monte Carlo simulation of electron swarms at low reduced electric fields” *Phys. Rev. E* **49** (4), 3264–3273.
- [41] Reid, I. 1979 “An Investigation of the Accuracy of Numerical Solutions of Boltzmann’s Equation for Electron Swarms in Gases with Large Inelastic Cross Sections” *Aust. J. Phys.* **32**, 231.
- [42] Vahedi, V. and Surendra, M. 1995 “A Monte Carlo collision model for the particle-in-cell method: applications to argon and oxygen discharges” *Comput. Phys. Commun.* **87**, 179–198.
- [43] Opal, C. B., Peterson, W. K., and Beaty, E. C. 1971 “Measurements of Secondary-Electron Spectra Produced by Electron Impact Ionization of a Number of Simple Gases” *J. Chem. Phys.* **55**, 4100–4106.
- [44] Kim, Y.-K. 1995 *Atomic and Molecular Processes in Fusion Edge Plasmas* New York: Springer Science, Business Media.
- [45] Boeuf, J. P. and Marode, E. 1982 “A Monte Carlo analysis of an electron swarm in a nonuniform field: the cathode region of a glow discharge in helium” *J. Phys. D Appl. Phys.* **15**, 2169–2187.
- [46] Dujko, S., White, R. D., Petrović, Z. L., and Robson, R. E. 2010 “Benchmark calculations of nonconservative charged-particle swarms in DC electric and magnetic fields crossed at arbitrary angles” *Phys. Rev. E* **81** (4), 046403.
- [47] Raspopovic, Z. M., Sakadzic, S., Bzenic, S. A., and Petrovic, Z. L. 1999 “Benchmark calculations for Monte Carlo simulations of electron transport” *IEEE Trans. Plasma Sci.* **27**, 1241–1248.

- [48] Mirić, J., Bošnjaković, D., Simonović, I., Petrović, Z. L., and Dujko, S. 2016 “Electron swarm properties under the influence of a very strong attachment in SF<sub>6</sub> and CF<sub>3</sub>I obtained by Monte Carlo rescaling procedures” *Plasma Sources Sci. Technol.* **25**, 065010.
- [49] Nolan, A. M., Brennan, M. J., Ness, K. F., and Wedding, A. B. 1997 “A benchmark model for analysis of electron transport in non-conservative gases” *J. Phys. D Appl. Phys.* **30**, 2865–2871.
- [50] Hockney, R. W. and Eastwood, J. 1988 *Computer simulation using particles (1st ed.)* CRC Press.
- [51] Penetrante, B. M., Bardsley, J. N., and Pitchford, L. C. 1985 “Monte Carlo and Boltzmann calculations of the density gradient expanded energy distribution functions of electron swarms in gases” *J. Phys. D Appl. Phys.* **18**, 1087–1100.
- [52] Petrović, Z., Raspopović, Z., Dujko, S., and Makabe, T. 2002 “Kinetic phenomena in electron transport in radio-frequency fields” *Appl. Surf. Sci.* **192**, 1–25.
- [53] White, R. D., Brennan, M. J., and Ness, K. F. 1997 “Benchmark simulations for electron swarms in crossed electric and magnetic fields” *J. Phys. D Appl. Phys.* **30**, 810.
- [54] Blevin, H. A. and Fletcher, J. 1984 “Electron transport and rate coefficients in Townsend discharges” *Aust. J. Phys.* **37**, 593.
- [55] Pinhão, N. R., Loffhagen, D., Vass, M., Hartmann, P., Korolov, I., Dujko, S., Bošnjaković, D., and Donkó, Z. 2020 “Electron swarm parameters in C<sub>2</sub>H<sub>2</sub>, C<sub>2</sub>H<sub>4</sub> and C<sub>2</sub>H<sub>6</sub>: measurements and kinetic calculations” *Plasma Sources Sci. Technol.* **29**, 045009.
- [56] Dujko, S., Bošnjaković, D., Vass, M., Hartmann, P., Korolov, I., Pinhão, N. R., Loffhagen, D., and Donkó, Z. 2023 “Scanning drift tube measurements and kinetic studies of electron transport in CO” *Plasma Sources Sci. Technol.* **32**, 025014.
- [57] Loureiro, J. and Amorim, J. 2016 *Kinetics and Spectroscopy of Low Temperature Plasmas* John Wiley & Sons.
- [58] Lucas, J. and Saelee, H. T. 1975 “A comparison of a Monte Carlo simulation and the Boltzmann solution for electron swarm motion in gases” *J. Phys. D Appl. Phys.* **8**, 640–650.
- [59] Ness, K. F. and Robson, R. E. 1986 “Velocity distribution function and transport coefficients of electron swarms in gases. II. Moment equations and applications” *Phys. Rev. A* **34** (3), 2185–2209.
- [60] O<sub>2</sub> on IST-Lisbon data, [www.lxcat.net](http://www.lxcat.net).
- [61] Ar on IST-Lisbon data, [www.lxcat.net](http://www.lxcat.net).
- [62] Šimek, M. and Bonaventura, Z. 2018 “Non-equilibrium kinetics of the ground and excited states in N<sub>2</sub>-O<sub>2</sub> under nanosecond discharge conditions: extended scheme and comparison with available experimental observations” *J. Phys. D Appl. Phys.* **51**, 504004.
- [63] Brandenburg, R., Bruggeman, P., and Starikovskaia, S. 2017 “Fast pulsed discharges” *Plasma Sources Sci. Technol.* **26**, 020201.

- [64] Gousset, G., Ferreira, C. M., Pinheiro, M., Sa, P. A., Touzeau, M., Vialle, M., and Loureiro, J. 1991 “Electron and heavy-particle kinetics in the low pressure oxygen positive column” *J. Phys. D Appl. Phys.* **24**, 290–300.
- [65] Guerra, V. and Loureiro, J. 1999 “Kinetic model of a low-pressure microwave discharge in O<sub>2</sub>-H<sub>2</sub> including the effects of O-ions on the characteristics for plasma maintenance” *Plasma Sources Sci Technol.* **8**, 110–124.
- [66] Belostotsky, S. G., Economou, D. J., Lopaev, D. V., and Rakhimova, T. V. 2005 “Negative ion destruction by O(<sup>3</sup>P) atoms and O<sub>2</sub>(a<sup>1</sup>Δ<sub>g</sub>) molecules in an oxygen plasma” *Plasma Sources Sci. Technol.* **14**, 532–542.
- [67] Lopaev, D. V., Malykhin, E. M., and Zyryanov, S. M. 2010 “Surface recombination of oxygen atoms in O<sub>2</sub> plasma at increased pressure: II. Vibrational temperature and surface production of ozone” *J. Phys. D Appl. Phys.* **44**, 015202.
- [68] Booth, J.-P. et al. 2020 “Determination of absolute O(<sup>3</sup>P) and O<sub>2</sub>(a<sup>1</sup>Δ<sub>g</sub>) densities and kinetics in fully modulated O<sub>2</sub> DC glow discharges from the O<sub>2</sub>(X<sup>3</sup>Σ<sub>g</sub><sup>−</sup>) afterglow recovery dynamics” *Plasma Sources Sci. Technol.* **29**, 115009.
- [69] Loureiro, J. and Ferreira, C. M. 1986 “Coupled electron energy and vibrational distribution functions in stationary N<sub>2</sub> discharges” *J. Phys. D Appl. Phys.* **19**, 17–35.
- [70] Massabieaux, B., Gousset, G., Lefebvre, M., and Pealat, M. 1987 “Determination of N<sub>2</sub>(X) vibrational level populations and rotational temperatures using CARS in a D.C. low pressure discharge” *J. Phys. France* **48**, 1939–1949.
- [71] Lo, A., Cessou, A., Boubert, P., and Vervisch, P. 2014 “Space and time analysis of the nanosecond scale discharges in atmospheric pressure air: I. Gas temperature and vibrational distribution function of N<sub>2</sub> and O<sub>2</sub>” *J. Phys. D Appl. Phys.* **47**, 115201.
- [72] Steeg, A. W. van de, Butterworth, T., Bekerom, D. C. M. van den, Silva, A. F., Sanden, M. C. M. van de, and Rooij, G. J. van 2020 “Plasma activation of N<sub>2</sub>, CH<sub>4</sub> and CO<sub>2</sub>: an assessment of the vibrational non-equilibrium time window” *Plasma Sources Sci. Technol.* **29**, 115001.
- [73] Colonna, G., Laricchiuta, A., and Pietanza, L. 2020 “Time dependent selfconsistent electron energy distribution functions during nano-second repetitive discharges in reacting N<sub>2</sub>/H<sub>2</sub> mixtures” *Plasma Phys. Control. Fusion* **62**, 014003.
- [74] N<sub>2</sub> on IST-Lisbon data, [www.lxcat.net](http://www.lxcat.net).
- [75] Chandra, R., Dagum, L., Kohr, D., Menon, R., Maydan, D., and McDonald, J. 2001 *Parallel programming in OpenMP* Morgan Kaufmann.
- [76] Guennebaud, G., Jacob, B., et al. 2021 *Eigen v3.3*.
- [77] Amdahl, G. M. 1967 “Validity of the single processor approach to achieving large-scale computing capabilities” *AFIPS Conference Proceedings* **30**, 483–485.

- [78] Bond, M. D., Nethercote, N., Kent, S. W., Guyer, S. Z., and McKinley, K. S. 2007 “Tracking Bad Apples: Reporting the Origin of Null and Undefined Value Errors” *Proceedings of the 22nd Annual ACM SIGPLAN Conference on Object-Oriented Programming Systems, Languages and Applications* New York, NY, USA: Association for Computing Machinery, 405–422.

# 4

## The role of anisotropic scattering in electron-neutral collisions: H<sub>2</sub>O rotational collisions as an example

### Chapter summary

In the previous chapter, we assumed isotropic scattering for electron-neutral collisions, except for ionization. Here, we demonstrate that a general *anisotropic* scattering model can be easily incorporated into a Monte Carlo formulation.

The significance of considering anisotropic scattering is exemplified in water vapor (H<sub>2</sub>O), where electron kinetics is greatly influenced by the angular distribution in rotational collisions. Additionally, we compare the Monte Carlo results with two-term solutions, which account for anisotropic scattering under approximations valid specifically for rotational collisions.

The H<sub>2</sub>O cross-section set and the inclusion of anisotropic scattering are validated by the electron swarm analysis technique. The inclusion of anisotropic scattering in rotational collisions significantly improves the agreement between calculations and measurements of the electron drift velocity, reduced mobility, characteristic energy, reduced Townsend ionization coefficient and reduced attachment coefficient. The use of LoKI-MC also validates the cross-section set against parameters that cannot be obtained by LoKI-B, such as the longitudinal diffusion coefficient or the bulk transport coefficients.

This chapter draws heavily from the work of Budde et al. [1] and it is important to note that this research is also part of Maik Budde's doctoral thesis. Notably, Maik Budde is solely responsible for developing the comprehensive and self-consistent cross-section dataset for H<sub>2</sub>O, including the calculation of rotational cross sections using dipole-Born theory. In contrast, the discussion on how to include anisotropic scattering in a two-term solver and the analysis of the results is a shared work. Finally, I implemented anisotropic scattering into the Monte Carlo code LoKI-MC and performed the corresponding calculations.

## 4.1 Introduction

The impact of anisotropic scattering on electron kinetics has been investigated in various studies, including: model gases by Reid [2]; N<sub>2</sub> by both Phelps and Pitchford [3] and Casey et al. [4]; Ar by Janssen et al. [5]; and CO by Vialletto et al. [6]. Generally, anisotropic scattering has been found to significantly influence the results and, therefore, its effects should be appropriately considered whenever necessary. In particular, Vialletto et al. [6] demonstrated that accurately accounting for the forward angular scattering of rotational collisions in CO can lead to an improved agreement between calculations and measurements of electron transport coefficients, specially for reduced electric fields  $E/N \lesssim 1$  Td.

In this chapter, we explore the effects of anisotropic scattering on electron-neutral rotational collisions in H<sub>2</sub>O. In a previous paper [7], we presented a complete and self-consistent set of cross-sections (CSs) for H<sub>2</sub>O, assuming isotropic scattering. However, to achieve agreement with experimental electron transport coefficients, we introduced a scaling factor of 0.3 and applied a cut-off beyond 12 eV in the calculation of the rotational CSs [7]. In the present work, we demonstrate that a more thorough description of rotational collisions, considering an angular distribution consistent with the Dipole-Born theory used to calculate the CS, leads to significantly improved agreement with experiments, without requiring any changes to the calculations.

Note that water plays a crucial role in a manifold of applications. For instance, water molecules can serve as abundant hydrogen source in plasma gas conversion [8, 9] or surface functionalization [10], as probe in atmospheric [11] or astronomic environments [12], as prominent constituent in primordial Earth's atmosphere [13] or as direct target of processing like water purification [14]. Additionally, water is an impurity present in many applications [15, 16].

This chapter is organized as follows. Section 4.2 discusses the angular distribution of dipole rotational collisions in H<sub>2</sub>O. Sections 4.3 and 4.4 present how anisotropic collisional scattering is implemented in two-term Boltzmann equation and Monte Carlo solvers, respectively. Section 4.5 presents the cross-section set for H<sub>2</sub>O. Section 4.6 validates both two-term and MC approaches by comparison against experiments. Section 4.7 elaborates on the role of rotations in the electron kinetics, for the case of H<sub>2</sub>O. Section 4.8 closes the chapter with some final remarks.

## 4.2 Angular distribution of dipole rotational collisions

Before addressing the anisotropic scattering in rotational collisions, the proper notation of the rotational quantum state of H<sub>2</sub>O must be clarified. Since it has been introduced in a preceding paper [7], only a summary is given here. The H<sub>2</sub>O molecule is an asymmetric-top rotor whose rotational quantum state  $\mathbf{J}$  is characterized by three quantum numbers: the principal rotational quantum number  $J$  (not to be confused with the notation of the rotational state itself  $\mathbf{J}$ ),  $K'$  and  $K''$ , which represent the projection of

$J$  along the axis of smallest and largest moment of inertia, respectively. The latter two are often combined to the pseudo-quantum number  $\tau = K' - K''$ . The rotational state is then given as  $\mathbf{J} = JK'K'' = J\tau$  [7, 17].

The kinematics of a scattering event  $i$  is ruled by its differential cross section (DCS)  $\frac{d\sigma_i(\varepsilon, \theta)}{d\Omega}$ , where  $\varepsilon$  is the incident electron energy,  $\theta$  is the polar scattering angle and  $d\Omega = \sin\theta d\theta d\phi$  is the differential solid angle, assuming symmetry regarding the azimuthal angle  $\phi$ . In the case of dipole transitions in asymmetric-top rotor molecules like water, Itikawa derived the following expression under the Born approximation [18, 19]

$$\frac{d\sigma_i(\varepsilon, \theta)}{d\Omega} = \sqrt{\frac{\varepsilon'}{\varepsilon}} \frac{2D^2}{3(2J+1)} \frac{S_i}{\varepsilon' + \varepsilon - 2\sqrt{\varepsilon'\varepsilon} \cos\theta}, \quad (4.1)$$

where primed quantities are after the collision,  $D = 0.728$  is the dipole moment of water in atomic units and  $S_i$  is the line strength of the rotational transition [20], which is taken from King, Hainer, and Cross [21]. In fact, the Born approximation is a simplification as, for instance, short-range effects and the polar nature of  $\text{H}_2\text{O}$  are neglected. However, it has been proven that the approximation often remains valid even for low electron energies, as the effective interaction occurs distant from the molecule. The wave function of the incident electron is then only marginally distorted [6, 22, 23]. See particularly Vialletto et al. for an in-depth discussion [6].

By integrating the DCS over the solid angle and assuming azimuthal symmetry, we obtain the integral cross section (ICS):

$$\sigma_i^{\text{Int}}(\varepsilon) = \frac{4\pi D^2 S_i}{3(2J+1)} \frac{1}{\varepsilon} \ln \left| \frac{\sqrt{\varepsilon} + \sqrt{\varepsilon'}}{\sqrt{\varepsilon} - \sqrt{\varepsilon'}} \right| = \frac{8\pi D^2 S_i}{3(2J+1)} \frac{1}{\varepsilon} \ln \left( \frac{\sqrt{\varepsilon} + \sqrt{\varepsilon'}}{\sqrt{V_{J\tau, J'\tau'}}} \right). \quad (4.2)$$

where  $V_{J\tau, J'\tau'} = |\varepsilon_{J'\tau'} - \varepsilon_{J\tau}|$  is the absolute difference between the energies of the final and initial rotational states. Additionally, we can define the angular distribution function  $I_i(\varepsilon, \theta)$  by normalizing the DCS with the ICS:

$$I_i(\varepsilon, \theta) = \frac{1}{\sigma_i^{\text{Int}}(\varepsilon)} \frac{d\sigma_i(\varepsilon, \theta)}{d\Omega}. \quad (4.3)$$

This function provides insight about the angular distribution of the scattered electrons, independently of the ICS of the collisional process. Taking into account equations (4.1) and (4.2), the angular distribution function in dipole-rotational collisions is written as

$$I_i(\varepsilon, \theta) = \frac{1}{4\pi} \frac{\sqrt{\varepsilon}\sqrt{\varepsilon'}}{\varepsilon' + \varepsilon - 2\sqrt{\varepsilon'\varepsilon} \cos\theta} \left[ \ln \left( \frac{\sqrt{\varepsilon} + \sqrt{\varepsilon'}}{\sqrt{V_{J\tau, J'\tau'}}} \right) \right]^{-1}, \quad (4.4)$$

The angular distribution function given by equation (4.4) is plotted in figure 4.1 for the transition from  $(J, \tau) = (1, -1)$  to  $(J', \tau') = (1, 1)$ . The long-range dipole interaction yields a highly anisotropic angular distribution where small-angle scattering is dominant, with an increasing effect with electron energy.

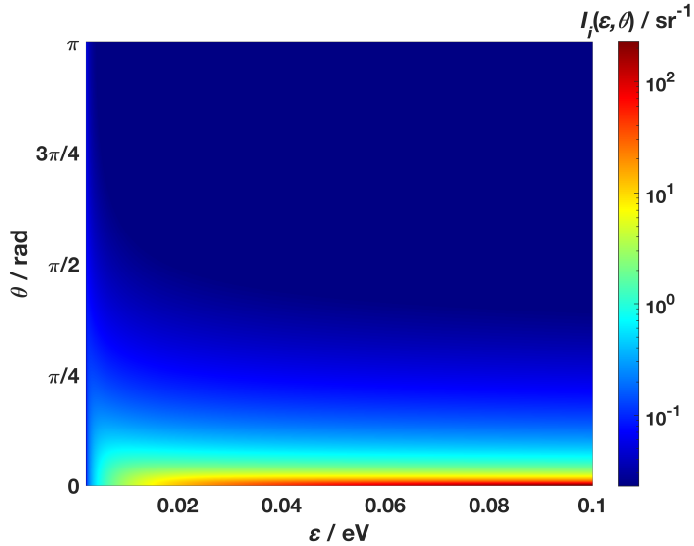


**Figure 4.1:** Angular distribution function  $I_i(\varepsilon, \theta)$  from dipole-Born theory, for the rotational transition in water from  $(J, \tau) = (1, -1)$  to  $(J', \tau') = (1, 1)$ , whose threshold is  $V_{J\tau, J'\tau'} = 0.0023$  eV.

Finally, using the classical definition of the momentum transfer cross section (MTCS) [24],

$$\sigma_i^{\text{MT}}(\varepsilon) = 2\pi \int_0^\pi \frac{d\sigma_i(\varepsilon, \theta)}{d\Omega} (1 - \cos \theta) \sin \theta d\theta , \quad (4.5)$$

for dipole rotational collisions in water, the MTCS is given by,

$$\sigma_i^{\text{MT}}(\varepsilon) = \frac{4\pi D^2 S_i}{3(2J+1)} \frac{1}{\varepsilon} \left( 1 - \frac{(\sqrt{\varepsilon} - \sqrt{\varepsilon'})^2}{2\sqrt{\varepsilon\varepsilon'}} \ln \frac{\sqrt{\varepsilon} + \sqrt{\varepsilon'}}{\sqrt{\varepsilon} - \sqrt{\varepsilon'}} \right) . \quad (4.6)$$

This component is important for the inclusion of anisotropic scattering in a two-term solver, as shown in the next section. Note that the MTCS definition is not unique and some authors [25] consider a different formula for inelastic processes. This is extensively discussed in [6]. In this chapter, whenever talking about momentum transfer, we refer to the definition (4.5).

### 4.3 Anisotropic scattering in a two-term Boltzmann solver

The inclusion of anisotropic scattering in the two-term Boltzmann equation is detailed in [6]. Here, we focus on the main aspects.

Under azimuthal symmetry, similarly to what is done for the electron velocity distribution, the DCS can be expressed as an expansion in Legendre polynomials  $P_j(\cos \theta)$  [26],

$$\frac{d\sigma_i(\varepsilon, \theta)}{d\Omega} = \sum_{j=0}^{\infty} \frac{2j+1}{4\pi} \sigma_i^j(\varepsilon) P_j(\cos \theta) , \quad (4.7)$$

where the terms  $\sigma_i^j(\varepsilon)$  are the  $j$ th partial cross sections (PCSSs), which can be obtained using the orthogonality relation of the Legendre polynomials:

$$\sigma_i^j(\varepsilon) = 2\pi \int_0^\pi \frac{d\sigma_i(\varepsilon, \theta)}{d\Omega} P_j(\cos \theta) \sin \theta d\theta . \quad (4.8)$$

Notice that the zeroth PCS is always equal to the ICS and the first PCS vanishes for isotropic processes. Moreover, the MTCS defined in (4.5) can be written as a function of the first two PCSSs:

$$\sigma_i^{\text{MT}} = \sigma_i^0 - \sigma_i^1. \quad (4.9)$$

Using the two-term approximation, the anisotropic collisional effects can be considered by extending the total (effective) electron-neutral cross section for momentum transfer in the following way<sup>1</sup>:

$$\begin{aligned} \Omega_c(\varepsilon) = & \left\{ \sum_k \delta_k \sigma_{k,\text{ela}}^{\text{MT}}(\varepsilon) + \sum_{k,l>k} [\delta_k \sigma_{k,l}^0(\varepsilon) + \delta_l \sigma_{l,k}^0(\varepsilon)] \right\} \\ & - \left\{ \sum_{k,l>k} \delta_k \frac{\varepsilon + V_{k,l}}{\varepsilon} \sigma_{k,l}^1(\varepsilon + V_{k,l}) \frac{f_1(\varepsilon + V_{k,l})}{f_1(\varepsilon)} \right\} - \left\{ \sum_{k,l>k} \delta_l \frac{\varepsilon - V_{k,l}}{\varepsilon} \sigma_{l,k}^1(\varepsilon - V_{k,l}) \frac{f_1(\varepsilon - V_{k,l})}{f_1(\varepsilon)} \right\} , \end{aligned} \quad (4.10)$$

where  $\delta_k$  is the fraction of molecules in state  $k$ ,  $f_1(\varepsilon)$  is the first anisotropic component of the normalized electron velocity distribution and  $V_{k,l}$  is the absolute energy difference between the two involved states. The first group of terms represents, in order, the momentum transfer due to elastic collisions with molecules in state  $k$ , electron-impact excitations  $k \rightarrow l$  and de-excitations  $l \rightarrow k$ . This part is identical to what is implemented in most two-term Boltzmann solvers, describing the loss of momentum in isotropic collisions. The second and third group consist of the first order corrections due to the anisotropic nature of excitations and de-excitations, respectively<sup>1</sup>.

Take note that the superelastic partial cross sections  $\sigma_{l,k}^j$  are obtained through the microreversibility relation, expressing the principle of detailed balance [27]:

$$\sigma_{l,k}^j(\varepsilon) = \frac{g_k}{g_l} \frac{\varepsilon + V_{k,l}}{\varepsilon} \sigma_{k,l}^j(\varepsilon + V_{k,l}) , \quad (4.11)$$

where  $g_k$  and  $g_l$  denote the statistical weights of the levels  $k$  and  $l$ , respectively.

As evidenced in figure 4.1, the angular distribution in rotational collisions of H<sub>2</sub>O is highly anisotropic and the extended total CS in equation (4.10) is required. However, the anisotropic terms can be further simplified for rotational collisions. Unless the incident electron energy is very low, the difference between the electron energies before and after rotational collisions can be neglected such that  $\varepsilon \pm V_{J\tau,J'\tau'} \sim \varepsilon$ .

---

<sup>1</sup>In [1], the second and third groups of terms are not correct. However, this does not influence the subsequent derivation for rotations.

Consequently,  $f_1(\varepsilon \pm V_{J\tau, J'\tau'})/f_1(\varepsilon) \sim 1$  and the contribution of the rotational collisions for momentum transfer can be approximately written as

$$\Omega_c(\varepsilon) \approx \left\{ \sum_k \delta_k \sigma_{k,\text{ela}}^{\text{MT}}(\varepsilon) + \sum_{k,l > k \notin \text{rot.}} [\delta_k \sigma_{k,l}^0(\varepsilon) + \delta_l \sigma_{l,k}^0(\varepsilon)] \right\} + \sum_{J\tau, J'\tau'} [\delta_{J\tau} \sigma_{J\tau, J'\tau'}^{\text{MT}}(\varepsilon) + \delta_{J'\tau'} \sigma_{J'\tau', J\tau}^{\text{MT}}(\varepsilon)] \quad (4.12)$$

where in the last term equation (4.9) was used. In other words, in low-energy threshold processes such as rotational collisions, the anisotropy can be approximately considered by replacing the ICSs of rotational collisions by the MTCSSs.

Expression (4.12) is implemented in the latest version of LoKI-B [28] and is used in the present simulations. Pay attention that in the case of other collisional processes, e.g. vibrational and electronic excitations/de-excitations, the original form in (4.10) should be used instead.

## 4.4 Anisotropic scattering in a Monte Carlo solver

The Monte Carlo method used in LoKI-MC is described in chapter 3. In short, it simulates the accelerated electron transport in a background gas by following the stochastic trajectory of a representative ensemble of  $N_e$  electrons. Each electron performs a series of free flights interrupted by elastic, inelastic or superelastic collisions with gas molecules. The collision-free times and the collision dynamics are calculated by generating random numbers sampled from probability distributions based on the underlying physics. During the simulation, the information of the electrons is stored in order to calculate distribution functions, transport coefficients and other relevant quantities.

In the first code release, with the exception of ionization, electron collisions are assumed isotropic. Here, we generalize its application to anisotropic scattering based on the work by Vialetto et al. [6], to be included in the next release. The scattering angles after electron-molecule collisions can be sampled according to a theorem of probability [29], by inverting the following equation:

$$p_\theta = 2\pi \int_0^{\theta'} I(\varepsilon, \tilde{\theta}) \sin \tilde{\theta} d\tilde{\theta}, \quad (4.13)$$

where  $p_\theta$  is a random number uniformly distributed between 0 and 1, and the scattering angle  $\theta' \in [0, \pi]$  is randomly distributed according to a probability distribution function  $P(\varepsilon, \tilde{\theta}) = 2\pi I(\varepsilon, \tilde{\theta}) \sin \tilde{\theta}$  that is normalized to 1 in  $[0, \pi]$ . We should remark that this procedure is general and valid for any kind of electron-impact process. Contrarily to the two-term solution, no approximations are needed to include anisotropic scattering. Upon the knowledge of  $I(\varepsilon, \tilde{\theta})$ , equation (4.13) can be inverted to obtain  $\theta'$ .

For isotropic scattering, the angular distribution is constant,  $I(\varepsilon, \theta) = \frac{1}{4\pi}$ , and  $\theta' = \arccos(1 - 2p_\theta)$  (cf.

equation (3.13)).

For dipole-Born interactions, the substitution of equation (4.4) into (4.13) leads to [6]:

$$\theta' = 1 + \frac{2\xi^2}{1 - \xi^2} (1 - \xi^{-2p_\theta}) , \quad (4.14)$$

where the energy-dependent variable  $\xi(\varepsilon)$  is given by:

$$\xi(\varepsilon) = \frac{V_{J\tau, J'\tau'}}{(\sqrt{\varepsilon \mp V_{J\tau, J'\tau'}} + \sqrt{\varepsilon})^2} , \quad (4.15)$$

and the minus (plus) sign corresponds to the inelastic (superelastic) process. In this way, dipole-Born anisotropic scattering is rigorously included in the MC algorithm and we can quantify the accuracy of the approximations made in the two-term Boltzmann solver.

## 4.5 Anisotropic Cross Section Set

The complete anisotropic cross section set proposed in this chapter is plotted against the electron energy  $\varepsilon$  in figure 4.2. We remind that the CS set has been produced by Maik Budde, and not by the author of this thesis. The CSs are grouped in (i) conservative processes with a constant number of electrons, on the left, and (ii) non-conservative processes, i.e. ionization and attachment, on the right. With the exception of rotational processes, the anisotropic set is entirely equal to the isotropic set of [7]. For that reason, differences of the optimized CSs in the isotropic set with respect to the original references are only briefly addressed here and the reader is referred to [7] for details. In short, to improve the agreement with experimental transport coefficients with the isotropic set, in [7] the original CSs for  $\tilde{\alpha}^3B_1$ ,  $\tilde{A}^1B_1$  and  $O^1S_0$  are multiplied with a constant factor within their range of uncertainty, the high-energy tail of the elastic CS is slightly decreased and the effective excitation CS leading to  $H_2O^*$  is introduced.

In the isotropic set, the rotational ICSs are decreased by a factor 0.3 relatively to equation (4.2) and set to zero after 12 eV, to compensate for the isotropic assumption, leading to an effective decrease of the momentum-transfer. In that case, no additional MTCSSs are needed since they are equal to the ICSs. In the anisotropic set proposed here, the ICSs and MTCSSs are calculated entirely according to equations (4.2) and (4.6), with no modification. This approach leads to a significantly better agreement with experiments, as is shown in section 4.6.

To put the proposed rotational CSs into perspective, figure 4.3 shows the CS for the rotational transition  $(JK'K'') = (000) \rightarrow (111)$ . Dashed lines correspond to CSs that we propose in this publication (light blue lines) or in the previous isotropic set (grey line) [7], all based on the Born approximation. The dash-dotted blue line is taken from [30] including a short-range correction to the Born approximation based on R-matrix calculations with a fixed-nuclei approximation. The solid green line is taken from the

supplementary material of [31] that is in principle based on [30]. Note that [31] recommends only the high-energy part of the CS beyond the maximum. From figure 4.3, a clear difference between the simple Born approximation and the more sophisticated approach is seen. The discussion of the best rotational CSs is ongoing and is not to be settled by the present study as the electron swarm analysis method yields an optimized set of CS but does not allow for conclusions about individual CSs. The conclusion that can be drawn though, is that our proposed anisotropic CS set yields excellent agreement with experimental electron transport coefficients as is shown in section 4.6.

The inclusion of anisotropic scattering is limited to rotational collisions in the present set. We specifically decided to focus on anisotropic scattering in low-energy threshold rotational collisions for two reasons. On the one hand, this is motivated by the fact that anisotropic scattering in dipole rotational collisions has been demonstrated to have large effects on calculated electron transport coefficients [6]. On the other hand, it has been shown that the choice of the angular scattering model for higher energy threshold conservative collisions has only a minor influence on the calculated electron transport coefficients [3, 5]. The present results confirm these observations from literature as good agreement between experimental and calculated transport coefficients for low  $E/N$  is obtained with only anisotropic rotational scattering, while isotropic scattering is sufficient for the remaining collisional processes. However, it is worth mentioning that equations (4.10) and (4.13) are general and can principally be applied to any scattering process.

In summary, the anisotropic set includes one elastic [32], 147 rotational integral and 147 rotational momentum transfer [18], two vibrational [33, 34], three electronic excitation [35, 36], three dissociation [37–39], three dissociative attachment [32, 40] and five ionization CSs [41]. In figure 4.2, the sum of all individual ICSs and MTCSs, see equations (4.2) and (4.6), weighted by the population of the lower rotational state is shown (dashed lines) for illustration. In total 310 cross sections, where  $294 = 2 \times 147 = n_{\text{ICS}} + n_{\text{MTCS}}$  are rotational CSs, are included. However, note that the rotational MTCSs are not used for LoKI-MC calculations, since the anisotropic angular distribution is directly taken into account in the generation of the scattering angle, see section 4.4. The reader is referred to [7] for more details on the cross section set.

## 4.6 Validation

The complete CS set of figure 4.2 is validated by the electron swarm technique using the two-term Boltzmann solver LoKI-B [28] and the Monte Carlo simulation tool LoKI-MC [43], both freely available as open-source codes [44]. Anisotropic rotational scattering is included in both solvers through the methods described in sections 4.3 and 4.4.

Contrarily to the recommendation in [7], where it is suggested to discretise the energy axis of the LoKI-B simulations in 2000 cells, as a good compromise between accuracy and computation time, here

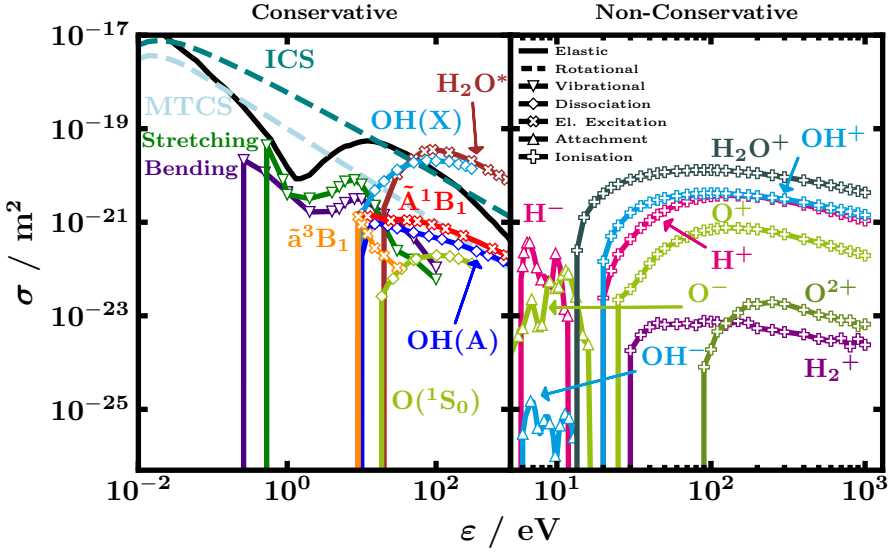


**Figure 4.2:** Proposed cross sections  $\sigma$ , plotted against the electron energy  $\varepsilon$ , divided into conservative and non-conservative collisional processes. ICS and MTCS (dashed lines) are the sums of all individual rotational cross sections weighted by the populations of the lower rotational levels assuming a Boltzmann distribution at 293 K. In the left-side panel, the elastic and rotational cross section extend down to sub-meV range which is not shown for better visibility of the remaining conservative collision cross sections. CSs are obtained from [18, 32–41]. See the main text and [7] for more details.

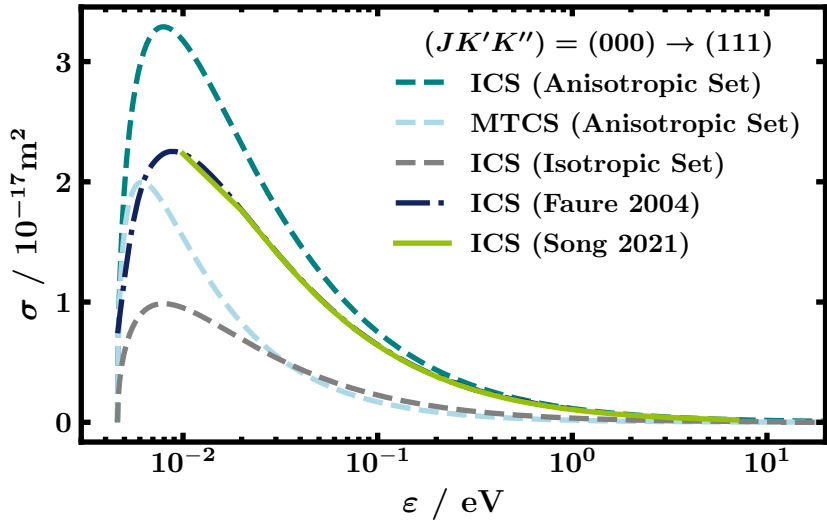


**Figure 4.3:** Illustration of differences in rotational cross sections  $\sigma$  by means of the rotational transition  $(JK'K'') = (000) \rightarrow (111)$ . Dashed lines correspond to CSs that we recommend either here (light blue lines) or in our isotropic set (grey line) [7]. The dash-dotted dark blue line is taken from Faure, Gorfinkel, and Tennyson [42] and the solid green line from Song et al. [31].

the energy axis is discretised in 8000 cells to facilitate the comparison between the isotropic and anisotropic sets. This large cell number assures an accurate treatment of the low-energy thresholds of the rotational CSs [7]. Note that the maximum energy of the grid is dynamically adjusted [28]. It is between 0.8 eV for lowest and 140 eV for highest  $E/N$  used, respectively, divided into the above-mentioned number of equally sized cells. The LoKI-MC simulations follow the dynamics of an ensemble of  $2 \times 10^5$  electrons. After the electron swarm relaxes to a stationary state, the transport coefficients are calculated by averaging over all electrons at  $10^5$  fixed time instants. The standard deviation for the coefficients shown in this work is always below 1%. For more details, see section 2.6 of [43].

The electron transport coefficients collected from literature have been presented already in a previous publication [7]. Briefly, they are the electron drift velocity  $v_D$  [45–54], the reduced mobility  $\mu N$  [45], the characteristic energy  $\varepsilon_{\text{char}} = D_T/\mu$  [55, 56], the reduced Townsend coefficient  $\alpha/N$  [57, 58], the reduced attachment coefficient  $\eta/N$  [55, 57–60] and the reduced effective Townsend coefficient, defined as the difference of the latter two [47, 57, 58]. Here,  $N$  is the total gas number density,  $\mu$  the electron mobility,  $D_T$  the transverse diffusion coefficient,  $\alpha$  the Townsend coefficient and  $\eta$  the attachment coefficient. When not given explicitly, the reduced mobility is calculated from  $\mu N = v_D N/E$  with  $E$  being the electric field. In contrast to the space-homogeneous two-term Boltzmann solver LoKI-B, MC and density gradient expansion codes can also provide the reduced longitudinal diffusion coefficient  $D_L N$  [52, 61], allowing to extend the validation to one more parameter, and bulk transport parameters for comparison with the experimental values for high  $E/N$  values.

Special attention should be taken on how the transport coefficients are measured to optimally compare them with calculations. On the one hand, in time-of-flight (TOF) experiments the electron number is growing in time. Drift velocity and diffusion coefficients are measured in TOF conditions. On the other hand, Townsend and attachment coefficients are usually measured in so-called steady-state Townsend (SST) conditions, i.e. with the electron number growing in space. Both TOF and SST measurements usually yield bulk transport coefficients [62, 63].<sup>2</sup>

In the calculations, the measurements are emulated by making use of the concepts of *temporal/spatial growth* as introduced by Hagelaar and Pitchford [64], where first the energy dependence of the electron distribution function is separated from the time- and space-dependent electron density  $n_e$ , and it is either assumed that  $n_e$  grows exclusively in time with a net production frequency or in space with a constant net spatial grow rate [64]. These concepts are borrowed by LoKI-B [28]. On the contrary, the current version of LoKI-MC simulates only TOF configurations. However, the Townsend and attachment coefficients in SST conditions can be derived from the TOF bulk parameters using the approximate relation presented in equation (3.32).

Figure 4.4 demonstrates the agreement between the calculated transport coefficients (lines) with the

---

<sup>2</sup>The arrival time-spectra drift velocity of Hasegawa, Date, and Shimozuma [47] can be converted to bulk data following the corrections in [62].

experimentally determined ones from literature (markers). Please pay attention that  $\mu N$  and  $(\alpha - \eta)/N$  (both  $y$ -axis labels on the right) are plotted linearly while all other parameters are presented in logarithmic scale. Whenever known, the uncertainty of the experimental electron transport coefficients is shown as error bars. From top to bottom,  $v_D$ ,  $\mu N$ ,  $\varepsilon_{\text{char}}$ ,  $\alpha/N$ ,  $(\alpha - \eta)/N$  and  $\eta/N$  are plotted. Note that compared to [7], the  $E/N$  range below 9 Td is not shown since no difference is observable there between the isotropic and anisotropic sets and for better visibility of the differences of the remaining data. We refer to [7] for a discussion of the electron transport coefficients. According to the discussion in the preceding paragraph and as indicated by the arrows in the centre two panels,  $v_D$ ,  $\mu N$  and  $\varepsilon_{\text{char}}$  are calculated under TOF conditions with temporal growth of the electron number while  $\alpha/N$ ,  $(\alpha - \eta)/N$  and  $\eta/N$  are calculated under SST conditions with spatial growth of the electron number.

In figure 4.4, we see how the good agreement of the calculation using the isotropic set in LoKI-B (solid green line) with the experimental values is further improved when the anisotropy of the rotational collisions is taken into account (dashed magenta line). In particular, excellent accordance is found now in  $\mu N$  and  $\varepsilon_{\text{char}}$ . The calculated values of  $\alpha/N$  and  $\eta/N$  agree very well with the experiment and are rather similar for both sets, except for a small shift in  $\eta/N$  for  $E/N$  below 70 Td, comparable with the dispersion of the experimental points. Moreover, it should be noted that effects of anisotropic scattering for rotational collisions appear to be relevant still for  $E/N > 80$  Td, see also section 4.7. This is an important difference with respect to results obtained for electrons in CO [6], where anisotropic scattering is relevant only for  $E/N < 5$  Td. It is related to the different dipole moment magnitude, i.e. 0.728 for H<sub>2</sub>O compared with 0.0432 for CO, and to the shape of elastic MTCSSs for the two molecules.

A just as excellent agreement with experimental data can be seen in figure 4.4 when using LoKI-MC. In particular, the flux results from LoKI-MC (dash-dotted blue line) almost perfectly align with the anisotropic results obtained from LoKI-B.

When ionization and attachment start to play a major role, the split between the flux and bulk components (dotted light blue line) can be evidenced from  $\mu N$  for  $E/N > 100$  Td in figure 4.4. In fact, within a careful analysis these details can be accounted for [62, 65]. However, considering the overall spread of the experimental data, it is noted that both flux and bulk calculated components follow the experiments fairly well with about 20 % difference between the two. In total, it is the agreement with the bulk parameters, despite the fact that they were not considered in the previous work, that should be emphasized.

The experimental longitudinal diffusion coefficient times gas number density  $D_L N$  is plotted in figure 4.5 against the reduced electric field, together with calculation results from LoKI-MC, using both the anisotropic and isotropic sets. Although the results with the isotropic set are satisfactory, the rigorous inclusion of anisotropic scattering remarkably improves the agreement with experiment for  $E/N$  below 100 Td. Furthermore, it should be emphasized that the proposed CS set gives good agreement (i) with

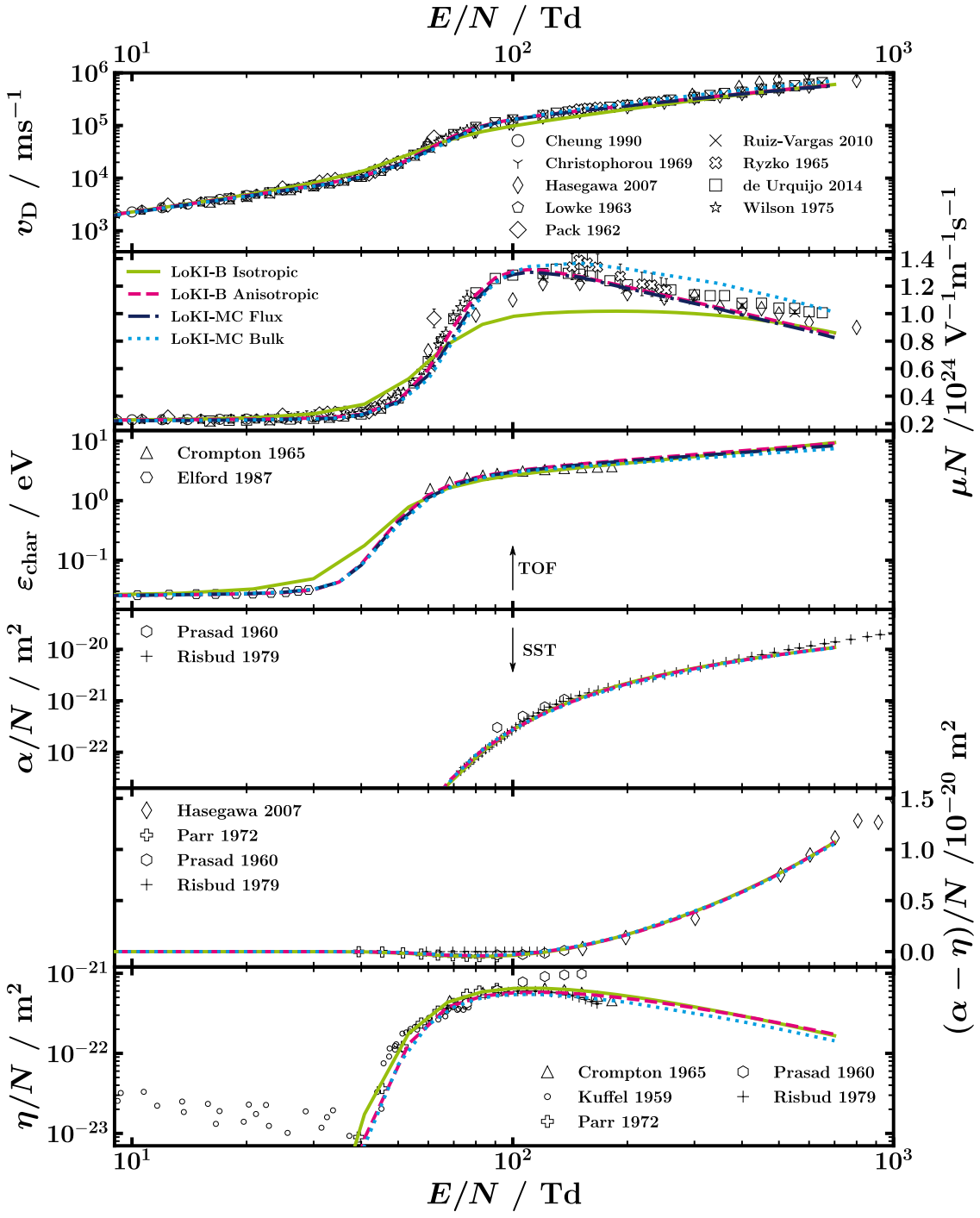


**Figure 4.4:** Comparison of experimental transport coefficients (markers), when known with error bars, with those obtained from LoKI-B or LoKI-MC simulations with the proposed isotropic [7] and anisotropic cross section sets (lines). References to the experimental transport coefficients can be found in the text. As indicated by the arrows in the centre two panels,  $v_D$ ,  $\mu N$  and  $\epsilon_{\text{char}}$  are calculated assuming temporal growth of the electron number while for  $\alpha/N$  and  $\eta/N$  spatial growth is assumed. LoKI-B provides exclusively flux transport coefficients and all shown LoKI-MC results include anisotropic rotational scattering.

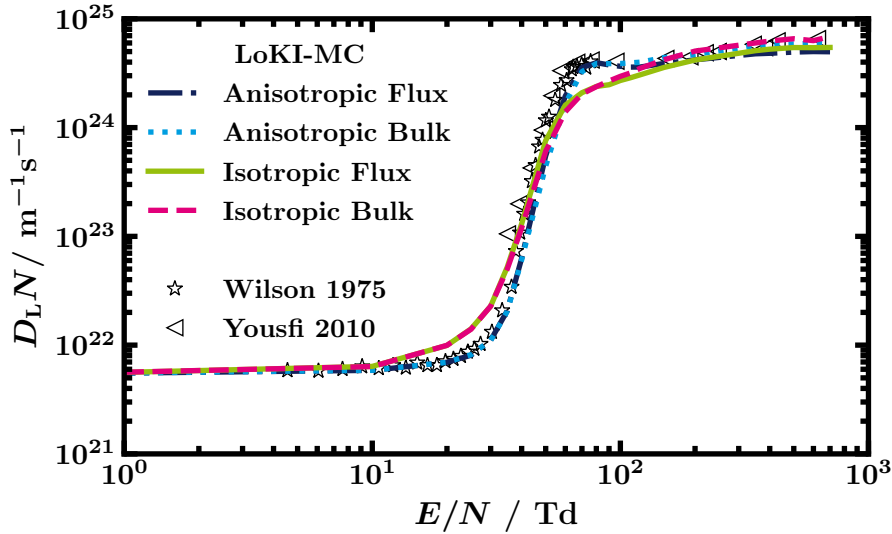


**Figure 4.5:** Longitudinal diffusion coefficient times gas number density  $D_L N$  against the reduced electric field  $E/N$  in water vapour from literature and calculations with Monte Carlo simulation tool LoKI-MC [52, 61].

a transport coefficient that at no point has been used for the optimization of the set, as it is not accessible with the used two-term code, and (ii) using the Monte Carlo instead of the two-term approach. It is worth highlighting that the second point is not guaranteed when using a CS set optimized with the two-term approximation in a more accurate methodology like MC simulation [66]. In figure 4.6, we also show that the EEDFs for both calculation methods agree very well. This underlines the validity and wide applicability of the proposed CS set.

## 4.7 The importance of rotational collisions in H<sub>2</sub>O

The preceding section demonstrates the substantial impact of rotational collisions on electron transport coefficients, spanning a range from low to high values of  $E/N$ . The importance of rotations is well evidenced in Figure 4.7, which illustrates the normalized electron power-transfer among different collisional channels. Notably, up to an  $E/N$  of around 30 Td, rotational collisions dominate the electron power losses. Beyond this value, the power loss is characterized by the presence of vibrational, electronic, attachment and ionization collisions, each process appearing in that order.

Interestingly, the characteristic energy shown in figure 4.4 is closely linked to the profile of electron power losses in rotational collisions. This connection offers additional evidence for the pronounced role of rotations in water. Furthermore, it justifies the relevance of appropriately considering the strongly anisotropic scattering that arises from dipole rotational collisions in H<sub>2</sub>O.

The fact that the two-term approximation yields accurate results in H<sub>2</sub>O might appear surprising. This is noteworthy given that the two-term approximation is expected to break down when inelastic

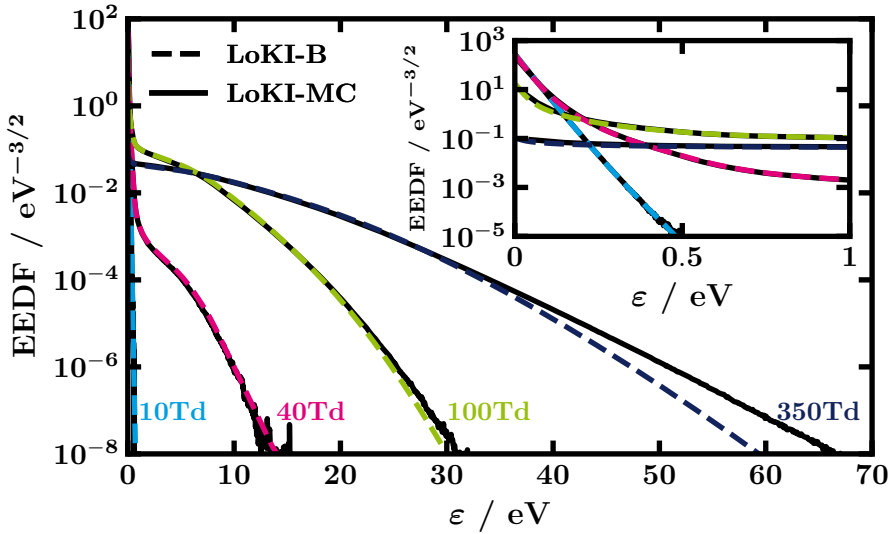


**Figure 4.6:** EEDFs of water vapour as calculated with the present cross sections using either LoKI-B (dashed) or LoKI-MC (solid) for four different reduced electric fields. The inset on the top right shows the very low energy part of the same EEDFs.

processes dominate over elastic processes and, across a wide range of  $E/N$  values, rotational collisions indeed surpass elastic collisions, as illustrated in figure 4.2 on the left. To further analyze this question, figure 4.8 depicts the ratio of the lower-order anisotropies, averaged over all energies, denoted as  $\frac{\langle |f_{1,2}| \rangle}{\langle f_0 \rangle} \equiv \int_0^\infty |f_{1,2}(\epsilon)| d\epsilon / \int_0^\infty f_0(\epsilon) d\epsilon$ , which are calculated using LoKI-MC. Notably, the ratio  $\frac{\langle |f_2| \rangle}{\langle f_0 \rangle}$  remains below 0.1 for  $E/N \leq 100$  Td. However, due to the very low energy threshold of many rotational excitations, sometimes around  $10^{-4}$  eV, the energy transferred per collision in this type of inelastic excitation is also minimal. Consequently, rotational collisions tend to be quasi-elastic processes, thus justifying the sufficiency of the two-term approximation.

## 4.8 Conclusion

Even though water molecules are frequently encountered in many innovative plasma applications, there is room for improvement of the H<sub>2</sub>O-electron collision cross sections which are required for the determination of the EEDF. In particular, since water molecules are asymmetric-top rotors with permanent dipole moment, the rigorous inclusion of electron-impact rotational collisions is rather challenging.

In a previous work [7], we presented a complete cross section set for H<sub>2</sub>O, under the typical isotropic assumption present in most electron Boltzmann two-term solvers. Since the rotational collisions in H<sub>2</sub>O are highly anisotropic, the corresponding cross sections were artificially decreased in [7] so as to diminish the momentum transfer due to these processes. This approach was validated against experimental measurements, but there were still visible deviations between the calculations and the experimental data in the reduced mobility and the characteristic energy.

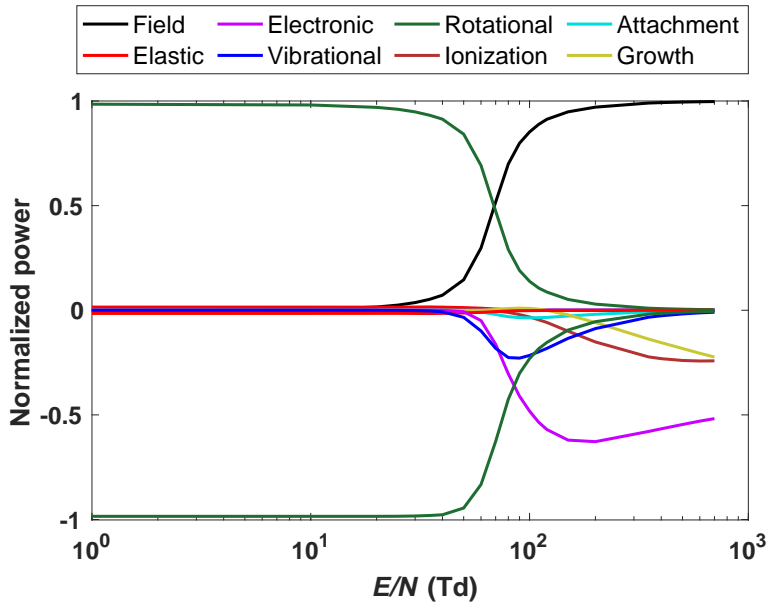


**Figure 4.7:** Normalized electron power transferred to various channels in  $\text{H}_2\text{O}$ , as a function of the reduced electric field. The positive and negative values correspond, respectively, to electron energy gain and loss.

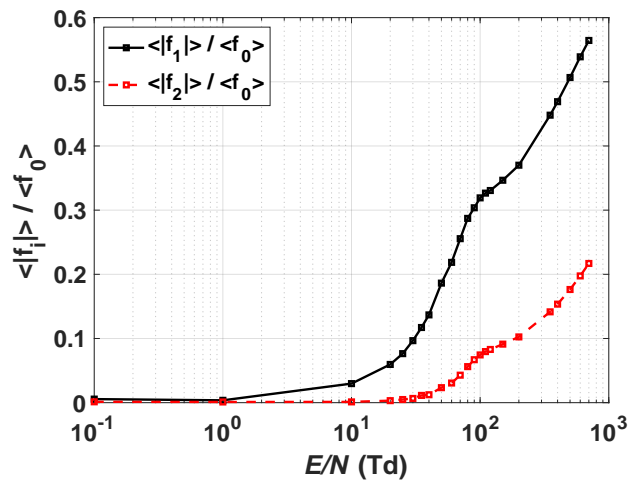


**Figure 4.8:** Average anisotropy ratios in  $\text{H}_2\text{O}$ , as a function of  $E/N$ :  $\frac{\langle |f_1| \rangle}{\langle f_0 \rangle}$  (black full lines);  $\frac{\langle |f_2| \rangle}{\langle f_0 \rangle}$  (red dashed).

In this work, we pursued a different path and included the influence of anisotropic electron scattering in rotational collisions. Without modifying the cross section of any other process besides rotations and using directly the rotational cross sections from dipole-Born theory, the agreement with experiment for the mobility and the characteristic energy is now excellent.

The usage of the Monte Carlo simulations code LoKI-MC allowed us to gain insight into the applicability of the present cross section set. First, we could verify that the electron transport coefficients calculated with the two-term Boltzmann solver LoKI-B agree very well with the MC solution, both when using the isotropic or the anisotropic sets. Note that this agreement is somewhat coincidental and not due to a firm physical background, although this might be related with the very low energy thresholds for rotational excitations in water, as discussed in section 4.7. We conclude that there is a de facto a posteriori verification that the two-term approximation yields accurate results with the developed cross section set for H<sub>2</sub>O and that the set is not exclusively suited for use in two-term Boltzmann solvers but also in the more accurate MC simulation method.

Additionally, we could extend the validation to parameters that cannot be obtained by LoKI-B, such as the bulk transport coefficients or the longitudinal diffusion coefficient. The excellent agreement between LoKI-MC calculations and measurements of the latter, that were not considered in our previous analysis, is a further confirmation of the validity of the present cross section set.

This work shows that the correct treatment of the angular distribution of the scattered electrons is essential to have an accurate description of electron swarms in water. This can be easily handled with the two open-source codes LoKI-B and LoKI-MC.

The cross section set developed here will be available in the IST-Lisbon database on LXCat, and can be used directly in LoKI-B and LoKI-MC to calculate more accurate electron distribution functions and the corresponding electron parameters, leading to more refined plasma-chemistry models. For codes where anisotropic scattering cannot be included, the cross section set presented in our previous work [7] remains useful data to describe the electron kinetics in systems containing water vapour.

In a future work, we plan to quantify the importance of anisotropic scattering for the main gases of interest in the plasma community.

## References

- [1] Budde, M., Dias, T. C., Vialletto, L., Pinhão, N., Guerra, V., and Silva, T. 2023 “Electron-neutral collision cross sections for H<sub>2</sub>O: II. Anisotropic scattering and assessment of the validity of the two-term approximation” *J. Phys. D: Appl. Phys.* **56**, 255201.
- [2] Reid, I. 1979 “An Investigation of the Accuracy of Numerical Solutions of Boltzmann’s Equation for Electron Swarms in Gases with Large Inelastic Cross Sections” *Aust. J. Phys.* **32**, 231.

- [3] Phelps, A. V. and Pitchford, L. C. 1985 “Anisotropic scattering of electrons by N<sub>2</sub> and its effect on electron transport” *Phys. Rev. A* **31** (5), 2932–2949.
- [4] Casey, M. J. E., Cocks, D. G., Boyle, G. J., Brunger, M. J., Dujko, S., Urquijo, J. de, and White, R. D. 2019 “Thermal induced NDC of electron swarms in N<sub>2</sub> and N<sub>2</sub>-like gases: the role of temperature and collision operator approximations” *Plasma Sources Sci. Technol.* **28**, 115005.
- [5] Janssen, J. F. J., Pitchford, L. C., Hagelaar, G. J. M., and Dijk, J. van 2016 “Evaluation of angular scattering models for electron-neutral collisions in Monte Carlo simulations” *Plasma Sources Sci. Technol.* **25**, 055026.
- [6] Vialletto, L., Moussa, A. B., Dijk, J. v., Longo, S., Diomede, P., Guerra, V., and Alves, L. L. 2021 “Effect of anisotropic scattering for rotational collisions on electron transport parameters in CO” *Plasma Sources Sci. Technol.* **30**, 075001.
- [7] Budde, M., Dias, T. C., Vialletto, L., Pinhão, N., Guerra, V., and Silva, T. 2022 “Electron-neutral collision cross sections for H<sub>2</sub>O: I. Complete and consistent set” *J. Phys. D: Appl. Phys.* **55**, 445205.
- [8] Damen, M. A., Martini, L. M., and Engeln, R. 2020 “Vibrational quenching by water in a CO<sub>2</sub> glow discharge measured using quantum cascade laser absorption spectroscopy” *Plasma Sources Sci. Technol.* **29**, 095017.
- [9] Verheyen, C., Silva, T., Guerra, V., and Bogaerts, A. 2020 “The effect of H<sub>2</sub>O on the vibrational populations of CO<sub>2</sub> in a CO<sub>2</sub>/H<sub>2</sub>O microwave plasma: a kinetic modelling investigation” *Plasma Sources Sci. Technol.* **29**, 095009.
- [10] Médard, N., Soutif, J.-C., and Poncin-Epaillard, F. 2002 “CO<sub>2</sub>, H<sub>2</sub>O, and CO<sub>2</sub>/H<sub>2</sub>O Plasma Chemistry for Polyethylene Surface Modification” *Langmuir* **18**, 2246–2253.
- [11] Thorn, P., Campbell, L., and Brunger, M. 2009 “Electron excitation and energy transfer rates for H<sub>2</sub>O in the upper atmosphere” *PMC Phys. B* **2**, 1.
- [12] Bodewits, D., Országh, J., Noonan, J., Ďurian, M., and Matejčík, Š. 2019 “Diagnostics of Collisions between Electrons and Water Molecules in Near-ultraviolet and Visible Wavelengths” *Astrophys. J.* **885**, 167.
- [13] Micca Longo, G., Vialletto, L., Diomede, P., Longo, S., and Laporta, V. 2021 “Plasma Modeling and Prebiotic Chemistry: A Review of the State-of-the-Art and Perspectives” *Molecules* **26**, 3663.
- [14] Giardina, A., Tampieri, F., Biondo, O., Marotta, E., and Paradisi, C. 2019 “Air non-thermal plasma treatment of the herbicides mesotrione and metolachlor in water” *Chem. Eng. J.* **372**, 171–180.
- [15] Meunier, N., Laribi, S., Dubois, L., Thomas, D., and De Weireld, G. 2014 “CO<sub>2</sub> Capture in Cement Production and Re-use: First Step for the Optimization of the Overall Process” *Energy Procedia* 12th International Conference on Greenhouse Gas Control Technologies, GHGT-12 **63**, 6492–6503.

- [16] Chang, Y., Mendrea, B., Sterniak, J., and Bohac, S. V. 2016 “Effect of Ambient Temperature and Humidity on Combustion and Emissions of a Spark-Assisted Compression Ignition Engine” *J. Eng. Gas Turbines Power* **139**.
- [17] Šimečková, M., Jacquemart, D., Rothman, L. S., Gamache, R. R., and Goldman, A. 2006 “Einstein A-coefficients and statistical weights for molecular absorption transitions in the HITRAN database” *J. Quant. Spectrosc. Radiat. Transf.* **98**, 130–155.
- [18] Itikawa, Y. 1972 “Rotational Transition in an Asymmetric-Top Molecule by Electron Collision: Applications to H<sub>2</sub>O and H<sub>2</sub>CO” *J. Phys. Soc. Jpn.* **32**, 217–226.
- [19] Gianturco, F. A. and Jain, A. 1986 “The theory of electron scattering from polyatomic molecules” *Phys. Rep.* **143**, 347–425.
- [20] Crawford, O. H. 1967 “Scattering of Low-Energy Electrons from Polar Molecules” *J. Chem. Phys.* **47**, 1100–1104.
- [21] King, G. W., Hainer, R. M., and Cross, P. C. 1947 “Expected Microwave Absorption Coefficients of Water and Related Molecules” *Phys. Rev.* **71**, 433–443.
- [22] Shimamura, I. and Takayanagi, K. 2013 *Electron-molecule collisions* Berlin: Springer.
- [23] Takayanagi, K. 1966 “Rotational and vibrational excitation of polar molecules by slow electrons” *J. Phys. Soc. Jpn.* **21**, 507–514.
- [24] Pitchford, L. C. et al. 2013 “Comparisons of sets of electron–neutral scattering cross sections and swarm parameters in noble gases: I. Argon” *J. Phys. D: Appl. Phys.* **46**, 334001.
- [25] Makabe, T. and Petrović, Z. 2015 *Plasma electronics 2nd edn* New York: CRC.
- [26] Makabe, T. and Petrović, Z. 2014 *Plasma electronics: Applications in microelectronic device fabrication, second edition*, 1–369.
- [27] Klein, O. and Rosseland, S. 1921 “Über Zusammenstöße zwischen Atomen und freien Elektronen” *Z. Physik* **4**, 46–51.
- [28] Tejero-del-Caz, A., Guerra, V., Gonçalves, D., Silva, M. L. d., Marques, L., Pinhão, N., Pintassilgo, C. D., and Alves, L. L. 2019 “The LisbOn KInetics Boltzmann solver” *Plasma Sources Sci. Technol.* **28**, 043001.
- [29] Longo, S. 2000 “Monte Carlo models of electron and ion transport in non-equilibrium plasmas” *Plasma Sources Sci. Technol.* **9**, 468–476.
- [30] Faure, A., Gorfinkel, J. D., and Tennyson, J. 2004a “Electron-impact rotational excitation of water” *Mon. Not. R. Astron. Soc.* **347**, 323–333.
- [31] Song, M.-Y., Cho, H., Karwasz, G. P., Kokouline, V., Nakamura, Y., Tennyson, J., Faure, A., Mason, N. J., and Itikawa, Y. 2021 “Cross Sections for Electron Collisions with H<sub>2</sub>O” *J. Phys. Chem. Ref. Data* **50**, 023103.

- [32] Magboltz 11.9 <https://magboltz.web.cern.ch/magboltz/>, r. o. M. 1. 2022 *Transport of electrons in gas mixtures*.
- [33] Seng, G. and Linder, F. 1976 “Vibrational excitation of polar molecules by electron impact. II. Direct and resonant excitation in H<sub>2</sub>O” *J. Phys. B: Atom. Mol. Phys.* **9**, 2539–2551.
- [34] Khakoo, M. A., Winstead, C., and McKoy, V. 2009 “Vibrational excitation of water by electron impact” *Phys. Rev. A* **79**, 052711.
- [35] Ralphs, K., Serna, G., Hargreaves, L. R., Khakoo, M. A., Winstead, C., and McKoy, V. 2013 “Excitation of the six lowest electronic transitions in water by 9–20 eV electrons” *J. Phys. B: At. Mol. Opt. Phys.* **46**, 125201.
- [36] Matsui, M., Hoshino, M., Kato, H., Silva, F. F. da, Limão-Vieira, P., and Tanaka, H. 2016 “Measuring electron-impact cross sections of water: elasticscattering and electronic excitation of the  $\tilde{\alpha}3B_1$  and  $\tilde{\Lambda}1B_1$  states” *Eur. Phys. J. D* **70**, 77.
- [37] Harb, T., Kedzierski, W., and McConkey, J. W. 2001 “Production of ground state OH following electron impact on H<sub>2</sub>O” *J. Chem. Phys.* **115**, 5507–5512.
- [38] Beenakker, C. I. M., de Heer, F. J., Krop, H. B., and Möhlmann, G. R. 1974 “Dissociative excitation of water by electron impact” *Chem. Phys.* **6**, 445–454.
- [39] Kedzierski, W., Derbyshire, J., Malone, C., and McConkey, J. W. 1998 “Isotope effects in the electron impact break-up of water” *J. Phys. B: At. Mol. Opt. Phys.* **31**, 5361–5368.
- [40] Triniti database [www.lxcat.net](http://www.lxcat.net), r. o. D. 9. 2021 *Triniti database*.
- [41] Itikawa database [www.lxcat.net](http://www.lxcat.net), r. o. D. 9. 2021 *Itikawa database*.
- [42] Faure, A., Gorfinkel, J. D., and Tennyson, J. 2004b “Low-energy electron collisions with water: elastic and rotationally inelastic scattering” *J. Phys. B: At. Mol. Opt. Phys.* **37**, 801–807.
- [43] Dias, T. C., Tejero-del-Caz, A., Alves, L. L., and Guerra, V. 2023 “The LisbOn KInetics Monte Carlo solver” *Comput. Phys. Commun.* **282**, 108554.
- [44] IST-Lisbon GitHub <https://github.com/IST-Lisbon>, r. o. D. 5. 2022 *IST-Lisbon GitHub*.
- [45] Cheung, B. and Elford, M. T. 1990 “The drift velocity of electrons in water vapour at low values of E/N” *Aust. J. Phys.* **43**, 755–763.
- [46] de Urquijo, J., Basurto, E., Juárez, A. M., Ness, K. F., Robson, R. E., Brunger, M. J., and White, R. D. 2014 “Electron drift velocities in He and water mixtures: Measurements and an assessment of the water vapour cross-section sets” *J. Chem. Phys.* **141**, 014308.
- [47] Hasegawa, H., Date, H., and Shimozuma, M. 2007 “Electron swarm parameters in water vapour” *J. Phys. D: Appl. Phys.* **40**, 2495–2498.
- [48] Lowke, J. J. and Rees, J. A. 1963 “The Drift Velocities of Free and Attached Electrons in Water Vapour” *Aust. J. Phys.* **16**, 447–453.

- [49] Pack, J. L., Voshall, R. E., and Phelps, A. V. 1962 “Drift Velocities of Slow Electrons in Krypton, Xenon, Deuterium, Carbon Monoxide, Carbon Dioxide, Water Vapor, Nitrous Oxide, and Ammonia” *Phys. Rev.* **127**, 2084–2089.
- [50] Ruíz-Vargas, G., Yousfi, M., and de Urquijo, J. 2010 “Electron transport coefficients in the mixtures of H<sub>2</sub>O with N<sub>2</sub>, O<sub>2</sub>, CO<sub>2</sub> and dry air for the optimization of non-thermal atmospheric pressure plasmas” *J. Phys. D: Appl. Phys.* **43**, 455201.
- [51] Ryzko, H. 1965 “Drift velocity of electrons and ions in dry and humid air and in water vapour” *Proc. Phys. Soc.* **85**, 1283–1295.
- [52] Wilson, J. F., Davis, F. J., Nelson, D. R., Compton, R. N., and Crawford, O. H. 1975 “Electron transport and ion clustering reactions in water vapor and deuterated water vapor” *J. Chem. Phys.* **62**, 4204–4212.
- [53] Christophorou, L. G. and Christodoulides, A. A. 1969 “Scattering of thermal electrons by polar molecules” *J. Phys. B: Atom. Mol. Phys.* **2**, 71–85.
- [54] Bailey, V. A. and Duncanson, W. E. 1930 “XIV. On the behaviour of electrons amongst the molecules NH<sub>3</sub>, H<sub>2</sub>O, and HCl” *Lond. Edinb. Dublin philos. mag. j. sci.* **10**, 145–160.
- [55] Elford, M. T. 1987 “The Radio DT/ for Electrons in Water Vapour at 294K and Low E/n Values” *Proceedings of the XVIII International Conference on the Phenomena in Ionized Gases* Swansea, Wales: Hilger, London, 130.
- [56] Crompton, R. W., Rees, J. A., and Jory, R. L. 1965 “The diffusion and attachment of electrons in water vapour” *Aust. J. Phys.* **18**, 541.
- [57] Risbud, A. V. and Naidu, M. S. 1979 “Ionization and Attachment in Water Vapour and Ammonia” *J. Phys. Colloques* **40**, C7–C7–78.
- [58] Prasad, A. N. and Craggs, J. D. 1960 “Measurement of Ionization and Attachment Coefficients in Humid Air in Uniform Fields and the Mechanism of Breakdown” *Proc. Phys. Soc.* **76**, 223–232.
- [59] Kuffel, E. 1959 “Electron Attachment Coefficients in Oxygen, Dry Air, Humid Air and Water Vapour” *Proc. Phys. Soc.* **74**, 297–308.
- [60] Parr, J. E. and Moruzzi, J. L. 1972 “Electron attachment in water vapour and ammonia” *J. Phys. D: Appl. Phys.* **5**, 514–524.
- [61] Yousfi, M., Bekstein, A., Merbahi, N., Eichwald, O., Ducasse, O., Benhenni, M., and Gardou, J. P. 2010 “Basic data for atmospheric pressure non-thermal plasma investigations in environmental and biomedical applications” *Plasma Sources Sci. Technol.* **19**, 034004.
- [62] Ness, K. F., Robson, R. E., Brunger, M. J., and White, R. D. 2012 “Transport coefficients and cross sections for electrons in water vapour: Comparison of cross section sets using an improved Boltzmann equation solution” *J. Chem. Phys.* **136**, 024318.

- [63] Robson, R. E., White, R. D., and Ness, K. F. 2011 “Transport coefficients for electrons in water vapor: Definition, measurement, and calculation” *J. Chem. Phys.* **134**, 064319.
- [64] Hagelaar, G. J. M. and Pitchford, L. C. 2005 “Solving the Boltzmann equation to obtain electron transport coefficients and rate coefficients for fluid models” *Plasma Sources Sci. Technol.* **14**, 722–733.
- [65] Kawaguchi, S., Takahashi, K., Satoh, K., and Itoh, H. 2016 “Electron transport analysis in water vapor” *Jpn. J. Appl. Phys.* **55**, 07LD03.
- [66] Petrović, Z. L., Dujko, S., Marić, D., Malović, G., Nikitović, Ž., Šašić, O., Jovanović, J., Stojanović, V., and Radmilović-Radenović, M. 2009 “Measurement and interpretation of swarm parameters and their application in plasma modelling” *J. Phys. D: Appl. Phys.* **42**, 194002.



# 5

## Exploring the electron kinetics under magnetic field and AC/DC electric fields

### Chapter summary

This chapter presents a numerical study of the electron kinetics under AC/DC electric fields and DC magnetic fields crossed at arbitrary angles. The physical phenomena are studied both in model gases (Reid-ramp and Lucas-Saelee) and in real gases ( $N_2$  and Ar). The simulations are carried out with an upgraded version of the Monte Carlo open-source code LoKI-MC.

The code is compared against several independent benchmark calculations available in the literature. In addition, new benchmark calculations for electron kinetics solvers are produced in conditions of co-existent AC electric and DC magnetic fields, accounting for the effect of the crossing angle between the fields and discriminating the evolution along the AC cycle.

The role of the magnetic field is discussed, distinguishing the configurations with DC and AC electric fields. In DC electric fields, the oscillatory motion caused by the magnetic field decreases the efficiency of the electron acceleration, which manifests on the power absorbed by the electric field and on the electron mean energy. Notably, an exceptional behavior is found in Ar for small regions of  $E/N$  and  $B/N$ , where: for constant  $B/N$ , the mean energy decreases with increasing  $E/N$ ; and, for constant  $E/N$ , it increases with increasing  $B/N$ . These phenomena were firstly reported by Ness and Makabe in 2000 and are now confirmed by means of Monte Carlo simulations. In AC electric fields, when the electron cyclotron frequency is similar to the angular frequency of the electric field, the synchronization of the cyclotron motion with the electric field enhances electron acceleration, through the well-known electron cyclotron resonance. However, for conditions where the mean collision frequency is much higher than the cyclotron frequency, the synchronization tends to breakdown and the magnetic field is detrimental for the electron acceleration, as in the DC electric field case.

All results presented in this chapter have been published in [1].

## 5.1 Introduction

The first version of LoKI-MC addressed only configurations with constant electric field and null magnetic field, as presented in chapter 3. However, the study of the electron kinetics under the simultaneous influence of electric and magnetic fields is relevant not only from the theoretical point of view, but also due to the practical applications on the modelling of LTP, such as: magnetron sputtering [2], plasma propulsion [3, 4] and inductively coupled discharges [5]. The theoretical efforts made in the recent decades are reviewed in [6–9]. The electron transport in these conditions has been studied in various gases, *e.g.*: Ar[10–12], CH<sub>4</sub> [10, 13–15], O<sub>2</sub> [9, 16], N<sub>2</sub> [17–19] and CF<sub>4</sub> [8].

Although the literature is relatively vast, to the best of our knowledge, the community is still lacking a flexible electron kinetics open-source solver, not depending on the low-anisotropy assumption, able to easily address such configurations. Herein, we extend the formulation implemented in LoKI-MC to AC/DC electric fields together with DC magnetic fields crossed at arbitrary angles.

The implementation of this significant additional feature requires an extensive benchmark/verification, besides the one already done in our previous work for DC electric fields [20]. The benchmark procedure for the verification of electron kinetics solvers is very well established in the LTP community. The use of gas models with analytical cross sections is fundamental to assure that the differences between the results obtained with different codes/formulations do not stem from the input data. The most popular ones are the Reid-ramp model [21] and the Lucas-Saelee model [22]. Albeit simple, they can capture the main features evidenced in real gases, while showing the limitations of the low-anisotropy approximation. Along the last decades, two groups from Australia [23–25] and Serbia [6, 9, 26, 27] made very important contributions to the publication of reference calculations in diverse conditions, using either Monte Carlo or multi-term formulations. For the conditions of interest in this work, some examples of such calculations are: (i) AC electric and null magnetic fields [23, 24]; (ii) DC electric and DC magnetic fields [25–27]; (iii) AC electric and DC magnetic fields [9].

The purpose of the present work is clear and threefold: (i) present and verify an upgraded version of LoKI-MC, accounting for DC magnetic and AC/DC electric fields, comparing it against previous independent benchmark calculations, reinforcing the confidence on the present code and on the past calculations; (ii) extend the set of benchmarks available in the literature to assess the influence of other physical parameters, specially in conditions involving coexistence of AC electric fields and DC magnetic fields; (iii) gain insight into the underlying physics of the electron swarm kinetics in these configurations, with emphasis on the phenomenon of electron-cyclotron resonance. The kinetic effects are explored not only in the Reid-ramp and Lucas-Saelee models, but also in real gases, both molecular (N<sub>2</sub>) and atomic (Ar). The updates in LoKI-MC discussed in this work are included in the open-source distribution of the code and are freely available to the community [20].

This chapter is organized as follows: section 5.2 summarizes the generalization of LoKI-MC to AC/DC

electric fields and DC magnetic fields; section 5.3 presents the results using model and real gases, and discusses the physical phenomena involved; section 5.4 closes this work with the main conclusions and prospects for future work.

## 5.2 Electron free flight under electric and magnetic fields

The Monte Carlo formulation employed in LoKI-MC has been presented in chapter 3, initially restrained to DC electric fields and null magnetic fields. In this chapter, we relax the applicability to AC/DC electric and DC magnetic fields. The generalization is straightforward, where the main change is on the integration of the electron motion during the time-interval between collisions ( $t_c$ ).

The electron position ( $\mathbf{r}$ ) and velocity ( $\mathbf{v}$ ) are advanced during  $t_c$  by integrating analytically the Newton equations of motion, under the influence of an electric field ( $\mathbf{E}$ ) and a magnetic field ( $\mathbf{B}$ ):

$$m_e \frac{d\mathbf{v}}{dt} = -e(\mathbf{E} + \mathbf{v} \times \mathbf{B}) \quad , \quad \frac{d\mathbf{r}}{dt} = \mathbf{v} , \quad (5.1)$$

where  $e$  and  $m_e$  are the electron charge and mass, respectively. Here,  $\mathbf{E}$  can be either AC or DC,  $\mathbf{B}$  is constant, and the fields are crossed at an arbitrary angle  $\Psi \in [0, 180^\circ]$ :

$$\mathbf{E}(t) = (E_{x,0}\mathbf{e_x} + E_{z,0}\mathbf{e_z}) \cos(\omega t) \quad , \quad \mathbf{B} = B\mathbf{e_z} , \quad (5.2)$$

where  $\omega = 2\pi f$  is the angular frequency of the field,  $E_{x,0} = \sin \Psi E_0$ ,  $E_{z,0} = \cos \Psi E_0$  and  $E_0$  is the electric field amplitude. The analytical solutions for the propagation of  $\mathbf{r}$  and  $\mathbf{v}$ , from an time-instant  $t_0$  up to  $t_0 + t_c$ , are presented in appendix 5.A, together with other particular cases, such as  $\omega = 0$ ,  $B = 0$  and  $\omega = \Omega = eB/m_e$  (electron cyclotron resonance). Take note that the angle  $\Psi$  could be taken between 0 and  $90^\circ$ , since extension to  $90$  and  $180^\circ$  can be made through use of symmetry properties [28]. However, we let it lie between 0 and  $180^\circ$  as the complexity of the equations of motion does not change.

## 5.3 Results and discussion

This section presents and discusses results of the electron swarm kinetics in the presence of a magnetic field. The MC simulations are run with  $10^4 - 10^6$  electrons and each electron performs typically between  $10^4$  and  $10^6$  collision-free flights. All simulations assume isotropic collisional scattering and consider a gas density  $N = 3.54 \times 10^{22} \text{ m}^{-3}$  and gas temperature  $T_g = 300 \text{ K}$ , unless mentioned otherwise. However, the results presented here are independent of the value used for the gas density, with exception of section 5.3.2.

In this work, we consider two well-known model gases: Reid-ramp [21] and Lucas-Saelee [22]. The

Reid-ramp model [21] is constituted by the following elastic and excitation cross sections:

$$\begin{cases} \sigma_{\text{el}} = 6 \times 10^{-20} \text{ m}^2 \\ \sigma_{\text{exc}} = (u - 0.2) \times 10^{-19} \text{ m}^2 \end{cases}, \quad (5.3)$$

where the electron energies  $u$  are given in eV and the threshold of the excitation cross section is 0.2 eV. The Lucas-Saelee [22] model is composed by elastic, excitation and ionization cross sections:

$$\begin{cases} \sigma_{\text{el}} = 4u^{-1/2} \times 10^{-20} \text{ m}^2 \\ \sigma_{\text{exc}} = 0.1(1 - F)(u - 15.6) \times 10^{-20} \text{ m}^2 \\ \sigma_{\text{ion}} = 0.1F(u - 15.6) \times 10^{-20} \text{ m}^2 \end{cases}, \quad (5.4)$$

where the threshold of the excitation and ionization cross sections is 15.6 eV, and  $F \in [0, 1]$  is a parameter controlling the intensity of ionization. In the Reid-ramp model, the heavy species mass is  $M = 4$  a.m.u., whereas in Lucas-Saelee,  $M = 1000 m_e$ . In both models, the thermal motion of the heavy species is not considered. Notice that Ness and Robson [29] extended the Lucas-Saelee model to include as well an attachment process. For simplicity, we do not consider it here, since LoKI-MC already passed this benchmark test in conditions of DC electric field and null magnetic field, as presented in section 3.4.1.

For both DC and AC electric fields, we start by benchmarking LoKI-MC results against previously published calculations, using the Reid-ramp and Lucas-Saelee model gases. We also employ the Reid-ramp model in different conditions from those available in the literature, exploring the angle between the fields and evidencing that the dynamics is ruled only by density-reduced quantities. These results constitute additional benchmark calculations for verification of future codes. Then, we study the electron kinetics in real gases - N<sub>2</sub> and Ar - using the cross-section sets available at the IST-Lisbon database of LXCat [30]. For more details on these cross sections, see sections 4.4.2 and 4.5 of [20]. Lastly, let us note that the present calculations also agree very well with the available benchmark results for AC electric fields and null magnetic fields, as shown in appendix 5.B.

### 5.3.1 DC electric field

This subsection studies the effect of the magnetic field together with a DC electric field. First, we need to assure that LoKI-MC passes the typical benchmark tests. Figure 5.1 shows a comparison between the present calculations and the MC results of Raspopovic et al. [26], using the Reid-ramp model, for  $E/N = 12$  Td (1 Td = Townsend =  $10^{-21}$  Vm<sup>2</sup>) and different  $B/N$  (1 Hx = Huxley =  $10^{-27}$  Tm<sup>3</sup>), with the electric field **E** perpendicular to the magnetic field **B** ( $\Psi = 90^\circ$ ). The mean energy  $\langle \epsilon \rangle$  and the non-null components of the drift velocity  $v_{d,i}$  and the diffusion matrix  $ND_{ij}$  agree remarkably well with [26]. For the reference frame used in this work, the Hall diffusion coefficient is defined as:  $D_{\text{Hall}} = -(D_{xy} + D_{yx})$  [25]. For an extended interpretation of these results, the reader is referred to [25, 26]. We point out that, with increasing  $B/N$ , the electrons become magnetized and (i) the electron energy is

strongly reduced due to a smaller efficiency of the electric-field acceleration, (ii) the drift velocity along  $\mathbf{E}$  decreases and a component along  $\mathbf{E} \times \mathbf{B}$  arises, (iii) the diffusion perpendicular to  $\mathbf{B}$  is damped, while in the parallel direction barely changes.

Note that, since the Reid-ramp model conserves the number of electrons, flux and bulk components are equivalent. To verify the effect of non-conservative processes, as well as the angle between  $\mathbf{E}$  and  $\mathbf{B}$ , we employ the Lucas-Saelee model for different ionization factors  $F$  and angles  $\Psi$ , comparing with the MC results of Dujko et al. [27]. The electron mean energy  $\langle \epsilon \rangle$ , bulk drift speed  $\|v_d^b\|$  and ionization coefficient  $k_{\text{ion}}$  are shown in figure 5.2, as a function of  $\Psi$ , for  $E/N = 10$  Td,  $B/N = 200, 1000$  Hx and  $F = 0, 0.5, 1$ . There is an excellent agreement between the present results and the ones reported in [27]. Although not shown here, the accordance in the three components of  $\mathbf{v}_d^b$  is also very good<sup>1</sup>. Concerning the influence of ionization, we find that with increasing  $F$ ,  $\langle \epsilon \rangle$  decreases, while  $\|v_d^b\|$  and  $k_{\text{ion}}$  increase. Additionally, as in the previous case, a higher  $B/N$  leads to a lower  $\langle \epsilon \rangle$ . The effect of  $\mathbf{B}$  is null/maximal, when  $\mathbf{B}$  is parallel/perpendicular to  $\mathbf{E}$ , as expected. The flux drift speed  $\|v_d^f\|$  is not shown here but, for all values of  $F$ , is identical to  $\|v_d^b\|$  for  $F = 0$ , as it does not depend on the change of the electron number.

After the verification in model gases shown in figures 5.1 and 5.2, we focus now on the electron swarm kinetics in real gases ( $\text{N}_2$  and Ar), keeping  $\mathbf{E}$  perpendicular to  $\mathbf{B}$  ( $\Psi = 90^\circ$ ). Figures 5.3a and 5.3b present the electron mean energy  $\langle \epsilon \rangle$  and reduced Townsend coefficient  $\alpha/N$ , as function of  $E/N$  and  $B/N = 0 - 3000$  Hx, for  $\text{N}_2$  and Ar, respectively. For  $\text{N}_2$ , the calculated values of  $\alpha/N$  are in quite good agreement with the measurements of Heylen and Dargan [31]. Notice that the same comparison between calculated and measured  $\alpha/N$  has been performed with similar success in previous works [17, 18]. In both gases, the magnetic field decreases dramatically the energy of the electrons and, consequently,  $\alpha/N$ .

Figures 5.4a and 5.4b illustrate  $\langle \epsilon \rangle$  in wider conditions of  $E/N$  and  $B/N$ , for  $\text{N}_2$  and Ar, respectively. The variation of  $\langle \epsilon \rangle$  in  $\text{N}_2$  exhibits the expected behavior: for constant  $B/N$ , it increases monotonically with  $E/N$ , while for constant  $E/N$ , it decreases with increasing  $B/N$ . In Ar, the trend is generally similar, except for local regions where the opposite occurs: (i)  $\langle \epsilon \rangle$  decreases with increasing  $E/N$  and (ii)  $\langle \epsilon \rangle$  increases with increasing  $B/N$ . The first feature is well observed for  $B/N = 1000$  Hx in the 4 Td region. The second feature is evident in the crossing between the curves of  $B/N = 5000$  and  $10000$  Hx.

These interesting phenomena were reported for the first time in 2000 by Ness and Makabe [11]. Nevertheless, to the best of our knowledge, until now, it has not been confirmed by other authors, even though Ness and Makabe conclude the manuscript stating that the finding should be verified by an independent study, such as a Monte Carlo simulation investigation. For a detailed discussion of the physics behind this effect, the reader is referred to [11]. In short, the exceptional behavior in argon occurs due to the rapidly increasing magnitude of the elastic cross section after the Ramsauer minimum,

---

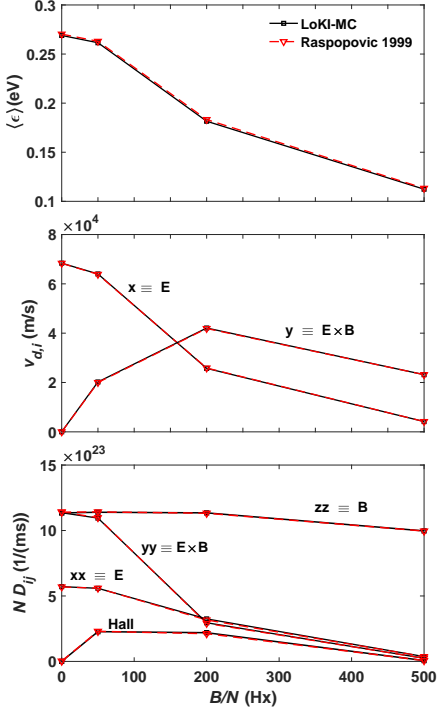
<sup>1</sup>Since Dujko et al. [27] use a different reference frame (D), the results need to be converted to the one used in this work:  $\mathbf{e}_x = \cos \Psi \mathbf{e}_y^D - \sin \Psi \mathbf{e}_z^D$ ;  $\mathbf{e}_y = \mathbf{e}_x^D$ ;  $\mathbf{e}_z = -\sin \Psi \mathbf{e}_y^D - \cos \Psi \mathbf{e}_z^D$ .

from  $\sim 0.25$  up to  $10$  eV, followed by the sudden appearance of strong inelastic processes after  $\sim 11$  eV, as illustrated in figure 5.5. For constant  $B/N$ , when  $E/N$  is increased, electrons are accelerated to energies where the collisionality increases significantly. For null and weak magnetic fields, this causes only a decrease in the  $\langle \epsilon \rangle$  slope. However, for  $B/N \gtrsim 500$  Hx, the magnetic field cooling is contributing somehow to enhance this effect, leading to small transient regions where  $\langle \epsilon \rangle$  decreases with  $E/N$ . The transient increase of  $\langle \epsilon \rangle$  with increasing  $B/N$  can be explained in a similar manner [11].

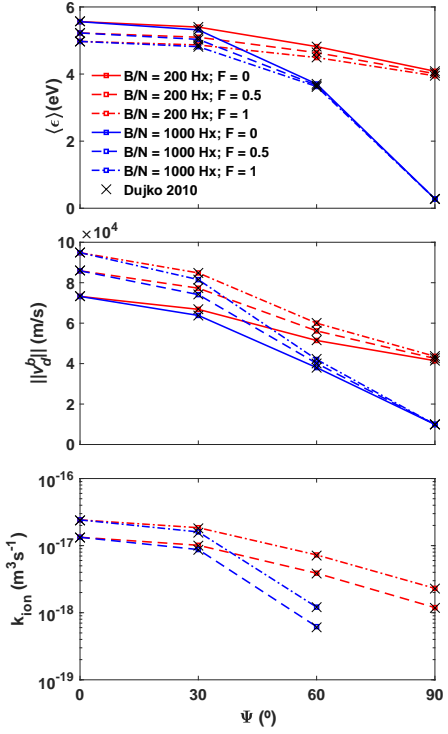
The black-dashed curves represent the MC solutions with  $B = 0$  and an effective AC electric field with the corresponding cyclotron frequency,  $\omega/N = \Omega/N = eB/(Nm_e)$ , and  $E_{\text{rms}}/N = E_{\text{DC},B \neq 0}/N$ . The similarity of these curves with the ones in the presence of a magnetic field shows that, from the energetic point of view, the effect of the magnetic field is approximately equivalent to the introduction of an AC component in the electric field, as expected (*cf.* equation 5.6 further below). Such behavior could also be predicted by inspecting the electron Boltzmann equation, under a low-anisotropy expansion on spherical harmonics over the velocity space and on the limit of very high frequencies, where the solution of the isotropic component of the electron velocity distribution takes the same form in both AC electric fields and DC magnetic fields (for more details, see chapter 4.2.2 of [32]). However, at  $B/N = 10$  and  $100$  Hx, the effective AC E-field leads to significantly different results. The deviations are particularly evident for N<sub>2</sub> at  $E/N \gtrsim 30$  Td.

Figure 5.6 presents the relaxation of the electron swarm energy in N<sub>2</sub>, for  $E/N = 100$  Td and different  $B/N$ , and compares with the solutions using an effective AC electric field. For lower  $B/N$ , the AC field cannot capture neither the initial relaxation nor the mean steady-state value. When the cyclotron frequency  $\Omega$  is much larger than the average frequency for energy relaxation  $\nu_e$ , the equivalence becomes very good. In the particular conditions of figure 5.6,  $\omega/\nu_e$  is 5.2, 30.8, 95.9 and 6350, for  $B/N = 100$ , 500, 1000 and 5000 Hx, respectively. In any case, a proper implementation of the magnetic field should be always considered, in order to obtain a correct description of the transport properties, such as the diffusion coefficients and the drift velocity. The only aim of the present discussion is to provide insight into the effect of the magnetic field from the energetic point of view.

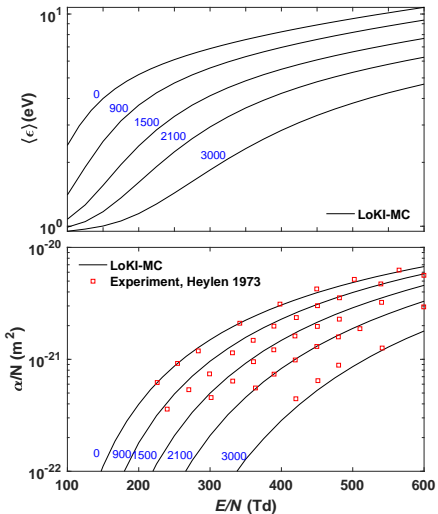
Lastly, figures 5.7a and 5.7b show the electron energy distribution functions (EEDF) at  $E/N = 100$  Td and various  $B/N$ , together with the respective solution with an effective AC electric field and null magnetic field. The EEDFs evidence the remarkable decrease of the high energy electrons caused by the magnetic field, as well as the approximative equivalence between the magnetic field and effective AC electric field cases, failing more at lower  $B/N$ .



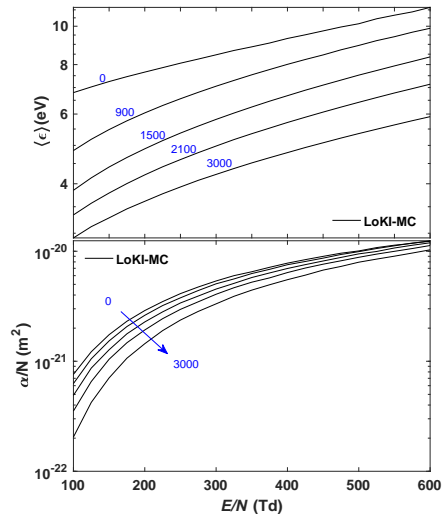
**Figure 5.1:** Electron mean energy  $\langle \epsilon \rangle$ , drift velocity  $v_{d,i}$ , and diffusion coefficients  $ND_{ij}$ , in the Reid-ramp model, as a function of  $B/N$ , for  $E/N = 12$  Td and  $\Psi = 90^\circ$ . The calculations are compared with the MC results of Raspopovic et al. [26].



**Figure 5.2:** Electron mean energy  $\langle \epsilon \rangle$ , bulk drift speed  $\|v_d^b\|$  and ionization coefficient  $k_{ion}$ , in the Lucas-Saelee model, as a function of  $\Psi$ , for  $E/N = 10$  Td,  $B/N = 200, 1000$  Hz and  $F = 0, 0.5, 1$ . The calculations are compared with the MC results of Dujko et al. [27].



(a)



(b)

**Figure 5.3:** Electron mean energy  $\langle \epsilon \rangle$  and reduced Townsend coefficient  $\alpha/N$ , in  $N_2$  (a) and  $Ar$  (b), as a function of  $E/N$ , for various  $B/N$ . For  $N_2$ ,  $\alpha/N$  is compared against experiments [31].

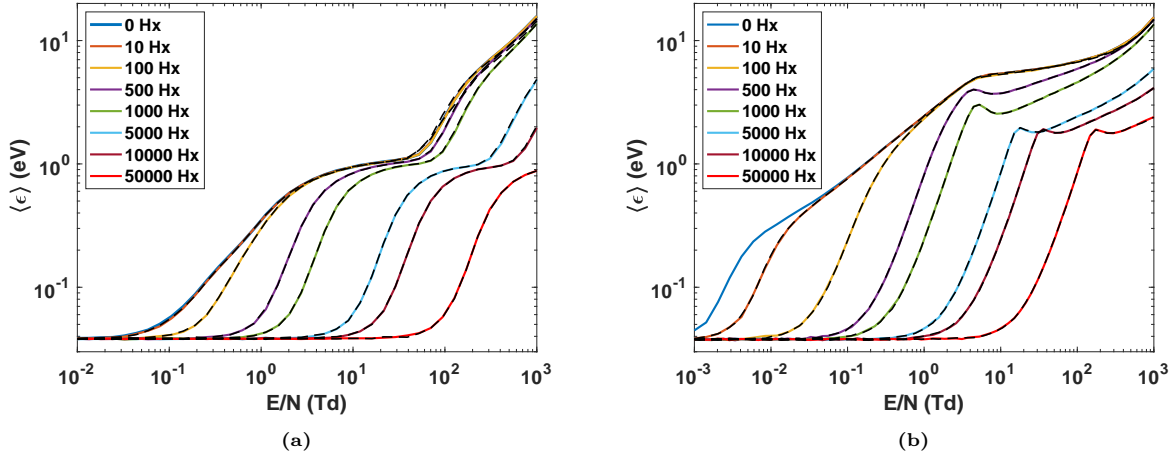


**Figure 5.4:** Electron mean energy  $\langle \epsilon \rangle$ , in  $N_2$  (a) and  $Ar$  (b), as a function of  $E/N$ , for  $B/N = 0 - 50000$  Hz. In  $N_2$ , the results for  $B/N = 0$  and  $10$  Hz are almost superposed. The black-dashed lines represent the results with null  $B$  and an effective AC E-field.

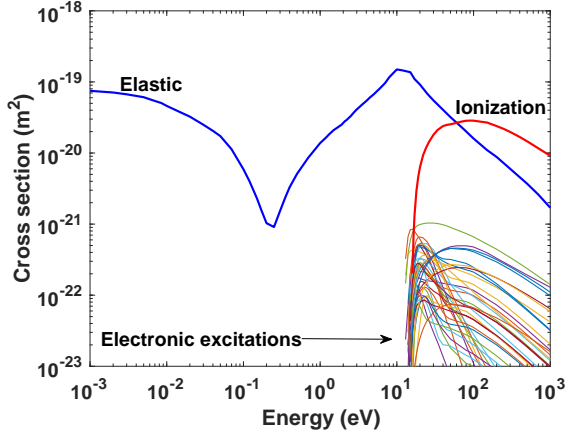


**Figure 5.5:** Electron-impact cross sections in  $Ar$ , available at the IST-Lisbon database of LXCat [30]

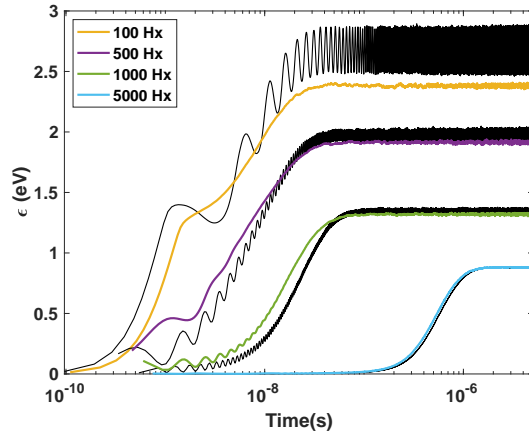


**Figure 5.6:** Temporal evolution of the electron swarm energy ( $\epsilon$ ) in  $N_2$ , for  $E/N = 100$  Td and different  $B/N$ . The black curves represent the results with null  $B$  and an effective AC E-field.

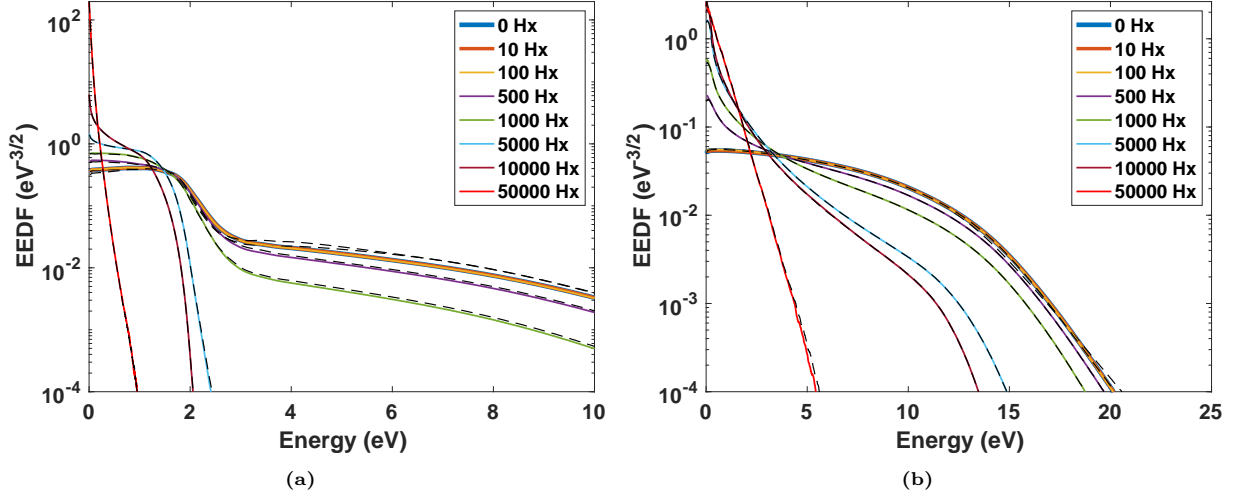


**Figure 5.7:** EEDFs in  $\text{N}_2$  (a) and  $\text{Ar}$  (b), at  $E/N = 100$  Td and  $B/N = 0 - 50000$  Hz. The results for  $B/N = 0, 10, 100$  Hz are almost superposed. The black-dashed lines represent the results with an effective AC E-field.

### 5.3.2 AC electric field: phenomenon of electron cyclotron resonance

The impact of the magnetic field on the electron kinetics may be substantially different when the electric field is oscillatory. In particular, if the angular frequency  $\omega = 2\pi f$  of the AC electric field is comparable to the electron cyclotron frequency  $\Omega = eB/m_e$ , the magnetic field can increase the efficiency of the electric-field acceleration, due to the well-known phenomenon of electron cyclotron resonance (ECR)[32, 33].

We start the analysis of the ECR process using the Reid-ramp model, with  $\mathbf{E}$  perpendicular to  $\mathbf{B}$  ( $\Psi = 90^\circ$ ). Contrarily to the previous subsection, the results are now dependent on the gas density  $N$ . Therefore, keep in mind that  $N = 3.54 \times 10^{22} \text{ m}^{-3}$ , unless stated otherwise. Moreover, for this model, the root-mean-squared reduced electric field is  $E_{\text{rms}}/N = 10$  Td. Figure 5.8 shows the electron mean energy  $\langle \epsilon \rangle$  and reduced electric-field power  $\langle P_E/N \rangle$ , as a function of  $B/N$ , for different excitation frequencies  $f$ . The results are compared with the work by Dujko et al. [9] and slight differences are found, specially at higher frequencies<sup>2</sup>. After a careful analysis, no specific reason has been found for this small disagreement. Such deviations may be due to slightly different conditions of electric field and/or gas density; or inaccuracies due to the unavoidable truncation of a multi-term expansion, which is unlikely since in [9] four anisotropy degrees are considered and it was checked this gives a good accuracy. In principle, these differences do not stem from LoKI-MC, since they exist even at  $B = 0$  and our code is successfully benchmarked in these conditions (*cf.* section 5.B). Furthermore, the resonance peaks at high frequencies calculated using LoKI-MC tend to the solution of a DC electric field with  $E_{\text{DC}}/N = E_0/N/2 = E_{\text{rms}}/N/\sqrt{2}$  and null magnetic field, which is the expected result and constitutes

<sup>2</sup>Notice that the results of  $P_E$  from [9] (figure 10) need to be divided by  $10\sqrt{2}$ , i.e., the amplitude of  $E/N$  in Td.

an additional verification test, as discussed below.

The electron response to the magnetic field varies significantly with the frequency  $f$  of the electric field. For  $f = 50$  MHz,  $\langle \epsilon \rangle$  and  $\langle P_E/N \rangle$  decrease monotonically with  $B/N$ ; for  $f = 100$  MHz the ECR starts to play a role; and for  $f \geq 200$  MHz the resonance curve is clear. To understand this behavior, we need to examine closely the physics of ECR. This is better understood if we decompose the linearly-oscillating electric field as a sum of right-hand and left-hand circular electric-fields ( $\mathbf{E}_{\text{RH}}$  and  $\mathbf{E}_{\text{LH}}$ )<sup>[32]</sup>:

$$\mathbf{E}(t) = E_0 \cos(\omega t) \mathbf{e}_x = \mathbf{E}_{\text{RH}} + \mathbf{E}_{\text{LH}} = \frac{E_0}{2} (\cos(\omega t) \mathbf{e}_x + \sin(\omega t) \mathbf{e}_y) + \frac{E_0}{2} (\cos(\omega t) \mathbf{e}_x - \sin(\omega t) \mathbf{e}_y), \quad (5.5)$$

where it is considered that  $\Psi = 90^\circ$ . The cyclotron motion induced by the magnetic field (along  $\mathbf{e}_z$ ) occurs in the  $xy$  plane in the right-hand direction. When the electron cyclotron frequency  $\Omega$  is equal to the angular frequency  $\omega$ , the electrons can be continuously accelerated by  $\mathbf{E}_{\text{RH}}$ , leading to the ECR. However, when  $\omega$  is low compared to the collision frequency  $\nu$ , the collisions with the heavy-species tend to breakdown the synchronous motion and ECR is negligible.

Additional explanation of the effects reported in figure 5.8 can be obtained from the analysis of the angle between the electron drift velocity  $\mathbf{v}_d$  and  $\mathbf{E}_{\text{RH}}$ , as shown in figure 5.9a. At  $f = 50$  MHz, the drift motion is still largely affected by collisions, causing significant deviations from optimal acceleration by  $\mathbf{E}_{\text{RH}}$  (maximal at  $180^\circ$ ). For this reason, for low frequencies, ECR is not beneficial, and adding a magnetic field only decreases the overall electron acceleration, as in the DC cases shown in section 5.3.1. For high frequencies, the oscillations decrease and  $\mathbf{v}_d$  is mostly antiparallel to  $\mathbf{E}_{\text{RH}}$ ; in this case, the electron acceleration is approximately equivalent to the one in a DC electric field with  $E_{\text{DC}}/N = E_0/N/2$  and null  $B$ . This characteristic can be further confirmed in figure 5.10a, showing the reduced power gained due to the right-circular electric field,  $P_{E_{\text{RH}}}/N = -e\mathbf{v}_d \cdot \mathbf{E}_{\text{RH}}/N$ , along the AC period. On the other hand, the angle between  $\mathbf{v}_d$  and  $\mathbf{E}_{\text{LH}}$  varies between 0 and  $180^\circ$  (see figure 5.9b), since  $\mathbf{E}_{\text{LH}}$  rotates in the opposite direction of the cyclotron motion. Moreover, figure 5.10b shows that for higher frequencies where ECR is dominant, the average power due to  $\mathbf{E}_{\text{LH}}$  is approximately null.

For a complementary analysis of the results in figure 5.8, let us examine the reduced electric-field power considering a fluid (single velocity) formulation (see chapter 4.2 of [32] and [33]):

$$\left\langle \frac{P_E}{N} \right\rangle = \left\langle \frac{P_{E_{\text{RH}}}}{N} + \frac{P_{E_{\text{LH}}}}{N} \right\rangle = \frac{e^2}{4m_e} \left( \frac{k_m}{k_m^2 + (\omega/N - \Omega/N)^2} + \frac{k_m}{k_m^2 + (\omega/N + \Omega/N)^2} \right) \left( \frac{E_0}{N} \right)^2, \quad (5.6)$$

where  $k_m = \nu_m/N$  is the rate coefficient for the total momentum transfer. In resonance conditions, the first term (RH) is dominant only when  $\omega/N \gtrsim k_m$ . For reference, table 5.1 presents the values of  $\omega/N$  and  $(\omega/N)/k_m^{\text{typ}}$ , in the Reid-ramp model, N<sub>2</sub> and Ar, for the different frequencies  $f$  used here and considering  $N = 3.54 \times 10^{22} \text{ m}^{-3}$ . The momentum-transfer rate-coefficient  $k_m^{\text{typ}}$  is calculated from the solution with  $E_{\text{DC}}/N = E_0/N/2$  and null  $B$ , typical of the resonance peak. As expected, in the Reid-ramp model, for

$f = 100$  MHz,  $(\omega/N)/k_m^{\text{typ}} \sim 1$ , which corresponds to the frequency where ECR starts to be relevant.

Figure 5.11 shows the mean energy in N<sub>2</sub> and Ar, as a function of  $B/N$ , for the same conditions as in the Reid-ramp model, except for  $E_{\text{rms}}/N = 100$  Td. The physical behavior is essentially the same as the one found in the Reid-ramp model, which reinforces the interest of this simple gas model in the study of fundamental physical phenomena. By comparison with table 5.1, we find that the resonant peak in Ar appears at slightly lower values of  $(\omega/N)/k_m$  ( $\sim 0.5$ ) than in N<sub>2</sub> ( $\sim 1.7$ ), and this is related with the larger importance of elastic collisions in this gas. Furthermore, for both N<sub>2</sub> and Ar, the maximum of  $\langle \epsilon \rangle$  at high frequencies is in accordance with the theoretically predicted value (indicated in the horizontal lines).

The Reid-ramp model can still be considered to study the influence of other physical parameters besides the electric field frequency  $f$ . In particular, until now the gas density has been fixed to  $N = 3.54 \times 10^{22} \text{ m}^{-3}$ . Figure 5.12 shows the resonance curves of the energy and reduced power, for densities 10 times lower and higher than the default value, compensating  $f$  with the same factor, as to keep  $\omega/N$  constant. The exact equivalence between these curves confirms that the relevant parameter for ECR is  $\omega/N$ , as could be expected from the previous discussion and equation (5.6).

Finally, we analyze the ECR process when **E** and **B** are crossed with an arbitrary angle, varying  $\Psi$  from 0 to 180°, keeping  $f = 400$  MHz,  $N = 3.54 \times 10^{22} \text{ m}^{-3}$  and  $\omega = \Omega$ . Figure 5.13a shows that the electron mean energy is maximal at  $\Psi = 90^\circ$  and the intervals [0, 90]° and [90, 180]° are symmetric, as expected [28]. Figures 5.13b, 5.13c and 5.13d, represent the electron drift velocity along an AC cycle, in 3D, *xy* plane and *xz* plane, respectively, for  $\Psi = 0, 30, 60$  and 90°. These figures evidence the non-perturbation of the motion by the magnetic field for  $\Psi = 0^\circ$ , while for  $\Psi = 30, 60$  and 90°, an elliptical motion is formed, whose plane rotates according to the value of  $\Psi$ .

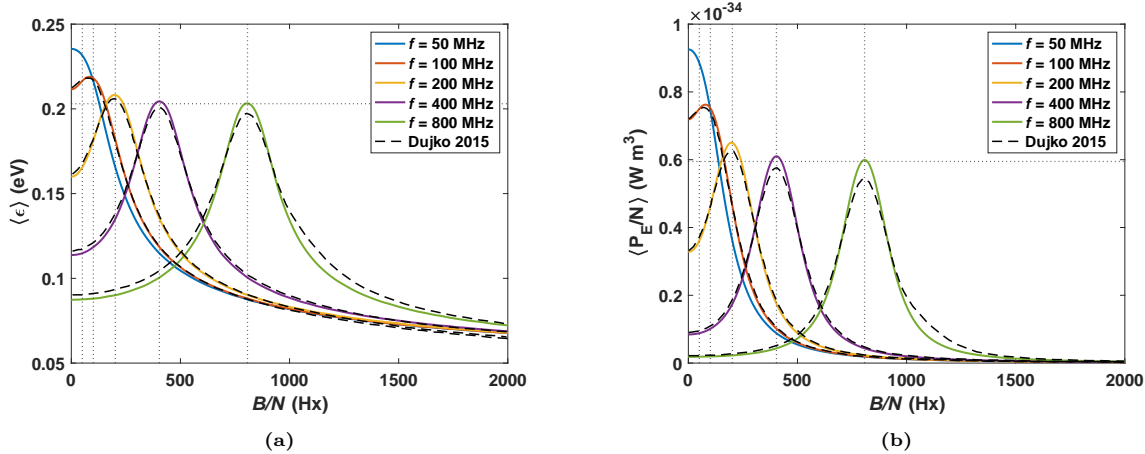


**Figure 5.8:** Electron mean energy  $\langle \epsilon \rangle$  (a) and reduced electric-field power  $\langle P_E/N \rangle$  (b), as a function of  $B/N$ , for different excitation frequencies  $f$ , in the Reid-ramp model. The results are compared against [9], except for  $f = 50$  MHz (value considered here to provide additional insight to the present study). Vertical dotted lines indicate the values of  $B/N$  for which ECR occurs. Horizontal dotted lines represent the calculations using a DC electric field with  $E_{\text{DC}}/N = E_0/N/2 = 10/\sqrt{2}$  Td and null magnetic field, and should match the value at ECR for high frequencies.

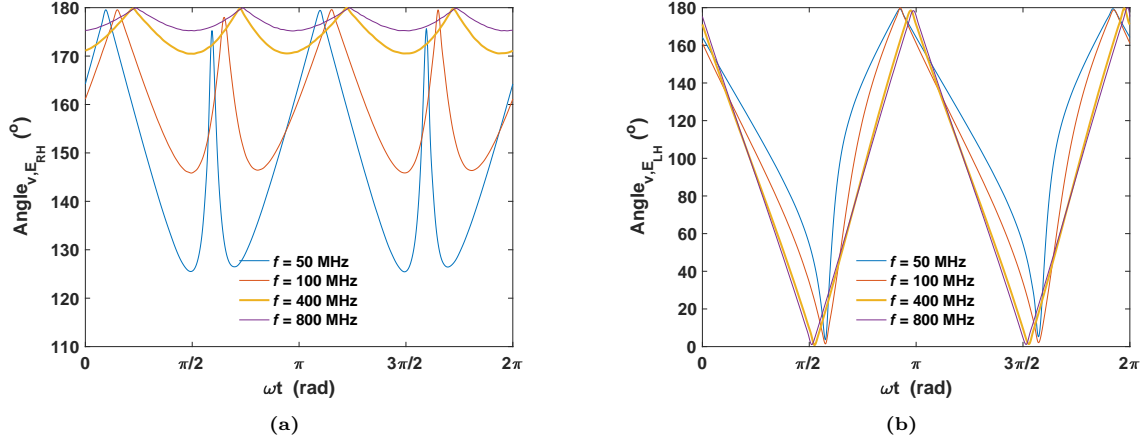


**Figure 5.9:** Angle between the electron drift velocity  $v_d$  and the right-hand (a) and left-hand (b) circular electric fields, along the AC period, in the Reid-ramp model.

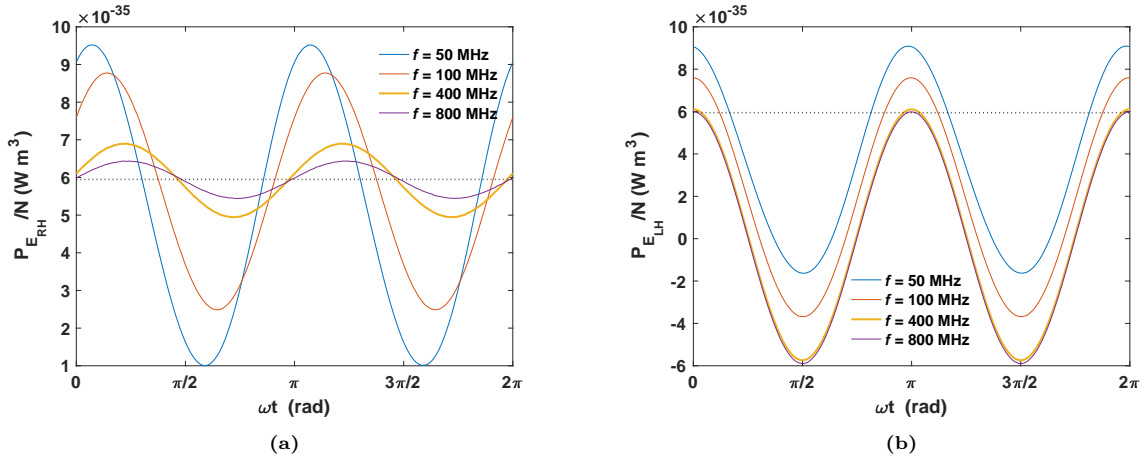


**Figure 5.10:** Reduced electric-field power absorbed due to the right-hand (a) and left-hand (b) circular fields, along the AC period, in the Reid-ramp model. The horizontal dotted line represents the power due to a DC electric field with  $E_{DC}/N = E_0/N/2 = 10/\sqrt{2}$  Td and null  $B$ .

**Table 5.1:** List of the AC frequencies  $f$  (in MHz), reduced angular frequencies  $\omega/N$  (in  $10^{-14}\text{rad s}^{-1}\text{m}^3$ ) and  $(\omega/N)/k_m^{\text{typ}}$  (in  $10^{-14}\text{rad}$ ), in the Reid-ramp model, N<sub>2</sub> and Ar. The gas density is  $N = 3.54 \times 10^{22}\text{m}^3$ . In the Reid-ramp model,  $E_{\text{rms}}/N = 10\text{Td}$ , while in N<sub>2</sub> and Ar,  $E_{\text{rms}}/N = 100\text{Td}$ .

Reid-ramp			N <sub>2</sub>			Ar		
$f$	$\omega/N$	$(\omega/N)/k_m^{\text{typ}}$	$f$	$\omega/N$	$(\omega/N)/k_m^{\text{typ}}$	$f$	$\omega/N$	$(\omega/N)/k_m^{\text{typ}}$
50	0.887	0.52	400	7.10	0.85	200	3.55	0.25
100	1.775	1.04	800	14.20	1.70	400	7.10	0.49
200	3.55	2.08	1600	28.40	3.40	800	14.20	0.98
400	7.10	4.15	2400	42.60	5.10	1200	21.30	1.48
800	14.20	8.31	3200	56.80	6.80	1600	28.40	1.97

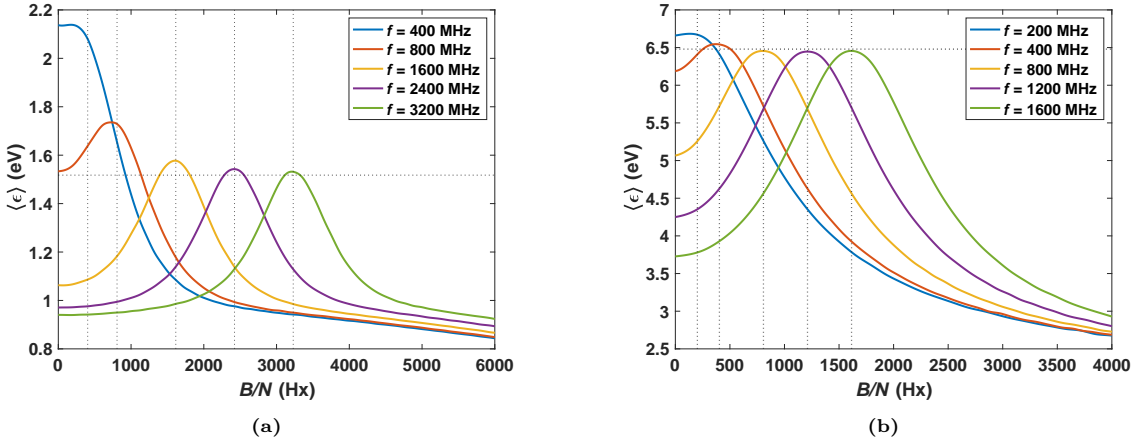


**Figure 5.11:** Electron mean energy  $\langle \epsilon \rangle$ , as a function of  $B/N$ , for different excitation frequencies  $f$ , in N<sub>2</sub> (a) and Ar (b). Vertical dotted lines indicate the values of  $B/N$  for which ECR occurs. Horizontal dotted lines represent the calculations using a DC electric field with  $E_{\text{DC}}/N = E_0/N/2 = 100/\sqrt{2}\text{Td}$  and null  $B$ .

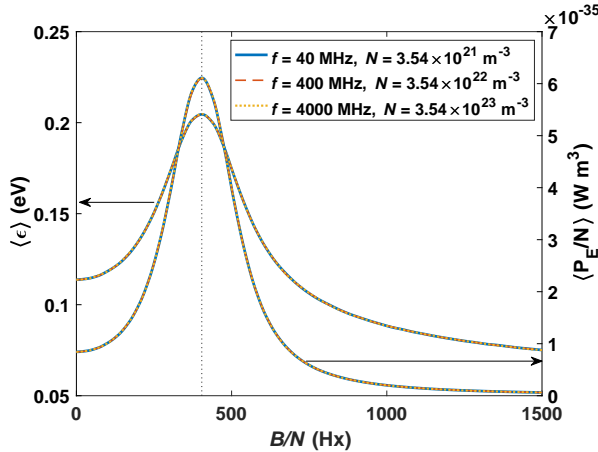


**Figure 5.12:** Electron mean energy  $\langle \epsilon \rangle$  (left) and reduced electric-field power  $\langle P_E/N \rangle$  (right), as a function of  $B/N$ , for three sets of  $f$  and  $N$  values, keeping  $\omega/N$  constant, in the Reid-ramp model.

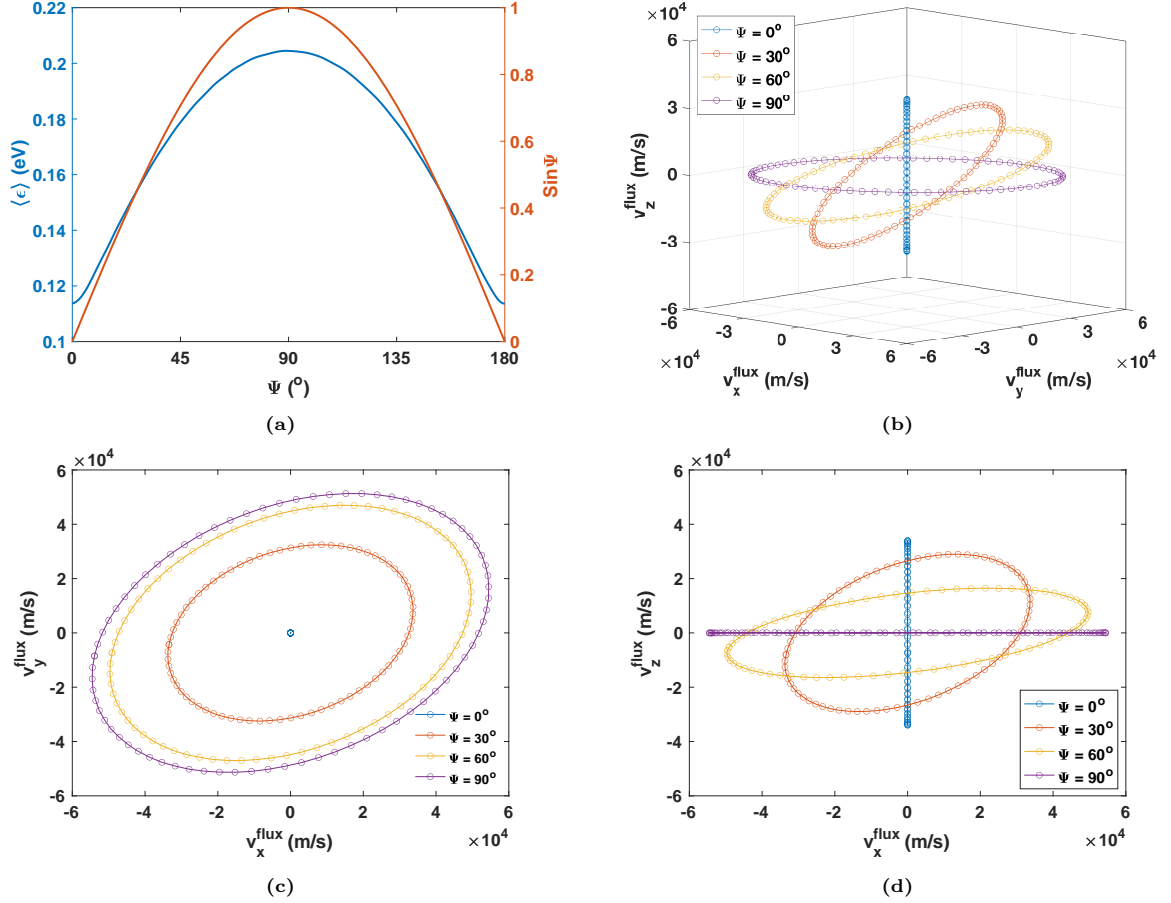


**Figure 5.13:** Time-averaged electron mean energy (a), as a function of  $\Psi$ . Electron drift velocity along an AC cycle, in 3D (b),  $xy$  plane (c) and  $xz$  plane (d), for  $\Psi = 0, 30, 60$  and  $90^\circ$ . The calculations are made in the Reid-ramp gas, with  $f = 400$  MHz,  $N = 3.54 \times 10^{22} \text{ m}^3$  and  $B/N$  such that  $\Omega = \omega$  (resonance conditions).

## 5.4 Final remarks

This chapter elaborates on the physical effect of the magnetic field on the electron kinetics under AC/DC electric fields. More specifically, the main aim of the present effort is to provide the community an open-source Monte Carlo code, extensively verified and benchmarked, that allows the study of the electron kinetics under AC/DC electric and DC magnetic fields crossed at arbitrary angles. This consists a significant update in comparison with the previous release of LoKI-MC [20], where only DC electric fields were considered. The most important modification is in the propagation of the electron position and velocity during the collision-free flights, which is taken into account with the analytical solutions of the equations of motion.

Another contribution of this work is the production of new benchmark calculations for electron kinetics solvers, in conditions of coexistent AC electric and DC magnetic fields. The calculations account for the temporal evolution along the AC cycle (figures 5.9 and 5.10), explore the effect of the crossing angle

between the fields (figure 5.13), and highlight that the relevant parameters for the resonance curves in perpendicular configuration are  $E/N$ ,  $B/N$  and  $\omega/N$  (figure 5.12).

The role of the magnetic field in the electron acceleration is discussed, separating the cases with DC and AC electric fields. In DC electric fields, the oscillatory motion caused by the magnetic field decreases the efficiency of the electron acceleration, which reflects on the power absorbed by the electric field and on the electron mean energy. However, in Ar, for small transient regions of  $E/N$  and  $B/N$ , we find conditions where (i) for constant  $B/N$ ,  $\langle \epsilon \rangle$  decreases with increasing  $E/N$  and (ii) for constant  $E/N$ ,  $\langle \epsilon \rangle$  increases with increasing  $B/N$ . These counter-intuitive characteristics were first reported by Ness and Makabe [11] and are now confirmed by means of an independent Monte Carlo simulation. The main source for this trend is related with the rapid increase of the elastic cross section from  $\sim 0.25$  up to 10 eV, followed by the steep appearance of strong inelastic losses after 11 eV.

In AC electric fields, when the magnetic field value is such that the electron cyclotron frequency  $\Omega$  is similar to the angular frequency  $\omega$  of the electric field, the synchronization of the cyclotron motion with the right-hand circular component of the electric field enhances electron acceleration, through the well-known electron cyclotron resonance. However, for conditions where the mean collision frequency is much higher than the cyclotron frequency, the synchronization tends to breakdown and the magnetic field is detrimental for the electron acceleration, as in the DC electric field case.

The results in real gases demonstrate the robustness of the formulation implemented in LoKI-MC, allowing to study systems with interest for applications. At the same time, the similarities with the results obtained in model gases reinforce the great interest of studying fundamental physical phenomena in electron kinetics using these simplified models, whose calculations can be easily reproduced with different codes.

LoKI-MC proves to be an efficient tool, capable of delivering a statistically accurate solution for a given condition within minutes, even when run on a standard laptop. The implementation of the magnetic field has little impact on the computational load, despite the increasing complexity of the equations of motion. However, when dealing with intermediate values of  $E/N$  in Ar, the magnetic field can result in noticeably longer computation times, reaching up to a few hours. This extended duration is due to an enhancement of null collisions, linked with a larger presence of electrons with energies near the Ramsauer minimum of the elastic cross section (cf. figure 5.5). Additionally, the issue is exacerbated by the considerable number of simulated electron-neutral collisions required for an elastic gas as argon, where the energy exchange in each collision is weak. In the future, this concern might be partly mitigated with the implementation of optimized versions of the null collision technique (see e.g., [34]).

Future research efforts may include the study of the electron kinetics under electric and magnetic fields in gases with relevance in different applications, such as Xe for plasma propulsion, and Cl<sub>2</sub>, SF<sub>6</sub> and CF<sub>4</sub> for plasma etching. Additionally, we could generalize the study to systems with AC magnetic

fields [6, 9], but this is not straightforward since in that case the integration of the collision-free motion cannot be performed analytically. Finally, it would be interesting to investigate transient phenomena in combined electric and magnetic fields during the temporal relaxation of the electron swarm, which can unveil very exotic physics, such as transiently negative diffusion coefficients, as shown, e.g., in [35, 36]. LoKI-MC is not yet prepared for such configurations, but the extension should be straightforward.

## 5.A Integration of the collision-free motion

This section presents the analytical solutions of the Newton equations (5.1) for the propagation of the electron position ( $\mathbf{r}$ ) and velocity ( $\mathbf{v}$ ), from a time-instant  $t_0$  up to  $t_0 + t_c$ , free of collisions. The general case ( $\omega \neq 0$  &  $B \neq 0$ ) is presented, as well as other particular conditions, such as  $\omega = 0$ ,  $B = 0$  and  $\omega = \Omega = eB/m_e$  (electron cyclotron resonance). The following auxiliar variables are used:

$$\begin{cases} v_{x,t_0} = v_x(t_0), v_{y,t_0} = v_y(t_0), v_{z,t_0} = v_z(t_0) \\ x_{t_0} = x(t_0), y_{t_0} = y(t_0), z_{t_0} = z(t_0) \\ \phi = \omega t_0 \end{cases} . \quad (5.7)$$

### General case ( $\omega \neq 0$ & $B \neq 0$ )

$$\begin{cases} v_x(t_0 + t_c) = \frac{eE_{x,0}(\omega \sin(\phi) \cos(\Omega t_c) - \omega \sin(\omega t_c + \phi) + \Omega \cos(\phi) \sin(\Omega t_c))}{m(\omega^2 - \Omega^2)} + v_{x,t_0} \cos(\Omega t_c) - v_{y,t_0} \sin(\Omega t_c) \\ v_y(t_0 + t_c) = \frac{eE_{x,0}(\omega \sin(\phi) \sin(\Omega t_c) + \Omega \cos(\omega t_c + \phi) - \Omega \cos(\phi) \cos(\Omega t_c))}{m(\omega^2 - \Omega^2)} + v_{x,t_0} \sin(\Omega t_c) + v_{y,t_0} \cos(\Omega t_c) \\ v_z(t_0 + t_c) = \frac{eE_{z,0}(\sin(\phi) - \sin(\omega t_c + \phi))}{m\omega} + v_{z,t_0} \\ x(t_0 + t_c) = \frac{eE_{x,0}(\sin(\phi)(\omega \sin(\Omega t_c) - \Omega \sin(\omega t_c)) + \Omega \cos(\phi)(\cos(\omega t_c) - \cos(\Omega t_c)))}{m\Omega(\omega^2 - \Omega^2)} + \frac{v_{x,t_0} \sin(\Omega t_c)}{\Omega} + \frac{v_{y,t_0} (\cos(\Omega t_c) - 1)}{\Omega} + x_{t_0} \\ y(t_0 + t_c) = \frac{eE_{x,0}(\sin(\phi)(\omega^2 \cos(\Omega t_c) - \omega^2 + \Omega^2) + \Omega(\omega \cos(\phi) \sin(\Omega t_c) - \Omega \sin(\omega t_c + \phi)))}{m\omega\Omega(\Omega^2 - \omega^2)} + \frac{v_{x,t_0} (1 - \cos(\Omega t_c))}{\Omega} + \frac{v_{y,t_0} \sin(\Omega t_c)}{\Omega} + y_{t_0} \\ z(t_0 + t_c) = \frac{eE_{z,0}(\omega t_c \sin(\phi) + \cos(\omega t_c + \phi) - \cos(\phi))}{m\omega^2} + t_c v_{z,t_0} + z_{t_0} \end{cases} \quad (5.8)$$

### $\omega = 0$

$$\begin{cases} v_x(t_0 + t_c) = -\frac{eE_{x,0} \sin(\Omega t_c)}{m\Omega} + v_{x,t_0} \cos(\Omega t_c) - v_{y,t_0} \sin(\Omega t_c) \\ v_y(t_0 + t_c) = \frac{eE_{x,0}(\cos(\Omega t_c) - 1)}{m\Omega} + v_{x,t_0} \sin(\Omega t_c) + v_{y,t_0} \cos(\Omega t_c) \\ v_z(t_0 + t_c) = v_{z,t_0} - \frac{t_c e E_{z,0}}{m} \\ x(t_0 + t_c) = \frac{eE_{x,0}(\cos(\Omega t_c) - 1)}{m\Omega^2} + \frac{v_{x,t_0} \sin(\Omega t_c)}{\Omega} + \frac{v_{y,t_0} (\cos(\Omega t_c) - 1)}{\Omega} + x_{t_0} \\ y(t_0 + t_c) = \frac{eE_{x,0}(\sin(\Omega t_c) - \Omega t_c)}{m\Omega^2} + \frac{v_{x,t_0} (1 - \cos(\Omega t_c))}{\Omega} + \frac{v_{y,t_0} \sin(\Omega t_c)}{\Omega} + y_{t_0} \\ z(t_0 + t_c) = -\frac{t_c^2 e E_{z,0}}{2m} + t_c v_{z,t_0} + z_{t_0} \end{cases} \quad (5.9)$$

$$\mathbf{B} = \mathbf{0}$$

$$\begin{cases} v_x(t_0 + t_c) = \frac{eE_{x,0}(\sin(\phi) - \sin(\omega t_c + \phi))}{m\omega} + v_{x,t_0} \\ v_y(t_0 + t_c) = v_{y,t_0} \\ v_z(t_0 + t_c) = \frac{eE_{z,0}(\sin(\phi) - \sin(\omega t_c + \phi))}{m\omega} + v_{z,t_0} \\ x(t_0 + t_c) = \frac{eE_{x,0}(\omega t_c \sin(\phi) + \cos(\omega t_c + \phi) - \cos(\phi))}{m\omega^2} + t_c v_{x,t_0} + x_{t_0} \\ y(t_0 + t_c) = t_c v_{y,t_0} + y_{t_0} \\ z(t_0 + t_c) = \frac{eE_{z,0}(\omega t_c \sin(\phi) + \cos(\omega t_c + \phi) - \cos(\phi))}{m\omega^2} + t_c v_{z,t_0} + z_{t_0} \end{cases} \quad (5.10)$$

$$\boldsymbol{\omega} = \boldsymbol{\Omega}$$

$$\begin{cases} v_x(t_0 + t_c) = -\frac{eE_{x,0}(\Omega t_c \cos(\Omega t_c + \phi) + \cos(\phi) \sin(\Omega t_c))}{2m\Omega} + v_{x,t_0} \cos(\Omega t_c) - v_{y,t_0} \sin(\Omega t_c) \\ v_y(t_0 + t_c) = -\frac{eE_{x,0}(\Omega t_c \sin(\phi) \cos(\Omega t_c) + \sin(\Omega t_c)(\Omega t_c \cos(\phi) - \sin(\phi)))}{2m\Omega} + v_{x,t_0} \sin(\Omega t_c) + v_{y,t_0} \cos(\Omega t_c) \\ v_z(t_0 + t_c) = \frac{eE_{z,0}(\sin(\phi) - \sin(\Omega t_c + \phi))}{m\Omega} + v_{z,t_0} \\ x(t_0 + t_c) = -\frac{eE_{x,0}(2\Omega t_c \sin(\Omega t_c + \phi) + \cos(\Omega t_c + \phi) - \cos(\phi - \Omega t_c))}{4m\Omega^2} + \frac{v_{x,t_0} \sin(\Omega t_c)}{\Omega} + \frac{v_{y,t_0} (\cos(\Omega t_c) - 1)}{\Omega} + x_{t_0} \\ y(t_0 + t_c) = \frac{eE_{x,0}(\Omega t_c \cos(\Omega t_c + \phi) - 2 \sin(\phi)(\cos(\Omega t_c) - 1) - \cos(\phi) \sin(\Omega t_c))}{2m\Omega^2} + \frac{v_{x,t_0} (1 - \cos(\Omega t_c))}{\Omega} + \frac{v_{y,t_0} \sin(\Omega t_c)}{\Omega} + y_{t_0} \\ z(t_0 + t_c) = \frac{eE_{z,0}(\Omega t_c \sin(\phi) + \cos(\Omega t_c + \phi) - \cos(\phi))}{m\Omega^2} + t_c v_{z,t_0} + z_{t_0} \end{cases} \quad (5.11)$$

## 5.B Benchmark with $B = 0$ and AC electric field

As additional info, and for completeness, we also present a comparison between LoKI-MC calculations and the results from [23], under an AC electric field and null magnetic field, using the Reid-ramp model. The reduced angular excitation frequency  $\omega/N$  varies from  $1.777 \times 10^{-17}$  to  $1.777 \times 10^{-14}$  rad m<sup>3</sup>/s, the root-mean-squared reduced electric field is  $E_{\text{rms}}/N = 10$  Td and the angle between the z-axis and the electric field is  $\Psi = 180^\circ$ . The mean electron energy  $\langle \epsilon \rangle$  and the drift velocity  $v_z$  are shown in figure 5.14 as a function of the period phase  $\omega t$ . The present calculations agree remarkably with the results from [23]. For an extended physical explanation of these results, the reader is referred to [23]. Here, we point out that, with increasing  $\omega/N$ , (i) the fluctuations of the mean electron energy decrease significantly and (ii) a phase shift between the drift velocity and the electric field is evident. Note that LoKI-MC also passed with success a similar benchmark for the Lucas-Saelee gas model [24] (not shown here).

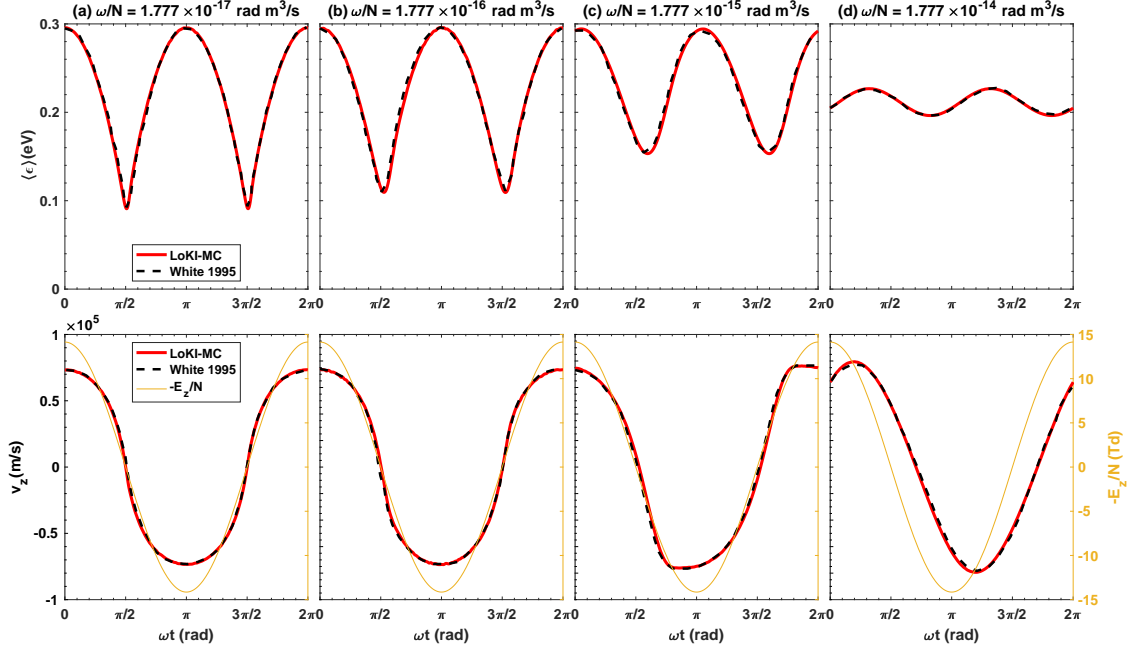


**Figure 5.14:** Comparison between the LoKI-MC calculations of the mean electron energy and drift velocity and the results from [23], for  $B = 0$ , different  $\omega/N$  and using the Reid-ramp model. The results are shown as a function of the period phase  $\omega t$  and the reduced electric field  $-\mathcal{E}_z/N$  is shown in yellow.

## References

- [1] Dias, T. C., Pintassilgo, C. D., and Guerra, V. 2023 “Effect of the magnetic field on the electron kinetics under AC/DC electric fields: benchmark calculations and electron cyclotron resonance” *Plasma Sources Sci. Technol.* **32**, 095003.
- [2] Shon, C. and Lee, J. 2002 “Modeling of magnetron sputtering plasmas” *Appl. Surf. Sci.* **192**, 258–269.
- [3] Keidar, M., Zhuang, T., Shashurin, A., Teel, G., Chiu, D., Lukas, J., Haque, S., and Brieda, L. 2014 “Electric propulsion for small satellites” *Plasma Phys. Control. Fusion* **57**, 014005.
- [4] Mrózek, K., Dytrych, T., Molíš, P., Dániel, V., and Obrusník, A. 2021 “Global plasma modeling of a magnetized high-frequency plasma source in low-pressure nitrogen and oxygen for air-breathing electric propulsion applications” *Plasma Sources Sci. Technol.* **30**, 125007.
- [5] Makabe, T. and Petrović, Z. 2015 *Plasma electronics 2nd edn* New York: CRC.
- [6] Petrović, Z., Raspopović, Z., Dujko, S., and Makabe, T. 2002 “Kinetic phenomena in electron transport in radio-frequency fields” *Appl. Surf. Sci.* **192**, 1–25.
- [7] White, R., Ness, K., and Robson, R. 2002 “Development of swarm transport theory in radio-frequency electric and crossed electric and magnetic fields” *Appl. Surf. Sci.* **192**, 26–49.

- [8] Dujko, S., Raspopović, Z. M., and Petrović, Z. L. 2005 “Monte Carlo studies of electron transport in crossed electric and magnetic fields in  $\text{CF}_4$ ” *J. Phys. D Appl. Phys.* **38**, 2952.
- [9] Dujko, S., Bošnjaković, D., White, R. D., and Petrović, Z. L. 2015 “Heating mechanisms for electron swarms in radio-frequency electric and magnetic fields” *Plasma Sources Sci Technol* **24**, 054006.
- [10] Nakamura, S., Ventzek, P. L. G., and Kitamori, K. 1999 “Monte Carlo simulation study of the scaling of electron transport parameters in crossed DC electric and magnetic fields” *J. Appl. Phys.* **85**, 2534–2539.
- [11] Ness, K. and Makabe, T. 2000 “Electron transport in argon in crossed electric and magnetic fields” *Phys. Rev. E* **62** (3), 4083–4090.
- [12] Raspopović, Z. M., Dujko, S., Makabe, T., and Petrović, Z. L. 2005 “Transport coefficients for electrons in argon in crossed electric and magnetic RF fields” *Plasma Sources Sci Technol* **14**, 293.
- [13] Biagi, S. 1999 “Monte Carlo simulation of electron drift and diffusion in counting gases under the influence of electric and magnetic fields” *Nucl. Instrum. Methods Phys. Res A* **421**, 234–240  
<http://magboltz.web.cern.ch/magboltz/>.
- [14] White, R., Robson, R., and Ness, K. 1999a “On approximations involved in the theory of charged particle transport in gases in electric and magnetic fields at arbitrary angles” *IEEE Trans Plasma Sci* **27**, 1249–1253.
- [15] White, R. D., Ness, K. F., and Robson, R. E. 1999 “Velocity distribution functions for electron swarms in methane in electric and magnetic fields” *J. Phys. D Appl. Phys.* **32**, 1842.
- [16] Dujko, S., White, R. D., Petrović, Z. L., and Robson, R. E. 2011 “A multi-term solution of the nonconservative Boltzmann equation for the analysis of temporal and spatial non-local effects in charged-particle swarms in electric and magnetic fields” *Plasma Sources Sci Technol* **20**, 024013.
- [17] Raju, G. R. and Gurumurthy, G. R. 1978 “Electron energy distributions and transport coefficients in  $\text{N}_2$  in  $E \times B$  fields” *International Journal of Electronics* **44**, 355–365.
- [18] Raju, G. and Dincer, M. 1990 “Monte Carlo simulation of electron swarms in nitrogen in uniform  $E \times B$  fields” *IEEE Trans Plasma Sci* **18**, 819–825.
- [19] Dincer, M. S., Tezcan, S. S., and Duzkaya, H. 2018 “Magnetic insulation in nitrogen subjected to crossed fields” *AIP Adv.* **8**, 095026.
- [20] Dias, T. C., Tejero-del-Caz, A., Alves, L. L., and Guerra, V. 2023 “The LisbOn KInetics Monte Carlo solver” *Comput. Phys. Commun.* **282**, 108554  
<https://github.com/IST-Lisbon/LoKI-MC>.
- [21] Reid, I. 1979 “An Investigation of the Accuracy of Numerical Solutions of Boltzmann’s Equation for Electron Swarms in Gases with Large Inelastic Cross Sections” *Aust. J. Phys.* **32**, 231.
- [22] Lucas, J. and Saelee, H. T. 1975 “A comparison of a Monte Carlo simulation and the Boltzmann solution for electron swarm motion in gases” *J. Phys. D Appl. Phys.* **8**, 640–650.

- [23] White, R. D., Robson, R. E., and Ness, K. F. 1995 “Anomalous anisotropic diffusion of electron swarms in A.C. electric fields” *Aust. J. Phys.* **48**, 925.
- [24] White, R. D., Robson, R. E., and Ness, K. F. 1999b “Nonconservative charged-particle swarms in ac electric fields” *Phys. Rev. E* **69**, 7457.
- [25] White, R. D., Brennan, M. J., and Ness, K. F. 1997 “Benchmark simulations for electron swarms in crossed electric and magnetic fields” *J. Phys. D Appl. Phys.* **30**, 810.
- [26] Raspopovic, Z. M., Sakadzic, S., Bzenic, S. A., and Petrovic, Z. L. 1999 “Benchmark calculations for Monte Carlo simulations of electron transport” *IEEE Trans. Plasma Sci.* **27**, 1241–1248.
- [27] Dujko, S., White, R. D., Petrović, Z. L., and Robson, R. E. 2010 “Benchmark calculations of nonconservative charged-particle swarms in DC electric and magnetic fields crossed at arbitrary angles” *Phys. Rev. E* **81** (4), 046403.
- [28] White, R. D., Ness, K. F., Robson, R. E., and Li, B. 1999 “Charged-particle transport in gases in electric and magnetic fields crossed at arbitrary angles: Multiterm solution of Boltzmann’s equation” *Phys. Rev. E* **60** (2), 2231–2249.
- [29] Ness, K. F. and Robson, R. E. 1986 “Velocity distribution function and transport coefficients of electron swarms in gases. II. Moment equations and applications” *Phys. Rev. A* **34** (3), 2185–2209.
- [30] N<sub>2</sub> and Ar on IST-Lisbon data, [www.lxcat.net](http://www.lxcat.net).
- [31] Heylen, A. E. D. and Dargan, C. L. 1973 “Electron-molecule collision frequencies in a crossed electric and magnetic field” *Int. J. Electron.* **35**, 433–451.
- [32] Loureiro, J. and Amorim, J. 2016 *Kinetics and Spectroscopy of Low Temperature Plasmas* John Wiley & Sons.
- [33] Asmussen, J. 1989 “Electron cyclotron resonance microwave discharges for etching and thin-film deposition” *J. Vac. Sci. Technol. A* **7**, 883–893.
- [34] Brennan, M. 1991 “Optimization of Monte Carlo codes using null collision techniques for experimental simulation at low  $E/N$ ” *IEEE Trans. Plasma Sci.* **19**, 256–261.
- [35] White, R. D., Dujko, S., Ness, K. F., Robson, R. E., Raspopović, Z., and Petrović, Z. L. 2008 “On the existence of transiently negative diffusion coefficients for electrons in gases in  $E \times B$  fields” *J. Phys. D: Appl. Phys.* **41**, 025206.
- [36] White, R. D., Dujko, S., Robson, R. E., Petrović, Z. L., and McEachran, R. P. 2010 “Non-equilibrium transport of positron and electron swarms in gases and liquids” *Plasma Sources Sci. Technol.* **19**, 034001.

# 6

## A close look at time-locality assumptions in nanosecond discharges

### Chapter summary

Obtaining a comprehensive solution of electron kinetics in gas discharges that accounts for dependencies in space, velocity and time is often unfeasible. Therefore, the electron behavior is frequently studied under one of two assumptions: the local-field approximation (LFA), which equates the solution of electron kinetics to the steady-state calculation with the local value of the reduced electric field ( $E/N$ ); the local-energy approximation (LEA), in which the rate coefficients and the electron power distribution among different collisional channels depend on the local value of the mean electron energy.

In this chapter, we focus on time-locality to assess the impact of the LFA and LEA assumptions on the calculation of the temporal evolution of electron kinetics in nanosecond discharges. To do so, we consider an accurate Monte Carlo (MC) time-dependent formulation as a golden standard. The MC formulation has been presented in previous chapters and is generalized here to include time-dependent  $E/N$  pulses. The study involves a nanosecond pulse mirroring typical conditions found in experiments. Moreover, we assess electron relaxation in two background gases (air and argon) and two pressures (10 and 100 Torr).

We find that the LEA generally provides more accurate results than the LFA, with increasing difference at lower pressures, where energy relaxation is slower. The greater accuracy of the LEA is due to the temporal effects introduced by the equation for the mean electron energy, which is absent in the LFA. Therefore, when a purely kinetic approach is not possible, the LEA should be adopted instead of the LFA.

Opting by the LFA can lead to serious degradation of model results. During the first nanoseconds, the excessively fast relaxation of the LFA leads to an overestimation of electron energy, resulting in an overvaluation of electron-impact ionization, dissociation and excitation. The exaggeration in ionization affects the electron density, which subsequently influences all heavy-species chemistry involving electron impact. The repercussions of the LFA can be even more pronounced during the late-decay phase of the pulse, where the LFA predicts a excessively fast decrease of electron energy. This inaccuracy is crucial because electron density can remain elevated for a considerable time after the pulse, influencing heavy-species chemistry. In repetitively-pulsed discharges, the accumulation of these systematic errors after each pulse could cause dramatic changes in the model predictions.

Finally, the comparison is extended to a two-term time-dependent solution (with a quasi-stationary approximation for the first anisotropy  $f_1$ ), using the LoKI-B solver. Notably, at the lower pressure of 10 Torr, the two-term approach cannot capture the initial transient non-equilibrium behavior.

## 6.1 Introduction

Interest in nanosecond-pulsed discharges (NPDs) is rapidly growing due to their remarkable non-equilibrium properties. However, their potential comes with considerable complexity, and a detailed study of the fundamental processes in the discharge is necessary to determine the most efficient configuration for a specific application. NPDs are characterized by very high reduced electric fields,  $E/N$ , that can be as high as  $\sim 1000$  Td, with rising times on the nanosecond timescale. These characteristics represent significant modeling challenges, particularly concerning electron kinetics and their coupling with heavy species.

The electron kinetics in gas discharges is described by the electron Boltzmann equation (EBE). However, obtaining a complete solution that accounts for dependencies in space, velocity and time is usually impractical. As a result, the electron behavior is often analyzed under one of two assumptions [1–3]. The first assumption, the local-field approximation (LFA) or the quasi-stationary approximation, equates the solution of the electron kinetics to the steady-state calculation of the EBE, using the local value (in space and time) of  $E/N$ . This approximation holds well when electron energy relaxation/thermalization is sufficiently fast. The second assumption is the local-energy approximation (LEA), in which the rate coefficients and the electron power distribution along different collisional channels depend on the local value of the mean electron energy. In this case, the EBE is typically solved for a wide range of  $E/N$  under steady-state conditions and the results are then converted into a lookup table as a function of the mean electron energy. Moreover, an additional equation for the mean electron energy is included, using the input power from the electric field and the power losses obtained from the lookup table.

It is important to acknowledge that while the two-term approximation to the EBE [4] is prevalent in modeling low-temperature plasmas, its adequacy for a specific system cannot be assured without benchmarking against more precise formulations, specially under extreme  $E/N$  values as in NPDs [5, 6].

Our study focuses on time-locality, assessing the impact of the LFA and LEA assumptions on the temporal evolution of electron kinetics in nanosecond pulses. Recent studies on the temporal relaxation of the electron kinetics following the instantaneous application of an electric field with fixed amplitude have been thoroughly reviewed by Boyle et al. [7]. For instance, investigations have been reported in He [8, 9], Xe [7, 10], Ne [11], Ar [9, 12], N<sub>2</sub> [8, 11, 13–15], N<sub>2</sub>-O<sub>2</sub> (air) [14, 16], and He-O<sub>2</sub> [17]. While most investigations focus on selected  $E/N$  values, the comprehensive study conducted by Boyle et al. [7] covers a broad range of  $E/N$  fields for Xe, revealing a pronounced dependence of thermalization time on  $E/N$ .

Regarding time-dependent  $E/N$  pulses, rather than step-like variations, studies of electron relaxation have been conducted in N<sub>2</sub> and N<sub>2</sub>-O<sub>2</sub> by Tejero-del-Caz et al. [14], where a time-dependent solution is compared with the LFA, and in He-O<sub>2</sub> by Bieniek, Walsh, and Hasan [17], where a time-dependent solution is compared with the LEA. However, these studies rely on the solution of the two-term Boltzmann equation along with a quasi-static approximation for the first anisotropy  $f_1$ . Besides the well-known

limitations of the former, the latter may not accurately capture the non-equilibrium behavior inherent in steep variations of  $E/N$ , as discussed in section 6.3 and in [8].

We should mention that the temporal relaxation of electron swarms in combined electric and magnetic fields has been studied in the recent years [18, 19] due to the appearance of interesting transient physical phenomena, such as transiently negative diffusion coefficients. However, such study is out of the work scope.

In this work, we employ the Monte Carlo techniques within LoKI-MC to investigate the temporal evolution of electron kinetics in nanosecond pulses, thereby obtaining the exact kinetic solution to the problem. The initial code version (detailed in chapter 3) was designed for configurations with homogeneous DC electric fields. Subsequently, its capabilities were expanded to accommodate AC/DC electric fields and DC magnetic fields, as discussed in chapter 5. Here, we further extend the formulation to arbitrary time-dependent electric fields. We then compare this accurate solution against the LFA, the LEA and the two-term time-dependent approaches in nanosecond pulses, varying the gas pressure (10 and 100 Torr) and considering both molecular ( $N_2-O_2$ ) and atomic (Ar) gases.

The chapter is structured as follows. Section 6.2 presents the theoretical background, where section 6.2.1 outlines the problem at the core of this study and the next three subsections elaborate on the different methods being compared in this research: section 6.2.2 introduces the time-dependent Monte Carlo solver; section 6.2.3 discusses the LFA and LEA assumptions; section 6.2.4 provides a concise overview of the two-term time-dependent solver. Section 6.3 presents and discusses the results obtained using the different methods. Section 6.4 closes the chapter with noteworthy observations and sets out future work.

## 6.2 Theoretical background

### 6.2.1 Problem statement

The focus of this chapter is the temporal evolution of electron kinetics in nanosecond  $E/N$  pulses under homogeneous conditions. We pay particular attention to selecting configurations that closely resemble those observed in experiments.

We use the following analytical expression for  $\frac{E}{N}(t)$  from Tejero-del-Caz et al. [14]:

$$\frac{E}{N}(t) = \frac{E_0}{N} \sqrt{\frac{t}{t_{\text{pulse}}}} \exp\left(-\frac{t}{t_{\text{pulse}}}\right), \quad (6.1)$$

where  $E_0/N = 500$  Td and  $t_{\text{pulse}} = 5$  ns. The corresponding temporal profile of  $E/N$  is illustrated in figure 6.1. It reaches a maximum value of approximately 300 Td after  $t = 2.5$  ns and decays to a value approximately 100 times lower after 32 ns. This expression mimics well typical profiles of nanosecond

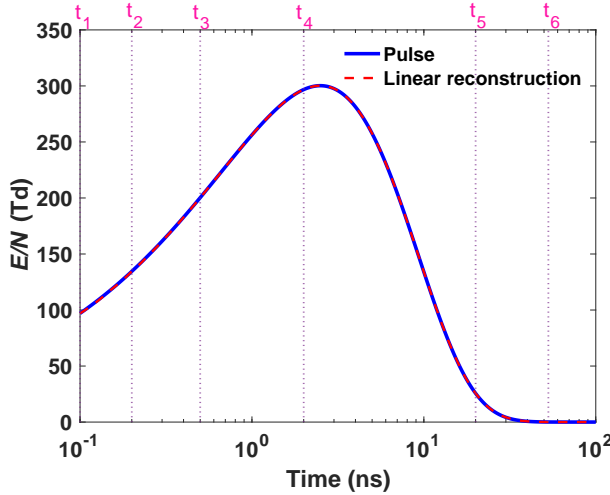


**Figure 6.1:** Reduced electric field pulse analyzed in this study, as defined by expression (6.1), with  $E_0/N = 500$  Td and  $t_{\text{pulse}} = 5$  ns. In addition, the figure presents a linear reconstruction of the  $E/N$  pulse, achieved by considering intervals between different slopes of 0.05 ns.

discharges; see, for instance, figure 6 in [20] and figure 2 in [21].

To assess the importance of collisionality in electron relaxation, we consider two gas pressure values: 10 and 100 Torr, which are commonly encountered in real conditions [20–22].

Finally, we investigate two distinct background gas mixtures, 80%N<sub>2</sub>-20%O<sub>2</sub> (air) and 100%Ar, in order to evaluate the electron kinetics across a wide range of conditions. In air, electron energy relaxation at low-to-medium energies is efficient and controlled by rotational and vibrational collisions, while in argon, it is less efficient and mainly controlled by elastic collisions. Consequently, the effectiveness of time-locality approximations may differ for these two background gas mixtures.

### 6.2.2 Monte Carlo time-dependent solver

The Monte Carlo algorithm implemented in LoKI-MC is detailed in chapter 3. It tracks the stochastic motion of multiple electrons over time, characterized by free flights punctuated with electron-neutral collisions. The time intervals between collisions are calculated according to the null-collision method, using a trial collision frequency denoted as  $\nu'$ . This frequency must be chosen sufficiently high to overestimate the total collision frequency. The overestimation of the collision frequency is then compensated by introducing null collisions, where no actual interaction takes place. The electron ensemble is synchronized at intervals of  $\nu'^{-1}$  in order to perform the sampling of swarm coefficients.

To ensure a constant number of electrons throughout the simulation, we employ a renormalization technique that adjusts particle counts to balance attachments and ionizations. However, as our goal is to study the temporal evolution across various time scales, we have incorporated the flexibility to track different numbers of electrons over different time intervals. This approach allows us to follow a large number of electrons ( $10^6 - 10^7$ ) during the rise and early decay of the pulse, a moderate number

$(10^5 - 10^6)$  during the midterm decay, and a smaller number  $(10^4 - 10^5)$  during the late decay phase. In this way, we can keep the computation time low, around tens of minutes, while ensuring good statistics for each time decade of interest.

When incorporating time-dependent electric fields, the free-flight integration needs to be modified. We divide the electron motion into smaller intervals, during which the electric field  $E$  varies linearly as  $\mathbf{E}(t_0 + \delta t) = -(E_0 + A\delta t)\mathbf{e}_z$ . The analytical solution for electron position and velocity between time instants  $t_0$  and  $t_0 + \delta t$  is as follows:

$$\begin{cases} x(t_0 + \delta t) = x_0 + v_{x0}\delta t \\ y(t_0 + \delta t) = y_0 + v_{y0}\delta t \\ z(t_0 + \delta t) = z_0 + v_{z0}\delta t + \frac{e\delta t^2}{m}(E_0/2 + A\delta t/6) \end{cases}, \quad \begin{cases} v_x(t_0 + \delta t) = v_{x0} \\ v_y(t_0 + \delta t) = v_{y0} \\ v_z(t_0 + \delta t) = v_{z0} + \frac{e\delta t}{m}(E_0 + A\delta t/2) \end{cases}. \quad (6.2)$$

Here,  $e$  and  $m$  represent the electron charge and mass, respectively. In the conditions of this study, assuming a single linear variation of the electric field along the free flight is accurate. The quality of this approximation is evident in figure 6.1, where the linear reconstruction is compared against the original  $E/N$  profile. It is important to note that the time interval used for the linear electric field variation is always equal to or smaller than the synchronization time. In the worst-case scenario under study, involving argon at 10 Torr, the synchronization time is approximately 0.01 ns. In the linear reconstruction example, we use a time interval five times larger than this value, specifically 0.05 ns. To further confirm the accuracy of this approach, we have divided the motion into 100 smaller parts and found no visible deviation of the results from the single-linear case.

### 6.2.3 The local-field and local-energy approximations

For a rigorous discussion on how the local-field and local-energy approximations appear in the context of fluid modelling, starting from the general electron Boltzmann equation, the reader is referred to the works by Dujko et al. [1] and Becker and Loffhagen [3].

The local-field approximation (LFA) involves calculating steady-state electron kinetics while assuming locality both in space and time. In this case, the electron energy distribution function (EEDF), the rate-coefficients and the transport parameters explicitly depend on the local and instantaneous value of  $E/N$ . This approximation remains valid as long as electron energy relaxation is faster than the characteristic time of  $E/N$  variation.

In the local-energy approximation (LEA), an equation for the mean electron energy  $\langle \epsilon \rangle$  is introduced, which can be expressed as follows [1, 3]:

$$\frac{\partial(n_e \langle \epsilon \rangle)}{\partial t} = en_e \mu_e E^2 + n_e P_{\text{coll}} + \Theta_{\text{transp}}. \quad (6.3)$$

Here,  $n_e$  is the electron density,  $\mu_e$  is the electron mobility and  $P_{\text{coll}}$  is the net power transferred by

collisions per electron. The term  $\Theta_{\text{transp}}$  represents a transport contribution that we omit since our focus is on temporal effects. Therefore, in homogeneous conditions, the equation for mean energy becomes:

$$\frac{d\langle\epsilon\rangle}{dt} = e\mu_e E^2 + P_{\text{coll}} - \langle\nu_{\text{eff}}\rangle\langle\epsilon\rangle, \quad (6.4)$$

where  $\langle\nu_{\text{eff}}\rangle$  denotes the average effective ionization frequency and  $-\langle\nu_{\text{eff}}\rangle\langle\epsilon\rangle$  represents the contribution of the electron growth (cf. section 3.2.7). In the context of the LEA,  $\mu_e$ ,  $P_{\text{coll}}$  and  $\nu_{\text{eff}}$  are considered functions of the mean electron energy  $\langle\epsilon\rangle$ . The approximated dependencies for these quantities are derived by solving steady-state electron kinetics across a wide range of  $E/N$  and then parameterizing the results as functions of  $\langle\epsilon\rangle$  [2, 23].

Lastly, in this work, we employ LoKI-MC for the accurate solution of steady-state electron kinetics, required for LFA and LEA, ensuring that any deviations from the exact time-dependent solutions arise due to the time-locality approximations.

#### 6.2.4 Two-term time-dependent solver

In addition to the calculations described in the previous sections, we employ the electron kinetics solver LoKI-B to solve the time-dependent electron Boltzmann equation (EBE) under the two-term approximation, as detailed by Tejero-del-Caz et al. [14, 24], aiming to evaluate the quality of the approach. For completeness, we provide an overview of the primary approximations involved in LoKI-B, while avoiding intricate mathematical details.

As a starting point, we assume that the *homogeneous* electron velocity distribution function, denoted as  $f_e(\mathbf{v}, t)$ , can be expanded in Legendre polynomials with respect to the velocity vector  $\mathbf{v}$ :

$$f_e(\mathbf{v}, t) = \sum_l f_l(v, t) P_l(\cos\theta) \simeq f_0(v, t) + f_1(v, t) \cos\theta. \quad (6.5)$$

Here,  $P_l(\cos\theta)$  is the Legendre polynomial of order  $l$ ;  $\theta$  is the polar angle of  $\mathbf{v}$  relative to the anisotropy direction (defined by the electric field);  $f_0$  and  $f_1$  correspond to the isotropic and first anisotropic components of the electron velocity distribution function, respectively. When written in terms of energy  $u$ , the isotropic part  $f_0(u, t)$  corresponds to the EEDF, normalized such that  $\int_0^\infty f_0(u, t) \sqrt{u} du = 1$ . Let us note that neglecting higher order terms in the Legendre expansion is only accurate if anisotropies are sufficiently low.

Upon inserting this expansion into the homogeneous EBE, we derive two equations: one for  $\frac{\partial f_0}{\partial t}$ , which depends on  $f_0$  and  $f_1$ , and another for  $\frac{\partial f_1}{\partial t}$ , which also depends on  $f_0$  and  $f_1$ . For higher order Legendre expansions, the second equation would involve  $f_2$  as well. Additionally, we assume that the term  $\frac{\partial f_1}{\partial t}$  can be neglected and is set to zero. This implies that the relaxation of  $f_1$  occurs significantly faster than that of  $f_0$  and the electric field  $E$ . This approximation holds well when the frequency of

momentum transfer is much larger than the characteristic frequencies of energy relaxation (typically the case) and the variation of  $E$ . Under this assumption,  $f_1$  can be expressed as a function of  $f_0$ , and  $\frac{\partial f_0}{\partial t}$  can be simplified to depend solely on  $f_0$ . Then, the equation for  $f_0$  can be solved over time. It is worth noting that the quasi-static assumption for  $f_1$  serves only to simplify the complexity of the system and is independent of the two-term approximation. However, in regions where the electric field variation is steep, this assumption may impact the accuracy of the solution, as demonstrated in the next section.

## 6.3 Results

This section presents the results of electron kinetics under the conditions outlined in section 6.2.1, comparing the rigorous Monte Carlo time-dependent approach with the other approximate methods described in sections 6.2.2 - 6.2.4. We begin by analyzing the temporal evolution of the electron swarm coefficients. Next, we discuss the importance of quantifying the characteristic relaxation frequencies. Finally, we examine EEDFs at various time instants.

### 6.3.1 Electron swarm coefficients

We start by detailing the time evolution of electron swarm coefficients in air, under the application of the  $E/N$  pulse depicted in figure 6.1. Figure 6.2 illustrates the temporal evolution of the mean electron energy ( $\langle \epsilon \rangle$ ), drift velocity ( $v_d$ ) and ionization coefficient ( $k_{\text{ion}}$ ), up to 100 ns, for conditions at (a) 10 Torr and (b) 100 Torr.

At 10 Torr (see figure 6.2a), the evolution of  $\langle \epsilon \rangle$  calculated by the local-field approximation (LFA) differs significantly from the rigorous time-dependent Monte Carlo (MC) approach. This discrepancy arises because at lower pressures electrons do not collide rapidly enough to adapt to fast  $E/N$  variations. After approximately 2 ns, the LFA and time-dependent calculations begin to converge. However, around 20 ns, when the  $E/N$  pulse has decayed to 25 Td, the LFA again deviates from the time-dependent solution. A similar trend is found for  $v_d$ . Notably, during the initial 2 ns, the LFA significantly overestimates electron production, quantified by the value of  $k_{\text{ion}}$ .

Both the LEA and two-term time-dependent approaches capture  $\langle \epsilon \rangle$ ,  $v_d$  and  $k_{\text{ion}}$  results closer to the time-dependent MC results than the LFA. Interestingly, the LEA and two-term outcomes of  $\langle \epsilon \rangle$  and  $v_d$  exhibit striking similarity during the first 0.2 ns. This resemblance arises due to shared approximations in the two methods: (i) the two-term time-dependent solution calculates the first anisotropy  $f_1$  using a quasi-static approximation, wherein  $f_1$  depends on instantaneous  $E/N$  and  $f_0$  values; (ii) in the LEA approach, electron mobility  $\mu_e$  (linked to  $f_1$ ) is computed using steady-state calculations parametrized as a function of the mean electron energy. These approximations also influence  $\langle \epsilon \rangle$  evolution, as Joule heating power depends on  $f_1$  or  $\mu_e$ . Nevertheless, these approximations yield satisfactory results after 0.2

ns. In the late pulse-decay phase, the two-term time-dependent solution aligns closely with the rigorous solution, while the LEA slightly deviates, although still closer than the LFA.

At 100 Torr (see figure 6.2a), where electron collisions are significantly more frequent than at 10 Torr, the LFA is valid over a broader time interval, being satisfactory from 0.4 ns to 30 ns. For clarity in the presentation of results, the two-term time-dependent solution is omitted from the figure in this case, although it closely matches the MC time-dependent calculation. Similar to the 10 Torr case, the LEA offers a better description than the LFA.

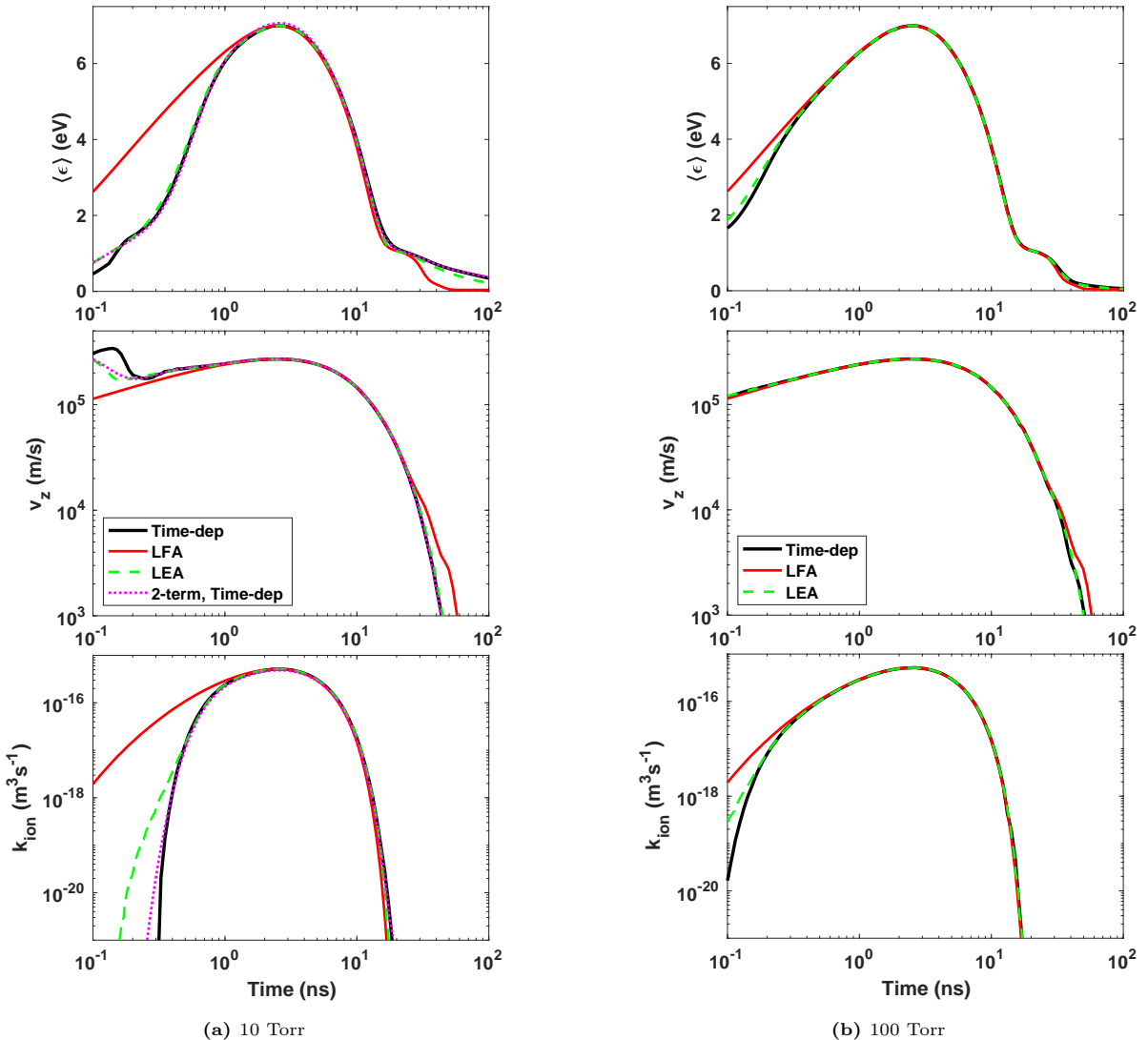


**Figure 6.2:** Temporal evolution of the mean electron energy ( $\langle \epsilon \rangle$ ), drift velocity ( $v_d$ ) and ionization coefficient ( $k_{ion}$ ), in air, at (a) 10 Torr and (b) 100 Torr conditions.

To demonstrate the influence of time-locality approximations on heavy-species chemistry, figure 6.3 illustrates the temporal evolution of electron-impact  $\text{O}_2$  dissociation (top),  $e + \text{O}_2(\text{X}) \rightarrow e + 2\text{O}({}^3\text{P})$ , and  $\text{N}_2^+$  dissociative recombination (bottom),  $e + \text{N}_2^+ \rightarrow 2\text{N}$ . At 10 Torr, during the initial nanosecond,  $\text{O}_2$  dissociation is strongly overestimated by the LFA and  $\text{N}_2^+$  dissociative recombination is underestimated. After 10–20 ns,  $\text{O}_2$  dissociation is underestimated by the LFA and  $\text{N}_2^+$  dissociative recombination is considerably overestimated. The pronounced overestimation of dissociative recombination must be highlighted, as it is one of the primary processes leading to electron loss. Therefore, the LFA may predict a much faster decay of electrons, which would subsequently influence the overall chemistry during the late decay phase. Once again, the LEA provides a much better result, albeit not perfect. At 100 Torr, the differences between the various approaches are smaller yet still discernible.

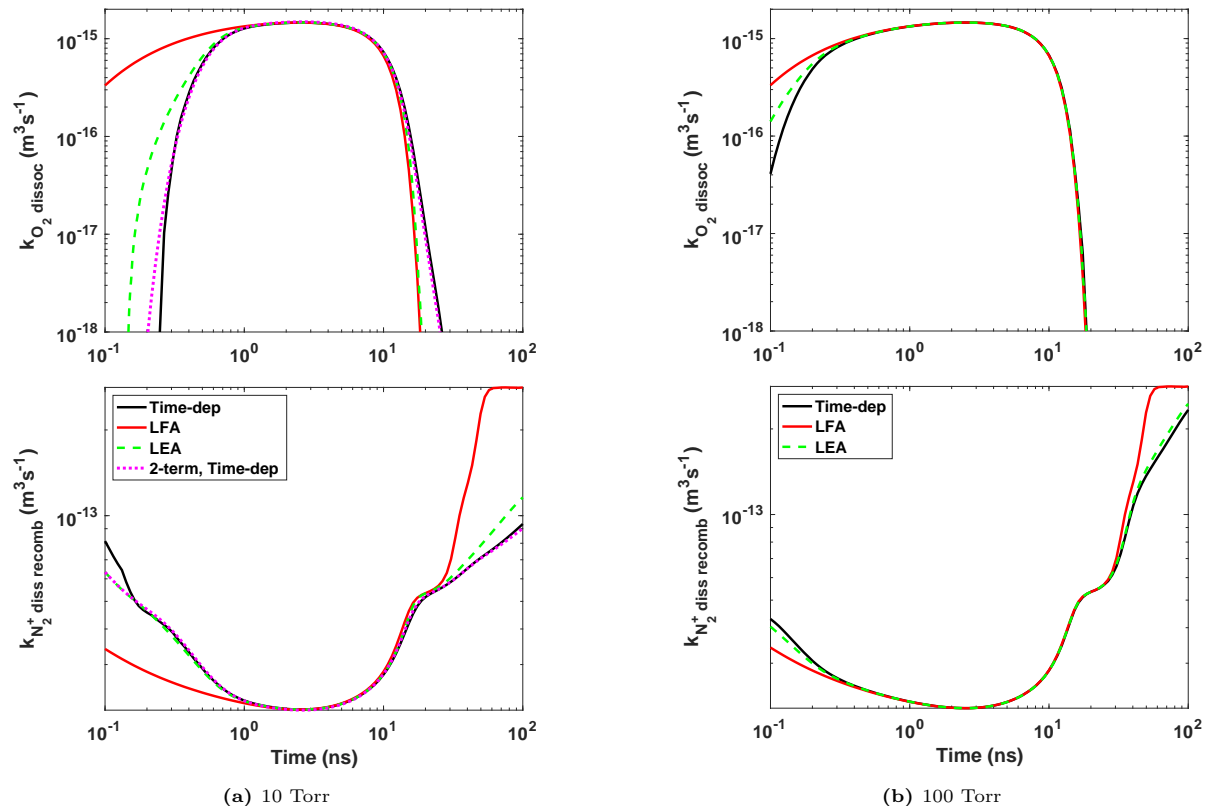


**Figure 6.3:** Temporal evolution of electron-impact  $\text{O}_2$  dissociation (top),  $e + \text{O}_2(\text{X}) \rightarrow e + 2\text{O}({}^3\text{P})$ , and  $\text{N}_2^+$  dissociative recombination (bottom),  $e + \text{N}_2^+ \rightarrow 2\text{N}$ , in air, at (a) 10 Torr and (b) 100 Torr conditions.

Next, we proceed to analyze the behavior in argon, where energy relaxation is generally much weaker. Figure 6.4 illustrates the temporal evolution of  $\langle \epsilon \rangle$ ,  $v_d$ , and  $k_{\text{ion}}$ , up to 1  $\mu\text{s}$ , for conditions at (a) 10 and (b) 100 Torr. The disparity between the LFA and rigorous time-dependent methods is even more pronounced in argon compared with air. The dramatic failure of the LFA in describing the late decay arises from the low energy-relaxation frequency of argon, as detailed in the following section. Both the

LEA and two-term time-dependent solutions provide much better descriptions than the LFA. However, similar to observations in air, neither of these approaches can accurately capture the steep increase of  $v_d$  during the first 0.2 ns. The two-term time-dependent solution matches the late decay perfectly, while the LEA yields satisfactory results. At 100 Torr, the LFA shows good results during the pulse rise after 0.3 ns but still fails notably for times longer than 30 ns, due to the assumed instantaneous adjustment of the EEDF to the reduced field when the energy relaxation is actually slow.

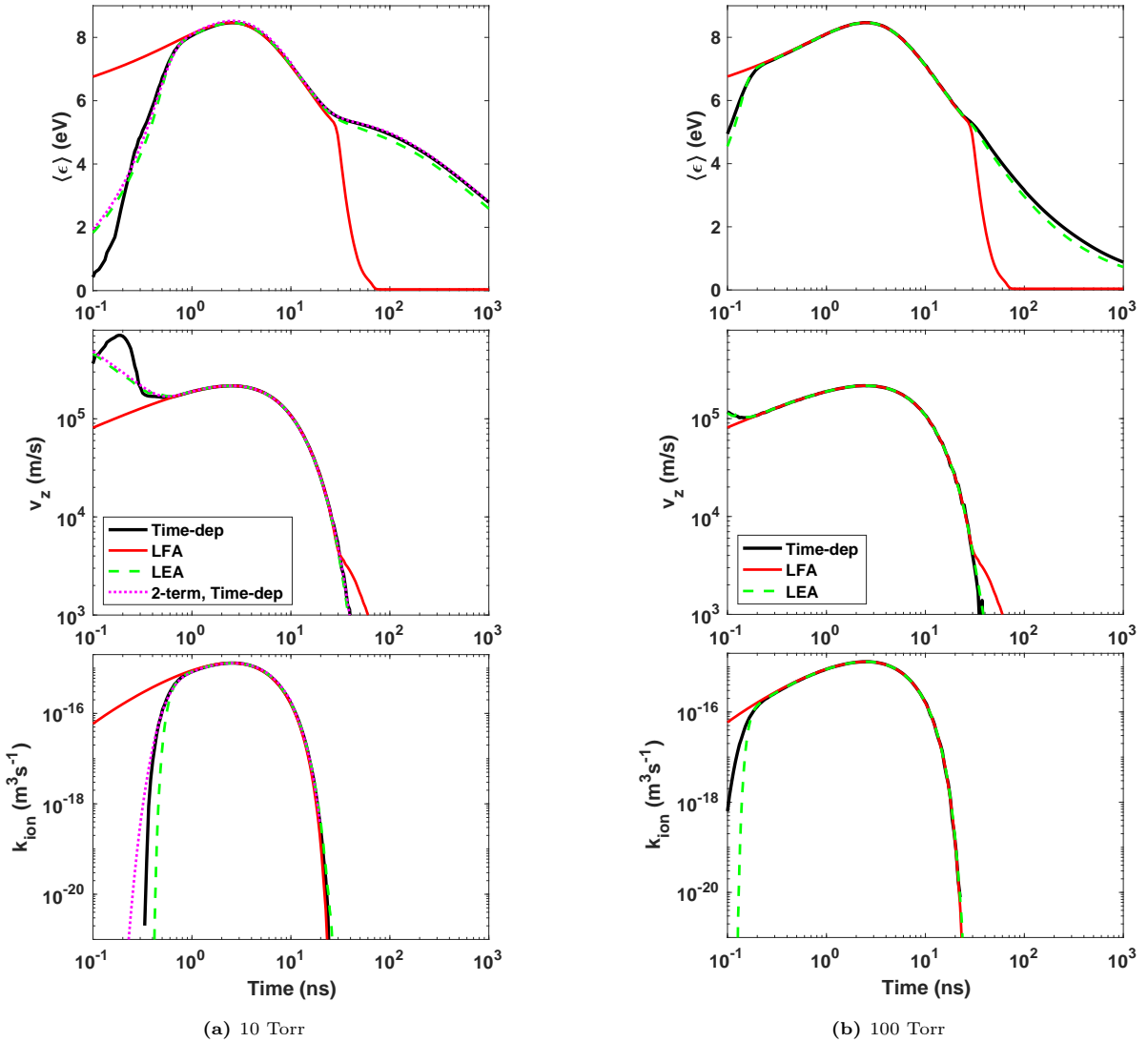


**Figure 6.4:** Temporal evolution of the mean electron energy ( $\langle \epsilon \rangle$ ), drift velocity ( $v_d$ ) and ionization coefficient ( $k_{ion}$ ), in argon, at (a) 10 Torr and (b) 100 Torr conditions.

### 6.3.2 Characteristic relaxation frequencies

The analysis of the characteristic relaxation frequencies can provide further insight into the deviations of different time-locality approximations from the accurate time-dependent solution and establish quantitative criteria to anticipate their domains of validity. The relaxation efficiency is determined by both the frequency of momentum transfer ( $\nu_m$ ) and the frequency of energy relaxation ( $\nu_\epsilon$ ). These frequencies can be estimated in the following way [25, 26]:

$$\nu_m(\epsilon) = \sqrt{\frac{2\epsilon e}{m}} \sum_i n_i \sigma_{m,i}(\epsilon), \quad (6.6)$$

$$\nu_\epsilon(\epsilon) = \sqrt{\frac{2\epsilon e}{m}} \left\{ \sum_{i \in \text{elast}} \frac{2m}{M_i} n_i \sigma_i(\epsilon) + \sum_{i \in \text{rot,vib,elec,ion}} \frac{|\Delta\epsilon_i|}{\epsilon} n_i \sigma_i(\epsilon) + \sum_{i \in \text{att}} n_i \sigma_i(\epsilon) \right\}. \quad (6.7)$$

Here,  $\epsilon$  is the electron energy in eV;  $n_i$  and  $M_i$  are the density and mass of the heavy target in collision  $i$ ;  $\sigma_{m,i}(\epsilon)$  and  $\sigma_i(\epsilon)$  are the corresponding momentum-transfer and integral cross sections, respectively, and they match under the assumption of isotropic scattering;  $\Delta\epsilon_i$  is the inelastic energy transfer, which is negative for inelastic collisions and positive for superelastic collisions. As expressed in equations (6.6) and (6.7), for momentum transfer, the sum is equally performed over all collision types, whereas for energy relaxation, the sum is separated into three parts: (i) elastic collisions; (ii) rotational, vibrational, electronic and ionization collisions; (iii) attachment collisions.

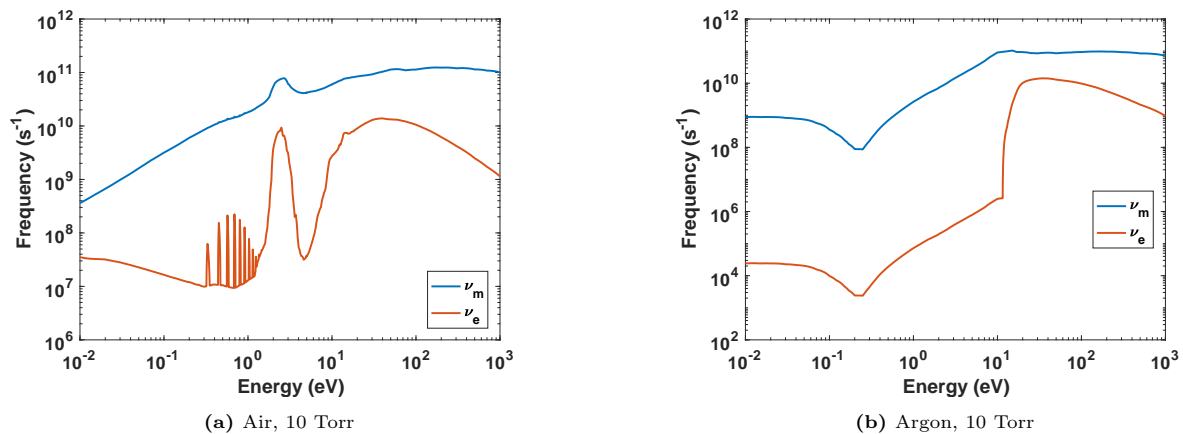
The energy-dependent frequencies  $\nu_m$  and  $\nu_\epsilon$  are depicted in figure 6.5, considering the lowest pressure of 10 Torr for the two background mixtures: (a) air and (b) argon. In both gases,  $\nu_m \gg \nu_\epsilon$ , which is expected. Furthermore,  $\nu_m$  and  $\nu_\epsilon$  show strong dependence on electron energy.

In the case of air,  $\nu_m$  exhibits a monotonically increasing trend with electron energy, except for a localized structure between 1 and 4 eV, where vibrational excitation of N<sub>2</sub> dominates. The spikes in  $\nu_\epsilon$  starting from 0.3 eV are attributed to resonance peaks in vibrational excitation of O<sub>2</sub>, while the relatively large values of  $\nu_\epsilon$  between 1 and 4 eV are due to vibrational excitation of N<sub>2</sub>. The deep in  $\nu_\epsilon$  at around 4.5 eV is a consequence of reduced vibrational excitation, and the rapid increase thereafter is associated with the excitation of higher-energy electronic states and ionization. The significant decrease in  $\nu_\epsilon$  after 100 eV is due to diminutions in both the magnitude of cross-sections and the ratios  $\frac{|\Delta\epsilon_i|}{\epsilon}$ .

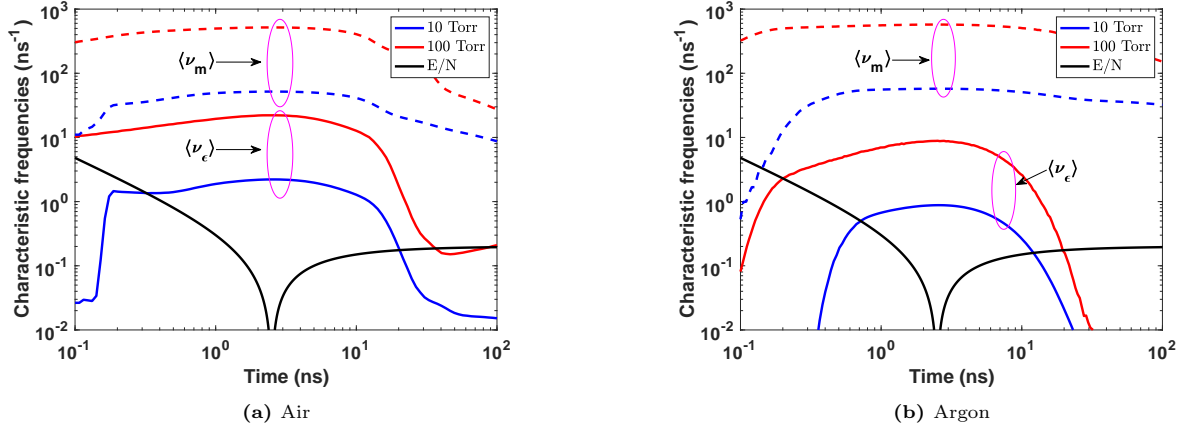
In argon, momentum transfer and energy relaxation are entirely controlled by elastic collisions up to approximately 12 eV. Consequently, in this interval, the trends of  $\nu_m$  and  $\nu_\epsilon$  mirror the shape of the elastic cross section, featuring the well-known Ramsauer minimum around 0.25 eV. Moreover, in the same region,  $\nu_\epsilon/\nu_m = \frac{2m}{M} \approx 2.7 \times 10^{-5}$ , indicating that energy relaxation is much less efficient than momentum transfer. The sharp increase of  $\nu_\epsilon$  after 12 eV is caused by the emergence of strong inelastic processes, including electronic excitations and ionization.

Figure 6.6 compares the temporal evolutions of the typical  $E/N$  variation frequency, defined as  $\nu_{E/N} = \left| \frac{d(E/N)}{dt} \right| / (E/N)$ , and the energy-averaged frequencies  $\langle \nu_m \rangle$  and  $\langle \nu_\epsilon \rangle$ , for both (a) air and (b) argon, at pressures of 10 and 100 Torr. In both air and argon,  $\langle \nu_m \rangle$  and  $\langle \nu_\epsilon \rangle$  exhibit variations across different orders of magnitude, corresponding to distinct mean electron energies. This figure demonstrates that in a considerable range of electron energies, the characteristic relaxation frequencies can be comparable to, or even much smaller than, the typical  $E/N$  variation frequency.

Temporal non-locality is better assessed by calculating the ratios  $\nu_{E/N}/\langle \nu_m \rangle$  and  $\nu_{E/N}/\langle \nu_\epsilon \rangle$ , which compare how fast is  $E/N$  varying with how fast are momentum and energy relaxing, respectively. These ratios are represented in figure 6.7 for both gases and both pressures. Starting with the analysis at 10 Torr, in both air and argon,  $\nu_{E/N}/\langle \nu_m \rangle \ll 1$  is not verified during the initial 0.2 ns. Therefore, the assumption of instantaneous relaxation of anisotropies is invalid within this interval, and the LEA and two-term time-dependent approaches provide inaccurate results. However, this assumption begins to hold well for later times. Concerning energy relaxation during the pulse rise,  $\nu_{E/N}/\langle \nu_\epsilon \rangle \ll 1$  only occurs after 1 ns, which is roughly when the LFA provides reasonable results. During the pulse decay, as electron energy and energy relaxation decrease significantly,  $\nu_{E/N}/\langle \nu_\epsilon \rangle \gtrsim 1$  after 10–20 ns, causing local energy relaxation to break down and the LFA to become inaccurate. However, momentum transfer remains sufficiently fast, with  $\nu_{E/N}/\langle \nu_m \rangle \ll 1$ . At 100 Torr, momentum transfer is efficient throughout the pulse in both gases. The increased collisionality enhances energy relaxation, but it remains insufficient to make the LFA accurate during the pulse rise and, specially, during the pulse decay. This discrepancy is more pronounced in argon, where for times longer than 20 ns,  $\nu_{E/N}/\langle \nu_\epsilon \rangle \gg 1$ .



**Figure 6.5:** Energy-dependent frequencies of momentum transfer ( $\nu_m$ ) and energy relaxation ( $\nu_\epsilon$ ), at 10 Torr, in (a) air and (b) argon.



**Figure 6.6:** Temporal evolution of energy-averaged frequencies of momentum transfer ( $\langle \nu_m \rangle$ , dashed) and energy relaxation ( $\langle \nu_e \rangle$ , full), at 10 and 100 Torr, in (a) air and (b) argon. The characteristic frequency of  $E/N$  variation ( $\nu_{E/N}$ ) is represented with full black lines.

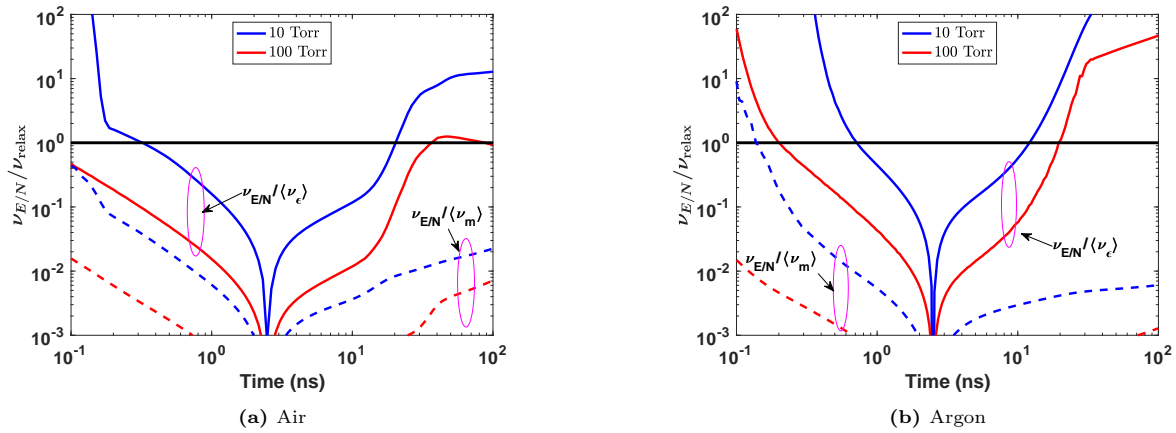


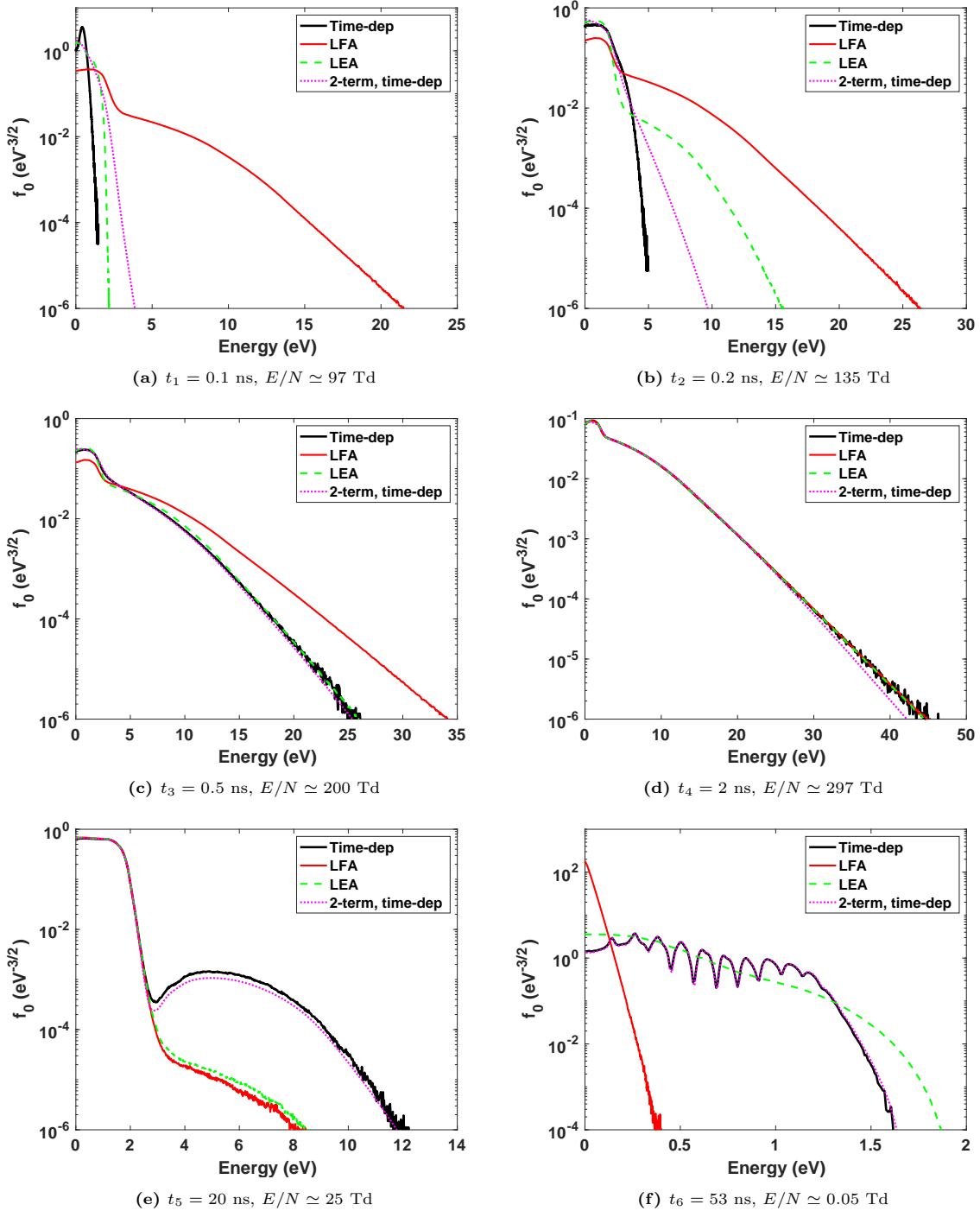
**Figure 6.7:** Temporal evolution of  $\nu_{E/N}/\langle \nu_m \rangle$  (dashed) and  $\nu_{E/N}/\langle \nu_e \rangle$  (full), at 10 and 100 Torr, in (a) air and (b) argon.

### 6.3.3 Distribution functions

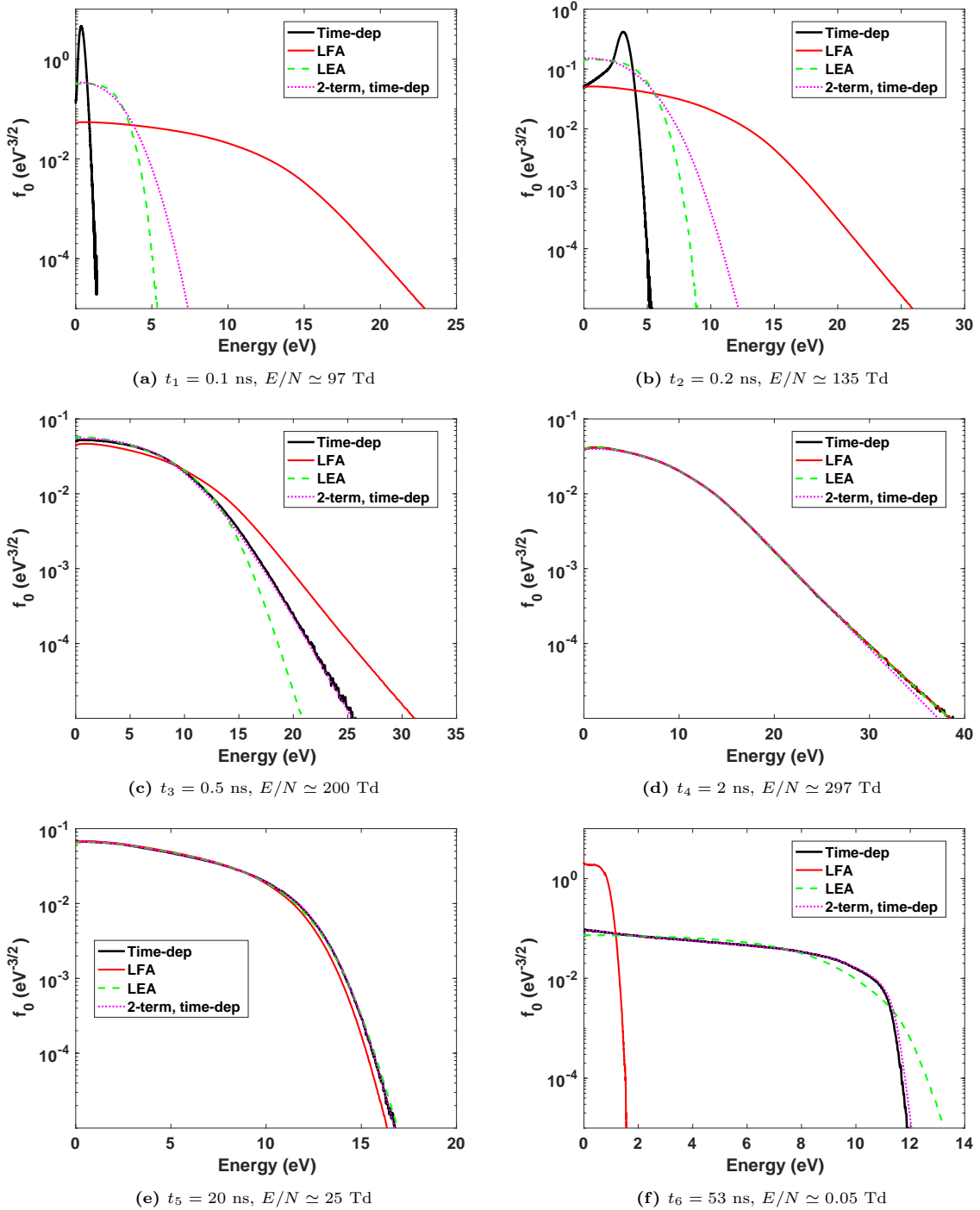
The strong energy dependence of relaxation frequencies, as demonstrated in figure 6.5, suggests that the time-dependent EEDFs can exhibit transient shapes significantly divergent from the typical steady-state ones.

Figure 6.8 showcases the EEDFs in air at six time points  $t_1 - t_6$  throughout the pulse (marked in figure 6.1), considering the lower pressure of 10 Torr. The corresponding instantaneous values of  $E/N$  are indicated in the captions of figure 6.8. At  $t_1 = 0.1$  ns and  $t_2 = 0.2$  ns, neither the LFA, the LEA nor the two-term time-dependent approaches capture the transient characteristics of the distribution. By  $t_3 = 0.5$  ns, the LEA and two-term time-dependent approaches begin to provide an accurate description, as momentum transfer is fast compared with the field variation. At  $t_4 = 2$  ns, temporal locality induces convergence among all four approaches. The minor deviation of the two-term time-dependent solution stems from a breakdown of the two-term approximation and not from temporal non-locality. By  $t_5 = 20$  ns, when the pulse has decayed to  $E/N \simeq 25$  Td, the various approximate approaches still predict well the values of the distribution up to 3 eV, but the LFA and LEA fail thereafter due to a decrease of energy-relaxation frequency (cf. figure 6.5a). This pronounced non-equilibrium characteristic can only be captured with kinetic descriptions like MC or two-term time-dependent approaches. Lastly, at  $t_6 = 53$  ns, with  $E/N$  having fallen to 0.05 Td, the LFA completely fails, and the LEA can only crudely replicate the distribution shape. Notably, the intriguing features in the EEDF are directly associated with spikes in  $\nu_e$ , as shown in figure 6.5a. Evidently, the differences in the EEDFs between the different approximations directly translate into the differences in the rate coefficients for  $O_2$  dissociation and  $N_2^+$  recombination shown in figure 6.3, which will have an impact in any time-dependent description of the plasma.

Figure 6.9 depicts the EEDFs in argon at the same time instances  $t_1 - t_6$  and 10 Torr. For the initial four time points, conclusions parallel those in air. At  $t_1 = 0.1$  ns and  $t_2 = 0.2$  ns, the non-equilibrium profile cannot be described with the three approximate methods. At  $t_3 = 0.5$  ns, the LEA and two-term time-dependent techniques already give good results. At  $t_4 = 2$  ns, electron kinetics attains quasi-static conditions and all time-locality approximations are valid. By  $t_5 = 20$  ns, the LFA fails in the high-energy tail, while the LEA and two-term time-dependent methods match the rigorous time-dependent solution. Finally, at  $t_6 = 53$  ns, the LFA completely collapses and the LEA still gives roughly good results, albeit with an overestimation of the high-energy tail. Again, the breakdown of the LFA may have a significant impact on the chemical description in the after-pulse phase.



**Figure 6.8:** EEDFs in air, at 10 Torr, for different time instants  $t_1$  -  $t_6$ .



**Figure 6.9:** EEDFs in argon, at 10 Torr, for different time instants  $t_1 - t_6$ .

## 6.4 Final remarks

This investigation has explored different techniques for modelling homogeneous electron kinetics in time-dependent  $E/N$  pulses, namely: the rigorous time-dependent Monte Carlo (MC), the local-field approximation (LFA), the local-energy approximation (LEA) and the two-term time-dependent methods. The latter has been studied using the open-source LoKI-B solver, which is detailed in [14, 24]. The steady-state results of electron kinetics, supporting the LFA and LEA approaches, were obtained through accurate MC calculations to ensure that any deviations arose from temporal non-locality. This study focused on electron relaxation within a typical nanosecond pulse, considering two background gases (air and argon) and two pressures (10 and 100 Torr).

From the comparison with accurate time-dependent MC solutions, it is evident that, in general, the LEA provides more accurate results than the LFA. This improvement in accuracy can be attributed to the temporal effects introduced by the equation for the mean electron energy in the LEA, which are absent in the LFA. For this reason, when a purely kinetic approach is not possible, the LEA should be adopted instead of the LFA. This recommendation is in line with other investigations in the community [1, 2].

At the lower pressure of 10 Torr, the typical two-term time-dependent solution (with a quasi-stationary approximation for the first anisotropy  $f_1$ ) cannot capture the initial transient non-equilibrium. However, at longer times, in this case, 0.2 ns, when momentum transfer becomes faster than the field variation,  $f_1$  approximates stationarity and the assumption holds well. Similar conclusions have been reported, for example, by Loffhagen and Winkler [8] and by Vialletto in chapter 2 of [27]. An analogous behavior is observed for the LEA method, which relies on steady-state mobilities parametrized as a function of mean electron energy.

We studied the EEDFs at various time instances and found rather exotic distributions at longer times, associated with varying relaxation rates at different energies. The accurate description of such distributions can only be achieved with a kinetic temporal formulation.

Since the LFA is commonly used, it is important to highlight the potential impacts of this approximation on results accuracy, specially at lower pressures. During the first nanosecond, the excessively fast relaxation of the LFA leads to an overestimation of electron energy, resulting in an overvaluation of electron-impact ionization, dissociation and excitation. The exaggeration in ionization affects the electron density, which subsequently influences all heavy-species chemistry involving electron impact. The repercussions of the LFA can be even more pronounced during the late-decay phase of the pulse. As  $E/N$  vanishes, the LFA predicts a strong decrease of electron energy, but energy relaxation might not be fast enough to adapt to the field decrease. This inaccuracy is crucial because electron density can remain elevated for a considerable time after the pulse, influencing heavy-species chemistry. In fact, figure 6.3 shows that the LFA can strongly overestimate dissociative recombination, a significant path for electron loss. This, in turn, influences the overall chemistry of heavy species. In repetitively-pulsed discharges,

the accumulation of these systematic errors after each pulse can lead to dramatic changes in the model predictions.

We have demonstrated that a thorough comparison between the characteristic frequencies of momentum transfer and energy relaxation, in conjunction with the rate of  $E/N$  variation, delineates the domains of validity for time-locality approximations, such as LFA and LEA. Temporal discrimination is fundamental in this examination, as mean electron energies and, consequently, relaxation frequencies, vary significantly over time.

In the future, a similar study could be conducted under the influence of a constant magnetic field. Furthermore, we plan to assess the effect of excited states on the electron kinetics and vice-versa. In many investigations, temporal and spatial evolution of electron kinetics is calculated under the “ground-state approximation”, where the evolution of the heavy-target chemistry is not considered. This can affect the quality of the electron kinetics solution, which then affects the heavy-species chemistry, and we aim to quantify under which conditions this approximation is satisfactory.

## References

- [1] Dujko, S., Markosyan, A. H., White, R. D., and Ebert, U. 2013 “High-order fluid model for streamer discharges: I. Derivation of model and transport data” *J. Phys. D: Appl. Phys.* **46**, 475202.
- [2] Grubert, G. K., Becker, M. M., and Loffhagen, D. 2009 “Why the local-mean-energy approximation should be used in hydrodynamic plasma descriptions instead of the local-field approximation” *Phys. Rev. E* **80** (3), 036405.
- [3] Becker, M. and Loffhagen, D. 2013 “Derivation of Moment Equations for the Theoretical Description of Electrons in Nonthermal Plasmas” *Adv. Pure Appl. Math.* **3**, 343–352.
- [4] Phelps, A. V. and Pitchford, L. C. 1985 “Anisotropic scattering of electrons by N<sub>2</sub> and its effect on electron transport” *Phys. Rev. A* **31** (5), 2932–2949.
- [5] White, R., Robson, R., and Ness, K. 1999 “On approximations involved in the theory of charged particle transport in gases in electric and magnetic fields at arbitrary angles” *IEEE Trans Plasma Sci* **27**, 1249–1253.
- [6] Dias, T. C., Tejero-del-Caz, A., Alves, L. L., and Guerra, V. 2023 “The LisbOn KInetics Monte Carlo solver” *Comput. Phys. Commun.* **282**, 108554  
<https://github.com/IST-Lisbon/LoKI-MC>.
- [7] Boyle, G. J., Casey, M. J. E., Cocks, D. G., White, R. D., and Carman, R. J. 2019 “Thermalisation time of electron swarms in xenon for uniform electric fields” *Plasma Sources Sci. Technol.* **28**, 035009.
- [8] Loffhagen, D. and Winkler, R. 1996a “Multi-term treatment of the temporal electron relaxation in He, Xe and N<sub>2</sub> plasmas” *Plasma Sources Sci. Technol.* **5**, 710.

- [9] Trunec, D., Španěl, P., and Smith, D. 2003 “The influence of electron–electron collisions on electron thermalization in He and Ar afterglow plasmas” *Chem. Phys. Lett.* **372**, 728–732.
- [10] Loffhagen, D. and Winkler, R. 1996b “Time-dependent multi-term approximation of the velocity distribution in the temporal relaxation of plasma electrons” *J. Phys. D: Appl. Phys.* **29**, 618.
- [11] Winkler, R., Loffhagen, D., and Sigeneger, F. 2002 “Temporal and spatial relaxation of electrons in low temperature plasmas” *Appl. Surf. Sci.* **192**, 50–71.
- [12] Trunec, D., Bonaventura, Z., and Nečas, D. 2006 “Solution of time-dependent Boltzmann equation for electrons in non-thermal plasma” *J. Phys. D: Appl. Phys.* **39**, 2544.
- [13] Li, Y. M. 1990 “Nonequilibrium Effects in Electron Transport at High E/n” in: *Nonequilibrium Effects in Ion and Electron Transport* Boston, MA: Springer US, 99–120.
- [14] Tejero-del-Caz, A., Guerra, V., Pinhão, N., Pintassilgo, C. D., and Alves, L. L. 2021 “On the quasi-stationary approach to solve the electron Boltzmann equation in pulsed plasmas” *Plasma Sources Sci. Technol.* **30**, 065008.
- [15] Dhali, S. K. 2022 “Transient behavior of drift and ionization in atmospheric pressure nitrogen discharge” *Plasma Sources Sci. Technol.* **31**, 025014.
- [16] Hoder, T., Loffhagen, D., Voráč, J., Becker, M. M., and Brandenburg, R. 2016 “Analysis of the electric field development and the relaxation of electron velocity distribution function for nanosecond breakdown in air” *Plasma Sources Sci. Technol.* **25**, 025017.
- [17] Bieniek, M. S., Walsh, J. L., and Hasan, M. I. 2021 “Modeling the thermalization of electrons in conditions relevant to atmospheric pressure He-O<sub>2</sub> nanosecond pulsed discharges” *Phys. Plasmas* **28**, 063501.
- [18] White, R. D., Dujko, S., Ness, K. F., Robson, R. E., Raspopović, Z., and Petrović, Z. L. 2008 “On the existence of transiently negative diffusion coefficients for electrons in gases in E × B fields” *J. Phys. D: Appl. Phys.* **41**, 025206.
- [19] White, R. D., Dujko, S., Robson, R. E., Petrović, Z. L., and McEachran, R. P. 2010 “Non-equilibrium transport of positron and electron swarms in gases and liquids” *Plasma Sources Sci. Technol.* **19**, 034001.
- [20] Pokrovskiy, G. V., Popov, N. A., and Starikovskaia, S. M. 2022 “Fast gas heating and kinetics of electronically excited states in a nanosecond capillary discharge in CO<sub>2</sub>” *Plasma Sources Sci. Technol.* **31**, 035010.
- [21] Zhu, Y., Lepikhin, N. D., Orel, I. S., Salmon, A., Klochko, A. V., and Starikovskaia, S. M. 2018 “Optical actinometry of O-atoms in pulsed nanosecond capillary discharge: peculiarities of kinetics at high specific deposited energy” *Plasma Sources Sci. Technol.* **27**, 075020.

- [22] Šimek, M. and Bonaventura, Z. 2018 “Non-equilibrium kinetics of the ground and excited states in N<sub>2</sub>-O<sub>2</sub> under nanosecond discharge conditions: extended scheme and comparison with available experimental observations” . *Phys. D Appl. Phys.* **51**, 504004.
- [23] Park, S.-K. and Economou, D. J. 1990 “Analysis of low pressure rf glow discharges using a continuum model” *J. Appl. Phys.* **68**, 3904–3915.
- [24] Tejero-del-Caz, A., Guerra, V., Gonçalves, D., Lino da Silva, M., Marques, L., Pinhão, N., Pintasilgo, C. D., and Alves, L. L. 2019 “The LisbOn KInetics Boltzmann solver” *Plasma Sources Sci. Technol.* **28**, 043001  
<https://github.com/IST-Lisbon/LoKI>.
- [25] Makabe, T., Nakano, N., and Yamaguchi, Y. 1992 “Modeling and diagnostics of the structure of rf glow discharges in Ar at 13.56 MHz” *Phys. Rev. A* **45** (4), 2520–2531.
- [26] Dujko, S., Raspopović, Z. M., and Petrović, Z. L. 2005 “Monte Carlo studies of electron transport in crossed electric and magnetic fields in CF<sub>4</sub>” *J. Phys. D Appl. Phys.* **38**, 2952.
- [27] Vialeto, L. 2021 “Modelling of plasma for CO<sub>2</sub> conversion: electron kinetics, chemistry and transport” PhD thesis Applied Physics and Science Education, Eindhoven University of Technology.

# 7

## Conclusion

Monte Carlo (MC) methods describe the physical dynamics by tracking the stochastic evolution of a representative ensemble of particles, allowing for a straightforward representation of all primary processes that each particle in the system may undergo. This doctoral thesis aimed to develop and apply modeling and simulation methods based on MC techniques to study low-temperature plasmas. These methods have been employed to describe both electron and heavy-species kinetics. In the following paragraphs, we summarize the efforts presented in each chapter along with the main conclusions.

Chapter 2 presents a Kinetic Monte Carlo (KMC) method for solving the complex chemical kinetics of heavy species in low-temperature plasmas [1], based on the algorithm developed by Gillespie [2]. To the best of our knowledge, this constitutes the first time that gas-phase chemistry in gas discharges has been described with a MC approach. When the system conforms to the thermodynamic limit, the results of the KMC formulation are entirely analogous to those of the deterministic method, which consists of continuous evolution determined by rate balance equations. Moreover, this MC-based method is applicable in situations where deterministic simulations may fail, such as when fluctuations and correlations play a significant role in the dynamics. The statistical precision of the KMC description scales with the number of particles in the simulation. However, computation time increases linearly with the number of particles. To address these challenges and reduce the statistical error associated with the description of minority-species densities without impacting computation time, two variance reduction methods were developed: Equal Reaction Weights (ERW) and Variable Species Weights (VSW). In simple terms, ERW compensates for the reaction choice so that each reaction has the same weight, regardless of the involved reactants. On the other hand, VSW compensates for the reaction choice by assigning weight to each species based on the inverse of the corresponding number of particles. While both techniques significantly improve the representation of rare species densities, ERW appears to be more promising as it preserves the accurate description of prevalent species, whereas VSW adds considerable noise. The application of variance reduction methods is essential to ensure an acceptable description of all species, including ions, which can have relative densities ranging from  $10^{-7}$  to  $10^{-10}$ . These variance reduction methods are applicable to real systems and address the multi-time-scale problem intrinsic to plasma chemistry in low-temperature plasmas, resulting in a substantial improvement in calculation times, on the order of  $10^4$  times, compared to the standard KMC approach.

Chapter 3 presents the first version of the LoKI-MC open-source code [3], which has been developed from scratch within the framework of this thesis. This simulation tool solves the electron transport in a gas subject to a uniform DC electric field using MC techniques. The code development arose from the need for a general electron kinetics solver openly available to the community that does not rely on the typical two-term approximation to solve the electron Boltzmann equation, whose accuracy is questionable in a wide range of conditions. Some of the key features of LoKI-MC include: (i) incorporation of the thermal motion of the gas molecules; (ii) straightforward insertion of gas internal levels and,

accordingly, of superelastic and stepwise processes; (iii) capability to describe anisotropic scattering in ionization, induced by momentum conservation, and availability of different models for the energy sharing between primary and secondary electrons; (iv) provision of the electron power balance over the various collisional channels. The formulation has been verified and benchmarked in model gases and real gases with remarkable success, through the comparisons with analytical solutions, previous works and other simulation tools. Additionally, it is found that: (i) the inclusion of the gas temperature effect is fundamental to obtain correct thermodynamic properties at low  $E/N$ ; (ii) anisotropic ionization scattering can lead to significant deviations of electron transport parameters at high  $E/N$ , when compared to the usual assumption of isotropic ionization scattering; (iii) superelastic collisions, involving rotational, vibrational or electronic levels, may have a large impact on the results, and this justifies the importance of easily considering arbitrarily complex gas mixtures, as in LoKI-MC. The code is written in C++, benefiting from an efficient object-oriented structure, and proves to be highly performant compared to the MC solver METHES [4]. LoKI-MC is freely available for users to perform electron kinetics calculations, and can be easily embedded in plasma-chemistry or fluid models for the calculation of electron rate coefficients and transport parameters.

Chapter 4 demonstrates how anisotropic scattering can be integrated easily and with generality into the MC formulation in LoKI-MC [5]. The significance of considering anisotropic scattering is evidenced in water vapor ( $H_2O$ ), where electron kinetics is significantly affected by the angular distribution in rotational collisions. In addition, the MC results are compared against solutions from the two-term Boltzmann equation, which accounts for anisotropic scattering under approximations valid specifically for rotational collisions. The  $H_2O$  cross-section set and the incorporation of anisotropic scattering are validated using the electron swarm analysis technique. The introduction of a proper anisotropic angular distribution in rotational collisions substantially enhances the agreement between calculations and measurements of the electron transport coefficients.

Chapter 5 expands the capabilities of LoKI-MC to handle configurations involving AC/DC electric fields and DC magnetic fields crossed at arbitrary angles [6]. The code performance is assessed through comparisons with various independent benchmark calculations from the existing literature. Additionally, we introduce novel benchmark calculations designed specifically for evaluating electron kinetics solvers in scenarios with coexistent AC electric and DC magnetic fields, accounting for the effect of the crossing angle between the fields and discriminating the evolution along the AC cycle. The impact of the magnetic field is studied both in model gases (Reid-ramp and Lucas-Saelee) and in real gases ( $N_2$  and Ar), distinguishing configurations with DC and AC electric fields. In DC electric fields, the oscillatory motion caused by the magnetic field decreases the electron acceleration efficiency, affecting the power absorbed by the electric field and the mean electron energy. Notably, a unique behavior is found in Ar for small regions of  $E/N$  and  $B/N$ , where: for constant  $B/N$ , the mean energy decreases with increasing  $E/N$ ; and, for constant

$E/N$ , it increases with increasing  $B/N$ . These phenomena were firstly reported by Ness and Makabe [7] in 2000 and are now confirmed by means of Monte Carlo simulations. In AC electric fields, when the electron cyclotron frequency is similar to the angular frequency of the field, the synchronization of the cyclotron motion with the electric field enhances electron acceleration, through the well-known electron cyclotron resonance. However, for conditions where the mean collision frequency is much higher than the cyclotron frequency, the synchronization tends to breakdown and the magnetic field becomes detrimental for the electron acceleration, as in the DC electric field case.

Chapter 6 extends the scope of LoKI-MC to encompass time-dependent  $E/N$  pulses. By considering the rigorous time-dependent MC solution as golden standard, we evaluate the accuracy of two common assumptions for solving space- and time- dependent electron kinetics. The first assumption is the local-field approximation (LFA), which equates the electron kinetics solution to the steady-state calculation, using the local value (in space and time) of  $E/N$ . The second is the local-energy approximation (LEA), where the rate coefficients and the electron power distribution among different collisional channels depend on the local value of the mean energy. The study is focused on time-locality, assessing the accuracy of the LFA and LEA for solving homogeneous electron kinetics in nanosecond-pulsed discharges. The investigation involves a typical nanosecond pulse and assesses electron relaxation in two background gases (air and argon) and two pressures (10 and 100 Torr). Our findings indicate that the LEA generally provides more accurate results than the LFA, with the differences becoming more pronounced at lower pressures where energy relaxation is slower. The enhanced accuracy of the LEA is due to the temporal effects introduced by the equation for the mean electron energy, which is absent in the LFA. Therefore, when a purely kinetic approach is not possible, the LEA is the preferred choice over the LFA. Opting by the LFA can lead to serious degradation of model results. During the first nanoseconds, the excessively fast relaxation of the LFA leads to an overestimation of electron energy, resulting in an overvaluation of electron-impact ionization, dissociation and excitation. The exaggeration in ionization affects the electron density, which subsequently influences all heavy-species chemistry involving electron impact. The repercussions of the LFA can be even more pronounced during the late-decay phase of the pulse, where the LFA predicts a excessively fast decrease of electron energy. This inaccuracy is crucial because electron density can remain elevated for a considerable time after the pulse, influencing heavy-species chemistry. In repetitively-pulsed discharges, the accumulation of these systematic errors after each pulse could cause dramatic changes in the model predictions. Moreover, we have demonstrated that a thorough comparison between the characteristic frequencies of momentum transfer and energy relaxation, in conjunction with the rate of  $E/N$  variation, delineates the domains of validity for time-locality approximations, such as LFA and LEA. Temporal discrimination is fundamental in this examination, as mean electron energies and, consequently, relaxation frequencies, vary significantly over time. Finally, we extended the comparison to a two-term time-dependent solution (with a quasi-stationary approximation for the first anisotropy

$f_1$ ), using the LoKI-B solver. Notably, at the lower pressure of 10 Torr, the two-term approach cannot capture the initial transient non-equilibrium behavior.

The research project goes beyond the four years of doctoral work and there are various directions to be pursued in the near future, concerning the development and exploitation of MC techniques to study low-temperature plasmas. Some of them are described in the following points.

- The next immediate step involves the development of a simulation model to investigate the coupled electron and heavy-species kinetics in nanosecond pulsed discharges. Our goal is to create a unified Monte Carlo formulation capable of stochastically solving the temporal evolution of electron kinetics while continuously advancing the gas-phase chemistry on the electron timescale. We will compare this unified formulation with the common ground-state approximation used for solving electron kinetics, where electron swarm coefficients (subsequently used in heavy-species kinetics) are calculated under the assumption of no excited or dissociated states. This comparison will allow us to assess the significance of properly accounting for the mutual influence between excited-state chemistry and electron kinetics, which is an inherent aspect of the unified formulation. Additionally, by comparing the chemistry results obtained with the unified formulation to those obtained with electron-impact coefficients calculated using the LFA or the LEA, we can quantify the impact of these time-locality assumptions for the electron kinetics on chemical kinetics. Finally, we aim at directly comparing the model results against experimental measurements in nanosecond discharges, including the ones of my secondment at IPP in Prague [8, 9].
- As extensively referenced throughout this thesis, the two-term approximation for solving the electron Boltzmann equation (EBE) has significant limitations in conditions of strong anisotropies in the velocity space, which occur when the electric field is high and/or inelastic collisions dominate over elastic collisions. The low-temperature plasma community has extensively reported comparisons between electron kinetics results obtained with the two-term approximation and more accurate formulations, such as multi-term expansions of the EBE or MC simulations. Nevertheless, systematic investigations into the direct impact of the two-term approximation on chemical kinetics remain limited. To address this gap, our objective is to assess the influence of the two-term approximation on self-consistent simulations of the positive column in a DC glow discharge, for various gas pressure and discharge current settings. The ultimate accuracy of the two-term approximation will be evaluated based on key results, including gas temperature, electron density and heavy-species densities. We have selected this simple discharge configuration due to its widespread use in modeling and experimental research. This study may offer insights into whether some discrepancies between model and experimental heavy-species values can be attributed to inaccuracies in the two-term approximation. Our investigations will cover common gas discharges, including O<sub>2</sub>, CO<sub>2</sub>, N<sub>2</sub> and Ar.

- We plan to leverage the capabilities of LoKI-MC presented in chapter 5 to model gas discharges in a presence of an external magnetic field. This will entail incorporating the electron kinetics results into 0D or fluid models, ultimately providing a deeper understanding of discharges in configurations relevant to various applications.
- Finally, we aim at coupling the KMC formulation for the heavy-species kinetics (presented in chapter 2) to the surface kinetics, to better understand plasma-induced surface modification [10, 11]. The interest in a KMC formulation for surface kinetics is justified by the possible failure of some approximations made in deterministic formulations to describe the surface diffusion of physisorbed species [10].

## References

- [1] Dias, T. C. and Guerra, V. 2020 “Kinetic Monte Carlo simulations of plasma-chemistry” *Plasma Sources Sci. Technol.* **29**, 115003.
- [2] Gillespie, D. 1976 “A General Method for Numerically Simulating the Stochastic Time Evolution of Coupled Chemical Reactions” *J. Comput. Phys.* **22**, 403–34.
- [3] Dias, T. C., Tejero-del-Caz, A., Alves, L. L., and Guerra, V. 2023 “The LisbOn KInetics Monte Carlo solver” *Comput. Phys. Commun.* **282**, 108554  
<https://github.com/IST-Lisbon/LoKI-MC>.
- [4] Rabie, M. and Franck, C. M. 2016 “METHES: A Monte Carlo collision code for the simulation of electron transport in low temperature plasmas” *Comput. Phys. Commun.* **203**, 268–277  
[www.lxcat.net/download/METHES](http://www.lxcat.net/download/METHES).
- [5] Budde, M., Dias, T. C., Vialatto, L., Pinhão, N., Guerra, V., and Silva, T. 2023 “Electron-neutral collision cross sections for H<sub>2</sub>O: II. Anisotropic scattering and assessment of the validity of the two-term approximation” *J. Phys. D: Appl. Phys.* **56**, 255201.
- [6] Dias, T. C., Pintassilgo, C. D., and Guerra, V. 2023 “Effect of the magnetic field on the electron kinetics under AC/DC electric fields: benchmark calculations and electron cyclotron resonance” *Plasma Sources Sci. Technol.* **32**, 095003.
- [7] Ness, K. and Makabe, T. 2000 “Electron transport in argon in crossed electric and magnetic fields” *Phys. Rev. E* **62** (3), 4083–4090.
- [8] Bílek, P., Dias, T. C., Prukner, V., Hoffer, P., Guerra, V., and Šimek, M. 2023a “Streamer-induced kinetics of excited states in pure N<sub>2</sub>: I. Propagation velocity, *E/N* and vibrational distributions of N<sub>2</sub>(C<sup>3</sup>Π<sub>u</sub>) and N<sub>2</sub><sup>+</sup>(B<sup>2</sup>Σ<sub>u</sub><sup>+</sup>) states” *Plasma Sources Sci. Technol.*

- [9] Bílek, P., Dias, T. C., Prukner, V., Guerra, V., and Šimek, M. 2023b “Streamer-induced kinetics of excited states in pure N<sub>2</sub>: II. Formation and quenching of N<sub>2</sub>(B<sup>3</sup>Π<sub>g</sub>,  $v = 0 - 12$ ) through advanced analysis of emission produced by the first positive system” *In preparation.*
- [10] Guerra, V. and Marinov, D. 2016 “Dynamical Monte Carlo methods for plasma-surface reactions” *Plasma Sources Sci. Technol.* **25**, 045001.
- [11] Marinov, D., Teixeira, C., and Guerra, V. 2017 “Deterministic and Monte Carlo methods for simulation of plasma-surface interactions” *Plasma Process Polym* **14**, 1600175.

